MULTI-SCALE STRUCTURAL HEALTH MONITORING USING WIRELESS SMART SENSORS

BY

HONGKI JO

DISSERTATION

Submitted in partial fulfillment of the requirements
for the degree of Doctor of Philosophy in Civil Engineering
in the Graduate College of the
University of Illinois at Urbana-Champaign, 2013

Urbana, Illinois

Doctoral Committee:

Professor Gul A. Agha, Chair
Professor Billie F. Spencer, Jr., Director of Research
Assistant Professor Larry A. Fahnestock
Assistant Professor Daniel B. Work
Adjunct Associate Professor Stephen D. Downing

ABSTRACT

Tremendous progress has been made in recent years in the wireless smart sensor (WSS) technology to monitor civil infrastructures, shifting focus away from traditional wired methods. Successful implementations of such WSS networks for full-scale SHM have demonstrated the feasible use of the technology. Much of the previous research and application efforts have been directed toward single-metric applications. Multi-metric monitoring, in combination with physics-based models, has great potential to enhance SHM methods; however, the efficacy of the multi-metric SHM has not been illustrated using WSS networks to date, due primarily to limited hardware capabilities of currently available smart sensors and lack of effective algorithms. This research seeks to develop multi-scale WSSN strategies for advanced SHM in cost effective manner by considering: (1) the development of hybrid SHM method, which combine numerical modeling and multi-metric physical monitoring, (2) multi-metric and high-sensitivity hardware developments for use in WSSNs, (3) network software developments for robust WSSN, (4) algorithms development to better utilize the outcomes from SHM system, and (5) full-scale experimental validation of proposed research. The completion of this research will result in an advanced multi-scale WSS framework to provide innovate ways civil infrastructure is monitored.

ACKNOWLEDGEMENT

First of all, I would like to deliver my sincere gratitude and respect to my advisor, Prof. B.F. Spencer, Jr. for his guidance on my PhD research as well as all his supports for my UIUC life. Being his student was one of the most fortunate things through my entire life. I learn really a lot from his deep academic insight, trustful attitude to his students, dedication to teaching, and nice human skills; which greatly would impact on my future academic life. Indeed, he is my ultimate role model in all aspects as researcher, advisor, lecturer, and father of kids.

I would also like to thank my committee members, Prof. Gul Agha for his heartfelt advice on my research and strong recommendation letter, Prof. Larry Fahnestock for helpful information for young faculty, Prof. Daniel Work for his in-depth introduction to the boundless world of Kalman filter, and Prof. Stephen Downing for his unconditional aid on my sensor development research. I sincerely appreciate their valuable comments, advice, and supports on my research and future career.

I deeply appreciate Prof. In-Won Lee, my former advisor for my M.S. study, for his big encouragement for me to study again. He was always proud of me. Prof. Chung-Bang Yun introduced the world of structural health monitoring research to me and provided continuous supports and heartfelt advice through my entire Ph.D. study. Prof. Hyung-Jo Jung always tried to support me in many aspects and enabled the Jindo Bridge Project, which would be one of the most brilliant assets in my academic career. I would never forget their supports and kind concern.

I am also grateful to Prof. Yozo Fujino for his unconditional support and strong recommendation letter, and Prof. Tomonori Nagayama for his valuable comments on my research.

I would like to thank all of the SSTL members, Prof. Jennifer Rice, Prof. Brian Phillips, Dr. Lauren Linderman, Dr. Jian Li, Dr. Ryan Giles, Dr. Chia-Ming Chang, Prof. Manuel Sandoval, Andrzej Tatkowski, Kaitlin White, Nicholas Wierschem, and Fernando Moreu for their helps to my research and kindness. Their academic excellence always stimulated and influenced me. I would never meet such excellent and nice colleague again in my academic life. Particularly, my senior Korean colleagues, Prof. Sung-Han Sim showed me the world of decentralized sensor network and served as my graduate-study mentor and best friend. I learn a lot about the full-scale bride experiment from Prof. Shinae Jang. I sincerely appreciate my junior Korean colleagues, Robin Kim for her confidence and warm heart to be a help to me, Hyungchul Yun for unconditional helps in lots of aspects.

I would like to express my gratitude to all Korean students in UIUC Civil Engineering department, Dr. Do-Soo Moon, Donghyuk Jung, and Prof. Jun-Hee Kim. I really enjoyed playing tennis with Sungwoo Moon, Dr. Moochul Shin's sincerity and mature mind always influence on me, and every day lunch and chatter with Seung Jae Lee and Byungmin Kim was a tonic for my UIUC life. Prof. Oh-Sung Kwon's exemplary life influenced on me a lot.

I would also like to thank my KAIST colleagues. I enjoyed in-depth research discussion with Dr. Soojin Cho and appreciate his helps during his Post Doc in SSTL. And I liked Jongwoong Park's joke and appreciate his helps to my strain sensor board development. Particularly, the Jindo Bridge project might not succeed without the efforts of these two guys and SeungSeob Jin.

I sincerely appreciate Kirill Mechitove for his helps to resolve many software issues in my Ph.D. research. And I enjoyed working with Parya Moinzadeh, one of my colleagues in computer science for the Jindo Bridge project.

The research in this dissertation has been supported by the National Science Foundation Grants CMS 06-00433 and CMS 09-2886 (Dr. S.C. Liu, program manager) and the Korea Research Foundation Grant NRF-2008-220-D00117. These supports are gratefully appreciated.

Last but not least, I thank my parents, parents in law, brother and sister for their unconditional support and belief on me. Particularly, I would like to deliver my sincere gratitude to my wife, MyungHwa Shim, for her boundless supports and love. Without my wife and two kids, Ashley and Elliott, I could not make it through rough times in completing my Ph.D. study. I LOVE YOU.

TABLE OF CONTENTS

LIST OF FIGURES

LIST OF TABLES

CHAPTER 1 INTRODUCTION

Declining conditions and performance of civil infrastructure, which would threat public safety, have been critical issues in most industrialized nations. Expenditure on maintaining and enhancing such aging civil systems has occupied significant portion of nations' capital investment. For example, the U.S. Department of Transportation (US DOT 2010) has reported that $46.6 billion was used for rehabilitating highways and bridges and $11.0 billion for system enhancements in 2008, of which sum is about 63.2% of the total $91.1 billion capital outlay by all levels of government, while $33.6 billion (36.8%) was used for system expansion. Improving and modernizing the infrastructure is an important part of current government policy on ensuring homeland security and maintaining economic vitality.

The ability to assess the performance of such civil infrastructure in timely manner and detect damages at an early state can potentially reduce the costs as well as downtime associated with repairing and rehabilitating the systems, all while providing increased public safety. Visual inspection has been a current practice in monitoring the safety of civil infrastructure. However, high costs and unreliability often limit the use of visual inspection to infrequent occurrences. Structural health monitoring (SHM) that combines various sensing technologies with embedded measurements provides an essential tool to assess real states of structures. Moreover, the principles of SHM and its application will aid not only in the inspection of existing infrastructure, but allow rapid assessment on the safety of emergency facilities and evacuation routes, including bridges and highways, after natural disasters. Continuous and automated structural health monitoring can facilitate these goals.

For timely and effective maintenance of structures, the current structural and environmental conditions first should be evaluated accurately, including applied loading conditions, structural responses to the loadings, structural damage status, and load carrying capacities of the structural members. Then, appropriate guidelines should be established for making decisions regarding whether the structures need to be retrofitted/rehabilitated or not, as well as assessing means to restore the structure to working condition.

A tremendous amount of research has been conducted on the topic of efficient and effective monitoring the civil infrastructure during past few decades. Detailed reviews of this work are provided by Doebling et al. (1996) and Sohn et al. (2003). Conventional systems based on wired sensors and data acquisition have long been the standard for SHM; however, realizations of such wired systems are limited by high-cost and scalability, as structures become larger and more complex. Because damage in civil infrastructure is intrinsically a local phenomenon, dense sensor deployment is required (Spencer, et al. 2004); as the sensors are located closer to the damage site, more accurate damage detection and assessment is possible. Realization of such a dense array of sensors using the traditional wired approaches is indeed challenging, due to difficulties in wiring and installing of sensors, central data collection, and high cost.

Recent advanced sensor technologies have enabled SHM using wireless smart sensor networks (WSSNs), which is a promising alternative to the traditional wired SHM approaches. The smart sensors are typically small, inexpensive, and capable of wireless communication and onboard computation (Spencer et al. 2004), addressing many of the concerns regarding wired monitoring. For example, easy installation and the associated reduction of installation cost, multi-hop communication, and decentralized in-network data processing are available with recent advances of WSSN; these attractive features enable the development of scalable

monitoring systems and dense sensor networks. Many academic and commercial smart sensors have been developed in the last decade and a half. Significant effort has been devoted to wireless data acquisition, high-precision synchronized sensing, damage detection in WSSNs, and autonomous WSSNs for long-term SHM, particularly focusing on realizing reliable and power efficient WSSNs for full-scale SHM (Lynch et al., 2003; Whelan et al., 2007; Pakzad et al., 2008; Jennifer et al., 2010; Jang et al., 2010; Cho et al., 2010). Such efforts have demonstrated the feasibility of WSSNs for SHM.

Several WSSNs have been successfully implemented for SHM applications in recent years; however, high-sensitivity sensing of various types of structural responses has not been readily available in WSSNs due to limited hardware and software capabilities of WSSNs. Moreover, they do not work in concert with one another to take advantage of the multi-metric SHM. Also, the network/power management software required for more robust and long-term operation of self-powered WSSNs has yet to be effectively integrated to allow extended and practical SHM applications.

Though the WSS technology is innovating the way for physical monitoring of structural integrity; however, identifying all potential damage locations is not possible. Computational modeling techniques have been remarkably advanced in recent years. Indeed, model-based SHM approaches have significant potentials if they can be utilized in conjunction with the physical monitoring methods.

The objective of this research is to provide multi-scale SHM framework using WSSNs by addressing the issues that have limited the applicability of WSSNs for multi-metric SHM and the realization of robust self-powered SHM system, overcoming the limitation of conventional monitoring method. In particular, this research address the following five aspects of realizing

multi-scale SHM using WSSNs: (1) the development of hybrid SHM strategy which combines numerical modeling and multi-metric monitoring, (2) the development of high-sensitivity multi-metric sensors for use with WSSs, (3) the software development for long-term and robust operation of self-powered WSSNs, (4) the development of multi-scale SHM strategies tailored for WSSNs, and (5) the full-scale long-term validation of the multi-scale SHM framework. The following paragraphs outline the key components of this research summarized in this dissertation.

Chapter 2 provides the background of this research. Research efforts on SHM, WSSNs for SHM, and full-scale implementation of WSSNs for SHM are reviewed. Technologies for multi-metric SHM and fatigue life assessment of civil systems are presented, and the limitations of these technologies for use in WSSNs are identified. An overview of the Kalman filter is presented, focusing on multi-metric data fusion.

Chapter 3 presents a new algorithm development to overcome the limitations of conventional SHM methods. A hybrid SHM strategy combining numerical modeling and physical monitoring proposes new paradigm by which civil infrastructure can be monitored. Specifically, the Kalman filter enables such a hybrid approach, allowing accurate estimation of any type of structural responses at arbitrary locations on structures. The efficacy of the hybrid SHM method is numerically validated with example applications for fatigue monitoring of a steel truss structure and displacement monitoring of a tall column structure.

In Chapter 4, the development of a variety of multi-metric hardware tailored for SHM applications using WSS is presented. A high-sensitivity accelerometer board is developed for low-level ambient acceleration monitoring, and a SHM data acquisition board is developed to accommodate external analog and digital sensors into WSSNs. A SHM strain board developed in this research provides autonomously balanceable Wheatstone bridge, onboard temperature

compensation, and onboard shunt calibration capabilities, allowing high-precision strain sensing. And the development of a 24-bits data acquisition board addresses many issues due to the limited resolution of WSSs.

Chapter 5 presents software developments that allow long-term and robust operation of WSSNs for SHM. Self-diagnostic power management software provides an enabling foundation for perpetual-like operation of WSSN. And the software development for autonomous monitoring of network/environment conditions provides key information for network management and assessment of environmental effects on structural integrity.

Chapter 6 presents new multi-scale SHM strategies to better utilize the outcomes from SHM systems. The multi-scale use of different-sensitivity sensors in WSSNs allows better identification of modal properties of structures in cost effective manner. The use of densely arrayed low-resolution GPS sensors improves the accuracy of dynamic displacement monitoring.

Chapter 7 describes full-scale validation of the developed SHM framework using WSSN, constituting the world's largest WSSN for civil infrastructure monitoring. The performance of the developed hardware, software, and selected algorithms are verified through long-term operation of WSSN for monitoring of a cable-stayed bridge in South Korea.

Chapter 8 summarizes the research presented in this dissertation and discusses possible direction for future studies to extend the WSSN framework for broader classes of applications.

CHAPTER 2 BACKGROUND

2.1 **Structural Health Monitoring**

Deteriorating civil infrastructure has long been of intense interest to the research community. Catastrophic structural failures, such as the Silver Bridge collapse in 1967 (USA) and Sungsu bridge collapse in 1994 (Korea) have resulted in the establishment government-mandated bridge inspection programs (Small et al. 1999).

Structural Health Monitoring (SHM) is often referred as a comprehensive process, encompassing all of the technology and algorithms for measuring structural responses, evaluating the condition of as-built or under-construction structures, detecting structural deficiencies, understanding load-response relationships, predicting future performance or remaining fatigue life, and consequently providing information for decision making about maintenance and safety. Doebling et al. (1996), Farrar (2001), Sohn et al. (2003), and Brownjohn (2007) have provided well-summarized overviews of SHM.

SHM systems have been deployed on many bridge structures during the past few decades. Some of representative full-scale examples include: the Golden Gate Bridge in San Francisco, CA (Chaffar et al. 1985a and 1985b), the Bill Emerson Memorial Bridge in Cape Girardeau, MO (Caicedo et al. 2002, Celebi 2006), the Tsing Ma Bridge in Hong Kong (Wong 2004, Wong 2007, Ni et al. 2010), the Stonecutters Bridge in Hong Kong (Wong 2004), the Akashi-Kaikyo Bridge in Japan (Fujino et al. 2000).

Despite successful implementations of these SHM systems, the applicability of the traditional SHM approaches using wired system has been limited to few signature structures. Most of small- and medium-scale structures have no such SHM systems, due primarily to high equipment

and installation costs. For example, the 350 sensing channels installed on the Tsing Ma Bridge cost approximately $8 million (Lynch and Loh 2006). And the 63 sensors deployed on the Humber Bridge required 32 km of cabling (Brownjohn 2007).

2.2 **Wireless Smart Sensor Network for SHM**

Recent advances in MEMS technology have provided new opportunities for wireless smart sensing, which has the potential to address a number of challenges related to the wider use of traditional wired SHM systems. "Smart" sensor has been defined as the sensor platform having the following four features: (i) on-board central processing unit (CPU), (ii) small size, (iii) wireless, and (iv) the promise of being low-cost (Spencer et al. 2004), emerging as promising alternative to traditional wired approaches.

Steady improvements have been made in wireless smart sensor technologies for SHM purpose during a past decade. Straser and Kiremidjian (1998) developed one of the earliest wireless modular monitoring systems, named WiMMS; subsequently, many researcher have developed academic wireless smart sensors, including: Bennett el al. (1999), Lynch et al. (2001), Mitchell et al. (2002), Shinozuka (2003), Farr et al. (2005), and Wang et al. (2005). On the commercial side, Crossbow licensed technology from Berkeley to provide the Rene mote in 1999 and subsequently, the Mica series (Mica, Mica2, and MicaZ) from 2002. Intel released the Imote smart sensor platform in 2003, and introduced the 2nd generation of the Intel Mote, the Imote2, in 2006. MoteIV has introduced the low-power wireless sensor platform, Telos(B)/Tmote Sky, and Microstrain also has provided various wireless sensor series including SG-Link wireless strain node and SG-Link wireless accelerometer node since 2003. Spencer et al. (2004) and Lynch and Loh (2006) provide extensive and comprehensive reviews on the wireless smart sensors.

2.2.1 Sensing using smart sensors

Since the various WSS platforms were introduced from the end of 1990's, accompanying sensor boards also have been developed and released to equip the platforms with diverse sensing capabilities. Researchers have also developed their own customized sensor boards due to the inability of available sensor boards to meet the high demands of SHM applications.

2.2.1.1 Acceleration sensing

Ruiz-Sandoval et al. (2003) developed a high-sensitivity accelerometer board for the Mica2 platform, as the accelerometer (ADXL202E) on the commercially available sensor board (MTS310CA, CrossBow 2003) for Mica2 showed poor performance. Though a low-noise high-sensitivity MEMS accelerometer (SD1221, SiliconDesigns Inc 2003) was used in the board, however, the 10-bit ADC resolution of the Mica2 could not support the high-quality sensing available from the accelerometer. The lack of anti-aliasing (AA) filters priors to signal digitization also limited the performance of the board.

Pakzad and Fenves (2004) developed a similar accelerometer board for the Mica2 platform, but overcame the resolution and AA filter issues by employing 16-bit A/D converter, as well as single-pole low-pass filters. In addition to the SD1221 low-noise accelerometer for ambient vibration measurements, the ADXL202 accelerometer also was considered for high-level vibration. Diverse calibration tests validated the dynamic and static performance of the sensor board.

Whelan and Janoyan (2009) developed a signal conditioning board for the Tmote Sky platform (MoteIv 2006) to interface with a single-ended analog accelerometer. To maximize the resolution of the conversion specific to the signal input range, a programmable gain amplifier

(PGA) was employed, and to correct the possible signal offset prior to amplification, such as gravitational offset of the accelerometer, the reference correction voltage was provided with 12-bit digital-to-analog (DAC) converter. A low-pass Butterworth filter was considered to prevent aliasing of unnecessary higher frequency signal. A two-axis MEMS accelerometer (LIS2L02AL, ST Microelectronics 2005) was used with the signal conditioning circuit for acceleration sensing.

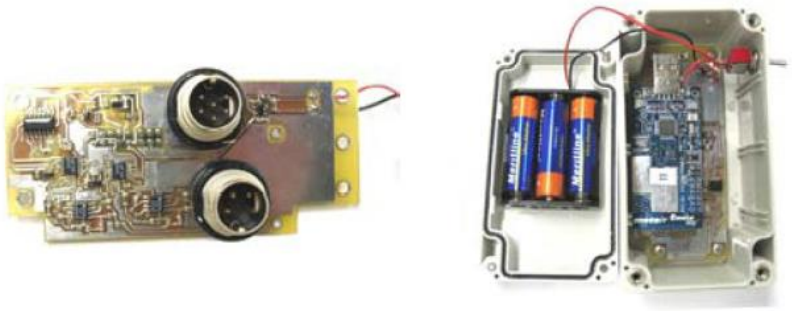

Figure 2.1. Prototype signal conditioning board for Tmote Sky platform and sensor node assembly (Whelan and Janoyan 2009).

The Imote2 platform had a commercially available multimetric sensor board that supported acceleration, temperature, humidity, light intensity measurements (ITS400C sensor board, Crossbow Technology 2007). The acceleration sensing feature of the board was evaluated to determine its appropriateness for SHM application by Nagayama and Spencer (2007). Results show a lack of flexibility in selecting the sampling rates, different sampling rates for different sensors, and even sampling rate fluctuation on a given sensor, rendering this sensor board inappropriate for SHM applications.

Nagayama and Spencer (2007) were able to resolve many of these sampling rate issues of the ITS400C sensor board through software approach using a resampling algorithm which involved timestamping the measured data. Rice and Spencer (2008) then addressed these problems in

hardware by developing a structural health monitoring sensor board (SHM-A board) for the Imote2 platform; the sampling rate issues were addressed by connecting an analog accelerometer to a high-quality ADC. The key component of the SHM-A board is the Quickfilter QF4A512 ADC, which is a versatile 4ch/16bit ADC and programmable signal conditioner with user-selectable sampling rate and programmable digital filters. Each channel has a programmable gain amplifier (PGA), an analog anti-aliasing (AA) filter with a 500 KHz cutoff frequency, individually selectable sampling frequencies and programmable digital FIR filters. The block diagram of the QF4A512 is shown in Figure 2.2. The LIS344ALH 3-axes MEMS accelerometer was used for the board, with a 0.3~0.6mg RMS noise over a 20Hz bandwidth observed in calibration tests. Though the 0.3~0.6mg is sufficient for medium to high level acceleration sensing, to broaden the applicability of wireless sensing using the Imote2 to low-level ambient vibration monitoring, particularly for large-scale civil infrastructure, further improvement for high-sensitivity sensing was still required.

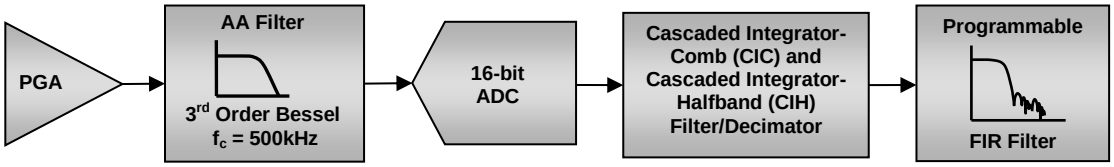

Figure 2.2. Functional block diagram of Quickfilter QF4A512 (Rice and Spencer 2008).

2.2.1.2 Strain sensing

Considerable research has been conducted on wireless strain monitoring. Hautamaki et al. (1999) conducted one of the earliest studies of wireless strain monitoring. A MEMS strain sensor, composed of a resistive-type strain gage, a signal processing unit, and an antenna, was embedded

in a polymer composite to investigate the effects of the wafer geometry and composite plate stiffness. Matsuzaki et al. (2005) developed a passive wireless strain sensing system to measure the strain induced in an automotive tire using the electrical capacitance changes in an oscillating circuit. The specific frequency in the oscillating circuit, which is composed of capacitors and resistors, represent strain changes and is transmitted wirelessly using an external antenna. More recently, use of a rectangular microstrip patch antenna for strain measurements has been demonstrated by Tata et al. (2009). The rectangular patch antenna was able to resonate at its own frequency dependent on the length or width of patch antenna, hence strain changes cause antenna length or width changes, which result in the shift of the corresponding frequency. The rectangular patch antenna has been used for wireless monitoring of fatigue crack growth (Erdmann et al. 2010), and a circular-shape patch antenna has also showed the possibility of a strain sensor by showing the resonant frequency is dependent on the radius (Daliri et al. 2010).

Though the aforementioned MEMS based oscillator and antenna technologies showed the feasibilities for wireless strain sensing; however, they are not appropriate for civil infrastructure SHM applications, which require high-throughput, highly accurate time synchronization, and dynamic monitoring. Galbreath et al. (2003) introduced a power-efficient and high-speed wireless sensor for civil infrastructure strain monitoring. A differential variable reluctance transducer (DVTR) was used to estimate strain response, and a data-logging transceiver platform was developed to convert the strain signals to readable values and wirelessly transmit them. The unit was composed of an 8-bit CPU, a 12-bit A/D converter, 2MB flash memory, and a 916.5 MHz transceiver module.

Subsequently, several researchers have developed strain sensor boards for various smart sensor platforms. Nagayama et al. (2004), Austin et al. (2005), and Choi et al. (2008) developed

prototype strain sensor boards for MEMSIC's Mica2 platform (2007) and O'Connor et al. (2010) for Narada wireless sensor (Swartz et al. 2005). However, the applicability of these basic-functioning strain sensor boards was limited to relatively high-level strains; low-level ambient strain measurement was not easily available with these proto-type boards due to insufficient accuracy of the Wheatstone bridge balance, which convert resistance change in strain gage into readable analog voltage signal, and limited resolution of A/D converter used.

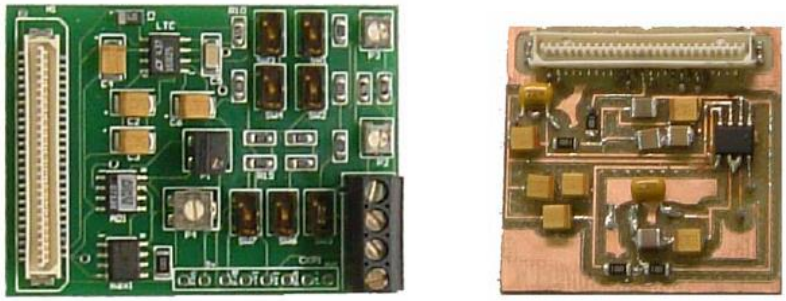

Figure 2.3. Strain sensor board for Mica2 (left) and 4-pole AA filter board (right) developed by Nagayama et al. (2004).

More advanced wireless strain sensing systems have been developed by Whelan and Janoyan (2009) and Bischoff et al. (2009) for the Tmote Sky platform (MoteIv 2006); which was introduced in the previous section. In addition to the single-ended analog signal conditioning circuit they developed, a differential analog signal conditioning circuit was implemented to handle the acquisition of differential sensor signals, such as produced by Wheastone-bridge resistive sensors. To this end, the ZMD31050 advanced differential sensor signal conditioner (ZMD 2004) was used. While the ZMD31050 signal conditioner features digitally programmable analog offset nulling, the approach to offset removal (i.e., by adding an analog

voltage to the signal) restricts the gain to a maximum of only 420, which is not sufficient for sub-microstrain level ambient strains. Commercial wireless strain sensors are recently available (Microstrain 2011; National Instrument 2010); however, these nodes either: (i) emulate wired monitoring systems, or (ii) act as simple data loggers. Neither of these approaches are scalable, and thus do not allow for dense instrumentation of large civil infrastructure; moreover, they are primarily intended for short-term monitoring campaigns.

2.2.1.3 Environment monitoring

Monitoring the environment and its effect on structural behavior have also been main interests in SHM. Various WSS platforms or sensor boards for the platform have provided such functionalities. For example, the SHM-A board for the Imote2 platform introduced in the Section 2.2.1.1 (Rice et al. 2010) included temperature, humidity, and light intensity sensing capabilities, in addition to 3-axis acceleration measurements. The temperature sensor on the board was even used for compensating the temperature effects on the acceleration measurements. And the 4^{th} channel of the board was left for integrating external analog sensor having 0~3.3V output. TelosB mote (Crossbow 2008) also provides similar sensing capabilities of temperature, humidity, and light intensity. Liu et al. (2011) used the TelosB to collect these various environmental sensory data as well as carbon dioxide levels. The collected information was utilized for various forestry applications such as carbon sequestration, fire risk prediction, and research on forest biodiversity. The climate sensor nodes that Kurata et al. (2011) used for SHM of a cable-suspension bridge in California measure wind speed, wind direction, and temperature with the Narada wireless sensor.

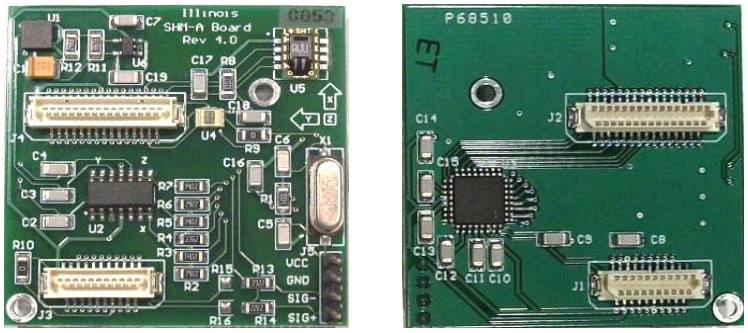

Figure 2.4. Multimetric sensor board (SHM-A board rev.4) for Imote2 platform by Rice et al. (2010); top (left) and bottom (right).

2.2.2 Network implementation

Fundamental, but critical, low-level network functionalities such as time synchronization and reliable communication have been successfully implemented to bridge the gap between the hardware components and the high-level application software. Many research teams have implemented time synchronization schemes for WSSN applications to SHM (Maroti et al. 2004; Lynch et al. 2005; Mechitov et al. 2004, Nagayama and Spencer 2007). Synchronized sensing has been successfully realized with recent efforts (Kim et al. 2007; Nagayama and Spencer 2007). Additionally, a protocol for reliable wireless communication has been developed by Nagayama and Spencer (2007), and multi-hop communciation for WSSN in SHM applications have been implemented successfully by Kim (2007) and Nagayama et al. (2010).

2.2.3 Data processing schemes in WSSN

In the SHM application of WSSN, which requires high-throughput data communication, one critical challenge is how the measured data is processed. Considering that smart sensors are typically battery-powered, power management is critical for long-term monitoring. Though

energy harvesting efforts (Rahimi et al. 2003; Jang et al. 2010) have been reported, an efficient power management strategy should still be considered for WSSN. As data communication in WSSN is one of the most significant sources of power consumption, reducing wireless communication becomes an important factor to realize practical WSSN implementations.

Traditional centralized approaches for acquiring and processing dynamic data require that all sensor data be collected at a single location; because of limitations in radio communication bandwidth for WSSN, such approaches are difficult to implement. Moreover, the problem is exacerbated as the size of the network increases, resulting in high power consumption and unreliable communication. Alternatively, decentralized in-network processing approaches have been introduced to reduce data communication. One such approach employs decentralized independent processing that condenses measured dynamic information on individual nodes using the smart sensor's onboard computation ability (Tanner et al. 2003; Lynch et al. 2004; Caffrey et al. 2004). The amount of data wirelessly transferred in the network is significantly reduced; however, all spatial information (*e.g.*, mode shape) is lost in such approaches. Gao et al. (2006) and Gao and Spencer (2008) proposed a coordinated computing strategy for damage detection that retains local spatial information, while concurrently reducing data communication in the network (see Figure 2.5). Nagayama and Spencer (2007) implemented a coordinated computing strategy in a WSSN employing the Imote2 sensor platform for system identification. Zimmerman et al. (2008) have implemented a decentralized data processing scheme on a WSSN using the Narada wireless sensors. An output-only identification approach, the Natural Excitation Technique (NExT) (James et al. 1993), was employed in conjunction with Eigensystem Realization Algorithm (ERA) (Juang and Pappa 1985). The NExT-based coordinated processing approach has been practically developed by integrating the services of

the Illinois Health Monitoring Project (ISHMP) Service Toolsuite (Sim and Spencer 2009). The efficiency of the decentralized processing over the centralized in terms of data transmission is found in Sim et al. (2010 and 2011) and Ye et al. (2011).

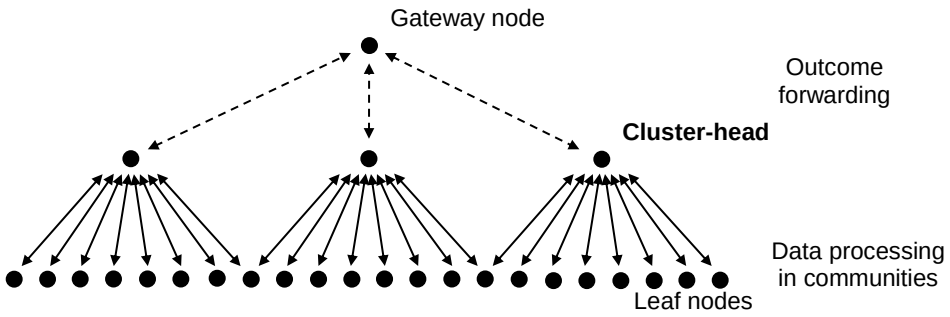

Figure 2.5. Coordinated computing stragegy in WSSN (Nagayama and Spencer 2007).

2.3 **Full-scale Implementation of Wireless Smart Sensor Network for SHM**

Though many wireless smart sensor technologies have been available for structural health monitoring application for nearly a decade, full-scale implementations on real-world structure are still limited. To apply WSSN to full-scale structures, particularly to ensure long-term and robust operation of the WSSN and to better utilize it for civil infrastructure SHM, many issues should be resolved, which include:

- Power efficient WSSN: Because wireless smart sensor (WSS) nodes are generally battery-powered, to make the WSSN power efficient and extend the life is essential.
- High-quality sensing: Considering the structural responses of civil infrastructure are relatively low-level, high-sensitivity sensing capabilities of WSS are required, while still keeping the low-cost feature of WSS. Moreover, synchronized sensing is one of the most critical factors for the success of vibration-based SHM.

- Autonomous operation of WSSN: For effective operation of WSSN for long period, autonomous operation of the network is required without operators.
- Fault tolerant WSSN: Contrary to laboratory tests, full-scale applications are subjected to many harsh environmental conditions that may effect on network stability. Also, the network size increases as structures becomes bigger and more complex, diverse wireless communication problems may be encountered. For full-scale deployments, the WSSN needs to be tolerant to such erroneous factors, without sacrificing the stability of entire network.

2.3.1 Full-scale SHM using WSSNs

Several deployments of smart sensors on full-scale structures have been reported for SHM purposes. Starser and Kiremidjian (1998) deployed 7 sensor nodes on the Alamosa Canyon Bridge for the proof-of-concept test of the author's prototype smart sensor (WiMMs). Arms et al. (2004) demonstrated the performance of Microstrain's wireless strain module with 10 sensor nodes on the Ben Franklin Bridge in Philadelphia. The Gumdang Bridge in Korea has been monitored by Lynch et al. (2006) using 14 sensor modules of the author's prototype, and Wang et al. (2008) reported a monitoring campaign to determine the modal properties of the Gi-Ju cable-stayed bridge in Taiwan using 12 wireless sensors combined with velocity meters. The Golden Gate Bridge in California (see Figure 2.6) has been tested with 64 MicaZ motes by Kim et al. (2006, 2007) and Pakzad et al. (2008).

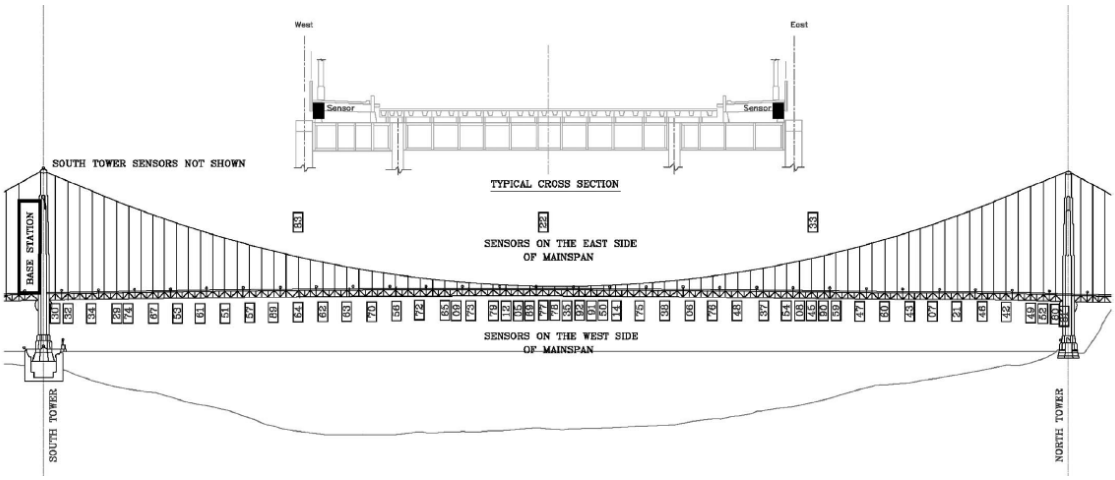

Figure 2.6. Sensor topology in main span of the Golden Gate Bridge (Pakzad et al. 2008).

Many applications using WSSN to diverse types of monitoring system have been actively tried, particularly for short term campaign monitoring purpose. Whelan et al. (2010) have deployed a densely arrayed WSSN in a multi-span prestressed concrete bridge for structural identification using the authors' wireless sensing platforms. For the 87.7m length multi-span concrete bridge, 9 reference sensors were installed in fixed locations and 29 roving sensors were used to cover total 72 locations over entire span. The densely arrayed WSSN by combining fixed reference sensors and mobile sensors allowed high-precision modal identification of the structure and model updating with limited number of sensors.

The applications of WSSN to underground structures have been reported by Bennett et al. (2010). For the London Underground and the Pague Metro, MICAz sensor platforms were installed, and inclinations and cracks of the underground railways tunnels were monitored. Total 28 wireless sensors were used for the Pague Metro and 25 nodes were installed in the London Underground. The particular radio communication environment, which is underground structure, was carefully investigated, and the relay chain network designed suitable for the underground

environmental conditions was proposed in their study. Table 2.1 shows the summary of full-scale implementations of WSSNs for SHM of civil infrastructure.

2.3.2 Autonomous and long-term operation of WSSN for SHM

More recent efforts have been devoted to long-term SHM application of WSSN. Zonta et al. (2010) reported a permanent monitoring of a historic building constructed in Italy in 13th century using 3MATE wireless sensor modules. The wireless sensor network (WSN) installed in the building consists of 16 sensor nodes, which measure acceleration and displacement responses of the structure.

Meyer et al. (2011) deployed 8 wireless sensor modules, including 1 relay node and 1 gateway node, using TmoteSky platform and the authors' customized sensor boards on a cable-stayed bridge (Stork Bridge) in Switzerland. Since the monitoring system was implemented in 2006, the sensors installed on the stay cables have measured the acceleration responses of stay cables with LIS2L06 MEMS analog accelerometer (ST Micronics) connected to 12 bit A/D converter. However, low-level ambient vibration of the stay cables were not effectively measured due to low resolution of A/D converter and the need for frequent battery replacement. Though scheduled sensing software that is operated on leaf-node itself allowed for autonomous operation, scalability of the network was not apparent.

As large-scale civil infrastructures require more scalable and systematic approaches for long-term SHM, autonomous WSSNs have been employed. Rice et al. (2010) proposed flexible WSSN framework for long-term full-scale SHM applications. Under Illinois Health Monitoring Project (ISHMP), a user-configurable multi-metric sensor for Imote2 WSS platform and an open-source software framework based on the design principles of service-oriented architecture

(SOA) were developed. The framework provides a software library of customizable services for SHM applications using WSSN, which implements key middleware infrastructure necessary for high-quality sensing and reliable wireless communication with the sensor network. The service-based software framework (ISHMP Service Toolsuite) provides various low-level foundation services for synchronized and reliable wireless network, as well as high-level application services, tools, and utilities including diverse numerical algorithms and automated wireless muti-metric sensing. Using the ISHMP Service Toolsuite, Rice et al. (2010) have developed autonomous network operation software for long-term SHM, which employs the triggering based sensing activation and sleep mode to reduce power consumption and increase the network life.

Using the ISHMP Service Toolsuite and the autonomous network operation software, Jang et al. (2010) and Cho et al. (2010) reported on a full-scale long-term SHM system on a cable-stayed bridge (the 2nd Jindo Bridge in Korea). A total 70 sensor nodes divided into two sub-networks were deployed, and 3-axes accelerations, temperature, humidity, light, and wind speed and direction were monitored in automated operational software. D-cell batteries were used to power most of the sensor nodes, but some of nodes were equipped with solar rechargeable system. The structural response measurements obtained from the WSSN were validated by comparison with existing wired SHM data and a numerical model.

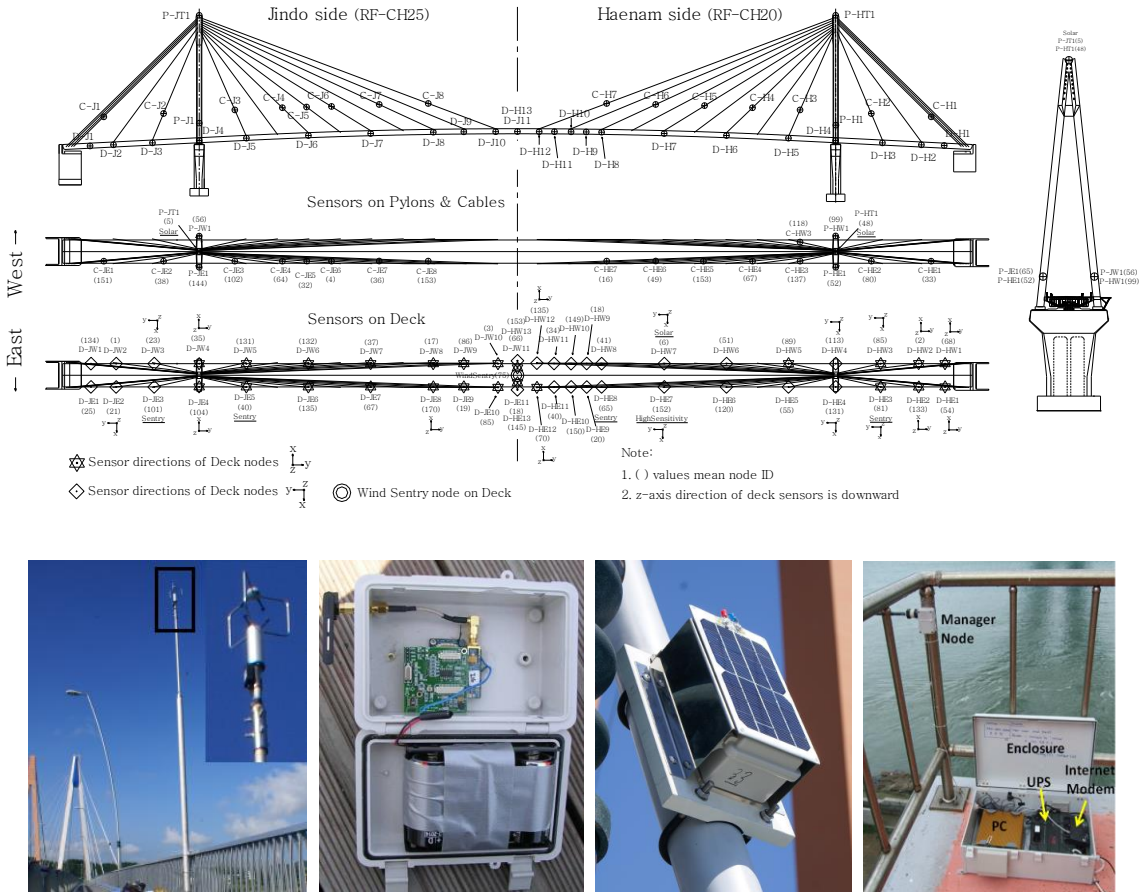

(a) (b) (c) (d)

Figure 2.7. WSSN deployment in the 2nd Jindo Bridge in Korea: (top) Sensor topology, (a) 3D ultra-sonic anemometer, (b) sensor node assembly, (c) solar powered cable node, (d) basestation (Jang et al. 2010; Cho et al. 2010).

Another similar long-term deployment has reported by Kurata et al. (2011) for a cable-suspension bridge (New Carquinez Bridge in California) using a network of 20 Narada sensors. Similarly to the 2nd Jindo Bridge deployment, automated network operation software was implemented, as well as energy harvesting system using solar power and wind turbine was adapted to power the sensor nodes.

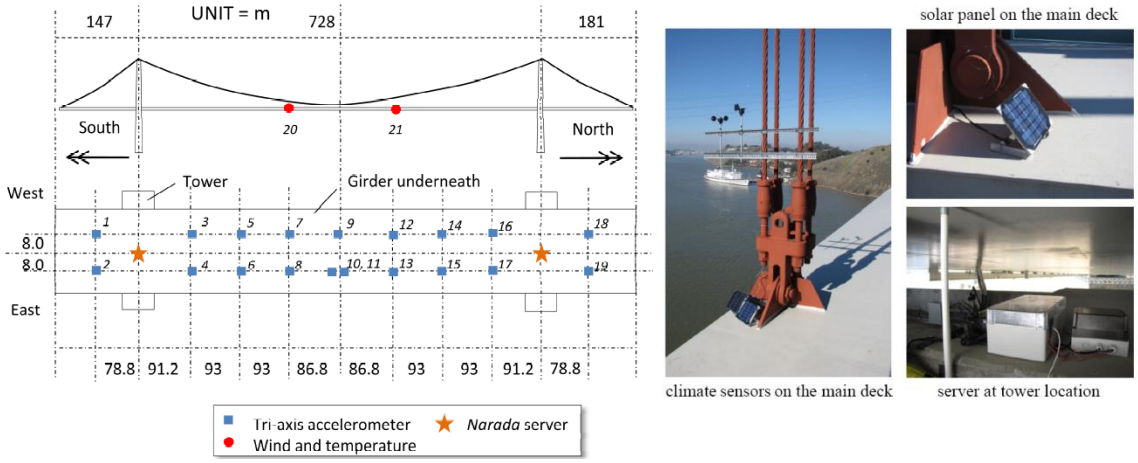

Figure 2.8. WSSN for SHM of New Carquinez Bridge in California (Kurata et al. 2011).

The efficacy of the reported fundamental frameworks for autonomous SHM has been verified through long-term operation of the WSSNs. However, some challenges still remain, such as multi-scale strategies of efficient network power management and network-self monitoring for long-term operation.

Table 2.1. Full-scale implementations of WSSNs for SHM of civil infrastructure.

	Sensor platform	Network size	Max sampling rate	Sensor type (# of channels)	Duration	Energy harvesting	Comments
Alamosa Canyon Bridge (Starser and Kiremidjian, 1998)	WiMMS	5 nodes	240Hz	Acceleration (5)	Short term	None	• Acceleration time history • Comparison with wired system
Ben Franklin Bridge (Arms et al., 2004)	Micro Strain SG-Link	10 nodes	32Hz	Strain (5) Temp. (5)	Mid term	None	Strain time history
Gumdang Bridge (Lynch et al., 2006)	Narada (author's prototype)	14 nodes	200Hz	Acceleration (14)	Short term	None	In-network processing (independent FFT)
Gi-Ju Bridge (Weng et al., 2008)	Narada	12 nodes	100Hz	Velocity	Short term	None	Velocity time history
Golden Gate Bridge (Kim et al., 2006; Pakzad et al., 2008)	MicaZ	64 nodes	1000Hz	Acceleration (256) Temp. (64)	Short term	None	• Acceleration time history • Multi-hop protocol
Wright Road (Whelan et al., 2007)	Tmote Sky	20 nodes	128Hz	Acceleration (29) Strain (11) Temp. (20)	Short term	None	Acceleration and strain time history
Nine Wells Rail Bridge (Whelan et al., 2010)	Tmote Sky	30 nodes	256Hz	Acceleration (30)	Short term	None	• Acceleration time history • Operational modal analysis
London Underground & Prague Metro (Bennett et al. 2010)	MicaZ	25 & 28 nodes	Sample/3 minutes	Crack meter (5 & 2) Inclinometer (16 & 10)	Short term	None	Multi-hop protocol

Table 2.1. Full-scale implementations of WSSNs for SHM of civil infrastructure (cont.).

	Sensor platform	Network size	Max sampling rate	Sensor type (# of channels)	Duration	Energy harvesting	Comments
The 2nd Jindo Bridge (Jang et al., 2010; Cho et al., 2010)	Imote2	70 nodes	50Hz	Acceleration (207) Temp. (69) Humidity (69) Wind (3)	Long term	Solar (8 nodes)	• Acceleration and wind time history • Autonomous operation
Aquila Tower (Zonta et al., 2010)	TRETEC's 3Mate	16 nodes	200Hz	Acceleration (3) Fiber optic sensor (2) Temp. (11)	Long term	None	Deformation time history using fiber optic sensor
Stork Bridge (Meyer et al., 2011)	Tmote Sky	6 nodes	100Hz	Acceleration (12) Temp. (6) Humidity (6)	Long term	None	• Autonomous operation • Stay cable vibration (acceleration) time history
New Carquinez Bridge (Kurata et al., 2011)	Narada	23 nodes	20Hz	Acceleration (47)	Long term	Solar (23 nodes)	• Autonomous operation • Acceleration time history

2.3.4 Illinois Structural Health Monitoring Project (ISHMP)

As the collaboration between the Smart Structures Technology Laboratory (director: Prof. B.F. Spencer, Jr.) from the Civil and Environmental Engineering Department and the Open Systems Laboratory (director: Prof. Gul Agha) from the Computer Science Department at University of Illinois at Urbana-Champaign, the Illinois Structural Health Monitoring Project (ISHMP) is developing hardware and software systems for the continuous and reliable monitoring of civil infrastructure using Imote2-based wireless smart sensor networks. The open-source software library of customizable services, developed under the ISHMP, provides services for SHM applications using Imote2 platform, implementing the key middleware infrastructure necessary for high-quality sensing, including: various low-level foundation services for synchronized and reliable network operation, as well as high-level application services, tools, and utilities. Some key service modules are briefly described as follow. More detail information about each service can be found at Rice and Spencer (2009), Sim (2011), and ISHMP website (http://shm.cs.uiuc.edu/).

- *ReliableComm*[1] – for reliable wireless communication of both short messages and long data records
- *SensingUnit* – flexible network-wide synchronized sensing service
- *RemoteSensing* – fault tolerant implementation of the *SensingUnit* service for time synchronization, wireless sensing, and storing the data to Flash memory
- *RemoteCommand* – service that supports the reliable dissemination of network and utility commands, some of Utility Commands used in this study include followings,
  - ✓ *Vbat* – read battery voltage

[1] Use of the *Italic font* designates a tool or service name in the ISHMP Services Toolsuite.

- ✓ *ReadTemp* – read temperature from the temperature sensor on the SHM-A sensor board
- ✓ *ChargeStatus* – check charging condition, and read charging voltage charging current, and battery voltage.
- ✓ *ReadLight* – read light intensity from the light sensor on the SHM-A sensor board

- *AutoMonitor* – application tool for autonomous and long-term operation of WSSN
- *ThresholdSentry* – service to support triggering-based network operation, which is managed as one of sub-software of *AutoMonitor*
- *CableTensionEstimation* – application service for vibration-based estimation of the stay cable tension, which is managed as one of sub-software of *AutoMonitor*
- *SnoozeAlarm* – service for extended-life WSSN utilizing periodical sleep mode

2.4 **Multimetric Sensing**

Multimetric sensing using a heterogeneous mix of measurands at various scales has the potential to provide more accurate characterization of the state of a structure (Sim et al. 2011). In particular, multimetric sensing is expected to enable better quality measurements from WSSN employing low-cost sensors and to enhance the performance of SHM without excessive cost. This section describes the use of acceleration, displacement, and strain in combination for the SHM purposes.

2.4.1 Displacement monitoring

Structural displacement or deformation information is particularly important when permanent deformation occur and is often more accurate than acceleration measurements for lower

frequencies. However, most current SHM approaches rarely support displacement monitoring, primarily due to the difficulty in measuring absolute displacements. Some of the commonly used displacement sensors include the Linear Variable Differential Transformer (LVDT), the Laser Doppler Vibrometer, and linear potentiometers, each of which provides relative displacement. Linear potentiometers have been combined with the National Instrument wireless sensor (Battista et al. 2011) and an LVDT has been connected to Imote2 WSS (Jang et al. 2012). However, the need for reference points to use these instruments makes deployment difficult for large civil infrastructure.

2.4.1.1 Structural deformation monitoring using GPS

Global Positioning System (GPS) technologies are able to provide reference-free absolute displacement measurements. A state-of-the-art Real-Time Kinematic (RTK) technique with dual-frequency GPS receivers that use L1/L2 carrier phases allows even sub-centimeter accuracy, which is applicable for SHM purposes. Many researchers have tried the RTK GPS system for bridge monitoring. Ashkenazi and Roberts (1997) installed two Ashtech Z-XII dual-frequency GPS receivers on the Humber Bridge (span 2220m) deck and the support towers to monitor the structural displacement of the bridge. Nakamura (2000) measured displacements of a Japanese suspension bridge having a main span of 720m and two side spans of 330m each, and compared the static deformation due to wind loading with the results from the FEM analysis and the wind tunnel tests. Meo et al. (2006) deployed a GPS monitoring system on the Nottingham Wilford Bridge for online monitoring of the bridge deck movements, and showed the feasibility of GPS to monitor dynamic displacements of a medium span suspension bridge in the low-frequency range. GPS has been broadly used for displacement monitoring of many other bridge structures

including; the Humen Bridge in China (Guo et al. 2005), the Akashi-Kaikyo Bridge in Japan (Fujino et al. 2000), the Batman Bridge in Australia (Watson et al. 2007).

2.4.1.2 Combined use of accelerometer and GPS for displacement monitoring

Though GPS now allows subcentimeter accuracy, the GPS is limited partially by multipath error, relatively low-frequency data, as well as the need to have good satellite coverage. In contrast, accelerometers have been proven useful for high-frequency responses, but reconstructed displacements from accelerations by double integral have inherent drift errors over time. To eliminate the drawbacks of the two separate measurands, integrated approaches of accelerometer and GPS have been investigated.

Roberts et al. (2004) proposed an algorithm for displacement reconstruction from acceleration measurements, for which drift error as a result of each integral process is compensated by GPS velocity and GPS position measurements. By integrating the two measurands, higher-frequency deformation information was estimated, which GPS could not obtain, while keeping the accuracy of lower-frequency deformation from RTK GPS measurements. The efficacy of the algorithm has been validated through testing of a suspension footbridge in Nottingham, England. Subsequently, other researchers have tried a combined use of RTK-GPS and accelerometer system (Li et al. 2006; Meng et al. 2007; Yi et al. 2010) for monitoring bridge and building structures. Of particular interest is an approach proposed by Smyth and Wu (2007) using multi-rate Kalman filter. The bias error which occurrs while double integrating acceleration data to estimated displacements was employed as an augmented state in the Kalman filter, and predicted displacement was updated by the displacement measurements in the Kalman filter. Such way to combine data sampled at different frequencies (GPS displacement

at lower sampling rate and acceleration measurement at higher frequency) significantly increased the accuracy of displacement response estimation both in low and high frequency range.

Though RTK-GPS technology can provide high-accuracy reference-free deformation monitoring tool, it is not suitable for WSSN yet due to high cost and power consumption. Though MICAz has a GPS embedded sensor board (MTS420CC, MEMSIC 2011), and other very low-power and low-cost GPS modules becomes available recently (GlobalTop Technology Inc., 2010; Garmin International Inc., 2008), they have low accuracy (several meters).

Figure 2.9. MTS420CC (with GPS module) board for Micaz platform (MEMSIC 2011).

2.4.1.3 Displacement reconstruction from other measurands: acceleration-based

Another way to estimate displacement is the reconstruction of displacement from other easy-to-measure and inexpensive measurands such as accelerations and strains.

As described already in previous sections, drift error introduced by integral process of acceleration signal to get displacement estimation poses the limitation of such approach. Gavin et al. (1998) proposed a drift-free integrator, which was achieved by high-pass filtering with

feedback stabilization; this approach was exceptionally accurate when integrating low-frequency signals, but produces phase and bias errors with wide-band signals.

Hong et al. (2010a, 2010b) proposed a regularization scheme and new type of FIR high-pass filters for displacement reconstruction from structural acceleration data. Displacement reconstruction is realized by solving an error-minimization problem, of which approach results in a kind of the high-pass FIR filter. The efficacy of the approach has been demonstrated through numerical simulations and a field experiment.

The acceleration-based displacement estimation approaches reported in this section have shown great performance in zero-mean dynamic displacement reconstruction. However, static and low-frequency displacement reconstruction have been rarely realized with acceleration-only-based methods. Though Park et al. (2005) have tried to determine bridge displacements, including pseudo-static response, from acceleration measurements, the initial displacement and velocity information have to be accurately estimated, which is rarely available for full-scale structures. Moreover, considering acceleration responses are proportional to the square of the frequency multiplied by displacement magnitude, use of acceleration responses is intrinsically difficult to use to obtain very low-frequency or static responses.

2.4.1.4 Displacement reconstruction from other measurands: strain-based

In contrast to acceleration responses, strain responses can include more static information. Vurpillot et al. (1996) have introduced a mathematical model for the static deflection estimation of simply a supported beam using the relation between the curvature of beam and strain response and validated the model through a 6-m timber beam experiment with 12-fiber optic sensors. Inaudi et al. (1999) applied the similar approach to pre-stressed concrete beams highway bridges

in Switzerland, and Cho and Kim (2004) tried fiber optic Bragg-grating (FBG) strain sensors instead for the static deflection estimation of a simply supported beam structure, and extended to find static deformation profile of a cable-suspension bridge (Cho and Kim, 2008).

Several studies have been conducted utilizing strain measurements to get dynamic as well as static displacements. Shin and Yun (2008) used the modal superposition method to find dynamic deformation of a simply supported beam structure from strain measurements. However, the accuracy of the method was heavily dependent on the number of modes used and appropriateness of the assumed modes; additionally, a larger number of strain sensors than the modes had to be used to get the deterministic solutions. Chang and Kim (2011) used modal decomposition methods to reduce higher-frequency noise effects in the strain signals. The mode shapes were estimated from a proper orthogonal decomposition (POD) and strain signal corresponding to each mode (obtained from empirical mode decomposition (EMD)) to produce the displacement responses for each mode. Then the total dynamic displacement responses were estimated from the combination of each modal displacement.

Though the above strain-based approaches for structural displacement estimation were experimentally validated, numerous strain measurements are required to get reasonable accuracy. For this reason, fiber optic sensors were preferred in previous studies; however, they are relatively expensive and difficult to implement for WSSN based SHM applications.

2.4.2 Strain sensing for SHM

Compared with acceleration responses, structural strain responses are more low-frequency and local in nature, while acceleration responses are higher frequency and global. As aforementioned, structural strain responses can be used to reconstruct both static and dynamic

structural deformation information (Vurpillot ea al. 1996; Inaudi et al. 1999; Cho and Kim 2004, 2008; Shin and Yun 2008; Chang and Kim 2010). In addition, strain responses can be directly used to detect damage, which is one of ultimate objectives of SHM, to characterize moving contact loadings, and to estimate fatigue life. In this section, the uses of strain for damage detection and traffic monitoring applications are described; use of strain for fatigue monitoring is presented in the subsequent section.

2.4.2.1 Strain sensing for damage detection

Abdalla et al. (1999) proposed the linear matrix inequality (LMI) method for structural damage detections utilizing displacement or strain measurements. Guan and Karbhari (2008) introduced the element modal strain damage index (EMSDI) to overcome observed limitations in modal curvature-based damage detection methods. Benedetti et al. (2011) utilized strain sensitivity to detect cracks in a wind tower, and Rahmatalla and Eun (2010) estimated vertical deflections and flexural curvature for beam structures from strain measurements; constraint forces were calculated and utilized as fundamental information to detect damage in beam structures. Jang et al. (2007) have used the damage locating vector (DLV) method combined with static strain measurements, named strain DLV, and experimentally verified the efficacy of the strain DLV method with a lab-scale 13-bay truss structure.

Multimetric approaches have also been tried for damage detection. Law et al. (2005) presented a wavelet-based approach for combined use of acceleration and strain responses to better identify damage locations, Kijewski-Correa et al. (2006) implemented a decentralized SHM strategy to use both strain and acceleration responses on a WSSN. More recent effort has

been devoted to the multimetric DLV method that use both strain and acceleration responses by Sim et al. (2011).

2.4.2.2 Strain sensing for vehicle loading identification

One of useful applications of strain responses is for bridge weigh-in-motion (BWIM). Because of the local and static characteristic of the measurements, strain sensors installed underneath bridges can detect vehicular loads. Since Moses (1976) first reported that truck weight could be predicted from strain measurements on a girder bridge, many studies have followed. Snyder and Moses (1985) introduced the use of the strain measurements and the bending moment influence lines for girders, and Znidaric et al. (1998) and O'Brien et al. (1999) proposed a way to adjust theoretical influence lines a calibration truck. To detect axle loads, however, the above methods still required axle detectors, such as tape switches, installed in the travel lanes.

More recent efforts have been devoted to non-intrusive approaches known as Free-of-Axle Detector (FAD) or Nothing-On-the-Road (NOR) methods to eliminate the need for devices to be installed on the road surface. Ojio and Yamada (2005) proposed the use of the reaction force influence line to identify moving vehicles on a bridge by measuring the strain responses in the stiffener for the bearing supports. The reaction force method has the advantage that even single-point measurements can provide useful information, including axle loads, moving direction, and speed of vehicle. However, the reaction force method has limited accuracy due to the effects of vehicle dynamics.

Studies to improve the accuracy of detecting axle loads from the strain responses of bridges with the non-intrusive methods have been conducted by Flood (2000) and Chatterjee et al. (2006). Flood (2006) used neural network systems to classify truck loads by estimating axle

information, and Chatterjee et al. (2006) used a wavelet-based approach to identify vehicle speed, axle spacing, axle weights, and gross vehicle weights.

2.5 **Fatigue Monitoring**

Another important application of strain sensing in SHM is fatigue monitoring. Fatigue, a progressive and localized structural damage mechanism, is one of the most critical problems in steel bridge structures (Fisher 1984). Though modern steel bridges designed after the mid-1980s may not be as susceptible to fatigue due to improved design specifications, fatigue-resistant details, and shop inspection, fatigue problems can still be found. Such problems are typically caused by construction errors or unexpected structural behavior/loads and are usually manifested in the first few years of the life of the bridges (Farrar et al. 2006; Gao and Spencer 2007). Moreover, steel bridges built before the implementation of modern fatigue design provisions continue to be susceptible to fatigue (Gnawali et al. 2006), which should be properly monitored and managed.

2.5.1 Current practice in fatigue monitoring

Currently, fatigue is assessed in primary two ways: (i) strain measurement and (ii) routine visual inspection. Strain measurement provides the most direct and accurate way to assess the fatigue life of a member (Zhou 2006, Kühn et al. 2008). The collected data is used to assess the remaining life of the member using damage accumulation algorithms such as the Palmgren-Miner rule (Palmgren 1924; Miner 1945; Sobczyk and Spencer 1992). To use the damage accumulation rule, first of all, stress/strain loading cycles should be identified within a complex load history. The rainflow cycle counting method proposed by Matsuiski and Endo (1968) can

be used to extract the stress/strain cycle information from raw data, but was intended to be carried out once entire strain history is known. The approach was updated and simplified by Downing et al. (1976) and Okamura et al. (1979). A 'one-pass' rainflow counting algorithm was presented by Downing and Socie (1982) that does not require entire strain history and facilitates real-time counting of the cycles. This 'one-pass' rainflow counting method has been adopted as standard practice for cycle counting in fatigue analysis in ASTM E-1049 (1985).

Many studies have been reported on the applications of fatigue assessment techniques to full-scale bridges, especially focusing on field strain measurements (Mohammadi et al. 1998; Heather et al. 2001; Chan et al. 2001; Lund and Alampalli 2004; Mori et al. 2007; Caglayan et al. 2009; Siriwardane et al. 2010; Fisher and Roy 2011). Zhou (2006) has well summarized the procedure for fatigue life assessment through field strain measurements.

However, high costs and difficulties in instrumentation limit the usage of the strain measurement to only a few locations with the highest potential risk (usually obtained by numerical modeling and experience). Moreover, these estimated risks may quickly become invalid due to unintended structural behaviors, possible construction errors, and changes in the structural and loading conditions.

Routine visual inspection is intended to compensate for the point-wise nature of strain measurement, allowing periodic investigation of unmeasured locations. However, the effectiveness of visual inspection is limited by the fact that fatigue is not apparent during the period of crack initiation, which can be up to 90% of the fatigue life. The fatigue failure on the San Francisco-Oakland Bay Bridge in 2009 (Reid 2010) illustrates the limit of the routine visual inspection. The fatigue failure of the eyebar shown in Figure 2.10 was found during an inspection in 2009 on the eastern truss span of the bridge; however, the crack was not reported in

the inspection of 2007, which means the fatigue had grown critical in the 2-year interval. Considering the recent bridge collapses were initiated from failure of one or a few members (Seongsu Bridge: Yun et al. 2003; I-35 Bridge: Hao 2010), such problems could result in yet another major bridge collapse. Therefore, an approach to continuously assess the remaining fatigue life of entire structure is needed.

Figure 2.10. San Francisco-Oakland Bay Bridge and cracked eye bar by fatigue.

2.5.2 Fatigue monitoring using WSSN

Recent advanced sensor technology enables fatigue monitoring at more locations using densely instrumented WSSN. A number of wireless strain sensing systems have been developed; however, few examples are found of fatigue monitoring of full-scale structures using WSSN.

Austin et al. (2005) developed a strain sensor board for the Mica2 smart sensor platform and used it for fatigue monitoring of moving construction machine. Strain was monitored for several days with the wireless unit, which included a rechargeable battery pack combined with solar panel. An algorithm for rainflow cycle counting (Downing and Socie 1982) was implemented in the sensor network to extract the stress loading cycle histogram. Arms et al. (2009) reported the use of MicroStrain's wireless strain sensor nodes for the fatigue monitoring of helicopter

components, as well as for strain monitoring of a member on the Ben Franklin Bridge. O'Connor et al. (2010) also implemented the rainflow cycle counting algorithm in Narada wireless sensor network for fatigue life monitoring of metallic structures and showed the efficacy of the decentralized cycle counting process through a fatigue specimen testing; however, this effort has not be deployed in full-scale applications.

2.5.3 Strain responses prediction and Fatigue life estimation

As described in Section 2.5.1, current fatigue management and assessment approaches employ the strain responses at a few pre-defined locations on the structure; due to various uncertainties, these locations may not be the most critical for determining remaining fatigue life. Moreover, if the desired locations for sensor placement cannot be accessed (e.g., underwater locations), estimating fatigue life may be even more challenging.

Papadimitriou et al. (2010) proposed a model-based approach for fatigue life estimation using the Kalman Filter, in which strain measurements at a limited number of locations were combined with a numerical model to predict stress responses at unmeasured locations. Numerical examples were provided which demonstrated that this approach can estimate the fatigue life at arbitrary locations for simple planar truss structures in which the model is relatively well known.

However, this single-metric approach (i.e., using only strain measurements) may be ineffective for as-built civil infrastructure, which is often complex and massive, because strain is an intrinsically local phenomenon. As a result, capturing the full dynamic response of the structure is difficult using only such local measurements. The applicability of this approach to full-scale structures needs to be further investigated.

2.6 **Kalman Filter Approach for SHM**

As shown in some of research introduced in previous sections, the Kalman Filter has been widely used in SHM area. In this section, various applications of the Kalman Filter and its usefulness in SHM are overviewed.

Kalman filter (KF) is a model-based mathematical tool introduced by R.E. Kalman (1960) which provides an efficient recursive means to estimate the state of a process in a way that minimizes the mean of the squared error. The filter has great potentials in several aspects: it supports estimation of past, present, and even future states (A.C. Harvey 1991, A. Salgado and L. Esteva 1996), and it can do so even when the precise characteristic of the modeled system is unknown. Hence, the KF approach has been used for a wide variety of purposes, including noise reduction in measurements (Lesniak et al. 2008; Solh 2006; Nikaido and Tamaru 2003), data fusion of different types of sensors (Sasiadek and Hartana 2000; Escamilla and Mort 2002), localization of moving objects (Jetto et al. 1999; Roumeliotis and Bekey 2000; Meng et al. 2000; Kim et al. 2011), etc.

The KF approaches have been used to enhance many SHM algorithms for civil infrastructures as well, e.g., structural parameter identification and detection of the parameter changes under damaged conditions (Yin et al. 2000; Sato et al. 2001; Yang et al. 2006; Turner et al. 2009), data fusion of acceleration and displacement measurements (Smyth et al. 2007), and behavior estimation of nonlinear RC structure (Lee and Yun 2008).

In particular, data fusion techniques using the KF provide an effective tool for better estimation of particle- or structural motions with multi-metric measurands. The multi-rate KF approach proposed by Smyth and Wu (2007), detailed in Section 2.4.1.2, allows data fusion of accelerations and displacements sampled at different rates. Kim et al. (2011) have applied the

multi-rate KF method for positioning an instrumented truck on a highway bridge to investigate vehicle-bridge interaction. Sadegh and Nazar (2009) provides a good summary of various KF methods for multi sensor data fusion.

2.7 **Summary**

This chapter shows that the necessity of SHM has been well recognized and that the steady efforts have been devoted to enhance the effectiveness and applicability of SHM technology. Though traditional approaches using wired monitoring system have been successfully implemented and validated through many SHM applications, the high cost and challenging installation process limit its use to few signature structures. The evolution of SHM research has seen a shift away from such traditional wired monitoring methods toward the use of WSSNs in recent years. Such WSSNs have shown the tremendous potential of densely deployable sensor networks, which is essential for vibration-based SHM. And recent successful implementations of WSSNs for full-scale SHM have demonstrated the practical use of the technology. However, the long-term stability of the self-powered WSSN with systematic power management strategies, particularly, in high-throughput SHM applications that require computationally intense operation has not been reported.

While multimetric approaches have great potential to enhance SHM, the efficacy of multimetric SHM has yet to be fully realized using WSSN, primarily due to the limited capabilities of currently available WSS, particularly, for low-level ambient vibration.

CHAPTER 3 HYBRID STRUCTURAL HEALTH MONITORING

A hybrid structural health monitoring strategy combining numerical models and multi-metric physical monitoring that is presented in this section resolves many of issues found in current SHM practice. Such a hybrid approach enables response monitoring of complex structures at arbitrary locations. In particular, the multi-metric use of strain (i.e., local and low frequency) and acceleration (i.e., global and higher frequency) responses in combination is explored to enhance the accuracy of the estimated structural responses; this approach is particularly attractive because the associated sensors are relatively low-cost, easy-to-use, and reference-free, This section first describes the Kalman Filter approach for structural response estimation using multi-metric measurements and then presents numerical examples to validate the efficacy of the hybrid method and to illustrate its various monitoring applications.

3.1 **Multi-metric Kalman Filter**

As a recursive linear state estimator, the Kalman filter can provide statistically optimal estimates of structural responses at arbitrary locations on a structure using limited measurement data. This section provides an overview of the conventional formulation of the Kalman filter to accommodate multi-metric measurements, as well as introduces an augmented Kalman filter approach to model the excitation.

Consider the equation of motion of an *N*-DOF linear dynamic system

$$\mathbf{M}\ddot{\boldsymbol{u}}(t) + \mathbf{C}\dot{\boldsymbol{u}}(t) + \mathbf{K}\boldsymbol{u}(t) = \mathbf{G}\boldsymbol{p}(t) \tag{3.1}$$

where $\boldsymbol{u}(t) \in \mathbb{R}^{N\times 1}$ is the displacement vector, its time derivatives $\dot{\boldsymbol{u}}(t)$ and $\ddot{\boldsymbol{u}}(t)$ are velocity and acceleration vectors, respectively, $\mathbf{M}$, $\mathbf{C}$, and $\mathbf{K} \in \mathbb{R}^{N\times N}$ are the mass, damping, and stiffness

matrices, respectively, $\boldsymbol{p}(t) \in \mathbb{R}^{n_p \times 1}$ is the excitation time histories of dimension n_p, and $\mathbf{G} \in \mathbb{R}^{N \times n_p}$ is the matrix to specify the force locations.

Introducing the state vector $\boldsymbol{x}(t) \in \mathbb{R}^{2N \times 1}$ composed of displacement and velocity vectors

$$\boldsymbol{x}(t) = \begin{Bmatrix} \boldsymbol{u}(t) \\ \dot{\boldsymbol{u}}(t) \end{Bmatrix} \tag{3.2}$$

the equation of motion can be expressed in the state space form as

$$\dot{\boldsymbol{x}}(t) = \mathbf{A}_c \boldsymbol{x}(t) + \mathbf{B}_c \boldsymbol{p}(t) \tag{3.3}$$

where the system matrix $\mathbf{A}_c \in \mathbb{R}^{2N \times 2N}$ and the matrix $\mathbf{B}_c \in \mathbb{R}^{2N \times n_p}$ are defined as

$$\mathbf{A}_c = \begin{bmatrix} \mathbf{0} & \mathbf{I} \\ -\mathbf{M}^{-1}\mathbf{K} & -\mathbf{M}^{-1}\mathbf{C} \end{bmatrix}, \quad \mathbf{B}_c = \begin{bmatrix} \mathbf{0} \\ \mathbf{M}^{-1}\mathbf{G} \end{bmatrix} \tag{3.4}$$

The output vector $\boldsymbol{y}(t) \in \mathbb{R}^{n_y \times 1}$ can also be expressed in the state space form as follows

$$\boldsymbol{y}(t) = \mathbf{H}_c \boldsymbol{x}(t) + \mathbf{D}_c \boldsymbol{p}(t) + \boldsymbol{v}(t) \tag{3.5}$$

where $\boldsymbol{v} \in \mathbb{R}^{n_y \times 1}$ is the measurement noise. The matrices $\mathbf{H}_c$ and $\mathbf{D}_c$ are determined depending on the outputs of interests. For example, if all the displacement, velocity, and acceleration outputs are estimated, the output vector $\boldsymbol{y}(t)$ is

$$\boldsymbol{y}(t) = \begin{Bmatrix} \boldsymbol{u}(t) \\ \dot{\boldsymbol{u}}(t) \\ \ddot{\boldsymbol{u}}(t) \end{Bmatrix} = \begin{bmatrix} \mathbf{I} & \mathbf{0} \\ \mathbf{0} & \mathbf{I} \\ -\mathbf{M}^{-1}\mathbf{K} & -\mathbf{M}^{-1}\mathbf{C} \end{bmatrix} \boldsymbol{x}(t) + \begin{bmatrix} \mathbf{0} \\ \mathbf{0} \\ \mathbf{M}^{-1}\mathbf{G} \end{bmatrix} \boldsymbol{p}(t) + \boldsymbol{v}(t) \tag{3.6}$$

where the coefficient matrices of $\boldsymbol{x}(t)$ and $\boldsymbol{p}(t)$ in Eqn. (3.6) above correspond to $\mathbf{H}_c$ and $\mathbf{D}_c$ in Eqn. (3.5), respectively.

In the Kalman filter formulation, the excitation (or process noise) is assumed to be a white noise excitation. To accommodate the nonwhite nature of the excitation of typical civil engineering structures, an augmented state-space model is introduced by combining filtered white noise

$$\dot{\boldsymbol{x}}_{\mathrm{f}}(t) = \mathbf{A}_{\mathrm{f}}\boldsymbol{x}_{\mathrm{f}}(t) + \mathbf{B}_{\mathrm{f}}\boldsymbol{w}(t) \tag{3.7}$$

where $\mathbf{A}_{\mathrm{f}}$ and $\mathbf{B}_{\mathrm{f}}$ are matrices describing the filter properties, and $\boldsymbol{w} \in \mathbb{R}^{n_p \times 1}$ is white noise excitation. The filtered input excitation is then

$$\boldsymbol{p} = \mathbf{H}_{\mathrm{f}}\boldsymbol{x}_{\mathrm{f}}(t) \tag{3.8}$$

Defining a new state vector $\boldsymbol{X}(t)$ as

$$\boldsymbol{X} = \begin{Bmatrix} \boldsymbol{x} \\ \boldsymbol{x}_{\mathrm{f}} \end{Bmatrix} \tag{3.9}$$

an augmented state-space equation is obtained

$$\dot{\boldsymbol{X}} = \mathbf{A}\,\boldsymbol{X} + \mathbf{B}\,\boldsymbol{w} \tag{3.10}$$

$$\mathbf{y} = \mathbf{H}\,\boldsymbol{X} + \boldsymbol{v} \tag{3.11}$$

where,

$$\mathbf{A} = \begin{bmatrix} \mathbf{A}_{\mathrm{c}} & \mathbf{B}_{\mathrm{c}}\mathbf{H}_{\mathrm{f}} \\ \mathbf{0} & \mathbf{A}_{\mathrm{f}} \end{bmatrix}, \quad \mathbf{B} = \begin{bmatrix} \mathbf{0} \\ \mathbf{B}_{\mathrm{f}} \end{bmatrix}, \quad \mathbf{H} = \begin{bmatrix} \mathbf{H}_{\mathrm{c}} & \mathbf{D}_{\mathrm{c}}\mathbf{H}_{\mathrm{f}} \end{bmatrix} \tag{3.12}$$

Eqn. (3.10) and (3.11) can represent multi-metric measurements, as well as the nonwhite nature of the excitation. Moreover, the process noise $\boldsymbol{w}(t)$ and the measurement noise $\boldsymbol{v}(t)$ can be assumed to be stationary, mutually uncorrelated stochastic processes following normal probability distributions $\mathbf{p}(\boldsymbol{w}) \sim \boldsymbol{N}(\mathbf{0}, \mathbf{Q})$ and $\mathbf{p}(\boldsymbol{v}) \sim \boldsymbol{N}(\mathbf{0}, \mathbf{R})$, where $\mathbf{Q} \in \mathbb{R}^{n_p \times n_p}$ and $\mathbf{R} \in \mathbb{R}^{n_y \times n_y}$ are the excitation and measurement noise covariances, which are assumed to be independent of time.

The Kalman filter is now used to produce an optimal state estimate $\hat{\boldsymbol{x}}(t)$ of $\boldsymbol{x}(t)$ using the sensor measurement $\boldsymbol{y}(t)$ in the sense of minimizing the steady-state stationary error covariance $\mathbf{P}$,

$$\mathbf{P} = \lim_{t \to \infty} \mathrm{E}(\{\boldsymbol{x}(t) - \hat{\boldsymbol{x}}(t)\}\{\boldsymbol{x}(t) - \hat{\boldsymbol{x}}(t)\}^{\mathrm{T}}) \tag{3.13}$$

where $\hat{\boldsymbol{x}}(t)$ is governed by

$$\dot{\hat{\boldsymbol{x}}}(t) = \mathbf{A}\hat{\boldsymbol{x}}(t) + \mathbf{L}\{\boldsymbol{y}(t) - \mathbf{H}\hat{\boldsymbol{x}}(t)\} \tag{3.14}$$

the Kalman gain factor **L** is given by

$$\mathbf{L} = \mathbf{P}\mathbf{H}^{\mathrm{T}}\mathbf{R}^{-1} \tag{3.15}$$

and the error covariance matrix **P** is obtained by solving the associated Riccati equation

$$\mathbf{A}\mathbf{P} + \mathbf{P}\mathbf{A}^{\mathrm{T}} - \mathbf{P}\mathbf{H}^{\mathrm{T}}\mathbf{R}^{-1}\mathbf{H}\mathbf{P} + \mathbf{B}\mathbf{Q}\mathbf{B}^{\mathrm{T}} = \mathbf{0} \tag{3.16}$$

3.2 **Multi-metric Model-based Fatigue Life Monitoring**

High-cost and difficulties in sensor installation restrains the use of strain measurements to only few locations of the highest potential risk, posing the limitation of current fatigue monitoring practice. The proposed hybrid method provides an innovative way to overcome such limitation of point-wise nature of strain measurements. Strain responses at arbitrary locations can be predicted by the Kalman Filter method and the predictions are accurately updated with multi-metric measurements.

3.2.1 Fatigue life estimation based on the Rainflow Counting algorithm

Once the optimal state is determined from Eqns. (3.13) ~ (3.16), strain response estimates are obtained through a linear transformation

$$\hat{\boldsymbol{\varepsilon}} = \mathbf{T}\,\hat{\boldsymbol{x}} \tag{3.17}$$

where $\hat{\boldsymbol{\varepsilon}}$ is the estimated strain vector, and **T** is the transformation matrix that associates the state vector to the desired strain estimates at the specified locations on the structure. Then, the corresponding stresses can be obtained.

Once the strain and stress responses are available at the desired locations, a strategy for fatigue life estimation is required. In this study, the Palmgren-Miner rule (Palmgren, 1924; Miner, 1945) is used to predict the damage accumulation due to fatigue, and the Rainflow counting algorithm (Downing and Socie, 1982) is employed to identify the cycles and means of stress/strain amplitude, which are used for estimating fatigue damage accumulation. For completeness, the Palmgren-Miner rule and Rainflow counting method are briefly reviewed in this section.

3.2.1.1 Fatigue Damage Accumulation

The fatigue damage corresponding to each cycle is an indication of the amount of damage imposed on the material due to the specific cycle. According to the Palmgren-Miner rule, the fatigue damage at a specific point subjected to variable amplitude stress cycles is linearly accumulated by the formula

$$D = \sum_{i}^{k} \frac{n_i}{N_i} \tag{3.18}$$

where n_i is the number of cycles at a stress level σ_i, N_i is the number of cycles required for failure at the amplitude of stress cycle σ_i, and k is the number of stress levels identified in a stress time history at the location of interest. Eqn. (3.18) implies that fatigue failure occurs when the value of D is equal to 1. An S-N fatigue curve is used to determine the value of N_i, which is obtained from laboratory tests for a specific specimen subjected to constant amplitude stress cycle σ_i $(= S_i)$. According to the AASHTO LRFD bridge design specification (2010), the S-N curve is expressed as

$$N_i = c\, S_i^{-3} \tag{3.19}$$

where c is the detail category constant varying with the type of detail and their fatigue strength. And the number of cycle n_i corresponding to the stress level σ_i is obtained from cycle counting algorithms (e.g., the rainflow counting method).

Once the damage accumulation index D is determined by Eqn. (3.18), the expected time to failure due to fatigue (fatigue lifetime) T_{life} can be obtained by

$$T_{\mathbf{life}} = \frac{T_{\mathbf{obr}}}{D} \tag{3.20}$$

where T_{obr} is the period of observation.

3.2.1.2 Rainflow Counting Algorithm

The Rainflow counting method, one of the most well-known and effective cycle counting algorithms, defines cycles as closed stress/strain hysteresis loops as illustrated in Figure 3.1. The closed hysteresis loops can be constructed from the strain-time history shown, and the four cycles (B~C, D~E, G~F, A~D) are easily identified from the closed hysteresis loops. The original Rainflow counting method proposed by Matsuiski and Endo (1968), however, is intended to be carried out once the entire strain history is known, which is not suitable for online fatigue monitoring.

A one-pass rainflow counting algorithm by Downing and Socie (1982) addressed this issue by arranging sampled strain time history measurements into an one-dimensional array, which allows keeping track of the peaks and valleys that have not formed a closed loop. Then, the typical Rainflow counting process is performed on the set of peaks and valleys, identifying closed hysteresis loops and strain cycles.

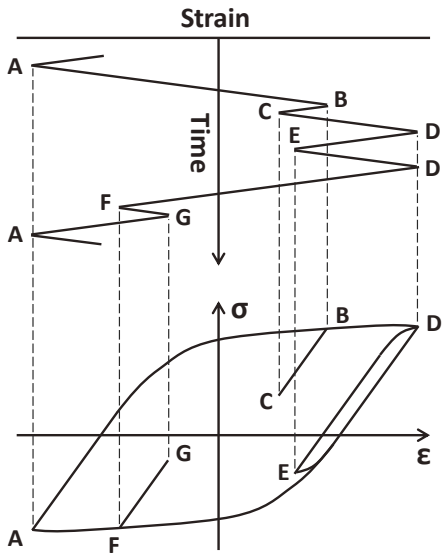

Figure 3.1. Rainflow cycle counting by closed-loop identification.

3.2.2 Numerical validation of Kalman filter-based fatigue life monitoring

3.2.2.1 Computational model of 14-bay steel truss structure

The effectiveness of the methodology and applicability to determining the stress/strain response and the associated fatigue life at arbitrary points on the structure is illustrated using a model of the simply-supported 14-bay truss structure shown in Figure 3.2. The truss structure consists of 53 frame elements and 55 DOFs. All elements have the same cross-sectional properties: area A_r = 5.454 × 10^{-4} m^2 and moment of inertia I = 2.607 × 10^{-8} m^4. For all member, the material density ρ = 7.83 × 10^3 kg/m^3 and modulus of elasticity E = 2.0 × 10^{11} N/m^2 are same. The length of each bay is L = 0.4 m and the height of the structure is h = 0.4 m.

Acceleration measurement noise of 70μg/√Hz and stain measurement noise of 10μstrain/√Hz are conservatively considered in simulated measurements based on data acquisition experience using wireless smart sensors (Jo et al., 2012; Jo et al., 2013). The value of the fatigue constant in Eqn. (3.19) is taken to be c = 20 × 10^{11}, assuming the truss member is categorized as B′ in the

AASHTO detail categories for load-induced fatigue. Model error of 5% is considered in the Kalman filter estimation; that is, an exact model is used for simulating structural responses, and 5% random perturbations are added to the stiffness matrix of the system for formulating Kalman filter.

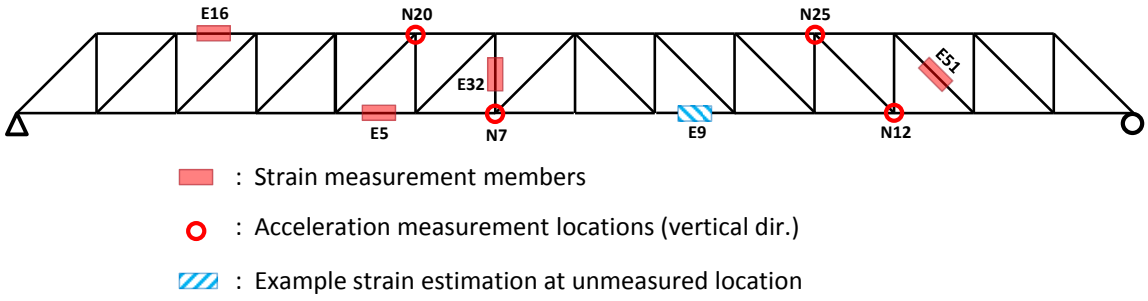

Figure 3.2. Computational model of 14-bay simply-supported truss structure.

A filtered white noise excitation is applied vertically to node 10 using the 2nd order filter equation as below,

$$\ddot{x}_f(t) + 2\xi_f\omega_f\dot{x}_f(t) + \omega_f^2 x_f(t) = -w(t) \tag{3.21}$$

where w is white noise excitation and x_f is the filtered displacement response in relative coordinates. State-space form of the Eqn (3.21) constructs the filter coefficient matrices $\mathbf{A}_f$, $\mathbf{B}_f$, and $\mathbf{H}_f$ of Eqns (3.7) and (3.8), and the input excitation is applied in the form of filtered acceleration $\ddot{x}_f$. The ω_f and ξ_f represent the frequency and damping information of the input. In this simulation, $\omega_f = 1$ rad/sec and $\xi_f = 0.9$ are used to provide more excitation energy in low-frequency range.

It should be noted that reasonable filter equation should be obtained for real-world application; which would be wind excitation, earthquake excitation, and any other excitations as long as it can be simulated from filtered white noise. Some types of excitations that cannot be represented with filtered white noise, such as vertical traffic loadings, require further study.

For real-world application of this method, discrete-time domain approach may be preferred, since the structural response measurements are discrete. The continuous system can be easily converted to discrete-time system, for example Papadimitriou et al. (2010) and Lourens et al. (2012). For this specific numerical simulation, the continuous-time Kalman filter is used.

Limited numbers of measurements are used to estimate strain responses at arbitrary locations on the structure, considering 4 case scenarios as follows:

Case-1: 2 strain measurements (only strain)

Case-2: 4 strain measurements (only strain, but increased number of sensors)

Case-3: 4 acceleration measurements (only acceleration)

Case-4: 2 acceleration and 2 strain measurements (multi-metric)

3.2.2.2 Strain Estimation Results

Figure 3.3 shows example results for the cases 1 ~ 4 at an unmeasured location. While the proposed approach can estimate the strain response at arbitrary locations on the structure, for this comparison, only the unmeasured strain for the element 9 is considered (see Figure 3.2).

For case 1 and case 2 (see Figure 3.3a, b), only strain measurements were used for the Kalman filter estimation, but different numbers of strain sensors were considered. When two strain measurements are used (case 1), the low-frequency response is captured. But the noise levels are relatively high and higher frequency information is relatively poor, as clearly shown in

the power spectrum at the right of Figure 3a. When the number of strain measurements employed is increase to four (case 2), somewhat better results are obtained, as is seen in the root-mean-square (RMS) noise comparison. However, substantial errors are still present in the high-frequency information. And the error covariance values (σ_9) that correspond to the strain response of the element 9 show similar trend.

Case 3 shows the results when only acceleration measurements are used for the Kalman filter estimation. To compare with the case 1 ~ 2, using only strains, much better performance is shown, particularly in the high-frequency range. The estimated strain response using the Kalman filter well represents most of the frequency peaks below 100Hz, but has a little worse performance in the very low-frequency area, which is the nature of acceleration measurements. Some discrepancy is observed between the reference signal and Kalman filter estimation, particularly in the time domain, as seen in the Figure 3.3c.

Case 4 uses multi-metric measurements (i.e., both strain and acceleration). The results indicate superior performance over the single-metric cases. The total number of sensors used is still four, which is the same with case 2 and case 3. But, the combined use of heterogeneous metric measurements of strain (i.e., for low frequency responses) and acceleration (i.e., for higher frequency responses) results in more accurate estimation of strain response both in the low-frequency and high-frequency ranges, as is seen in Figure 3.3d. And the least error covariance value is obtained among the four cases.

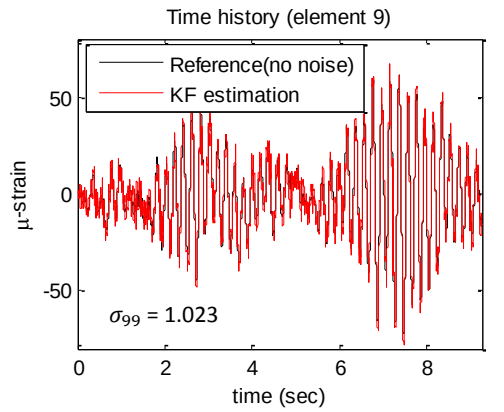

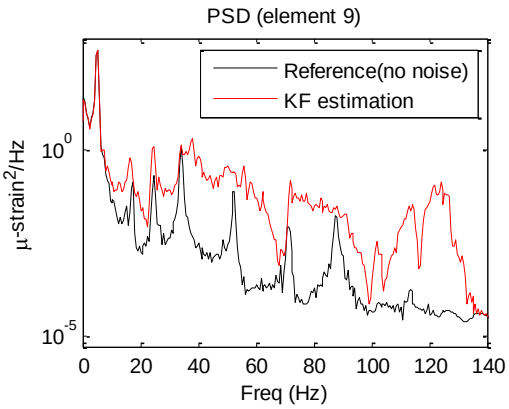

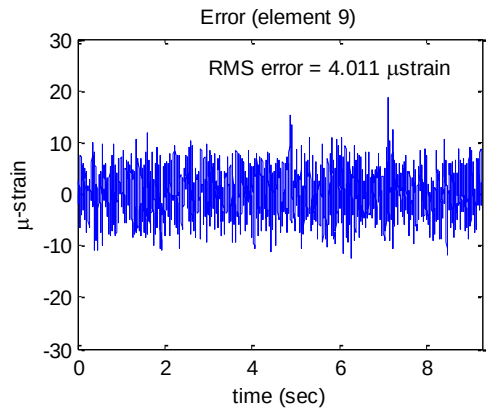

(a) Case 1: 2 strains

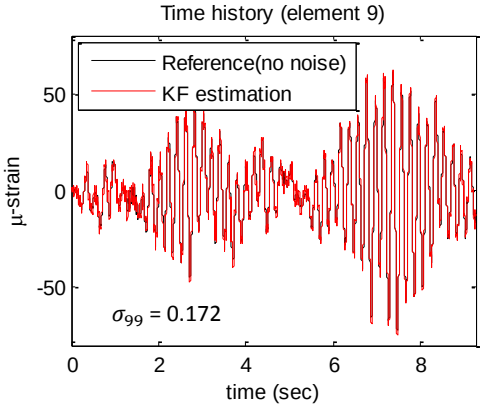

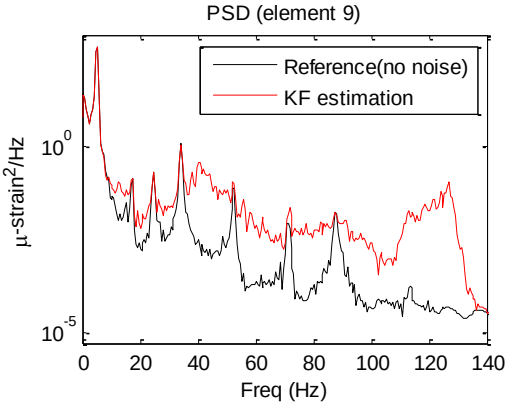

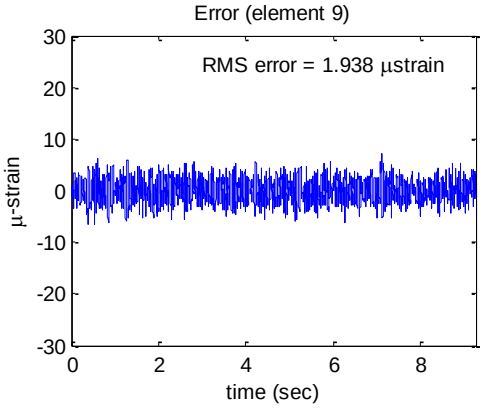

(b) Case 2: 4 strains

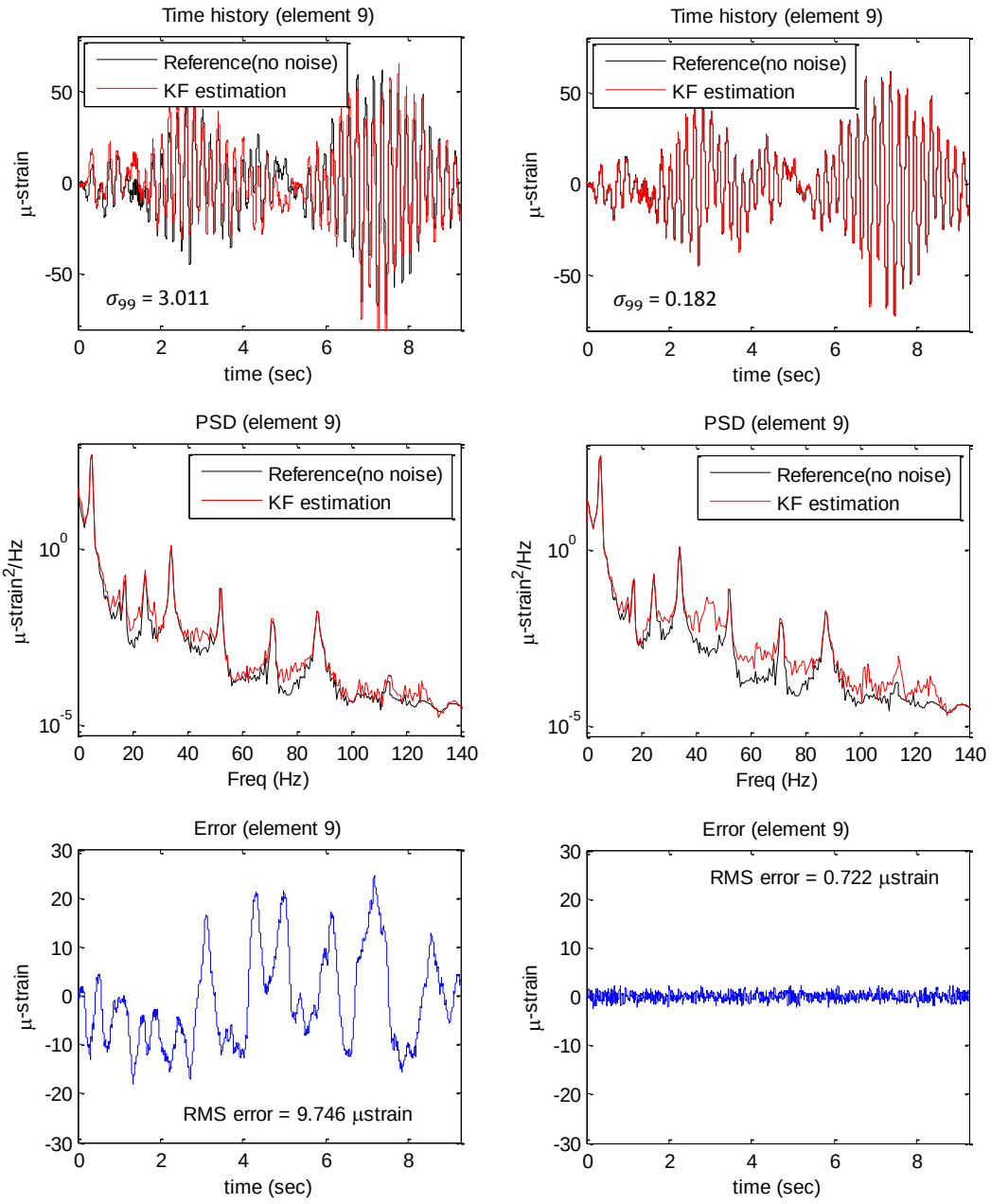

(c) Case 3: 4 accelerations (d) Case 4: 2 strains & 2 accelerations

Figure 3.3. Examples of strain response estimation (time histories and spectrum) at an unmeasured location using proposed multi-metric Kalman filter method.

3.2.2.3 Fatigue life assessment

The Rainflow counting method is now used to extract the strain/stress amplitude and number of cycle information from the strain response estimates by Kalman filter. Using the stress amplitude and cycle information obtained from the Rainflow method, the fatigue life of the structure can be estimated, in conjunction with the Eqns. (3.18) ~ (3.20). Figure 3.4 (left) shows the fatigue life estimation for each of the structural elements of the truss model; the right side of the Figure 3.4 zooms in for some of bottom chord members.

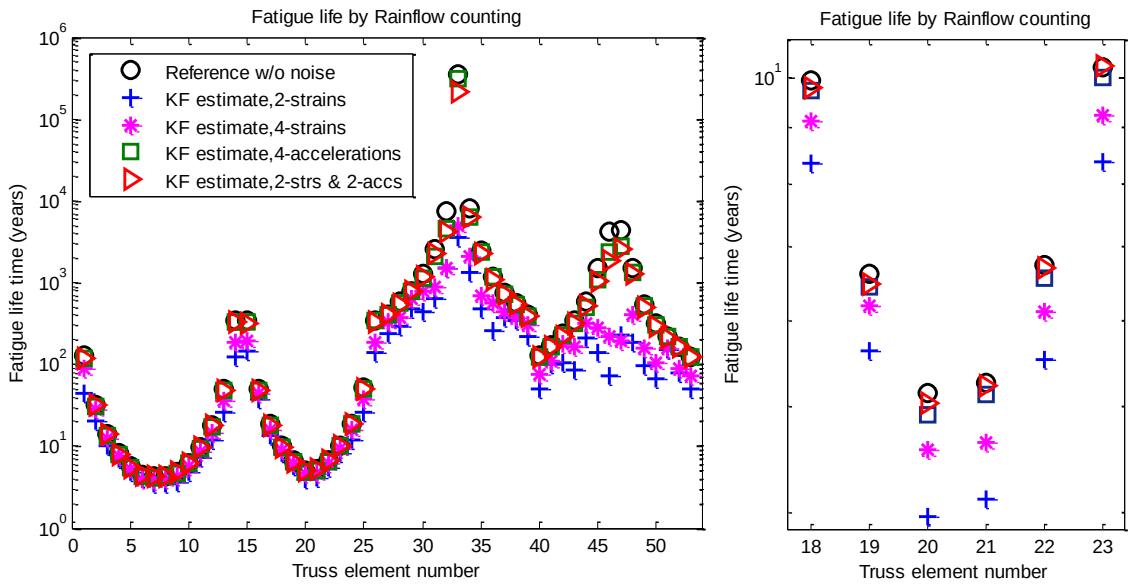

Figure 3.4. Fatigue life: (left) entire structural members, (right) detail for top chords.

The fatigue life estimation trends shown in the Figure 3.4 coincide well with the time-history and spectrum trend of the strain responses shown in the Figure 3.3. Case 1 using two strain measurements shows the worst performance; use of an increased number of strains (case 2) better estimates the fatigue life. As expected, case 4 using multi-metric measurements estimates

the fatigue life the best. However, the performance of case 3 using only accelerations is quite comparable to the case 4. Considering the stress cycle accumulation is the essential factor for fatigue life assessment, one can easily recognize that high-frequency strain/stress responses, which cause a larger number of stress cycles in a given time, are important. Hence, though the acceleration-only case 3 shows a little worse performance in the low-frequency range than the multi-metric case 4, the performance in fatigue life estimation is still quite good.

3.3 **Multi-metric Model-based Structural Displacement Monitoring**

Many of SHM approaches benefit from the availability of dynamic displacement measurements. However, current SHM technologies rarely support displacement monitoring, primarily due to the difficulty in measuring absolute displacement. The proposed hybrid method, described in section 3.1, is applied to estimate structural displacements at arbitrary locations on a structure, particularly focusing on how multi-metric measurements of strain and acceleration responses affect the accuracy improvement in displacement estimations of a low-frequency tall building structure.

3.3.1 Computational model of tall building structure

The effectiveness of the multi-metric model-based methodology and applicability to determining displacement responses at arbitrary points on the structure is illustrated using a model of a tall column structure shown in Figure 3.5. The column structure has a uniform sectional property along the axis; area A_r = 9.0 m^2 and moment of inertia I = 30.75 m^4. The material density ρ = 8.5 × 10^3 kg/m^3 and modulus of elasticity E = 2.1 × 10^{11} N/m^2 are also same along the line. And the total height of column H_t = 125 m.

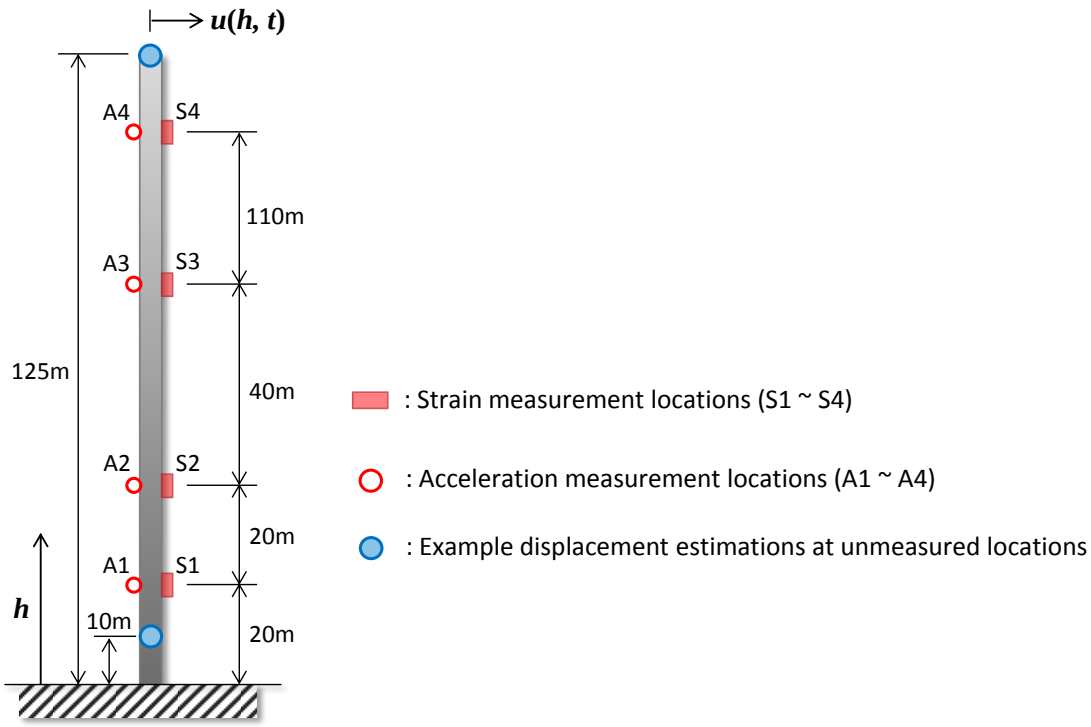

Figure 3.5. Numerical model of tall column structure.

The depth of neutral axis of the section y_c = 2.5 m, which is used to convert the curvature information of the column structure into strain information as below

$$\varepsilon(h,t) = -\kappa(h,t) \times y_c = -x''(h,t) \times y_c \tag{3.22}$$

where $\varepsilon(h,t)$ is strain response at the height h from the ground level and time t, $\kappa(h,t)$ is the curvature that is the second derivative of the lateral displacement $u(h,t)$ to the height h.

The assumed mode method is used for this simulation (Craig and Kurdilla, 2006) as below

$$u(h,t) = \sum_{i=1}^{N} \phi_i(h) \cdot q_i(t) \tag{3.23}$$

and the following function is used for the assumed mode

$$\phi_i(h) = \left(\frac{h}{H_t}\right)^{i+1}, \quad i = 1, 2, 3, \dots, N \tag{3.24}$$

where H_t (= 125 m) is the total height of the structure, *N* indicates the total number of modes used, and $q(t)$ is generalized modal coordinate. Total 6 modes (*N*=6) is used for this numerical study. Then the elements of mass and stiffness matrices are given as below

$$m_{ij} = \int_0^{H_t} \rho A_r \, \phi_i \phi_j dh\,, \qquad i,j = 1,2,3,\dots,N \tag{3.25}$$

$$k_{ij} = \int_0^{H_t} EI \, \phi_i^{"} \phi_j^{"} \, dh, \qquad i,j = 1,2,3,\dots,N \tag{3.26}$$

and the state vector is comprised of modal coordinate and its time derivative as below

$$\boldsymbol{x}(t) = \begin{Bmatrix} \boldsymbol{q}(t) \\ \dot{\boldsymbol{q}}(t) \end{Bmatrix} \tag{3.27}$$

In this simulation, 1.5% of modal damping is considered. The six natural frequencies of the structure from the eigenvalue analysis are 0.104Hz, 0.652Hz, 1.826Hz, 3.584Hz, 6.610Hz, and 10.541Hz.

A ground excitation is applied using the Kanai-Tajimi filter (Kanai, 1957; Tajimi, 1960), which uses the 2nd order filter equation form below; which is the same as Eqn. (3.21)

$$\ddot{x}_f(t) + 2\xi_f \omega_f \dot{x}_f(t) + \omega_f^2 x_f(t) = -w(t) \tag{3.28}$$

In this equation, the Kanai-Tajimi filter parameters to represent the dynamic characteristic of the ground are $\omega_f = 18.46\,\mathrm{rad/sec}$ and $\xi_f = 0.32$, which are in the reasonable range of general stiff soil condition (Pappa et al., 1992). In same way, Eqn. (3.28) can be put in the form of Eqns. (3.7) and (3.8) to construct the state-space form of the filter equation.

Measurement noise of 5% of the acceleration and strain responses, respectively, are conservatively considered in the simulation. And limited numbers of measurements are used to estimate displacement responses at arbitrary locations on the structure, considering 4 scenarios as follows:

Case-1: 2 strain measurements (only strain)

Case-2: 4 strain measurements (only strain, but increased number of sensors)

Case-3: 4 acceleration measurements (only acceleration)

Case-4: 2 acceleration and 2 strain measurements (multi-metric)

3.3.2 Displacement estimation results

The Figure 3.6 and 6.7 show example results for the case 1 ~ 4 at an unmeasured locations. For this comparison between cases, the horizontal displacements at the height h = 10 m and h = 125 m are used, while the method can estimate displacement responses for all DOFs.

For the displacement estimation at h = 10 m, the case 2 and case 3, Figure 3.6a, b, used only strain measurements for the displacement estimation but with different number of strain sensors. When two strain measurements are used (case 1), it successfully represents the low-frequency response. But the higher frequency information is not so accurate, as shown in the power spectrum (middle of Figure 3.6a). When the number of strain measurements employed is increased to four (case 2), a little better results are obtained in terms of RMS error. But substantial discrepancies between the reference and estimation for the higher frequency peaks still exist, as seen around the 5^{th} and 6^{th} peaks.

Case 3 (see Figure 3.6c) shows the results when only acceleration measurements (at four locations) are used. The power spectrum clearly shows the better estimation in higher frequency area to compare with the case 1 ~ 2, but substantial RMS error exists due to the inaccuracy in the low-frequency area.

The best results are obtained for case 4 using multi-metric measurements, as shown in the Figure 3.6d. Both the low-frequency response and higher-frequency dynamic behavior are well

represented. The combined use of multi-metric measurements of strain and acceleration results in accurate estimation of structural displacements both in low-frequency and high-frequency range.

The state vector in the assumed-mode approach is composed of modal coordinate and its time derivative. Hence the diagonal terms of the error covariance matrix obtained from the Kalman filter process represent the error components that influence on each mode. Table 3.1 shows the error covariance values that correspond to each mode at the location h = 10m. In general, low-level of error covariance is obtained through entire mode, and the case 4 shows the least error.

Table 3.1. Error covariance values corresponding to each mode (at h=10m).

	$\phi_1(h)\cdot\sigma_{11}$	$\phi_2(h)\cdot\sigma_{22}$	$\phi_3(h)\cdot\sigma_{33}$	$\phi_4(h)\cdot\sigma_{44}$	$\phi_5(h)\cdot\sigma_{55}$	$\phi_6(h)\cdot\sigma_{66}$
Case 1	1.1279	0.5815	0.1956	0.0353	0.0034	0.0002
Case 2	0.9779	0.5009	0.1709	0.0312	0.0031	0.0002
Case 3	2.9552	0.1777	0.0223	0.0041	0.0004	0.00002
Case 4	0.8109	0.1656	0.0335	0.0061	0.0006	0.00003

For the displacement estimation at the top of the structure (h = 125m), however, a somewhat different trend is observed. As shown in Figure 3.7, the high-frequency energies of the displacements at the top are very low for all four cases, even for the reference data. Since the displacement responses at the top of the structure do not contain the high-frequency information, the use of acceleration measurement is not that helpful. Therefore, significant noise and error are found in case 3 (see Figure 3.7c), even the multi-metric case (see Figure 3.7d) does not show better results than the strain only cases (case 1 ~ 2). The inaccuracy trend in high-frequency is even clearer in the error covariance values (see Table 3.2). The error covariance values for the 4^{th} ~ 6^{th} modes are really big, meaning that the estimation of high-frequency information is not reliable.

Table 3.2. Error covariance values corresponding to each mode (at h=125m).

	$\phi_1(h)\cdot\sigma_{11}$	$\phi_2(h)\cdot\sigma_{22}$	$\phi_3(h)\cdot\sigma_{33}$	$\phi_4(h)\cdot\sigma_{44}$	$\phi_5(h)\cdot\sigma_{55}$	$\phi_6(h)\cdot\sigma_{66}$
Case 1	17.624	113.565	477.576	1078.421	1307.339	806.923
Case 2	15.281	97.843	417.191	952.944	1163.609	721.010
Case 3	46.175	34.698	54.464	126.293	160.499	102.034
Case 4	12.671	32.349	81.673	187.120	238.059.0	150.971

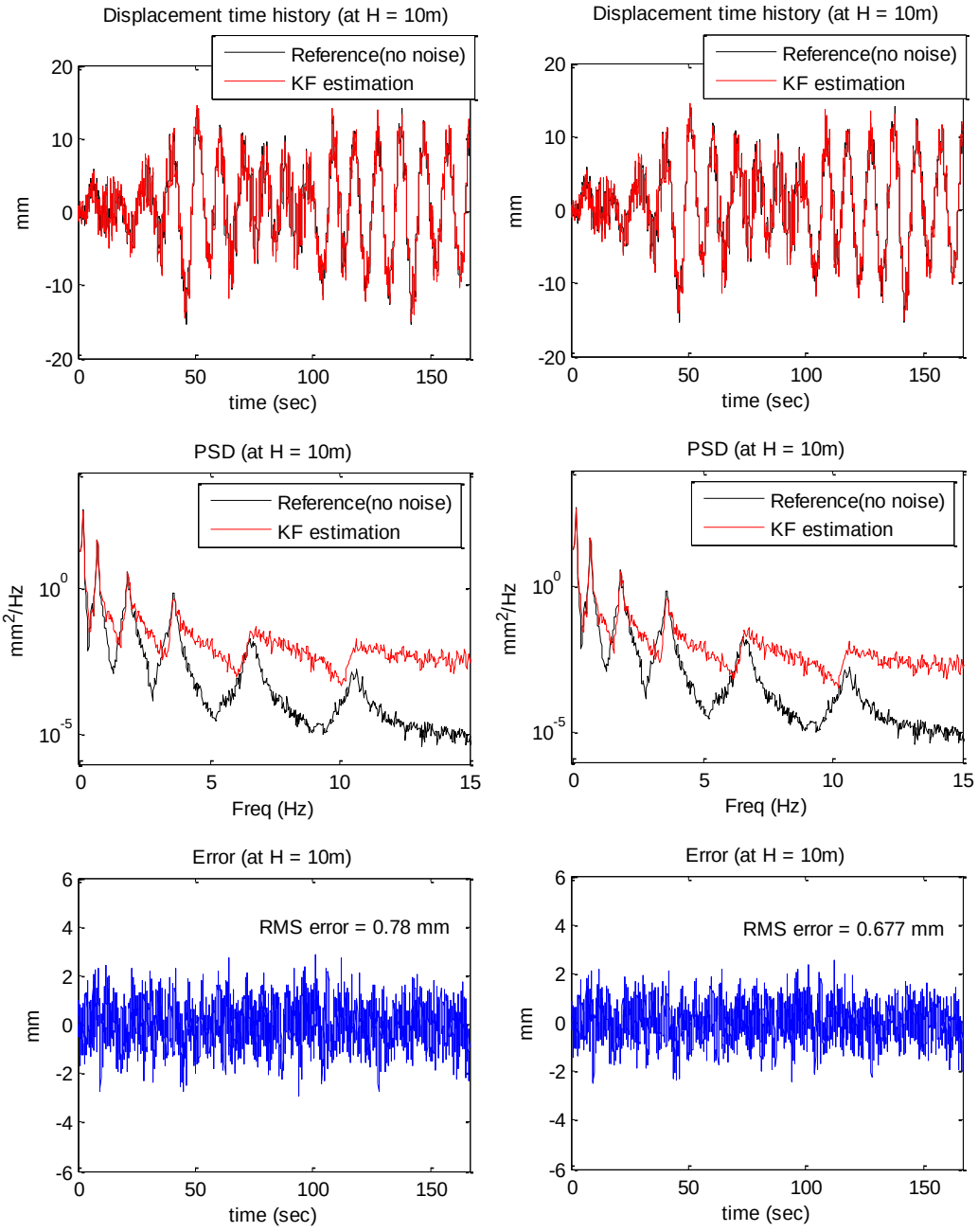

(a) Case 1: 2 strains

(b) Case 2: 4 strains

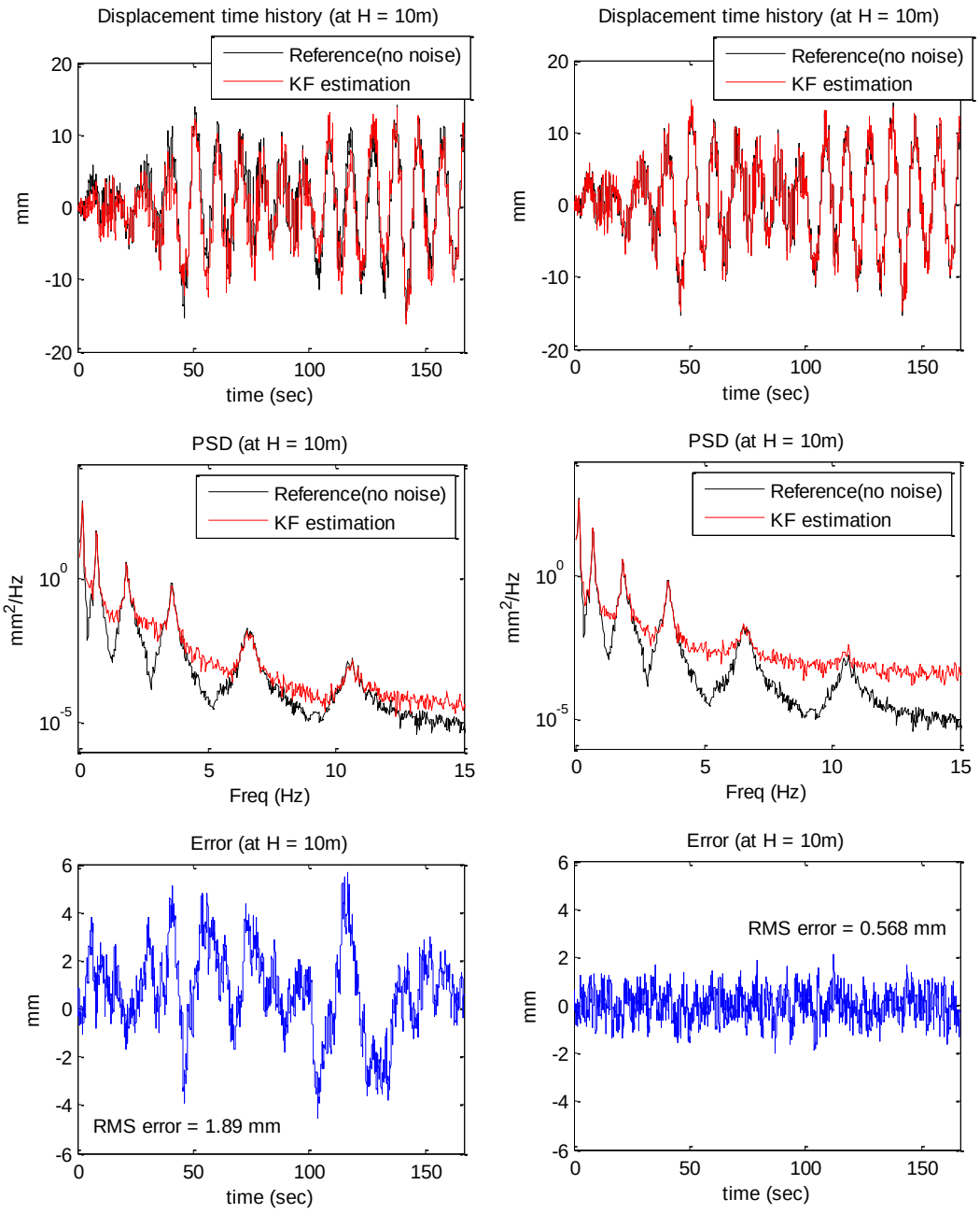

(c) Case 3: 4 accelerations (d) Case 4: 2 strains & 2 accelerations

Figure 3.6. Structural displacement estimation (time histories, spectrum, and RMS error) at an unmeasured location (h = 10m) using proposed hybrid method.

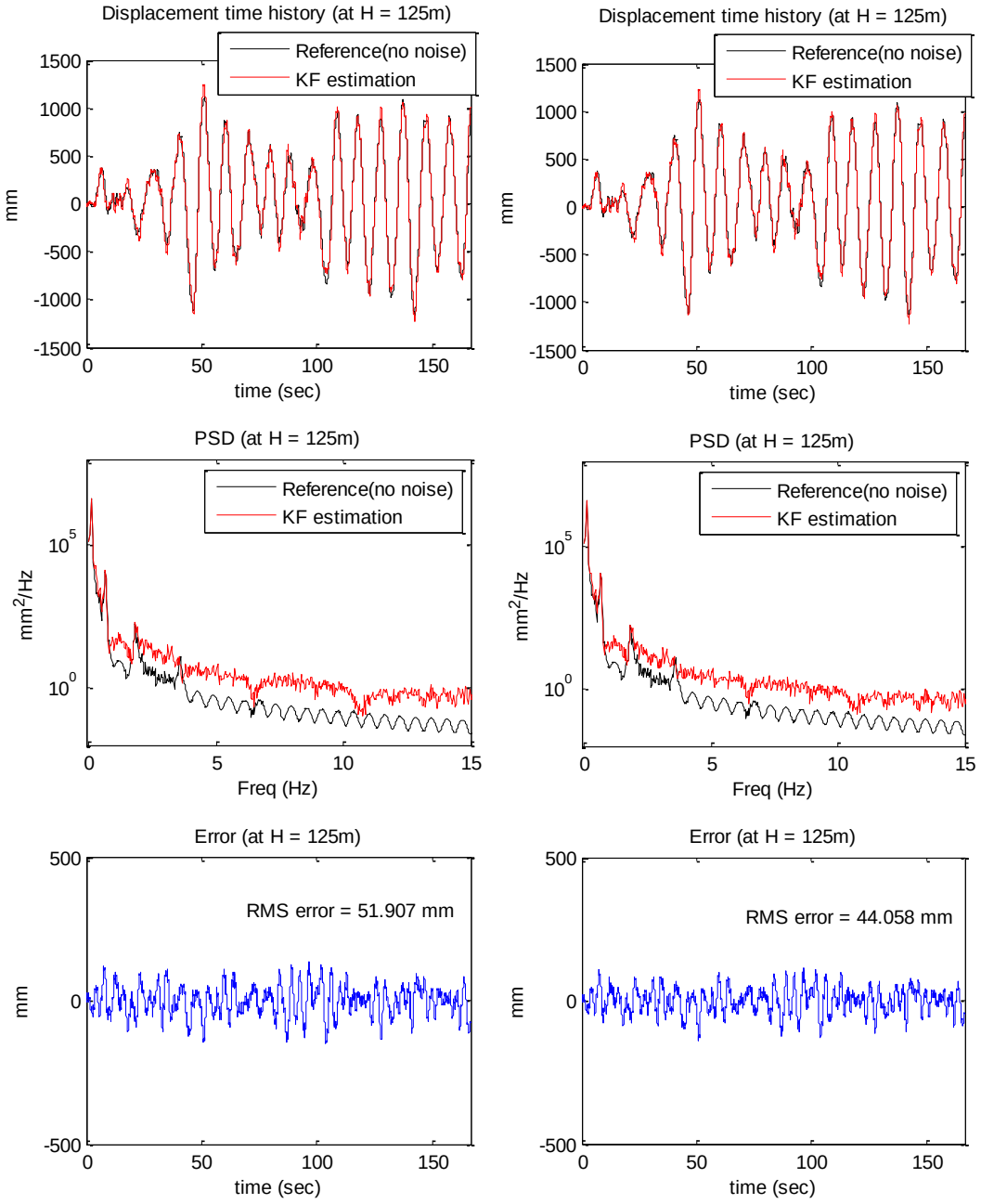

(a) Case 1: 2 strains

(b) Case 2: 4 strains

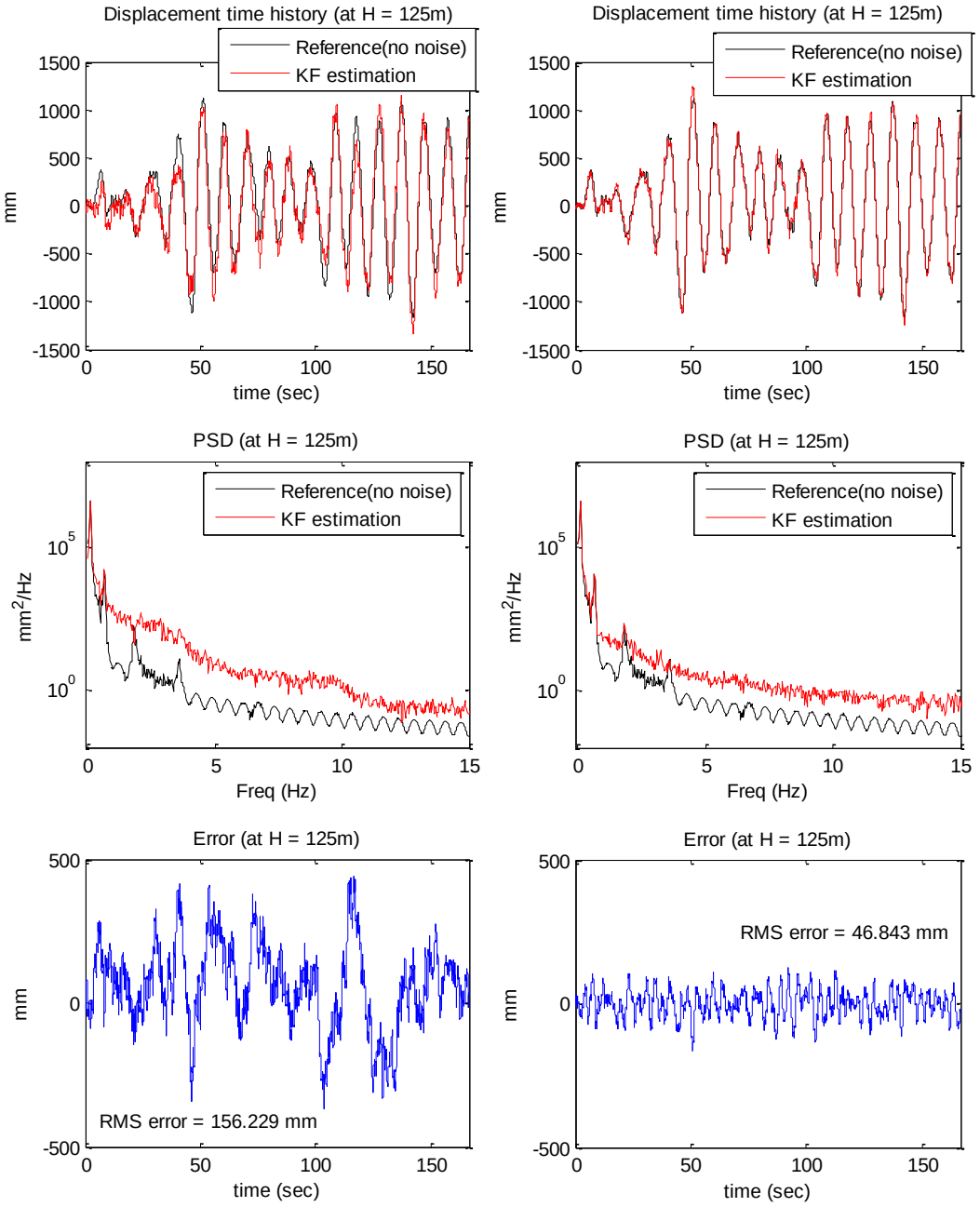

(c) Case 3: 4 accelerations (d) Case 4: 2 strains & 2 accelerations

Figure 3.7. Structural displacement estimation (time histories, spectrum, and RMS error) at an unmeasured location (h = 125m) using proposed hybrid method.

3.4 **Summary**

This chapter describes a hybrid structural monitoring strategy combining computational models and multi-metric physical monitoring. The Kalman filter enables a model-based approach, which allows estimation of structural responses at arbitrary locations using computational models and updates the prediction using measurements. An augmented state space representation modeling the non-white nature of the excitation has been included, as well as use of heterogeneous-metric measurements of strain and acceleration response in the measurement process. The multi-metric approach provided better accuracy in both the low- and high-frequency regions in general, and the efficacy of proposed method was numerically validated through the fatigue life monitoring application of a steel truss structure and the displacement monitoring of a tall building structure. The model-based Kalman Filter approach shows robust and accurate performance.

CHAPTER 4 MULTI-METRIC SENSOR BOARD DEVELOPMENTS

This chapter presents the hardware developments allowing high-sensitivity multi-metric SHM using WSSN. The hybrid monitoring approach mentioned in the previous chapter points to a promising new avenue for SHM. The use of multi-metric measurements shows great potential to enhance the quality of the obtained information. However, many of WSSs do not effectively support such multi-metric monitoring. In particular, its application to low-level ambient vibration has rarely been possible due to limited capabilities of currently available WSSs. The design and testing of a variety of high-sensitivity multi-metric sensor boards for Imote2 platform is presented; which include 1) high-sensitivity accelerometer (SHM-H) board, 2) data acquisition (SHM-DAQ) board, 3) high-precision strain (SHM-S) board, and 4) 24-bits data acquisition (SHM-DAQ24) board.

4.1 **High-sensitivity accelerometer sensor board (SHM-H board)**

4.1.1 Design Criteria

Efforts to improve the data quality from the sensor board require consideration of several factors. First, the noise floor of the sensor and other electrical components should be sufficiently low. Second, the sensitivity of the sensor, which is the relationship between the physical phenomena and output of the sensor, should be sufficiently high. The final factor is that the resolution at which the analog signal is digitized by the ADC should be fine enough.

A new high-sensitivity accelerometer sensor board, named SHM-H board, has been developed for measuring low-level ambient vibrations of structures. The SHM-H board is the extension version of the SHM-A board (general purpose acceleration board). The SHM-H board

also employs the Quickfilter ADC; however, the z-axis of the SHM-A board, which has the highest noise among the 3-axes, is replaced with a low-noise and high-sensitivity sensor. In addition, by reducing the span of the ADC, the resolution of the ADC can be improved.

4.1.2 Low-noise accelerometer

For the high sensitivity-acceleration board, the Silicon Designs SD1221L-002 low-noise accelerometer is used. This accelerometer is a micro-machined capacitive-type sensor with ±2g and DC to 400Hz sensing range. In particular, the 2g version has a noise density of $5\mu g/\sqrt{Hz}$ and a sensitivity of 2000mV/g with differential analog outputs. The SD1221 contains a temperature dependent current source that is useful for measuring the internal temperature of the accelerometer so that any previously characterized bias and scale factor temperature dependence can be corrected. The main features of the SD1221 are given in Table 4.1.

Table 4.1. SD1221L-002 accelerometer specifications.

Parameter	Value
Input Range	±2g
Frequency Response	0 ~ 400 Hz
Sensitivity (Differential)	2000 mV/g
Output Noise (Differential, RMS)	5 $\mu g/\sqrt{Hz}$ (10 $\mu V/\sqrt{Hz}$)_
Bias Temperature Shift	0.4 mg/℃ (max 1.2 mg/℃)
Scale Factor Temperature Shift	-1 ~ +1 mg/℃
Output Impedance	90 Ohms
Operating Voltage	Typ. 5 Volts (4.75 ~ 5.25 Volts)
Operating Current	Typ. 8 mA (max 10 mA)

4.1.3 Sensing range reduction

To support the low-noise performance of the accelerometer, the resolution of the QF4A512 ADC is improved by reducing the span of the ADC. If the full span of the SD1221L-002, ±2g, is used, the resolution that the ADC can achieve is just $4000 \text{ mg} / (2^{13.2} - 1) = 0.43\text{mg}$, assuming 13.2 effective number of bits (ENOB) of the Quickfilter ADC (2007). The resolution of 0.43mg is not sufficient for the ambient vibration of 1~2 mg level. By limiting the measurement range of the sensor to ±0.2g for horizontal acceleration and +0.8g ~ +1.2g for vertical acceleration, consequently the signals were 10 times amplified and shifted with OP-Amp circuits to fit in the ADC input range, a maximum resolution of $400 \text{ mg} / (2^{13.2} - 1) = 0.043\text{mg}$ is achieved, which is sufficient to capture low-level acceleration in the range of 1~2 mg.

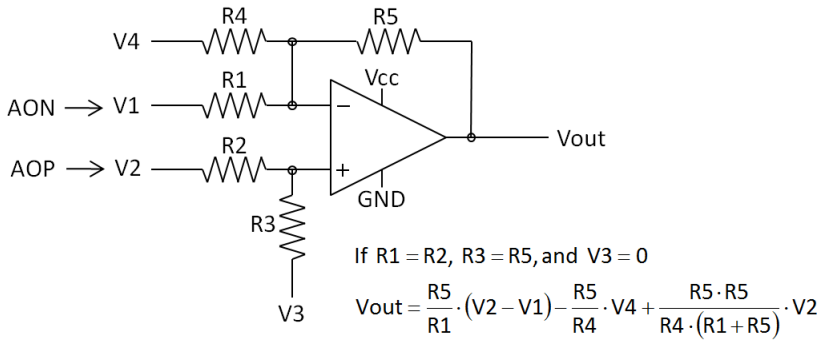

Figure 4.1. OP-Amp circuit for the amplification and shift of the signal.

4.1.4 Low-noise board design

The separation of the analog and digital sections of the PCB keeps the noisy digital signals away from the low level analog signals. The SHM-H board has a mostly solid ground plane on the bottom side, which is split between the digital and the analog ground plane. The digital signal lines are on the digital plane and the analog signal lines are over the analog ground plane. It is

important that the analog ground and the digital ground be connected together at the ADC. This approach allows a quick return for the ground currents as the analog and digital portions of the device communicate. The bridge to connect two ground planes is just below the Quickfilter ADC. Figure 4.2 and Figure 4.3 show the block diagram and sensor board design, respectively.

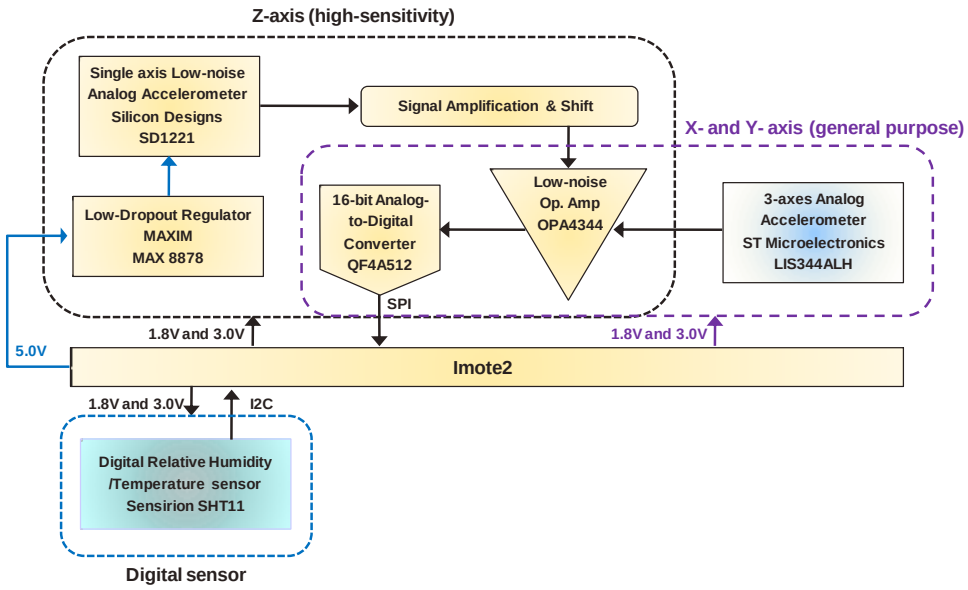

Figure 4.2. SHM-H sensor board block diagram.

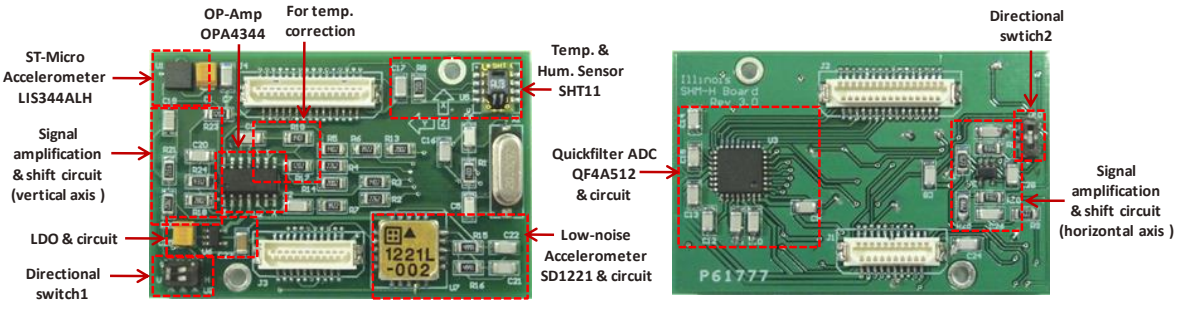

Figure 4.3. Top view (left) and bottom view (right) of SHM-H sensor board (Rev.3).

4.1.5 Calibration tests

To estimate the actual noise floor of the SHM-H sensor board and compare with the performance of the other MEMS accelerometers, static noise characteristic tests were conducted. Using the *RemoteSensing* application of ISHMP Services Toolsuite, the acceleration data from the SHM-H sensor board was measured and compared with the data from the SHM-A board and the ITS400 sensor board under the same conditions. As shown in Table 4.2 and Figure 4.4, the RMS noise of SHM-H sensor board is 0.05mg over 15Hz bandwidth (0.08mg over 70Hz bandwidth), which is about ~15 % of SHM-A board's noise level.

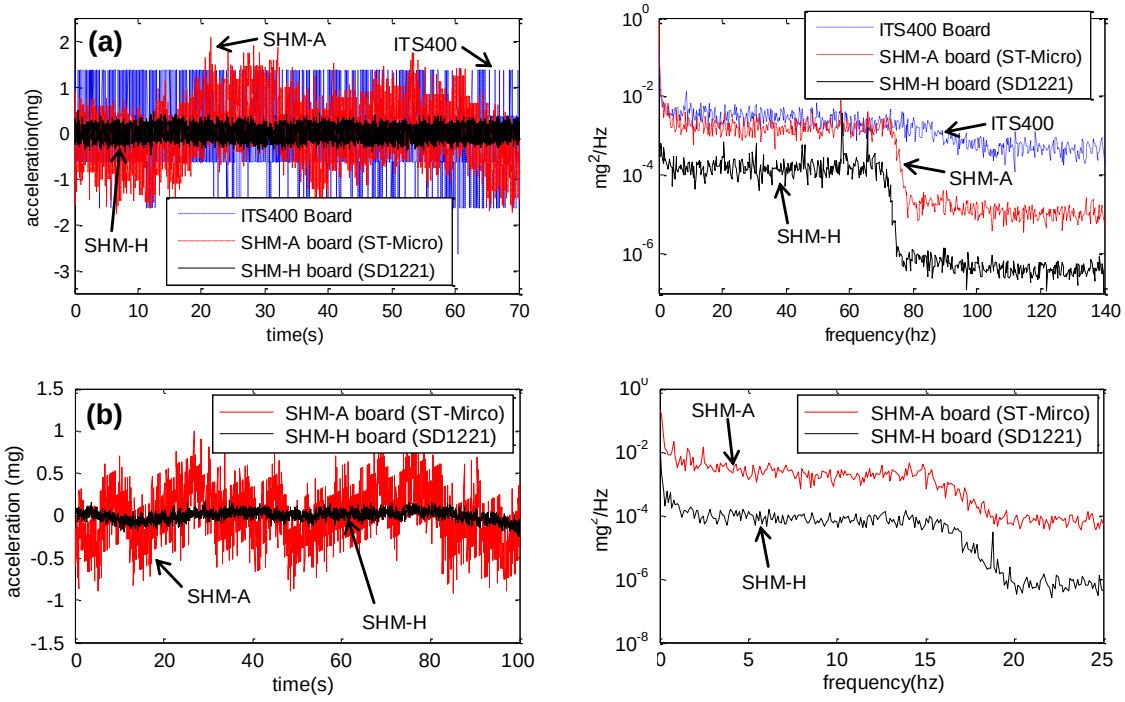

Figure 4.4. Sample static test results: time histories (left) and power spectral densities (right): (a) sampling rate fs = 280Hz, cutoff frequency fc = 70Hz (20,000 data points), (b) sampling rate fs = 50Hz, cutoff frequency fc = 15Hz (5,000 data points).

Table 4.2. Noise comparison of sensor boards for Imote2 platform.

Sensor board	RMS noise (fs = 280Hz, fc = 70 Hz)	RMS noise (fs = 50Hz, fc = 15 Hz)
ITS400	0.58 mg	N/A
SHM-A board	0.39 mg	0.31 mg
SHM-H sensor board	0.08 mg	0.05 mg

The SHM-H sensor board was tested on a vertical shaker to check that the sensor had predictable response and assess how well the response matches with the response from a conventional accelerometer. For this test, an electrodynamic shaker (LDS V408) and a piezo-electric type PCB393C accelerometer as a reference sensor were used. The PCB393C has 0.1mg resolution over 1~10,000 Hz broad band, which corresponds to 1 μg/√Hz noise density roughly. A 50Hz band-limited white noise excitation was used for the comparison of the SHM-H sensor board and the PCB393C. The results given in Figure 4.6 show excellent agreements between the wired sensor and the SHM-H sensor board in both time and frequency domain.

Figure 4.5. Electrodynamic shaker (left) and PCB393C accelerometer (right).

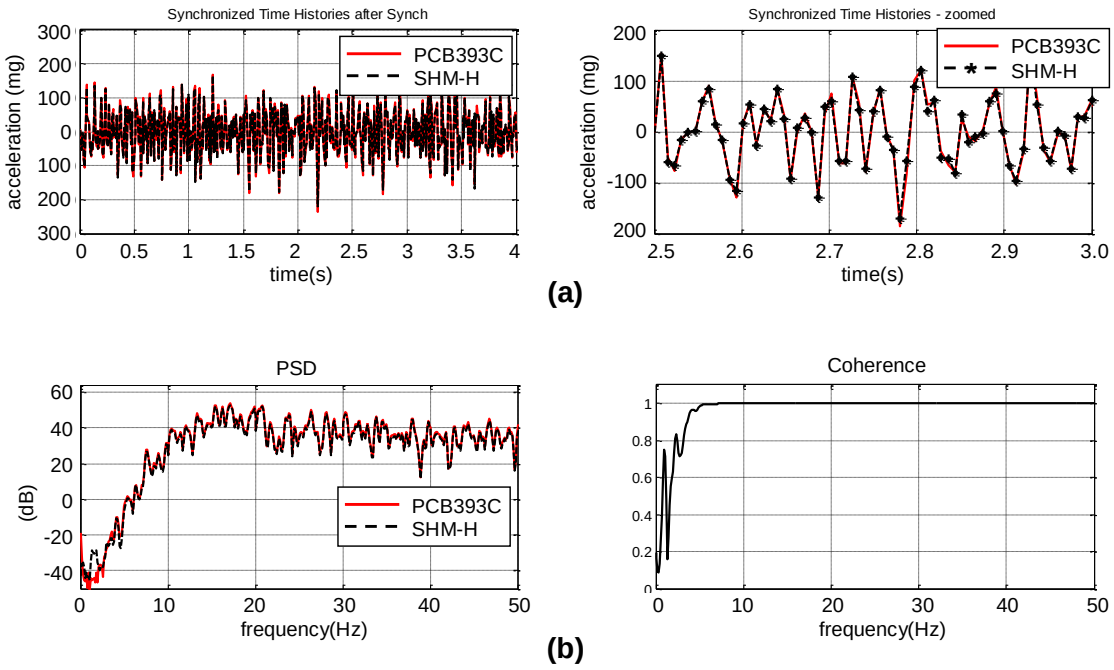

Figure 4.6. Shaker test results: (a) Time histories (left) and zoomed (right), (b) power spectral densities (left) and coherence (right).

4.1.6 Temperature compensation

The SD1221 accelerometer experiences the mean value drift due to temperature change; according to the datasheet, the bias temperature drift effect is about 0.4 mg/℃. Figure 4.7 shows the time history of a constant acceleration signal measured by the SHM-H board for 2000 seconds; as is seen, the signal drifts from -1mg ~ +2.5mg.

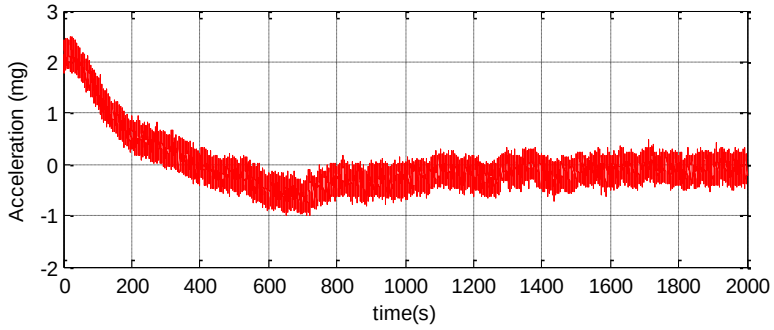

Figure 4.7. Mean-value drifted acceleration signal (2000 seconds measurement).

Although this drift usually does not affect the frequency content of the original signal, it is essential to consider in the case that the magnitude of the acceleration is important.

The SD1221 provides a temperature-dependent current source output. This temperature-dependent current is useful for the estimation of the temperature inside the sensor so that the associated drift can be corrected. The nominal output current at 25°C is ≈ 500μA and the nominal sensitivity is 1.5μA/℃. The current signal, however, should be converted to voltage signal that the Quickfilter ADC can read. The 4th channel of the ADC in the SHM-H board is used to measure this temperature dependent voltage signal. Figure 4.8 shows the OP-Amp circuit for converting the current signal to the voltage signal. For the temperature range of -15℃ ~ +85℃, the default setting of the circuit (R1 = 20K, R2 = 3.6K, and Vr = 1.8V) provides the voltage signal change of 3V ~ 0V.

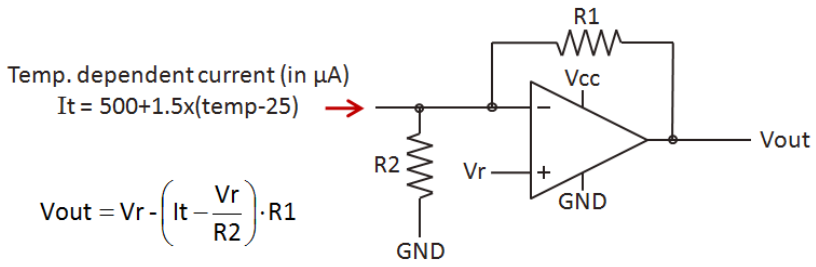

Figure 4.8. OP-Amp circuit for the signal converting (current → voltage).

Figure 4.9(b) shows the raw data of the temperature using the OP-Amp circuit shown in Figure 4.8; as is observed, the temperature signal has quite similar shape with the drifted acceleration signal shown in Figure 4.9(a); the linear relation is clearly apparent in Figure 4.9(c). Using the scaled temperature signal shown in Figure 4.9(d), the drifted acceleration signal can be corrected. The temperature corrected acceleration signal and its power spectrum are shown in Figure 4.10. It should be noted that the use of the scaled-smoothed temperature signal, which is

just temperature change trend, gives better correction than the use of just scaled raw temperature signal. Because the temperature signal itself can have some noise, it can add noise on the corrected acceleration signal. Figure 4.10(b) shows that the temperature correction using the scaled temperature data itself increases the noise level little in the low frequency range (see dotted box in the PSD) while the scaled-smoothed temperature trend does not affect the PSD.

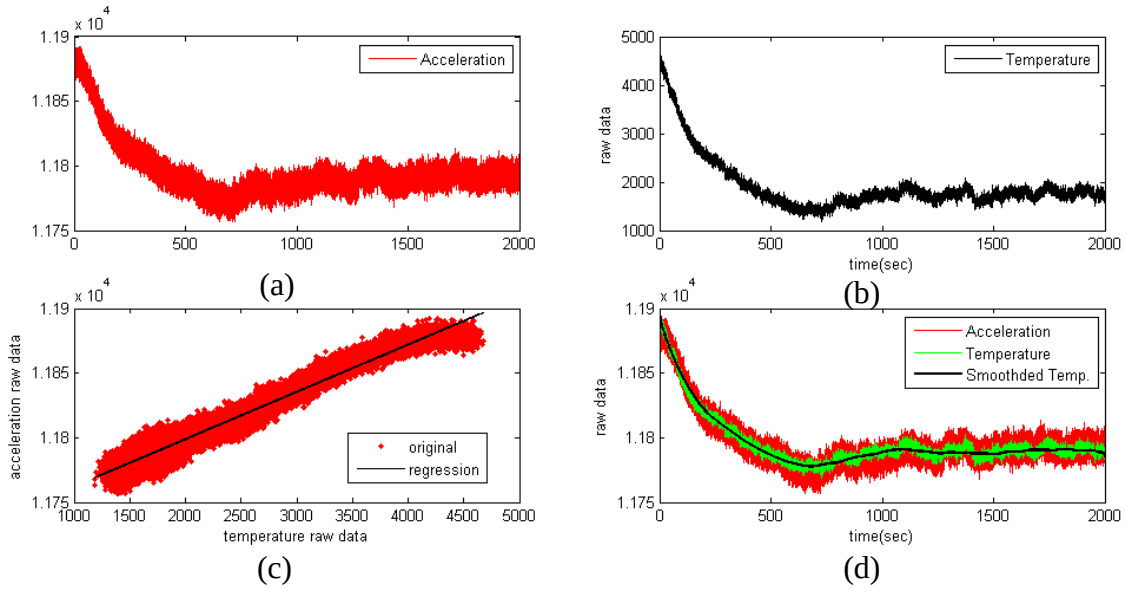

Figure 4.9. Relation between mean-value drift in acceleration signal and inside temperature: (a) raw acceleration data from ADC, (b) raw temperature data from ADC, (c) linear relation between the acceleration & the internal temperature, (d) scaled- and scaled-smoothed temperature signal.

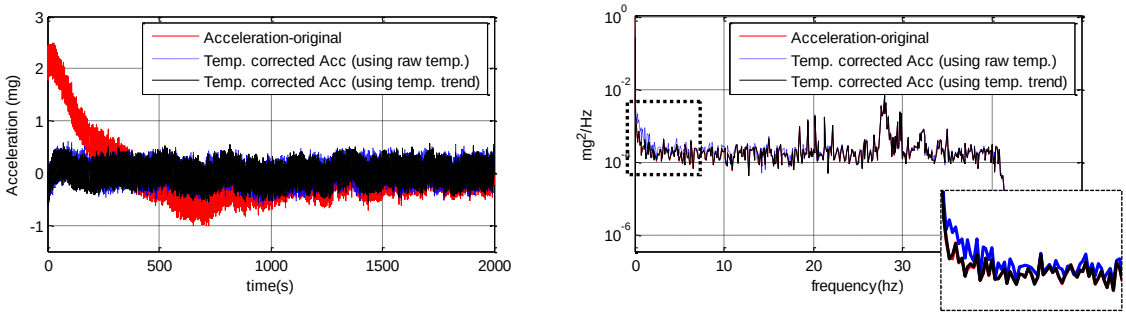

Figure 4.10. Time history (left) and power spectral density (right) of temperature corrected acceleration.

4.2 **Data acquisition board (SHM-DAQ board)**

4.2.1 Considerations for data acquisition board design

To allow more flexible multi-metric sensor inputs, a data acquisition board, named SHM-DAQ board, has been designeed with the following features :

- Many of analog sensors give differential or bipolar outputs, thus the data acquisition board needs to be designed to accommodate such differential and bipolar signals in addition to single-ended signals.
- To accommodate digital sensors as well, the digital interface of Imote2, such as SPI, I2C, and GPIO, needs to be provided through the data acquisition board.
- Flexible ways to connect external sensors and their signal to the data acquisition board should be provided.

4.2.2 Signal conditioning circuit

Considering the output range of DC-output analog sensors is generally 0 ~ 5V, the SHM-DAQ board has been set to accommodate that input voltage range for all four differential channels of the Quickfilter QF4A512 ADC by placing 40kohm resistor in front of input pins of the ADC based on the datasheet.

To support bipolar inputs, range of -5 ~ 5V was selected in this research, the signals need to be conditioned to be fitted into the 0 ~ 5V default input range of the ADC. An OP-Amp circuit similar to that used for the SHM-H accelerometer board was employed, as, illustrated in Figure 4.1. In Figure 4.1, setting the resistance ratio R5 and R3 to R1 and R2, respectively, to 0.5, and providing a 2.5V reference source to the V3 and GND (0V) to V1, then the output voltage is

$$Vout = 0.5 \times V2 + 2.5 \quad (4.1)$$

where V2 is the bipolar input signal on the interval -5 ~ 5V, and the 2.5V reference source is obtained from another OP-Amp circuit for a voltage divider. In other words, the amplitude of the bipolar signal of -5 ~ 5V is reduced by half, then the reduced signal (i.e. -2.5 ~ 2.5V) is shifted with the 2.5V reference source to fit into the default range of 0 ~ 5V.

4.2.3 Stackable design and digital input

The SHM-DAQ board has been designed to use most of the digital interfaces provided by Imote2. The board employs two terminal blocks on the both edges of the board (see Figure 4.12, left) to make the connection of external sensor to the board easy, which allow wire-to-board connection for all four ADC channels, the digital interface, and three different and regulated power supply voltage of 1.8V, 3.0V, 5.0V, and ground (GND) for excitation of external sensors.

The board has been designed to provide another way for interfacing external sensor signal with the board by employing advanced board-to-board connectors on the top of the board (see Figure 4.12, left). The connectors allow the other most of interfaces of Imote2, in addition to the functions that the terminal blocks provide. Furthermore, because stackable use of sensor boards is available with the board-to-board connectors, the stackable feature simplifies the design of another new sensor board that needs to use the same ADC; which means the DAQ board will play a role as the mother board to provide the ADC capability and connectors for other peripherals. Figure 4.11 shows the block diagram of the SHM-DAQ board design, and Figure 4.12 shows the top and bottom of the board, and an example of stackable use of external sensor board.

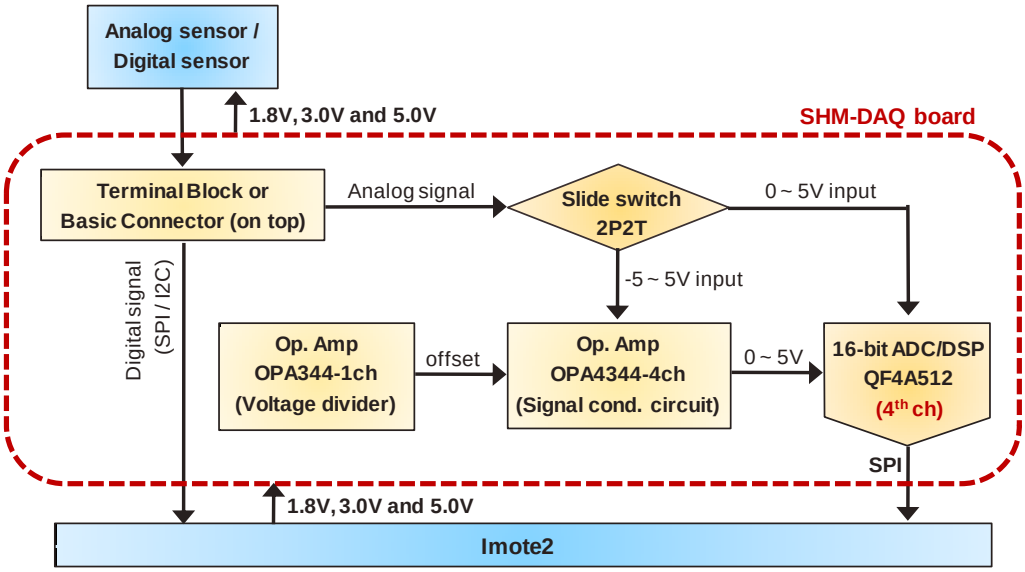

Figure 4.11. Block diagram of the SHM-DAQ board design.

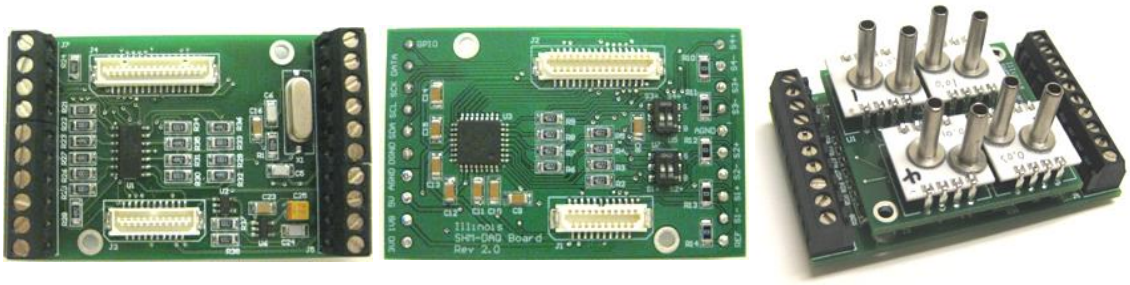

Figure 4.12. Top (left) and bottom (middle) of the SHM-DAQ board, and the pressure sensor board stacked on the SHM-DAQ board (right).

4.3 **High-precision strain sensor board (SHM-S board)**

4.3.1 Hardware design

4.3.1.1 Consideration for strain sensor board design

The first step in the design of a high-precision wireless strain sensor board is to secure sufficient signal amplification, as strain responses are generally just a few micro-strain (μs) for the ambient vibration of civil infrastructures. For example, consider a foil type 350-ohm strain gage having gage factor of 2; if the maximum level of strain is 1~2 μs, then the maximum corresponding resistance change in the strain gage is just 0.0007~0.0014 Ω. To convert the changes in resistance of the strain gage into a measurable voltage, a Wheatstone bridge circuit is generally used; then signal amplification is required to resolve such low-level signal variations. Considering that a 12~16bits ADC is generally adopted in wireless sensors for power efficiency and that the effective number of bit (ENOB) of the ADC is less than the specified resolution, signal amplification of several hundreds or thousands may be required.

Additionally, one of the most critical factors for successful use of a Wheatstone bridge combined with a signal amplifier is that the bridge circuit should be precisely balanced so that the signal is zero in the nominal state (i.e., equilibrium). If accurate balancing is not achieved (e.g., due to errors in resistance values of bridge arms or strain gage), then a non-zero offset will result, which when amplified, can easily saturate the A/D of the data acquisition system. Offset nulling of the amplified signal by adjusting the reference voltage of the amplifier would be one way to remove the non-zero offset effect. However, considering the available voltage range in WSS powered by batteries is quite limited, such an offset nulling approach may not be appropriate for the case for which high signal amplification is required. Therefore accurate bridge balancing is critical prior to signal amplification.

A second issue for accurate strain sensing is temperature compensation. Though some types of strain sensors provide temperature compensated measurements, most foil-type metal strain gages still have quite high thermal sensitivity (e.g., on the order of 10 με/°C). Temperature compensation, a practical issue to be addressed in real-world applications, is particularly important for cases involving large temperature changes or long-term measurements. Post compensation is possible by measuring temperature and using a correction curve provided by the manufacturers, however measuring the temperature of the structural element under consideration is not straightforward. A half-bridge circuit with a dummy gage can be used for correcting possible drift in the strain signal due to temperature changes.

Another practical issue to be considered for full-scale applications is strain sensor calibration. Considering that conditions at site are different from laboratory or shop conditions, prior calibration parameters may not be effective once installed at the site. Therefore embedded self-calibration capability is essential for broader application of strain sensing on full-scale structures. Shunt calibration verifies the output of the strain measurement system relative to a predetermined mechanical strain. This procedure involves simulating the predetermined strain input by shunting a known value of large resistor across the bridge arm connected to the strain gage, measuring the change of the output voltage, and estimating the sensitivity of the voltage output to the strain change.

Finally, compatibility of the strain sensor with other sensors in a WSSN is important. For the Imote2 WSS platform, several sensor boards have been developed: SHM-DAQ data acquisition board and SHM-H high-sensitivity accelerometer board in this research and SHM-A accelerometer board by Rice et al. (2010). All of those sensor boards use the same ADC, which is the Quickfilter QF4A512, a versatile 4-channel ADC and programmable signal conditioner

with user-selectable sampling rate and programmable digital filters. Design of the new strain sensor board using the same ADC platform will make available the services previously developed for the Imote2 including synchronized sensing and reliable communication.

4.3.1.2 Precisely balanceable Wheatstone bridge

Consider the balanced Wheatstone quarter-bridge circuit shown in Figure 4.13, which is composed of four resistive arms with an excitation voltage (V_{EXT}) applied across the bridge circuit. Three resistive arms have the same constant resistance R, while the other arm is an active resistor of value $R + \Delta R$, where ΔR is the resistance change proportional to strain change.

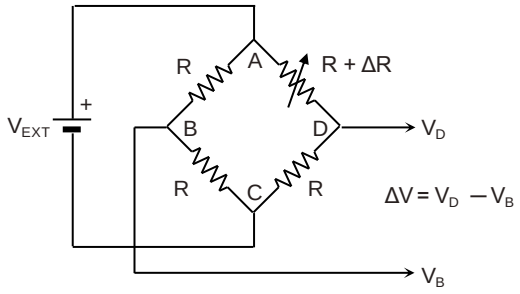

Figure 4.13. Wheatstone quarter-bridge circuit.

If the active resistor is a strain gage for which the gain factor $GF = (\Delta R/R)/\varepsilon$, where ε is strain, the output voltage becomes,

$$\Delta V = \left[\frac{-\Delta R}{4R + 2\Delta R}\right] \cdot V_{EXT} = -\frac{GF \cdot \varepsilon}{4}\left[\frac{2}{2 + GF \cdot \varepsilon}\right] \cdot V_{EXT} \approx? \frac{GF \cdot \varepsilon}{4} \cdot V_{EXT} = \frac{\Delta R}{4R} \cdot V_{EXT} \qquad (4.2)$$

Considering actual strain measurement ε is typically only a few micro-strain for ambient vibration and the gain factor of many of typical metal foil type strain gage GF is roughly 2~5, the nonlinear term of $(GF \cdot \varepsilon)/2$ in the denominator of the third term of Eqn. (4.2) is negligible.

Then the output voltage (ΔV) from the quarter-bridge is approximately proportional to the strain (ε), consequently the resistance change (ΔR) of the strain gage as shown in the last two terms of Eqn. (4.2).

As mentioned in previous the section, signal amplification from hundreds to thousands is required to measure sub-micron level ambient strain. However, if the Wheatstone bridge is not accurately balanced, any possible error in resistance values of bridge arms or strain gage can cause the bridge unbalance, which results in significant drift error in the output voltage after amplification and saturation of the ADC. For example, even a 1~2 ohm error in one of 350-ohm resistors or strain gage can cause 4.1~8.2V signal drift after 2000 times signal amplification, which exceeds the input range on the ADC used for wireless sensors.

To balance the bridge, the new strain sensor board (SHM-S board) uses a 2-channel non-volatile digital potentiometer (MAX5479 with 256-taps 100-kohms, MAXIM 2006). By connecting the 100-kohm digital potentiometer (DP) across the two of 350-ohm resistive bridge arms (see Figure 4.14), very accurate resistance adjustment, up to 0.0048ohm can be achieved. And use of a digital potentiometer allows software-controllable bridge balancing. The non-volatile memory on the potentiometer allows the wiper locations to be saved to the internal EEPROM, avoiding loss of the balanced condition during power cycling. For the SHM-S board, a variable-gain precision instrumentation amplifier (MAX4194, MAXIM 2003) is selected that supports single-voltage supply operation (2.7~7.5V), high gains (1~10000 times), and low-power consumption (93uA). The gain of the MAX4194 is determined by connecting a single external gain resistor and given by

$$Gain = 1 + \frac{50\text{k}\Omega}{R_{\text{G}}} \tag{4.3}$$

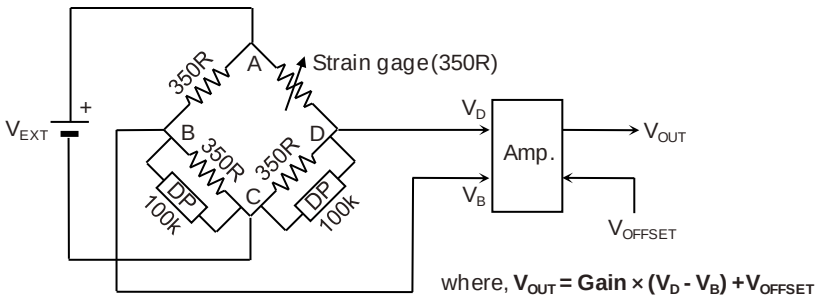

Figure 4.14. Adjustable-balance Wheatstone bridge and instrumentation amplifier circuit.

where R_G is the gain-setting resistor. For the SHM-S board, four different gains of 501, 1001, 2007, and 2507 are set by connecting four values of R_G which are obtained by four different parallel combinations of two 100-ohm and one 33.2-ohm resistors with a software controllable switch. The final output voltage from the amplifier is determined by multiplying the difference of the differential inputs (V_D and V_B in Figure 4.14) by the gain obtained from Eqn. (4.3) and adding the reference/offset voltage as follows:

$$V_{OUT} = Gain \times (V_D - V_B) + V_{OFFSET} \tag{4.4}$$

4.3.1.3 Temperature compensation and shunt calibration

Use of the half-bridge configuration with a dummy strain gage is one way to reduce the temperature effect. For all strain gages in a bridge at the same temperature and mounted at the same location, any change in temperature affects all gages in the same way. Therefore, the use of a dummy gage in the half-bridge configuration allows compensating the signal drift in the counter-part active gage due to the temperature change. Of course, the half-bridge option can be used to double the sensitivity of the bridge to strain with active strain gages for both arms. In the SHM-S board, the half-bridge configuration is user-selectable and even can be deactivated,

which then becomes a quarter-bridge configuration, with an analog switch (switch 2 in Figure 4.15).

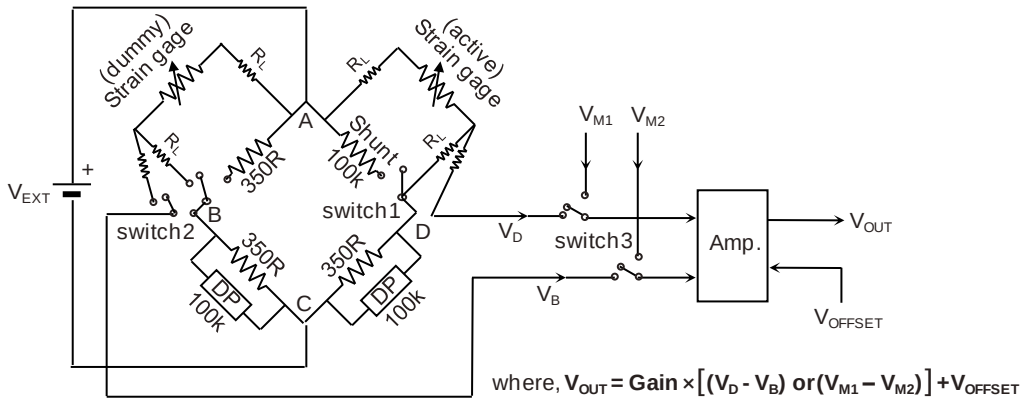

Figure 4.15. Strain bridge circuit including both temperature compensation and shunt calibration.

For shunt calibration, the SHM-S board employed a high-precision 100-Kohm resistor having 0.1% tolerance error and a software-controllable switch (switch 1 in Figure. 4.15). For the 350-ohm strain gage, connection of the 100-Kohm resistor across the strain gage results in about 1.221 ohm reduction in resistance, which corresponds to the strain input of about 1676.8 μs with GF = 2.08 (the GF = 2.08 is for the 350-ohm foil-type strain gage to be used subsequently for verification experiments).

4.3.1.4 Magnetic strain sensor

One of the disadvantages of strain measurements using the foil type strain gages is that the gage installation process is time consuming and can be difficult in the field. As an alternative, Tokyo

Sokki Kenkyujo (2005) has released a strain checker (FGMH-1) which is a non-destructive-type strain sensor composed of a frictional strain gage and magnet attachment (see Figure 4.16).

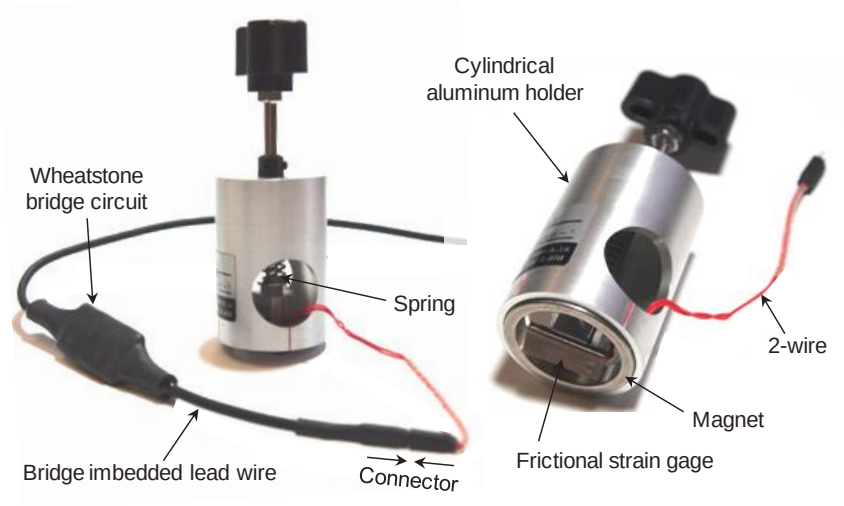

Figure 4.16. Friction-type magnet strain sensor (FGMH-1, Tokyo Sokki 2005).

While ordinary strain gages measure the strain through adhesive, the strain checker employs a cylindrical magnet which secures the aluminum holder to steel structure; a spring inside the holder press the strain gage onto the steel surface (see Figure 4.16). Because the base plate in which the 122-ohm strain gage is embedded, which will directly touch the surface, is coated by emery powder, the strain can be measured by friction (O'Brien et al 2008). With the strain checker, adhesives are not required; strain measurements even can be made without removing the paint of the structure. Combining the FGMH-1 with the SHM-S/Imote2 WSS node offers a powerful tool for investigating the performance of steel structures.

SHM-S board has been designed to properly interface with the magnet strain checker. Because the strain checker comes with a Wheatstone-bridge embedded in the lead wire (left of Figure 4.16), the differential voltage signals from the strain checker system needs to be fed to the

amplifier directly. By putting another analog switch (switch 3 in Figure 4.15) on the SHM-S board for bypassing the bridge of the board, direct use of the amplifier is possible.

4.3.1.5 Compatibility with other previous sensor boards

The SHM-S board has been designed to be stackable on the SHM-A accelerometer board or SHM-DAQ data acquisition board to utilize the ADC on the boards. The first three channels of the QF4A512 ADC on the SHM-A board are connected to the 3-channels MEMS accelerometer and the other 4th channel is left to accommodate an external analog sensor, which is used by the SHM-S board. For the SHM-DAQ board, all four channels are open to external analog input; for convenience, the strain signal from the SHM-S board is connected to the 1st channel of the SHM-DAQ board. An important advantage of the SHM-S board by using the same ADC as the SHM-A and SHM-DAQ boards is that it can fully utilize all functions of the SHM boards and ISHMP Services Toolsuite based network.

Figure 4.17 shows the block diagram of the SHM-S board design, and Figure 4.18 shows the SHM-S board stacked on the SHM-A (left) and on the SHM-DAQ board (right).

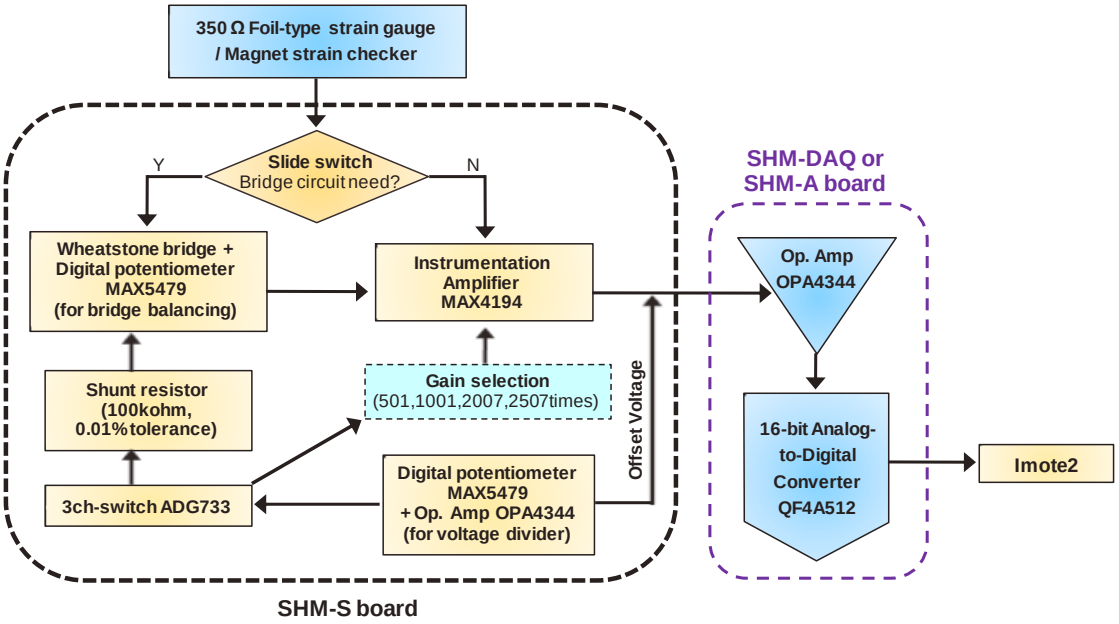

Figure 4.17. Block diagram of SHM-S board.

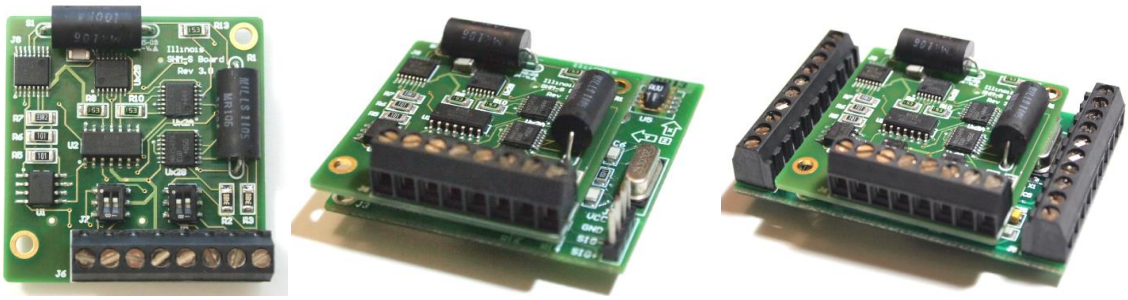

Figure 4.18. SHM-S board (left): stacked on SHM-A (middle) and on SHM-DAQ board (right).

4.3.2 Software design for strain sensor board

4.3.2.1 Autonomous bridge balancing and calibration

To effectively use the SHM-S board in the Imote2 based sensor network, software for autonomous bridge balancing and shunt calibration (*SHMSAutoBalance*; see Figure 4.19) was developed using the ISHMP ServicesToolsuite. The software operates to check the signal output

offset and then compensates the signal output offset to a designated level. The SHM-S board supports two methods of signal output offset compensation (i.e., zero shift): (1) reference voltage adjustment after signal amplification and (2) bridge balance control before signal amplification. If the offset error of the amplified signal is too large (i.e., beyond the output range (0~3V) of the (MAX4194) amplifier), it will be saturated at the top or bottom limit. In this case, the deviant signal needs to be guided by adjusting the reference voltage for the amplifier so that it will be in the range for which the bridge balancing process can work. Once the output voltage is in the proper range, then the bridge balancing process is carried out by adjusting the resistance of the digital potentiometers connected across the bridge arms, as shown in Figure 4.14 and Figure 4.15. This two-step compensation procedure allows an accurate zero shift up to 200% of the processable signal span.

Once the signal-offset error compensation process is complete, the shunt calibration process is conducted. By connecting the shunt resistor across the bridge arm using a programmable switch, a known-value of strain input is simulated. Then the ratio of the voltage change due to the simulated strain input to the amount of strain input is the sensitivity, which is used to convert the voltage output to physical strain units.

Figure 4.19 shows the simplified block diagram for the software (*SHMSAutoBalance*); detailed procedures for the autonomous bridge balancing and shunt calibration using the ISHMP Services Toolsuite are as follows:

1) Gateway node send a set of default parameters to a leaf sensor node using *ReliableComm*; i.e., minimum gain, default wiper position of the potentiometer and reference voltage of the amplifier, and sensing parameters.

2) Short-term sensing started in the leaf node using *SensingUnit* with the parameters received.
3) Mean of the voltage output measurement calculated.
4) If the voltage mean is larger than upper limit or less than lower limits, then adjust the reference voltage of the amplifier.
5) If the mean voltage, after (4) is carried out, is in the proper range, check if the mean is larger than default reference voltage.
6) If the mean voltage is larger than the reference voltage, adjust the resistance of the potentiometer connected across CD in Figures 4.14 and 4.15 to balance the bridge. Otherwise, adjust the potentiometer across BC.
7) Check the output mean voltage after short-term sensing with the balanced bridge.
8) Connect the shunt resistor and begin sensing.
9) Compare the mean voltages of (8) with (7), find the sensitivity of the output voltage to the strain, and send it to the gateway node.
10) Disconnect the calibration resistor from the bridge, and set new gain for actual sensing.

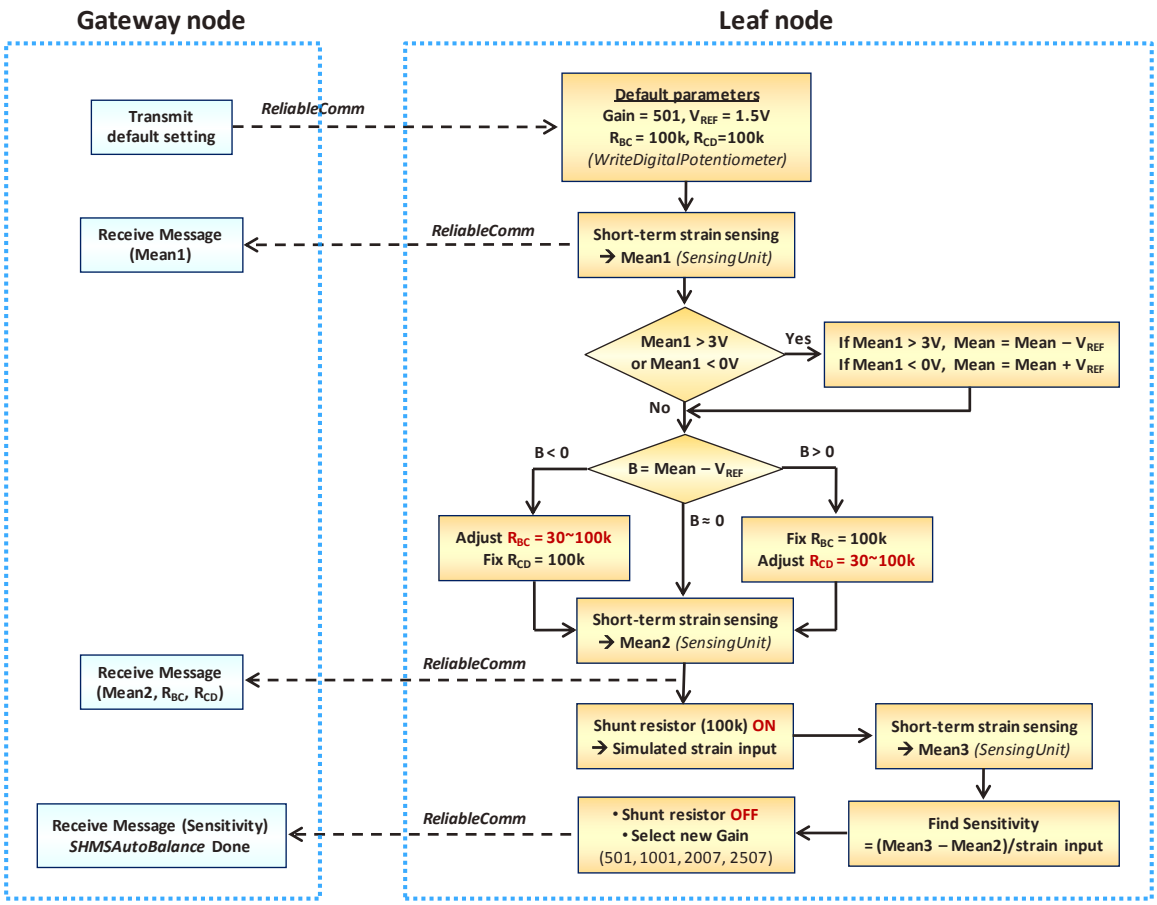

Figure 4.19. Block diagram of *SHMSAutoBalance* service in the ISHMP Services Toolsuite.

4.3.3 Validation of the high-precision strain sensor board

The performance of the developed wireless strain sensing system on the SHM-S board and the associated software has been verified through lab-scale tests. Strain measurements using the wireless strain sensing system are compared with a conventional wired system. The National Instrument (NI) DAQ system with SCXI-1520 universal strain gage input module combined with a SCXI-1314 front-mounting terminal block was used for the wired measurements (National Instrument 2007a,b). For this test, a one-bay 3-story shear building having steel-plate columns was used (see left part of Figure 4.20). Two foil-type 350-ohm strain gages with GF = 2.08 and

the magnet strain checker (FGMH-1) were attached on the exterior surface of the column around the 2nd floor (see right part of Figure 4.20). To check the performance of the SHM-S board in both the high-level and low-level strain range, long-time impulse responses were measured. Once an impulse load is applied to the structure, free vibration was measured until it approaches 1~2 μ-strain level. The strain response measurement using the SHM-S board was compared with the one measured by the NI-DAQ for two different cases in both the time and frequency domain:

- Case 1: SHM-S board with foil-type strain gage vs. Ni-DAQ (with AA filter of 10Hz cut-off) with foil-type strain gage.
- Case 2: SHM-S board with magnet strain checker vs. Ni-DAQ (with AA filter of 10Hz cut-off) with foil-type strain gage.

A 100Hz sampling rate was used for both wireless and wired system. The SHM-DAQ board was used to provide ADC (QF4A512) capability for the SHM-S board; a low-pass digital filter with a 30Hz cut-off, and a 100 Hz sampling rate was set.

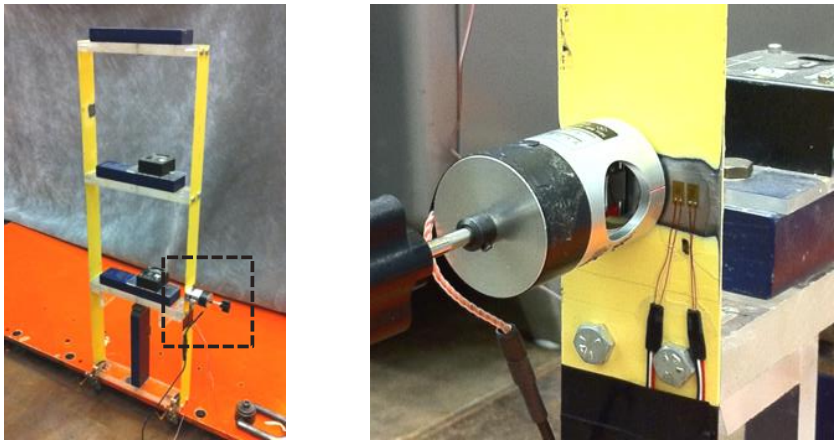

Figure 4.20. Strain sensor performance test using 3-story shear building.

4.3.3.1 SHM-S board with foil-type strain gage (Case 1)

The synchronized strain impulse responses for the Case 1 are shown in Figure 4.21. The response starts from about ±40 μs initial amplitude, tapering to close to ±1.0 μs after 200 seconds, as shown in Figure 4.21a. Three natural frequencies of 0.879Hz, 2.637Hz, and 4.004Hz were clearly found in the power spectral densities (PSD) of both the wired and wireless measurement (see Figure 4.21b). Figure 4.21c shows that the wireless and wired measurements are well matched at high strain levels. In Figure 4.21d, even for low-level strains of ±1.0 μs, both measurements show quite good agreement, though some noise and quantization are observed on the order of 0.2 μs.

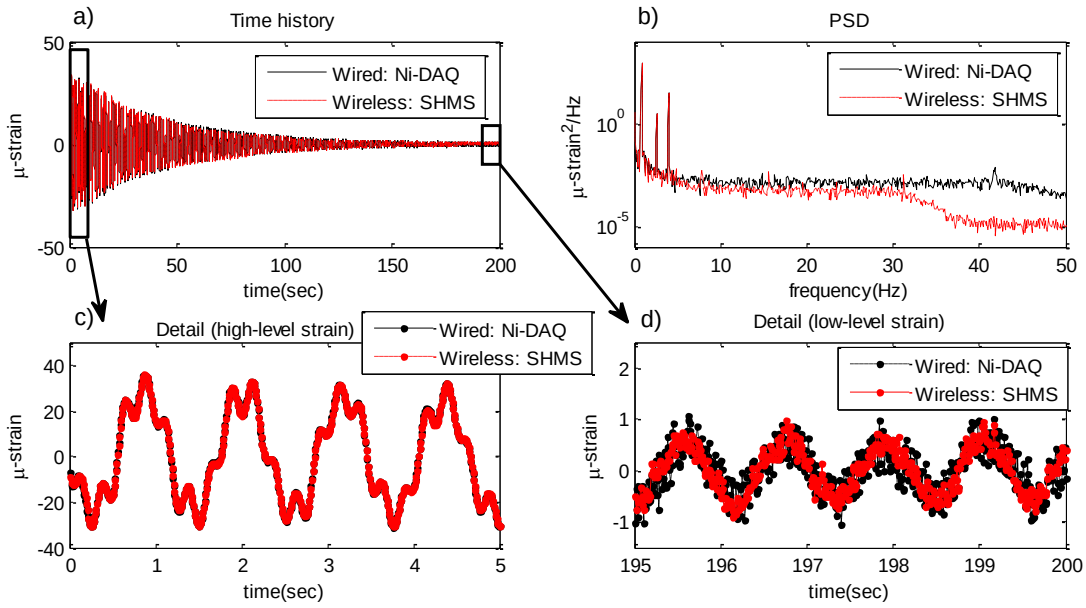

Figure 4.21. Strain impulse response, Case 1: Ni-DAQ with a foil-type strain gage (with AA filter of 10Hz cutoff) vs. SHM-S board with a foil-type strain gage.

4.3.3.2 SHM-S board with magnet strain checker (Case 2)

The performance of the magnet strain checker combined with the SHM-S board also has been compared with the NI-DAQ system. For this test, the bridge imbedded in the lead wire for the

strain checker was used and the differential signals from the strain checker system were directly connected to the amplifier, bypassing the Wheatstone bridge of the SHM-S board. As shown in Figure 4.22, the performance of the magnet strain checker was excellent at high strain levels (see Figure 4.22c). However, the magnet strain checker measurement was slightly noisier than the wired sensor at low-level strains, (see Figure 4.22d). One can see that the measurement by the magnet strain checker is noisier in frequency domain as well; the noise floor of the magnet strain checker is a bit higher than the one for NI-DAQ over entire frequency (see Figure 4.22b). For such low strain levels, a foil strain gage adhered in the traditional manner performed better than magnet strain checker using the friction interface.

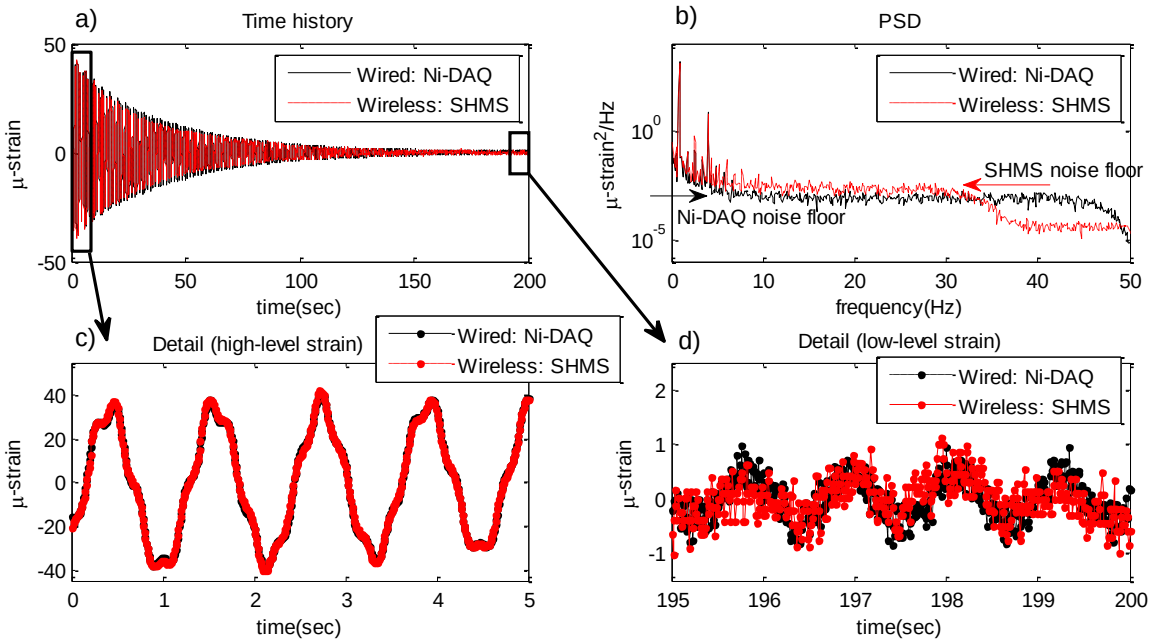

Figure 4.22. Strain impulse response, Case 2: Ni-DAQ with a foil-type strain gage (with AA filter of 10Hz cutoff) vs. SHM-S board with a magnet strain checker.

4.4 **24-bits Data Acquisition Board (SHM-DAQ24)**

4.4.1 Design Criteria

Many of issues in measuring low-level ambient vibration using existing wireless smart sensors are caused by the limited resolution of the A/D converter (ADC) on existing sensor boards. Though the QuickFilter's ADC (QF4A512) adopted in SHM-H, SHM-DAQ, and SHM-S boards provide many unique capabilities appropriate for SHM applications, the 16-bits of resolution (ENOB: 13.2bits) may not be sufficient for ambient vibration monitoring, such as low-level acceleration responses of high-rise buildings and micro level of strain responses in massive civil structures. The signal conditioning circuits employed in the design of the QuickFilter's ADC-based sensor boards (i.e., signal amplification, signal shift, and low-noise circuits) help to overcome such limitations, but they cause some by-products such as reduction of measurable sensing span. For example, the signal amplification used for the SHM-H board is roughly 10, resulting in only ±0.2g out of the ±2g sensing range of the SD1221 accelerometer that can be measured.

The use of 24-bits ADC resolves most of these concerns. The additional 8-bits of resolution, compared with 16-bits ADC, potentially results in signal amplification effect of 256 times (= 2^8) without sacrificing the sensing range. In the case of the SD1221 accelerometer, the 24-bits ADC allows sensing the full ±2g range acceleration at even better resolution.

4.4.2 Delta-sigma ADC

To obtain higher-resolution analog-to-digital conversion, the quantization noise floor should be lowered as much as possible. In general, the fixed amount of quantization noise ($q/\sqrt{12}$, where q=1.0 LSB) is evenly distributed over the transition band, which is from zero to the Nyquist

frequency (see Figure 4.23a). The oversampling process (i.e., increasing Nyquist frequency) allows the spread of the quantization noise over a broader band; subsequent low-pass digital filtering and decimation removes the noise distributed over the frequency range above the stopband of the digital filter (Figure 4.23b). And the quantization noise power is reduced by 3dB for every doubling of the oversampling ratio. This oversampling approach is usually employed to allow a general ADC to obtain better resolution; however, a higher sampling rate is required in this approach to obtaining a lower quantization noise floor. Note that increasing the sampling rate to such high level usually results in significant power consumption, which may be why 24-bits ADC are not yet available for wireless sensor applications.

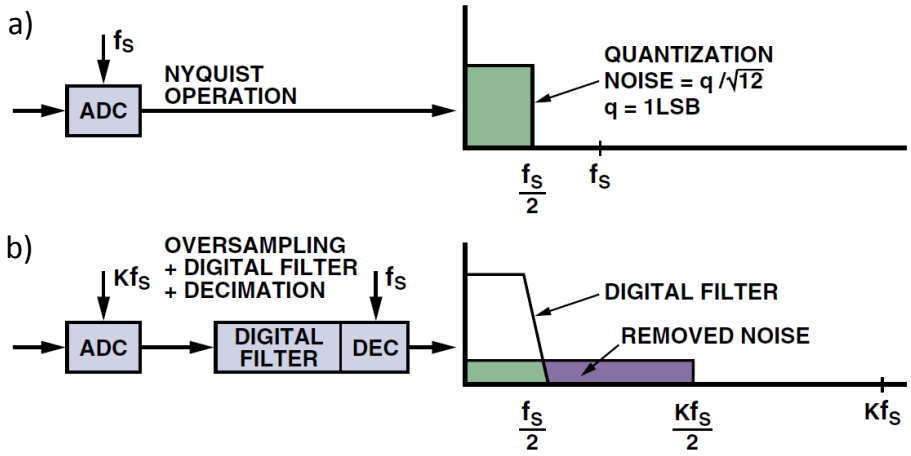

Figure 4.23. Principle of oversampling process (Walt, 2005).

Recent noise shaping technology using delta-sigma modulation (Candy and Temes, 1992) significantly enhanced the analog-to-digital conversion. Figure 4.24 shows the block diagram of the first-order delta-sigma modulator. Unlike most quantizers, the delta-sigma modulator includes an integrator before the actual comparator process (see Figure 4.24a), which consequently shapes the quantization noise.

The principle of noise shaping can be clearly illustrated in the frequency domain. In the Figure 4.24b, $X(k)$ represents the discrete time input signal, $d(k)$ the difference between the input and the feed-back signal (the instantaneous error signal), $H(z)$ is the loop filter represented by the integrator, $w(k)$ the output of the loop filter (frequency weighted error signal), and $Y(k)$ is the output signal. The quantizer output $Y(k)$ can be represented by the sum of the quantizer input w(k) and the quantizer noise $e(k)$,

$$Y(k) = w(k) + e(k) = H(z) \cdot [X(k) - Y(k)] + e(k) \tag{4.5}$$

Rewriting the Eqn. (4.5) in terms of $Y(k)$, $X(k)$, and $e(k)$,

$$Y(k) \cdot [1 + H(z)] = H(z) \cdot X(k) + e(k) \tag{4.6}$$

$$Y(k) = \frac{H(z)}{1 + H(z)} \cdot X(k) + \frac{1}{1 + H(z)} \cdot e(k) \tag{4.7}$$

The coefficient function of the $X(k)$ in the right side of the Eqn. (4.7) is the signal transfer function, which is specific for the feed-forward structure. And the coefficient function of the $e(k)$ represents the noise transfer function, which describes how the quantization noise is transferred to the output of the modulator. Considering the transfer function $H(z) = 1/z$ corresponds to the differential equation below

$$\frac{dw}{dt} = u \tag{4.8}$$

which represents the integrator of the first-order delta-sigma modulator, then Eqn. (4.7) can be simplified as below

$$Y(k) = \frac{1}{1 + z} \cdot X(k) + \frac{z}{1 + z} \cdot e(k) \tag{4.9}$$

The signal transfer function acts as a low-pass filter for the signal and the noise transfer function acts as a high-pass filter for the quantization noise; which consequently shape the noise as shown in Figure 4.25, pushing the noise to higher-frequency area.

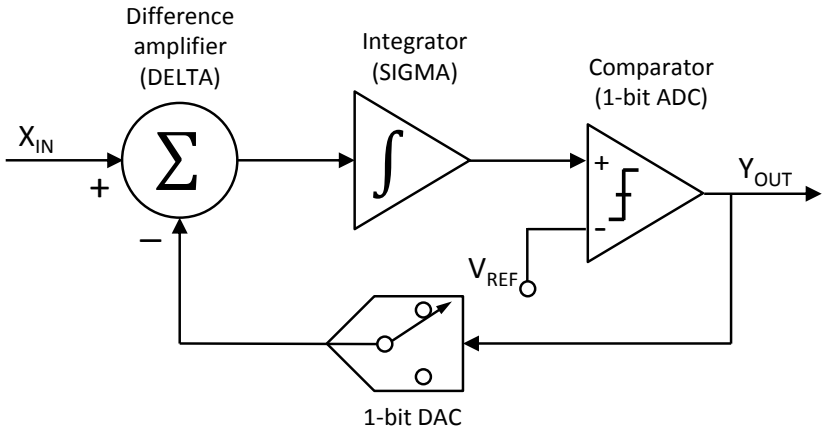

a) Time-domain representation (Walt, 2005)

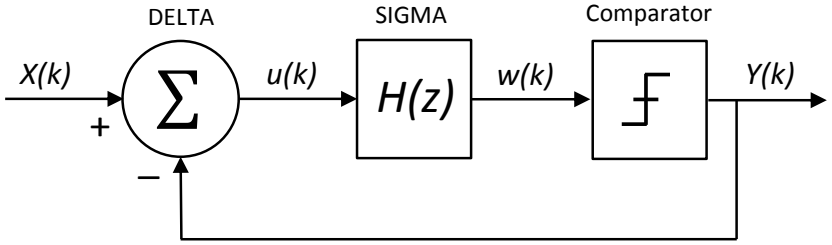

b) Frequency-domain representation (Janssen and Roermund, 2011)

Figure 4.24. Block diagram of first-order delta-sigma modulator.

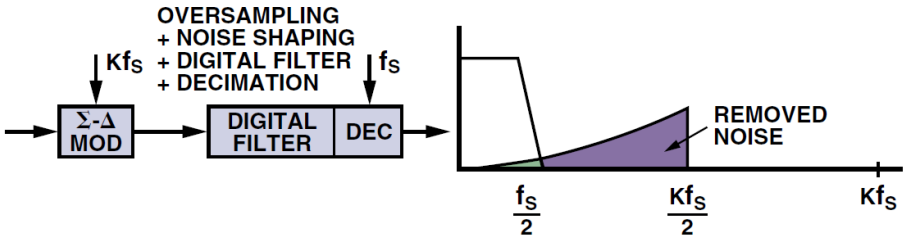

Figure 4.25. Principle of delta-sigma analog-to-digital conversion (Walt, 2005).

For the same rate of oversampling, more quantization noise can be removed by the noise-shaping technique, as compared with only the oversampling process shown in Figure 4.23b, in conjunction with digital filtering and decimation process (see Figure 4.25). In other words, for the same level of quantization noise power, a lower rate of oversampling is required, which consequently reduces the power consumption and lowers manufacturing cost. Most of the recent 24-bits ADC in the market are available using this delta-sigma modulation technique.

4.4.3 Texas Instruments ADS1274 and hardware design

Among the available 24-bits delta-sigma type ADCs currently the market, the Texas Instruments (TI) ADS1274 was selected. As a 4-channel 24-bit ADC, it provides four selectable operation modes, from low-speed mode (10,547 Hz sampling rate) allowing very low-power consumption of 7mW/ch to high-speed mode of 144,531 Hz. The required power of 1.8V ~ 5.0V can be supplied by Imote2, and the Imote2's SPI I/O can be used to interface with ADS1274.

The analog-to-digital conversion process employed by the ADS1274 is composed of two main functions: the delta-sigma modulation and the digital filtering. The modulator samples the input signal at a high rate (64× higher than the final data rate). The quantization noise is moved quickly to a higher-frequency range by the noise-shaping of the delta-sigma modulator, where the internal digital FIR filter removes it then. Such oversampling and noise shaping result in very low levels of noise within the signal passband. The block diagram of the ADS1274 is shown in the Figure 4.26.

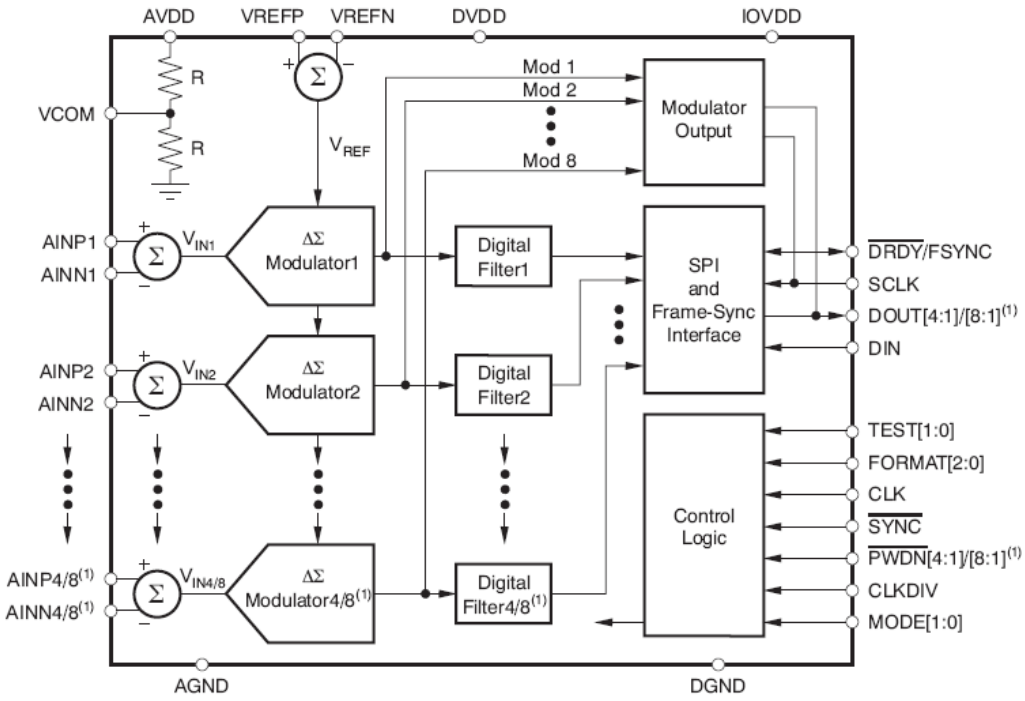

Figure 4.26. Block diagram of ADS 1274.

In addition to the ADS1274, a 27 MHz crystal oscillator (CTS CB3LV-5I-27M0000) is used as the master clock of the ADS1274. The accuracy in the sampling rate of the output signal depends on the accuracy of the external crystal, of which frequency stability is specified as ±25ppm with this CTS crystal.

A voltage regulator (MAXIM 8878_5V) is used to provide a clean 5V power to the ADS1274. The other 1.8V and 3.0V power required for the ADS1274 are provided by Imote2 with its own regulator. For the reference voltage to be used in the comparator process, which directly affects on the ADC performance, a low-noise low-drift voltage reference (TI REF5025) is used.

An additional flip-flop (TI SN74LVC2G74) and single inverter gate (TI SN74LVC1G04) components are used to re-clock the data output to accurately interface with SPI of Imote2, which potentially reduces the possible timing errors between the data output from the ADC and SPI clock of Imote2.

As employed in the SHM-DAQ board design, the same stackable configuration is used to accommodate inputs from daughter boards and external wired sensors. Figure 4.27 shows the block diagram of the board design and the Figure 4.28 shows the final prototype board, named SHM-DAQ24 sensor board.

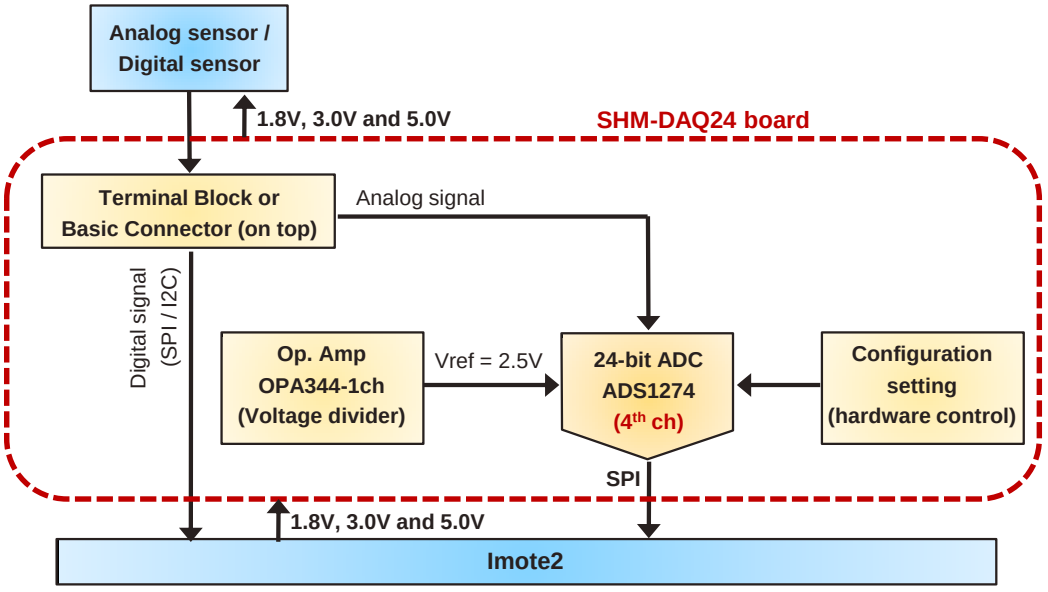

Figure 4.27. Block diagram of SHM-DAQ24 board design.

Figure 4.28. SHM-DAQ24 sensor board.

4.4.4 Software driver for ADS1274

A software driver for the SHM-DAQ24 sensor board is developed in TinyOS. The purpose of the driver is to control the function of the ADS1274 such as SPI (Serial Peripheral Interface) transactions between the ADC and Imote2, allocating buffer memory, timestamping, storing data, etc. The driver for the ADS1271 (the single-channel version of the ADS1274) has been develop by Intel and is extended for the ADS1274.

However, some issues were found in accommodating the four channels data from the ADS1274. Since the SPI is basically a data exchange protocol, as data is being clocked out, new data is being clocked in. However the ADS1274 sends out all four channel data (24bits × 4channels = 96bits) together in a transaction, while most of the multi-channel ADCs send out data channel by channel. Because the PXA271 (Intel's XScale processor) of Imote2 can only clock in up to 32 bits of data per each SPI transaction, the Imote2 cannot handle all the four channel data of 96 bits from this particular ADS1274 ADC. Hence, only the 1st channel data of the ADS1274 is considered as designed for the Imote2.

The driver first initializes the ADC and then triggers the sampling to start. During the sampling, the samples are released from the ADS1274, filtered by the additional digital decimation filter in real time, and then written to the Imote2 buffer as 32-bit integers; of which real-time digital decimation filtering process is described in more detail in following section.

4.4.5 Onboard real-time FIR filtering and decimation

The ADS1274 provides four user-selectable operation modes as seen below Table 4.3. Considering the power consumptions of the four modes and possible application to civil system, the low-speed mode is considered for this design, of which data rate is fixed to 10,547Hz. However, the sampling rate 10,547Hz is still too high for most civil engineering applications, although it would allow for broad applications. Considering the QuickFilter's QF4A512 ADC provides user configurable digital filtering and decimation imbedded in the analog-to-digital converting process, the ADS1274 providing only the four modes having fixed sampling configurations is not that flexible for general civil engineering applications.

Table 4.3. Operating mode performance summary of ADS 1274 (TI, 2011).

Mode	Data rate (Hz)	Passband (Hz)	SNR (dB)	Noise (μV_{RMS})	Power consumption (mW/ch)
High-speed	144,531	65,472	106	8.5	70
High-resolution	52,734	23,899	110	5.5	64
Low-power	52,734	23,889	106	8.5	31
Low-speed	10,547	4,798	107	8.0	7

So that the 24-bits sensor board (SHM-DAQ24) equipped with the ADS1274 can be more flexible for civil infrastructure applications, additional software for configurable digital

filtering/decimation is required. Additionally, such filtering and decimation processing allow a greater number of ENOB (effective number of bits) by further reducing the high-frequency noise; moreover, the onboard real-time operation of the process saves significant memory.

The ADS1274 ADC conducts oversampling to lower the quantization noise power. However, a much lower sampling rate of 675KHz (=10,547Hz × 64) is used, particularly for the low-speed mode, as opposed to 12.5MHz ~ 100MHz sampling rate of QuickFilter's QF4A412 16-bits ADC, because of the noise-shaping capability of the delta-sigma modulator. Followed by the digital filtering and decimation processing within ADS 1274, the actual data rates 10,547Hz is obtained. To get the desired data rate, additional real-time filtering and decimation process is required. The real-time digital FIR filtering and decimation software is developed using ISHMP Service Toolsuite in TinyOS. Figure 4.29 shows the block diagram of the onboard FIR filtering and decimation process for SHM-DAQ24 sensorboard.

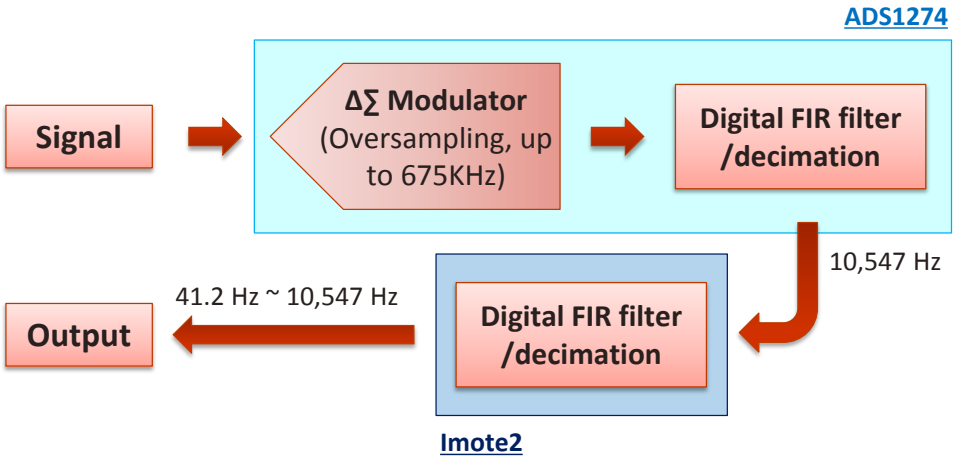

Figure 4.29. Block diagram of the onboard FIR filtering and decimation process for SHM-DAQ24 sensorboard (with low-speed mode of ADS1274).

The FIR filtering and decimation process for the SHM-DAQ24 board is designed to be used with one of decimation factors from K = 1 to K = 256, in a power of two, depending on applications; final data rate of 41.2Hz is obtained with K = 256 (10,547Hz / 256 = 41.2Hz) and 10,547Hz for K = 1.

4.4.6 Effective resolution enhancement

The additional digital filtering and decimation process not only allows flexible options in sampling rate selection, but also enhances the effective resolution by reducing high-frequency noise.

Figure 4.30 shows the root-mean-square (RMS) noise measured at both 10,547Hz (K=1) and 41.2Hz (K=256) sampling rates using the SHM-DAQ24 board. As clearly seen in the figure, the additional filtering and decimation process significantly reduces the noise; which consequently results in enhanced effective resolution (ER), calculated by the Eqn. (4.10) (TI, 2009), of 3.02 bits more (16.52 bits with K=1 vs. 19.55 bits with K=256).

$$\text{ER (in bits)} = \frac{20 \cdot \log\left(\frac{\text{Full scale range}}{\text{RMS noise}}\right)}{6.02} \tag{4.10}$$

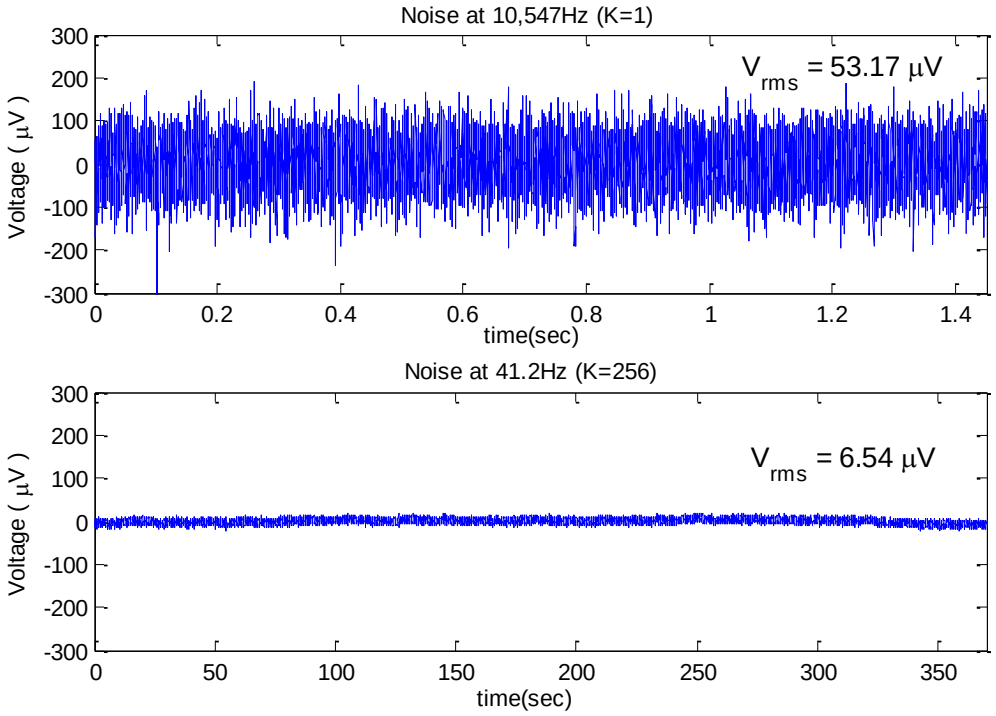

Figure 4.30. Quantization noise of the SHM-DAQ24 sensor board; measured at 10,547Hz with K=1 (top) and at 41.2Hz with K=256 (bottom).

4.5 **Summary**

This chapter has presented the designs of high-sensitivity multi-metric sensor boards for SHM applications using Imote2-based WSSNs. High-sensitivity accelerometer (SHM-H) board has been developed for low-level ambient acceleration monitoring. Silicon Designs low-noise accelerometer was used, signal conditioning circuits were carefully designed to overcome the limited resolution of 16-bit ADC; which finally allows up to 0.05mg RMS noise (over 15Hz bandwidth). Multi-purpose data acquisition (SHM-DAQ) board has been designed to accommodate external sensors into WSSNs. Any kind of digital sensors that use SPI, I2C, or GPIO interface and analog voltage-output sensors can be included in the Imote2 WSSN through

wire-to-board or board-to-board connection to the SHM-DAQ board. The high-precision strain sensor (SHM-S) board developed in this research provides an autonomously balanceable Wheatstone bridge circuit, which consequently contributes to obtaining up to 2500 times signal amplification. Temperature compensated strain measurements and onboard calibration are available with this board. Finally, 24-bits data acquisition (SHM-DAQ24) board has been developed for broader applications and overcoming the resolution limitation of previous 16-bits ADC-based sensing. Noise shaping technique by the delta-sigma modulator has been adopted to obtain better resolution at lower power consumption, and onboard real time digital decimation filtering has been implemented for applications to lower-frequency system, consequently providing more flexibility. The performances of the sensor boards developed in this research have been validated through a series of calibration tests.

CHAPTER 5 SOFTWARE DEVELOPMENT FOR LONG-TERM SHM

One of critical challenges in practical utilization of WSSs for SHM is the long-term operation of autonomous WSSN. The main objective of the long-term SHM is to characterize the status changes of a structure as it is subjected to loading and environmental condition changes for long-term period. To ensure the stable long-term operation of the WSSN, monitoring and managing the network status is essential.

Though energy harvesting efforts for WSSNs have been reported (Rahimi et al. 2003; Jang et al. 2010; Kurata et al. 2010; Miller et al. 2010), an efficient power management strategy should still be considered to realize the long-term, autonomous operation of self-powered WSSNs for SHM. In particular, the Imote2 never revives once the battery is dead due to possible insufficient charging power from long-period rainy or cold days, thus the battery must never be allowed to fall below the critical level.

This chapter presents software developments for autonomous network/environment monitoring and self-diagnostic charger control. Regular measurements of temperature, humidity, and light intensity will allow tracing environmental condition changes, and battery voltage and charging status monitoring will be helpful in making a plan for more stable and extended-life WSSN.

5.1 **Autonomous Network and Environment Monitoring**

Software for autonomous network and environmental monitoring, named *AutoUtilCommand*, has been newly developed using ISHMP Service Toolsuite. The *AutoUtilCommand* has been designed as one of sub-components of *AutoMonitor* developed for autonomous long-term operation of WSSN (Rice et al. 2010); existing sub-component software includes

ThresholdSentry and *CableTensionEstimation* (see the Section 2.3.3 for more detail). *AutoMonitor*, as the higher-level manager software, controls the complex operations of the several schedule- or triggering-based application software sub-components without making any conflicts between those operations. For the systematic operation, each of the software sub-components share flags to show its operational status with others.

Once all flags indicate that operations of all software sub-components are complete, then it will be ready for another operation of one of the software sub-components in the order of that the gateway node is aware. As the *AutoUtilCommand* is on the order of operation, (1) it wakes up the leaf nodes, of which nodeIDs are specified in the input file of the *AutoMonitor*, then (2) it carries out Utility Commands of *Vbat*, *ReadTemp*, *ChargeStatus*, and *ReadLight* (see the Section 3.2 for more detail) required for network status monitoring and environmental monitoring, which are specified in *AutoUtilCommand*. (3) The Utility Command readings are stored in the gateway node memory temporarily, (4) finally, it prints out the readings on a text file of which title contains the time when printing out.

Battery voltage and charging status checking for each leaf nodes provides useful information about the power condition of the WSSN. By checking the number of responsive nodes, one can have an idea about the network status. Temperature tracking also can be helpful to identify its effects on structural behavior. Figure 5.1 shows the flow diagram of the *AutoUtilCommand* newly developed by this research.

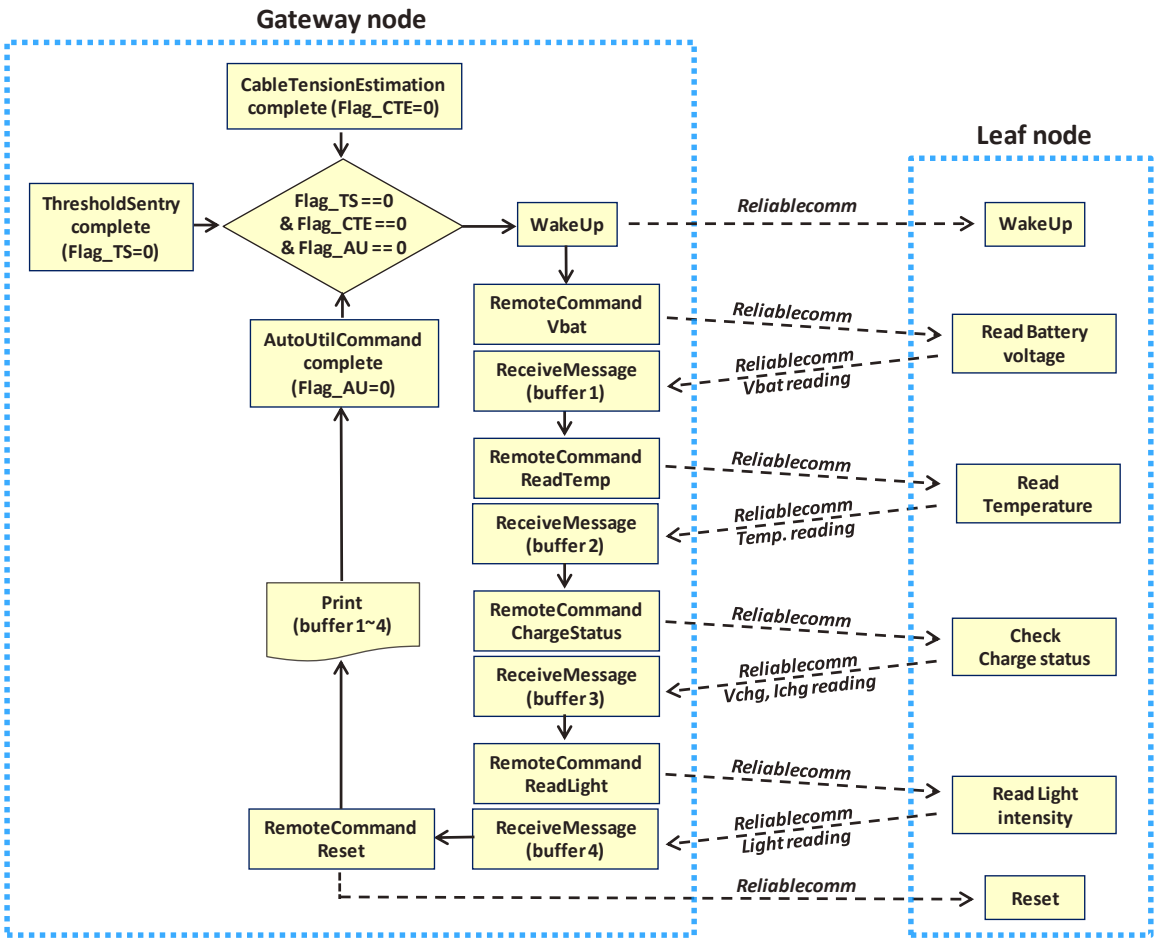

Figure 5.1. Block diagram of *AutoUtilCommand* using ISHMP Service Toolsuite.

5.2 **Self-diagnostic Charger Controller for Long-term Operation of WSSN**

Considering the possibility of various bad charging conditions, such as long-duration of rainy and cold days, which affect the charging performance of leaf node, and to make the WSSN survive under such bad charging condition, self-diagnostic charging control software has been developed using ISHMP Service Toolsuite. As the leaf node-operational software, which is independent of the gateway node operation, the long-term sleep algorithm implemented in *ChargerControl* checks the battery and charging conditions regularly and decide whether it will continue normal operation or go to long-term sleep mode until it will be fully charged.

To avoid the possible conflicts with another software operating on leaf node, *ThresholdSentry*, they share the flags to show their operational status as similar with *AutoMonitor*. Currently, *SnoozeAlarm* wakes up a node every 10 seconds and wait for half second to listen to a message, if any, from the gateway node or other leaf node; the wake-up interval and stay-on duration are decided by users considering the WSSN size and communication protocol. The node then goes back to sleep mode for 10 seconds, if there is no message from the network, and repeat this process. Because the battery and charging conditions do not change so quickly, checking the power condition each time it wakes up would be too frequent. In particular, because of very sharp decrease in voltage reading right after waking up, it needs to stay on for a while to be stabilized, about 1~2 second. Thus power condition checking each time it wakes up with the stay-on time for stabilization negates the advantages of *SnoozeAlarm* due to unnecessary power consumption from the stay-on time. Instead, in this study, power condition diagnostic every 10 minutes was considered.

One challenge regarding the every 10-minute power condition checking under the *SnoozeAlarm* operation is that absolute time is lost each time the node goes into sleep mode, thus

the leaf node cannot recognize the 10 minute interval. To address this issue, the leaf node stores the *SnoozeAlarm* count (SA count) information in the non-volatile flash memory of Imote2. Whenever it wakes up, it checks the count from the flash memory and increases by one. If the count reaches the corresponding value for the checking interval of 10 minutes, then it checks the power condition and decides what to do.

Once the leaf node goes to long-term sleep mode, it will not be included in the WSSN, hence no communication with other sensor node or gateway node occurs during the long-term sleep mode. Instead, it checks the power condition change every 2 hours, and decides whether it should return to long-term sleep or wake up from long-term sleep. Whenever the long-term sleep condition changes, from long-term sleep to awaken status or from normal condition to long-term sleep mode, the leaf node sends a message to the gateway node using *GenericComm*, so that the gateway node and users can be aware of what is happening in the WSSN. Otherwise the gateway node may not have any information about the leaf node that went to long-term sleep mode. Figure 5.2 shows a simplified block diagram of the self-diagnostic advanced *ChargerControl* software for long-term operation of WSSN.

5.3 **Summary**

This chapter has presented the development of software for long-term and robust operation of WSSN tailored for SHM applications. *AutoUtilCommand* has been developed using ISHMP Service Toolsuite for autonomous monitoring of network and environment conditions, such as battery and charging status of all sensor nodes in entire network, temperature and humidity. The self-diagnostic *ChargerControl* developed in this research allows long-term operation of self-powered WSSNs by autonomous control of the network activities and deep-sleep mode based on

the power conditions; each leaf node in the WSSN diagnoses the power condition and makes decision on how it is involved in the network activities. The performance on full-scale deployment can be found in Chapter 8.

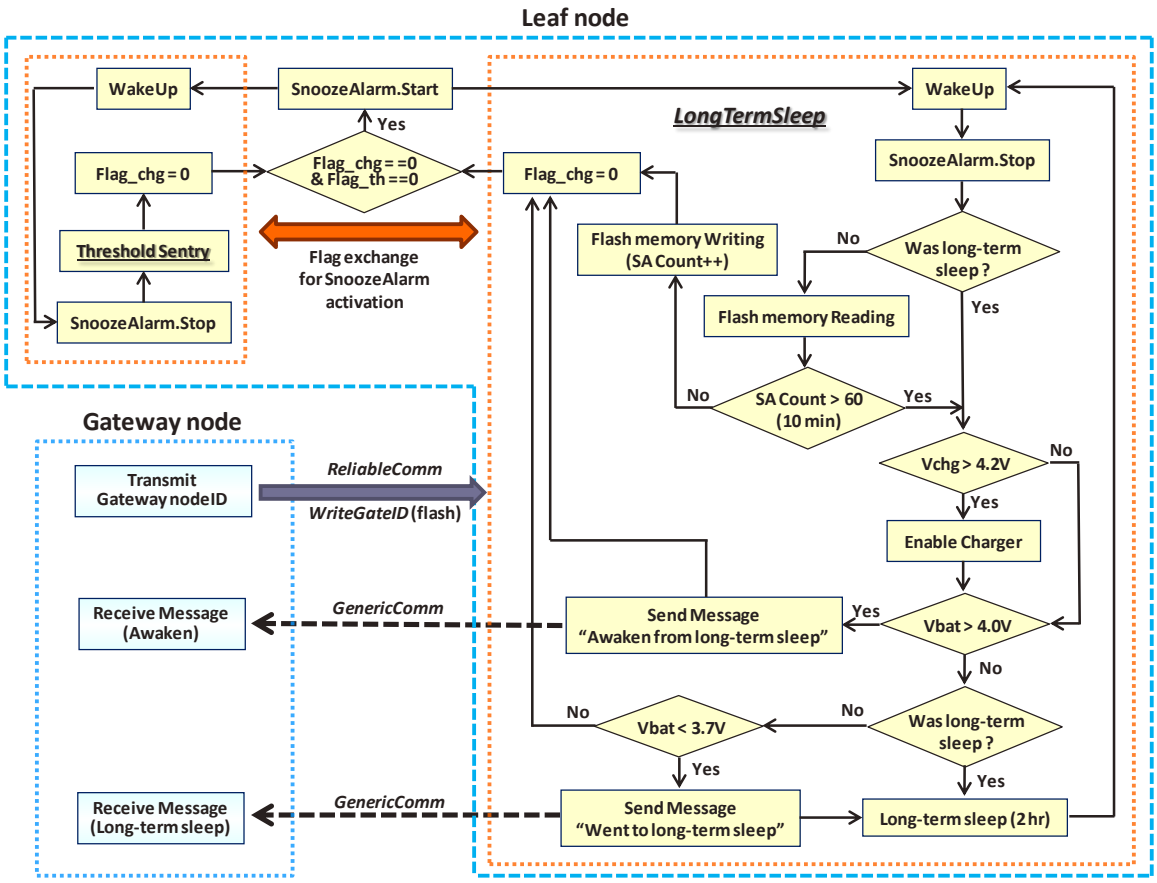

Figure 5.2. Block diagram of self-diagnostic advanced *ChargerControl* using ISHMP Service Toolsuite.

CHAPTER 6 MULTI-SCALE SHM STRATEGIES FOR WSSN

WSSNs require advanced SHM strategies to better utilize its limited hardware capabilities lower costs. This chapter presents multi-scale SHM strategies well suited for WSSNs and their experimental validations, including (1) multi-scale use of different-sensitivity sensors in WSSN for decentralized modal identification and (2) displacement monitoring strategies using dense-arrayed low-cost GPS receivers.

6.1 **Multi-scale Use of Different-sensitivity Sensors in WSSN**

Despite successful deployments of WSSNs on full-scale structures, application of WSSNs for low-level ambient vibration of structures has been limited. Considering that ambient vibration levels for civil infrastructure are typically on the order of 1 mg or less (Su et al. 2009; Nagayama et al. 2005; Nagayama et al. 2010), commonly used low-cost MEMS sensors often employed in WSSNs may not have sufficient resolution to be effective in such conditions. Low-noise, high-sensitivity sensors can overcome this limitation; however, high cost hinders the extensive use of such sensors in a large-scale WSSN.

In this section, a multi-scale use strategy employing different-sensitivity sensors in WSSN is presented. A small number of the high-sensitivity accelerometer (SHM-H) sensor boards, which have been introduced in the chapter 4, is utilized as reference sensor nodes in the NExT/ERA stochastic modal identification method; the remainder of the nodes are low-cost SHM-A boards,. And the efficacy of the approach is then experimentally validated.

6.1.1 Noise reduction through cross-correlation process

Nagayama et al. (2010) proposed the use of a limited number of high-sensitivity reference sensors to reduce the noise effect in estimation of cross-correlation functions, one of the fundamental inputs to the NExT-ERA method. The cross-correlation approach for noise reduction is described as below;

Consider two structural responses $x(t)$ and $y(t)$ and their measurements $x_m(t)$ and $y_m(t)$:

$$x_m(t) = x(t) + n_x(t) \tag{6.1}$$

$$y_m(t) = y(t) + n_y(t) \tag{6.2}$$

where $n_x(t)$ and $n_y(t)$ are measurement noise. The cross-correlation function between $x_m(t)$ and $y_m(t)$ is estimated as:

$$\begin{aligned} R_{x_m y_m}(\tau) &= E[x_m(t+\tau) y_m(t)] \\ &= R_{xy}(\tau) + R_{xn_y}(\tau) + R_{n_x y}(\tau) + R_{n_x n_y}(\tau) \end{aligned} \tag{6.3}$$

Consider another measurement of $y(t)$ with a larger signal-to-noise ratio than $y_m(t)$ as:

$$y_h(t) = y(t) + m_y(t) \tag{6.4}$$

where $m_y(t)$ is the measurement noise that is smaller than $n_y(t)$ in magnitude. The cross-correlation function of $x_m(t)$ and $y_m(t)$ is:

$$R_{x_m y_h}(\tau) = R_{xy}(\tau) + R_{xm_y}(\tau) + R_{n_x y}(\tau) + R_{n_x m_y}(\tau) \tag{6.5}$$

Because the noise component $m_y(t)$ is smaller than $n_y(t)$ in magnitude, the second and the fourth terms of Eqn. (6.5) are smaller than those of Eqn. (6.3). Therefore, the correlation function in Eqn. (6.5) is more accurately estimated. The use of a high-sensitivity sensor is thus considered to improve estimation of the correlation function, as well as the cross-power spectral density function.

Nagayama et al. (2010), however, demonstrated the feasibility of this approach by showing noise reduction effect in the cross power spectral densities of simulated and measured data using conventional wired high-accuracy accelerometers (Tokyo Sokushin CV-373, 2010) in conjunction with wireless smart sensors, Imote2 WSS platform equipped with the ITS400CA sensor board (MEMSIC 2010), only at a single point. Furthermore, use of wired sensors as references results in a heterogeneous network, which requires off-network processing for time synchronization, consequently cannot take many of the advantages of WSSN. The high-sensitivity wireless sensor reported in the Chapter 4 is compatible with the other low-resolution wireless sensors in a network and can realize the full potential of this new approach.

6.1.2 NExT-based decentralized stochastic modal identification

Decentralized strategies for data aggregation are preferred in WSSNs due to power and wireless communication limitations of WSS. One issue in such decentralized approaches is how to aggregate and process sensor data to effectively extract meaningful information. The correlation function and its Fourier transform, the cross power spectral density (CPSD) function, contain essential information for determination of the modal properties of dynamic systems. Moreover, the cross-correlation process showed the possibility of noise reduction by combined use of high-sensitivity sensors and low-resolution sensors, as discussed previously. Thus, if a decentralized network provides cross-correlation functions or CPSDs as the condensed information after in-network processing, it would be best suited for this combined-use strategy.

The NExT-based coordinated processing approach has been implemented using the Illinois Health Monitoring Project (ISHMP) Services Toolsuite (Sim and Spencer 2009), named as *DecentralizedDataAggregation* (DDA). The network topology employed in the NExT-based

coordinated processing consists of three types of sensor nodes that can be categorized based on the role in the sensor network (see Figure 6.1): (a) gateway node, (b) cluster head, and (c) leaf node. The gateway node is directly connected to the base station, controlling network-wide flow of information, sending commands to cluster heads and leaf nodes.

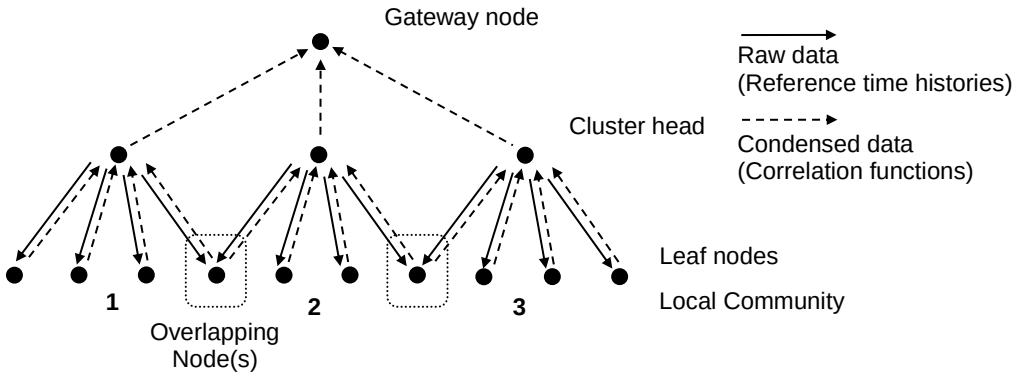

Figure 6.1. Cluster tree topology employed for NExT-based coordinated processing.

The DDA process can be divided in to four stages. (1) Network initialization: the gateway node broadcasts information regarding sensing, data processing, and the network topology to the cluster heads and leaf nodes. (2) Synchronized sensing: to get synchronized measurements, *SensingUnit* of ISHMP Service Toolsuite is used; which is one of the service components of ISHMP Services Toolsuite that performs synchronized sensing, outputs measured data using specified sensing parameters (i.e., sampling rate, data length, and sensing channel). (3) Decentralized data processing: once the synchronized data is ready at the cluster-heads and leaf nodes, the cluster heads coordinate with the leaf nodes to calculate the correlation functions; reference data from a cluster head is sent to the leaf nodes in the local sensor community, where cross-correlation functions are estimated, and the estimated cross-correlation functions are sent back to the cluster-head, while auto-correlation function are calculated in a cluster head. For the

correlation function estimation between two arrays of synchronized data, *CFE* (correlation function estimator) application service of ISHMP Services Toolsuite is used. (4) Collection of the correlation function: the correlation functions collected to the cluster heads are transferred to a gateway node and saved to a user-defined output file. For all wireless communication between leaf nodes, cluster heads, and a gateway node, *ReliableCommunication* in the ISHMP Services Toolsuite is used. *ReliableCommunication* is one of the foundation services to support higher-level application, ensures reliable data communications in a wireless sensor network. Then, the correlation functions are used to estimate global modal properties with ERA using overlapping leaf nodes between local sensor communities (see Figure 6.1); such a coordinated processing allows the sensor nodes to communicate with each other and share information to be able to keep spatial information that can be used to produce a global picture of a structural system. Figure 6.2 shows the information flow in the NExT-based coordinated processing scheme.

In addition, for SHM applications of WSSN, diverse unexpected failures during operation should be appropriately handled. Because the real environment for wireless communication at sites is not so favorable and the hardware performances are not always that perfect, fault-tolerant features for such conditions are considered to improve robustness of the WSSN. In this NExT-based decentralized WSSN, (1) unresponsive sensor nodes due to communication or power issues are removed from the network by the gateway node or the cluster-head, (2) the sensor topology is renewed with only responsive nodes, (3) if the unresponsive node is a cluster head, the gateway node removes the failed cluster-head from the network and tries to find a new one, and (4) each leaf node checks its battery level before sensing starts, and if the battery voltage is below than a threshold level, the leaf node is eliminated from the network, though the node is responsive before sensing.

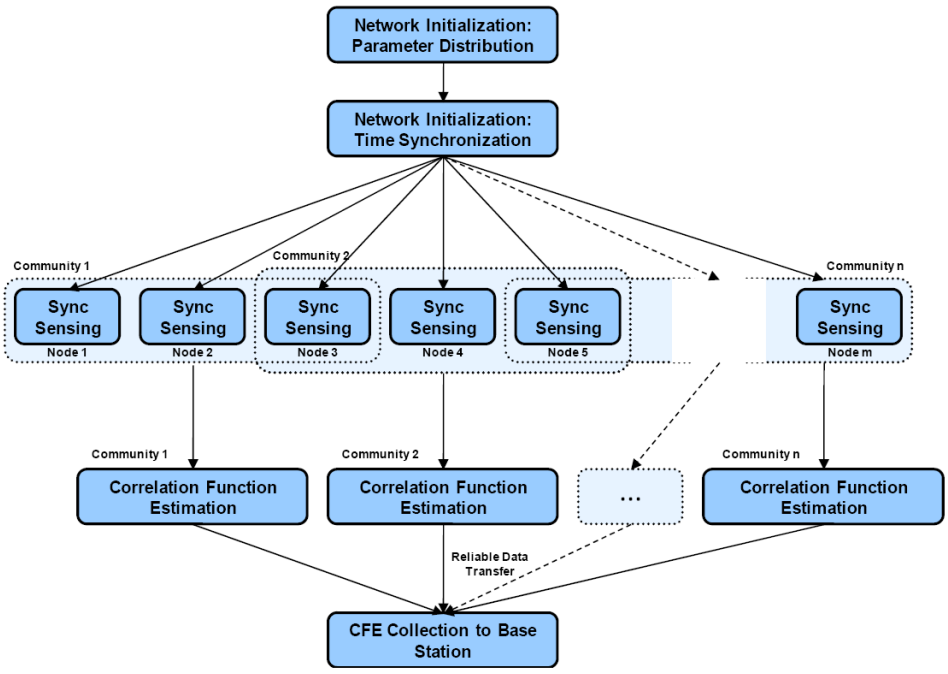

Figure 6.2. Information flow for NExT-based coordinated processing (Sim and Spencer 2009).

The efficacy and accuracy of the NExT-based decentralized WSSN are dependent of the network topology; which has been numerically validated by Sim et al. (2010 and 2011). In terms of data communication, having fewer local groups and more number of sensor nodes in each local group is advantageous because of relatively less amount of data being transmitted over the radio. And from the modal identification perspective, larger local groups having more number of sensor nodes and overlapping nodes better estimate the global mode shapes.

6.1.3 Experimental verification of decentralized stochastic modal identification using high-sensitivity reference sensor

The performance of the proposed decentralized stochastic modal identification using high-sensitivity reference sensors in WSSN is experimentally investigated with the truss structure shown in Figure 6.3. This simply supported 16-bay truss is constructed from steel pipes with an inner diameter of 0.428 inches and an outer diameter of 0.612 inches. An electrodynamic shaker (LDS V408) is used to vertically excite the truss with a band-limited white noise of 0–100 Hz. The SHM-H sensor board, which is developed in this research (see the Section 4.1.1), is employed as the high-sensitivity reference sensors for the cluster-heads, whereas the SHM-A sensor board (see the Section 2.2.1.1 and 2.2.1.3) are used in the leaf nodes. The NExT-based decentralized coordinated processing, which is available from ISHMP Service Toolsuite, installed on the Imote2 sensors is employed to calculate correlation functions.

A total of fourteen Imote2 sensors are installed on the top chord of the truss (see Figures 6.4 and 6.5). The sensor network is divided into three local sensor groups, each comprised of six sensor nodes. Cluster heads should be chosen based on structural analysis in advance, which can show the best capability of the modal feature extraction from each local network; particularly, which is important as network size increases. In this lab-scale small experiment, sensor nodes S4, S7, and S12 (i.e., the blue nodes in Figure 6.5) that located in center of each local sensor groups were chosen as cluster-heads for convenience. Thus, three Imote2 sensors with SHM-H sensor boards and eleven Imote2 sensors with SHM-A boards are employed as the cluster-heads and leaf nodes, respectively.

Figure 6.3. Simply supported 16-bay truss structure.

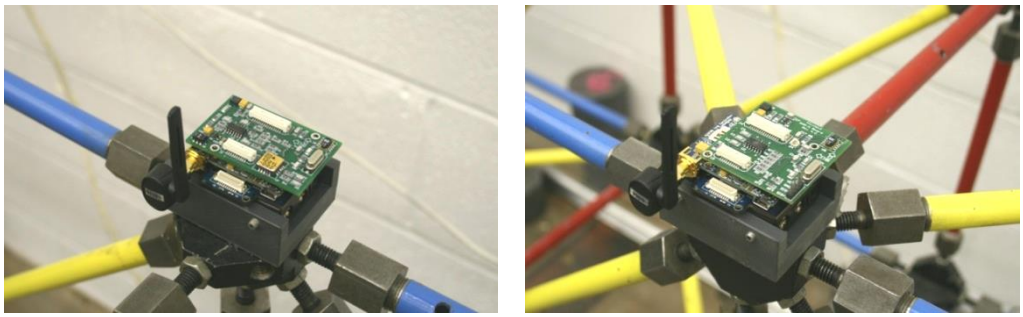

Figure 6.4. Imote2 sensor with SHM-H board (left) and with SHM-A board (right).

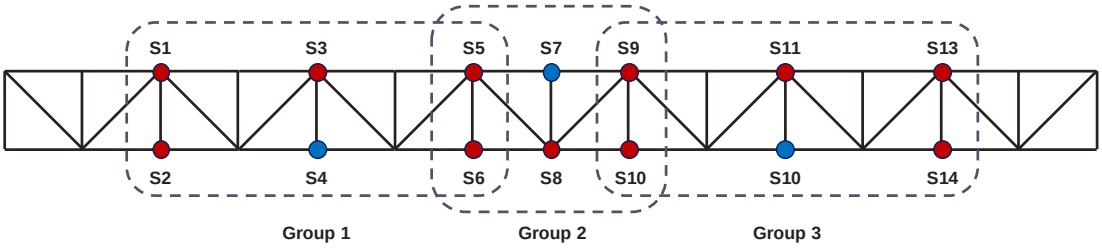

Figure 6.5. Sensor topology (plan view) (S4, S7, and S10 are cluster-heads using SHM-H sensor boards).

Vertical accelerations are measured on each sensor node with a sampling rate of 280 Hz, with a 70 Hz cutoff frequency. The measured acceleration time histories have 10,752 points,

allowing 20 averages if 1,024 FFT points and 50% overlap between windows are specified for correlation function estimation. Then, the NExT-based decentralized coordinated processing estimates the correlation functions within each cluser. Local modal properties are estimated by ERA, and then global modal properties are subsequently obtained using information at the overlapping nodes (Sim et al. 2010). In addition, raw acceleration time histories from all sensor nodes are centrally collected to provide a reference comparison.

The proposed decentralized modal identification approach using high-sensitivity reference sensors is compared with the case of using only general purpose inexpensive smart sensors are employed, as well as with the case where centralized processing is employed in the following four cases:

Case 1: NExT/ERA-based decentralized modal identification using SHM-H sensor boards for cluster heads and SHM-A board for the other leaf nodes.

Case 2: NExT/ERA-based decentralized modal identification using SHM-A boards only (cluster heads of Case 1 are replaced with SHM-A).

Case 3 (reference): Centralized processing with raw data (SHM-H sensor boards for cluster heads and SHM-A boards for the other leaf nodes).

Case 4 (reference): Centralized processing with raw data (SHM-A boards only; cluster heads of Case 3 are replaced with SHM-A).

To more clearly present the efficacy of the high-sensitivity reference sensors, two different excitation levels are considered: (1) high-level excitation: maximum acceleration responses of 100-200mg, which can be well measured by both the SHM-A and SHM-H sensor boards, and (2) low-level excitation: maximum acceleration responses of 1-2mg, of which measurement noise is significant compared to the resolution of the sensor boards.

In this study, the performance comparisons of Case 1 (SHM-H cluster heads) and Case 2 (SHM-A cluster heads) through experiments are the main focus of interest. The efficacy and accuracy of the NExT-based decentralized WSSN itself can be found in Sim et al. (2010 and 2011).

6.1.3.1 High-level Excitation

The truss structure was excited to produce maximum acceleration levels in the range of 100~200mg. Figure 6.6 shows sample acceleration time histories measured at S4 (using SHM-H sensor board) and S3 (using SHM-A board). Typical cross- and auto-power spectral density functions (CPSD and APSD) are shown in Figure 6.7. Figures 6.7a,c,e correspond to Case 1 using SHM-H cluster-head; Figures 6.7b,d,f correspond to Case 2 of SHM-A board only. The identified natural frequencies by ERA are given in Table 6.1, and the corresponding mode shapes are shown in Figure 6.8. For the high-level of structural response, no significant difference is found between Case 1 and Case 2. Moreover, compared to the case of the centralized processing using NExT/ERA, the decentralized processing approach estimates the natural frequencies and mode shapes with a high degree of accuracy.

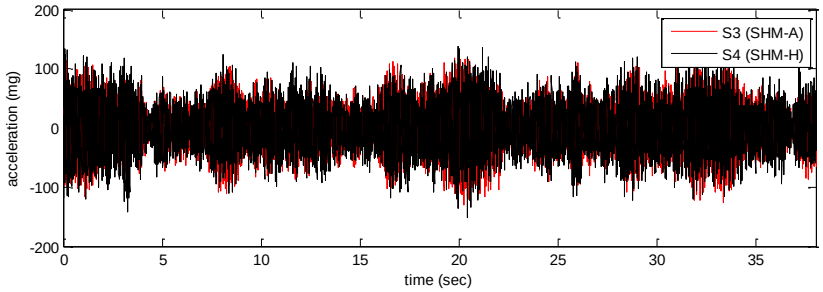

Figure 6.6. Acceleration time histories of sensor node S3 and S4 (100~150mg level).

Table 6.1. Identified natural frequencies.

Mode	Natural frequencies (Hz)			
	SHM-H sensor board as cluster head		SHM-A board only	
	Decentralized processing(Case 1)	Centralized processing(Case 3)	Decentralized processing(Case 2)	Centralized processing(Case 4)
1	20.73	20.80	20.66	20.65
2	33.90	33.85	33.75	33.84
3	41.63	41.63	41.31	41.63
4	64.59	64.69	64.51	64.66
5	69.48	69.56	69.16	69.51

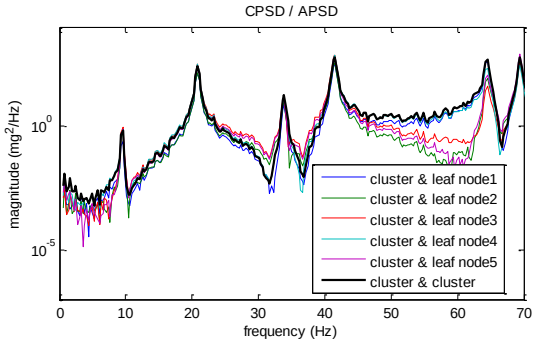

(a) using SHM-H cluster heads (Group 1)

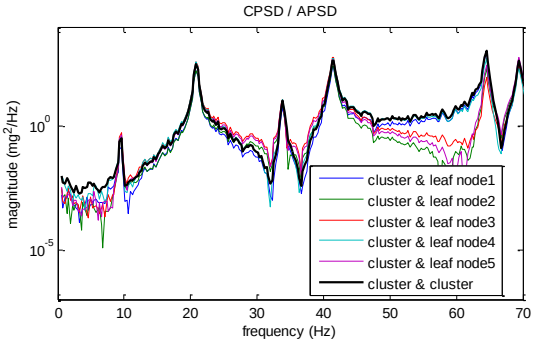

(b) using only SHM-A boards (Group 1)

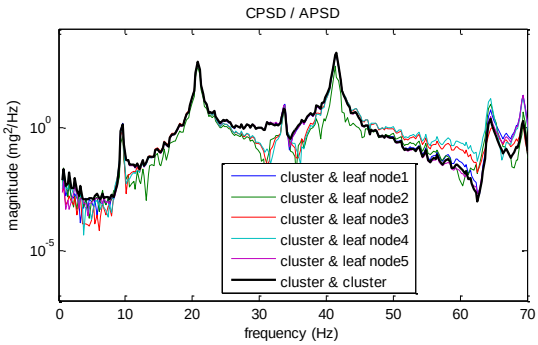

(c) using SHM-H cluster heads (Group 2)

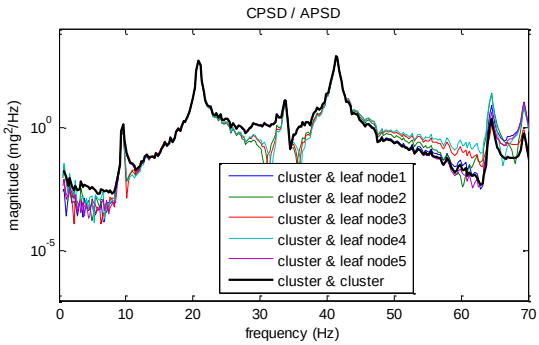

(d) using only SHM-A boards (Group 2)

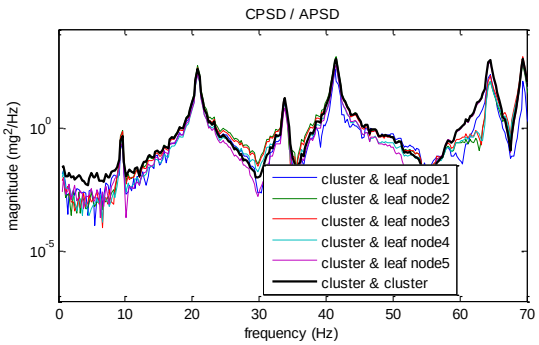

(e) using SHM-H cluster heads (Group 3)

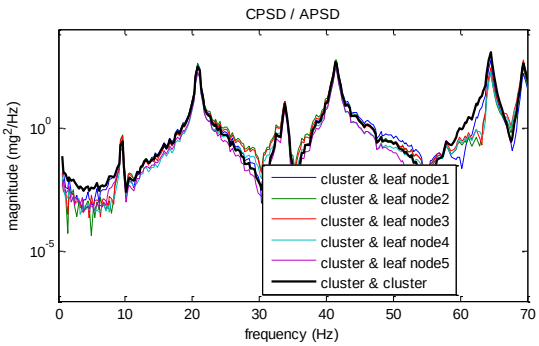

(f) using only SHM-A boards (Group 3)

Figure 6.7. Cross- and auto power spectral densities.

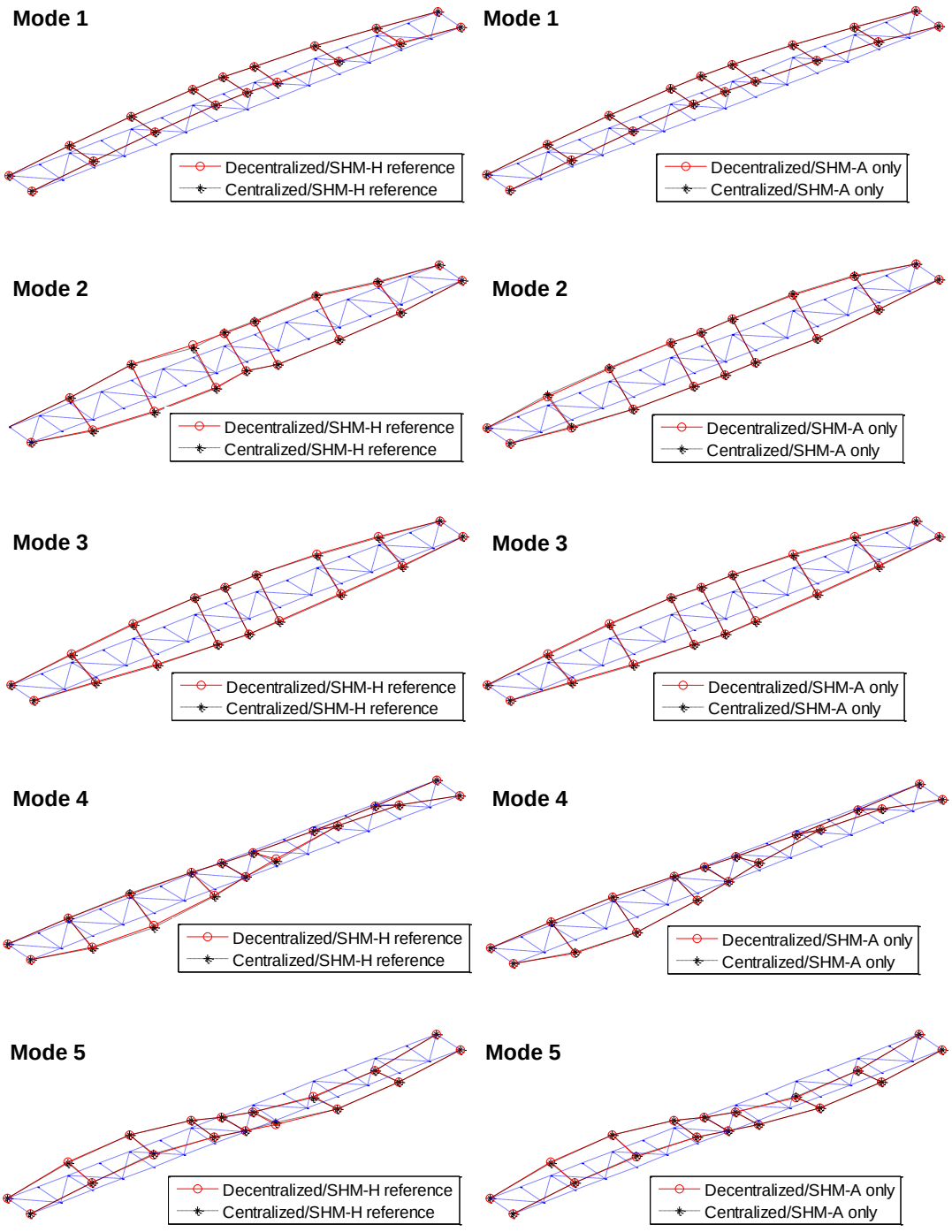

Figure 6.8. Identified global mode shapes: SHM-H sensor board for cluster heads (left column) and SHM-A boards only (right column).

6.1.3.2 Low-level Excitation

To assess the performances of the proposed approach for low-level ambient vibration, the truss structure was carefully excited to have acceleration response in the range of 1~2 mg. Sample acceleration time histories and cross-/auto power spectral densities are shown in Figures 6.9 and 6.10, respectively; as can be seen, the noise levels in the accelerations measured by the SHM-A sensor board are relatively high.

For low level excitation, because the signal-to-noise ratio is relatively small, the effects of noise reduction on the CPSD are more evident. Even though, lower noise levels are observed in the CPSDs of SHM-A sensor board data than in the APSDs of the SHM-A data as shown in the right column (Case 2) of Figure 6.10, with the exception of the peak corresponding to the 1st mode around 20Hz, all dynamic information is lost. In contrast, when SHM-H sensor boards are used as cluster heads (left column), numerous modal peaks can be observed. Because the noise level of the cluster-head data using the SHM-H sensor board is much lower than that of the SHM-A board, the CPSD with the reference SHM-H sensor board data also has a low noise level, which is sufficiently low to allow for extraction of modal properties.

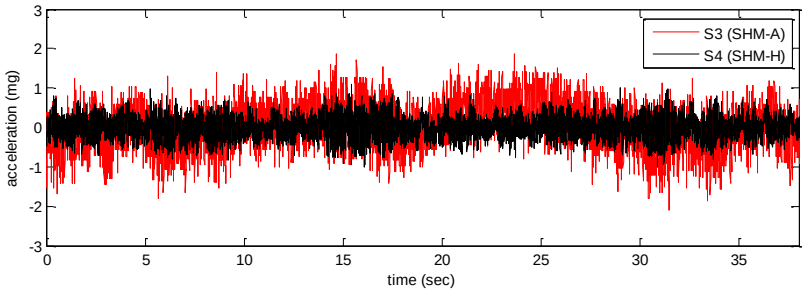

Figure 6.9. Acceleration time histories of sensor node S3 and S4 (1~2 mg level).

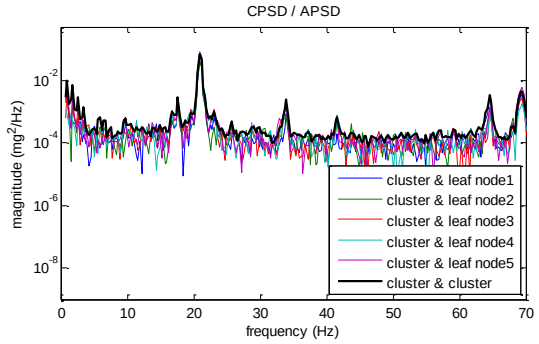

(a) using SHM-H cluster heads (Group 1)

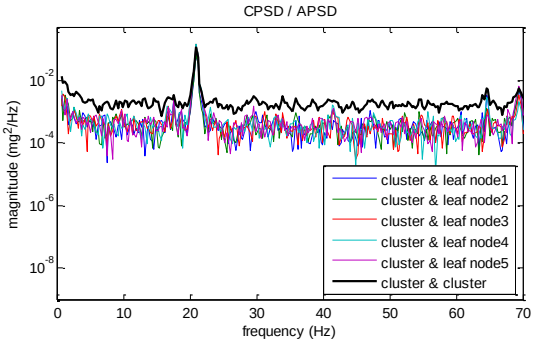

(b) using only SHM-A boards (Group 1)

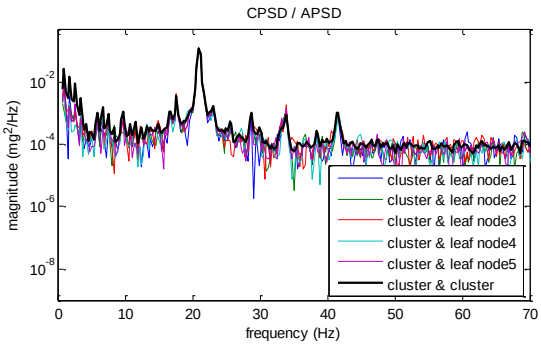

(c) using SHM-H cluster heads (Group 2)

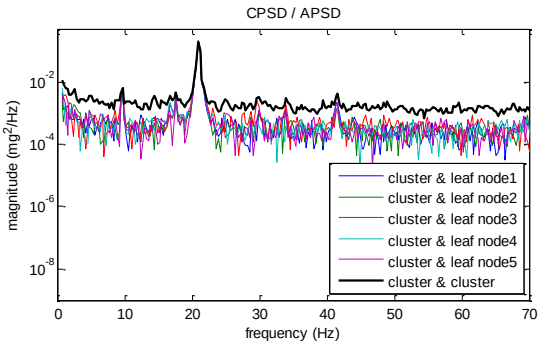

(d) using only SHM-A boards (Group 2)

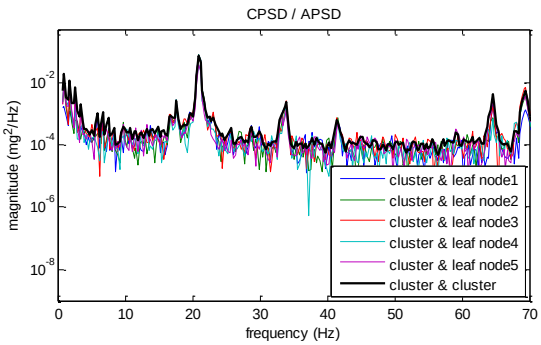

(e) using SHM-H cluster heads (Group 3)

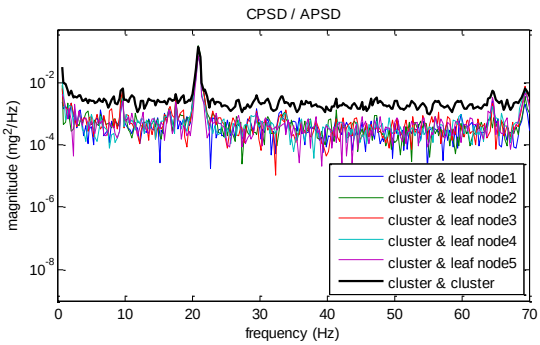

(f) using only SHM-A boards (Group 3)

Figure 6.10. Cross- and auto power spectral densities.

Figure 6.11 more clearly illustrates this point. The APSD of the SHM-A board data measured at S11 does not catch any of the peaks in the range of 21~70 Hz due to the high-level of noise in the SHM-A board, while the APSD of SHM-H sensor board data used for cluster-

head (S10) has several peaks in this range (*e.g.*, near 34, 42, and 65Hz). The CPSD between the SHM-H sensor board (S12) and SHM-A board (S11) allows the modes to be resolved, because of the low noise level in SHM-H sensor board data.

Although the case using the high-sensitivity cluster-heads (Case 1) better identifies the structural modes, some of the high-frequency modes do not appear (*e.g.*, in the 60 ~70Hz range for Group 2 – see Figure 6.10c). As illustrated in Figure 6.7 as well, the modes in this range have low amplitudes in the center part of the structure (*e.g.*, the 2nd bending mode), hence the nodes in Group 2 would have exceptionally low responses. Of course, the case using only the SHM-A boards also is not capable of finding the high frequency peaks in Group 2 (Figure 6.10d), either. Higher acceleration levels are required to better identify these modes.

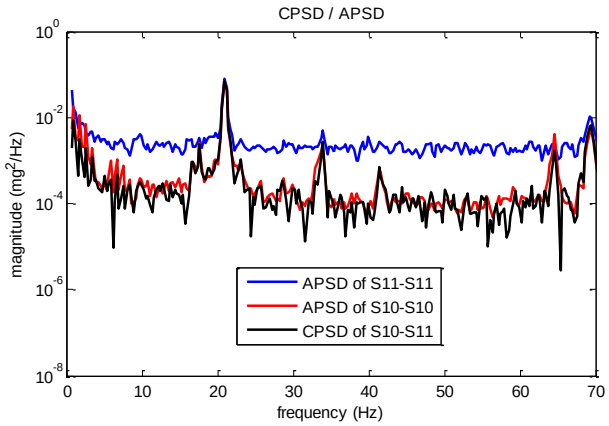

Figure 6.11. Reduction of noise effect on CPSD, S10 is SHM-H; S11 is SHM-A.

Table 6.2 summarizes the identified natural frequencies for the system identification methods; Figure 6.12 shows corresponding mode shapes. While the case using SHM-H sensor boards for cluster heads found 5 modes, the case using only SHM-A boards found only one mode. The modal frequencies identified using the SHM-H sensor board for the cluster heads agree well for

both the high-level and low-level excitations. However, the higher frequency mode shapes (e.g., modes 4 and 5) are not so accurate. This inaccuracy may be attributed to the very low-level of response in Group 2 for these modes, as well as the fact that nonlinear effects (*e.g.*, friction) will be more prevalent at these low levels of excitation.

Table 6.2. Identified natural frequencies.

Mode	Natural frequencies (Hz)			
	SHM-H sensor board as cluster-head		SHM-A board only	
	Decentralized processing(Case 1)	Centralized processing(Case 3)	Decentralized processing(Case 2)	Centralized processing(Case 4)
1	20.68	20.85	20.96	20.85
2	33.90	33.73	N/A	N/A
3	41.45	41.44	N/A	N/A
4	64.65	64.70	N/A	N/A
5	68.72	68.95	N/A	N/A

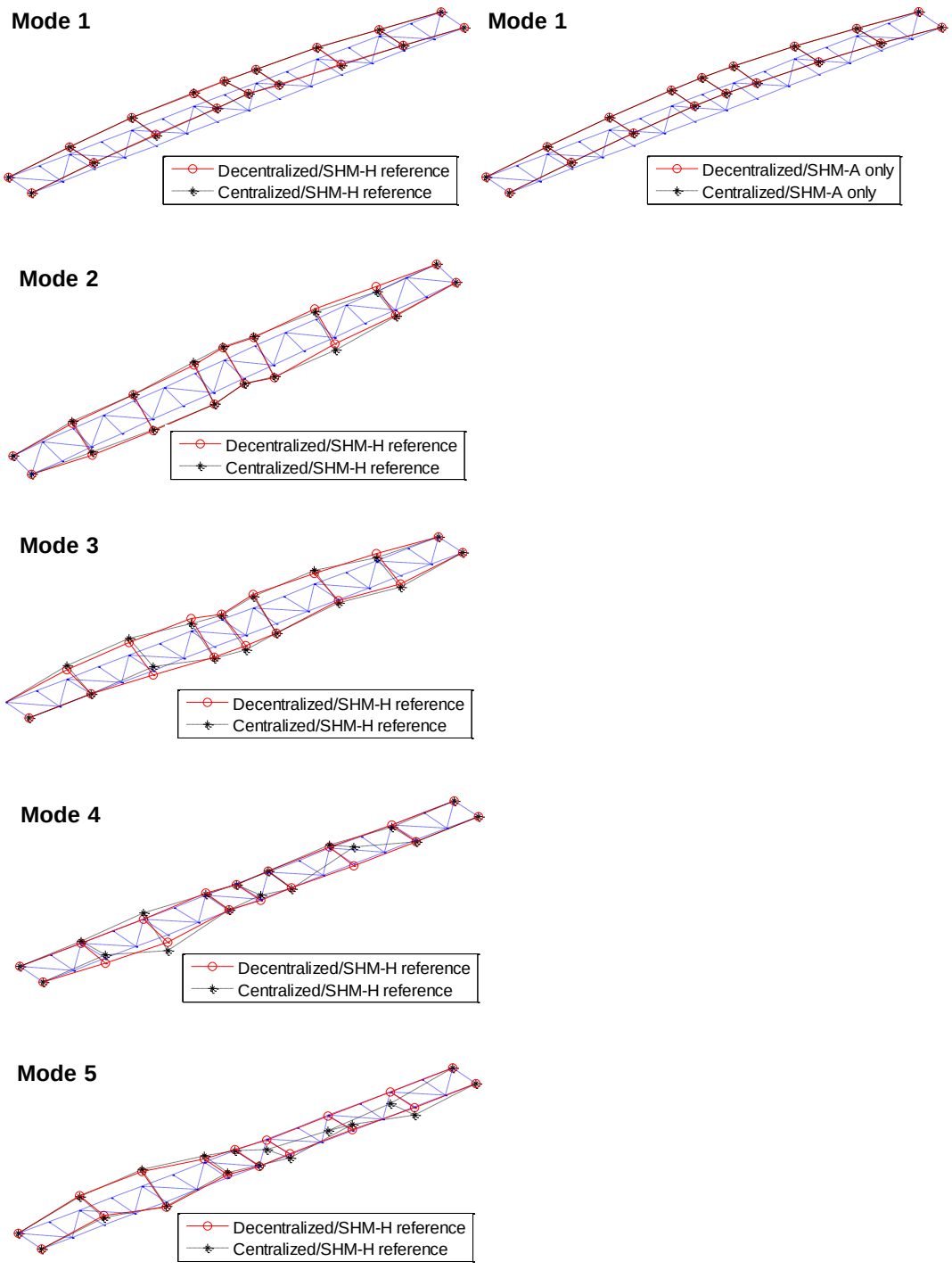

Figure 6.12. Identified global mode shapes: SHM-H sensor board for cluster heads (left column) and SHM-A boards only (top right).

6.1.4 Discussion

In this study, cost-efficient use of high-sensitivity accelerometer board (SHM-H sensor board) as reference sensors in the NExT/ERA-based approach has been investigaged for improved modal feature extraction. The efficacy of the NExT/ERA-based decentralized modal identification using high-sensitivity sensors has been experimentally verified on a steel truss structure using a small number of SHM-H sensor boards as the reference sensors and the lower-cost general purpose sensor board (SHM-A board) for the other leaf nodes in the sensor network. The results are compared to the case using only SHM-A boards for both cluster heads and leaf nodes. For high-levels of structural responses, both the case using the SHM-H sensor boards for reference sensors and the case using only SHM-A boards showed similarly good performance. In contrast, for low-level vibration, use of the SHM-H sensor board for the reference sensors better identified the modal information than the case using only SHM-A boards. Therefore, a small number of high-sensitivity sensors employed as reference sensors at the cluster heads can provide a cost-effective means of improving the performance of NExT/ERA-based decentralized WSSNs for SHM applications.

6.2 **Displacement Monitoring using Dense-arrayed Low-cost GPS Receivers**

Though Global Positioning System (GPS) technologies are able to provide absolute displacement measurements (e.g., Real-Time Kinematic (RTK) allowing sub-centimeter accuracy), unfortunately, this kind of dual-frequency GPS sensor is quite high in cost, making it unsuitable for dense deployments which are critical for damage detection. On the other hand, C/A code-based single-frequency low-cost GPS receivers generally used for navigation purposes are potentially suitable for dense deployments using WSSs due to their small size, low cost, and relatively low power consumption. However, the resolution of these low-cost GPS sensors is quite low (on the order of meters); therefore, their application to SHM has not yet been reported.

This section investigates the potential for using low-cost GPS sensors to obtain displacement measurements suitable for monitoring large civil infrastructure. Instead of using single GPS sensor, multiple low-cost GPS sensors are used to increase the accuracy. The accuracy of low-cost GPS modules is assessed through various static and dynamic tests and through analyzing the correlation characteristics of the noise in the GPS signals. Analytical studies are also considered to assess the potential of using dense arrays of such GPS sensors, based on the experimental results.

6.2.1 Electrolocation of a weakly electric fish

Mimicking biological signal processing strategies has tremendous potential for improving the quality of information obtained in WSSN applications. Inspiration for this work comes from weakly electric fish found in South America and Africa (see Figure 6.13). These fish generate electrical fields using a specialized electric organ located in the tail region of the fish (black bar in the right of Figure 6.13) to actively probe their environment (Nelson 2011). These fish emit

millivolt-level electrical discharges and detect microvolt-level voltage perturbations arising from nearby objects in the water. This phenomenon is called as electrolocation and is analogous to echolocation abilities found in bats and dolphins (see the right of Figure 6.13).

The body of a weakly electric fish is covered with around 15,000 electroreceptors. Each individual electroreceptor, however, is a relatively low-resolution sensor and does not provide reliable event detection. To compensate for this, the nervous system of the electric fish creates arrays of virtual sensors with the desired resolution and sensitivity by pooling information from multiple low-resolution skin sensors. This approach allows the fish to detect and localize targets in 3D space and assess target characteristics such as size, shape and electrical impedance. This suggests the possibility of designing a WSSN that achieves high-precision displacement measurements using a dense array of low-cost L1 C/A code-based GPS sensors.

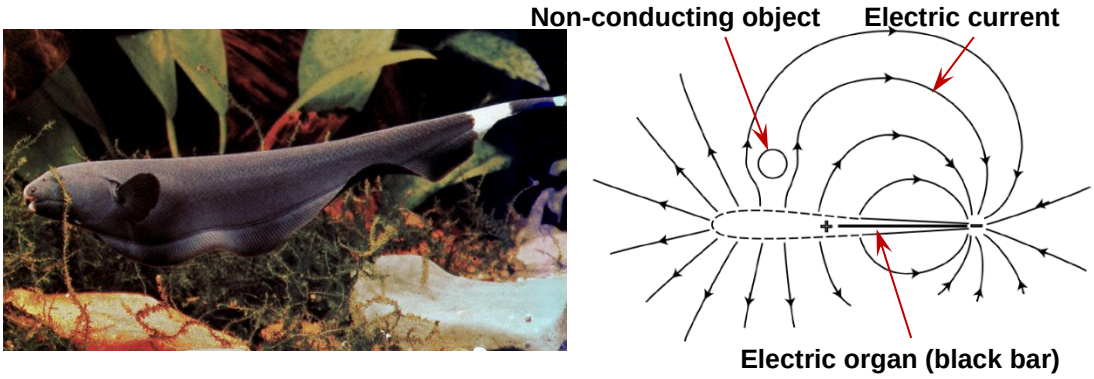

Figure 6.13. Weakly electric fish (left) and electrolocation (right) (Nelson, 2011).

6.2.2 C/A code based low-cost GPS receivers

6.2.2.1 GPS signals and frequencies

A navigation message broadcasted by a GPS satellite at a rate of 50 bps contains the information of satellite clock, satellite location, and status of the satellite. The messages are encoded using

Code Division Multiple Access (CDMA), allowing messages from individual satellites to be distinguished from one another based on unique encodings for each satellite. Two distinct types of CDMA encodings are used: coarse/acquisition (C/A) code, which is freely available to the public, and the precise (P) code, which is usually reserved for military applications. All satellites broadcast at the same two frequencies: one at 1575.42 MHz (10.23MHz × 154), called the L1 carrier, and a second at 1227.6 MHz (10.23 MHz × 120), called the L2 carrier. The C/A code is transmitted on the L1 carrier at 1.023 MHz, and the P code is transmitted on the both L1 and L2 carrier at 10.23 MHz, but 90° out of phase with C/A code on the L1. Figure 6.14 shows the modulation scheme of GPS signals.

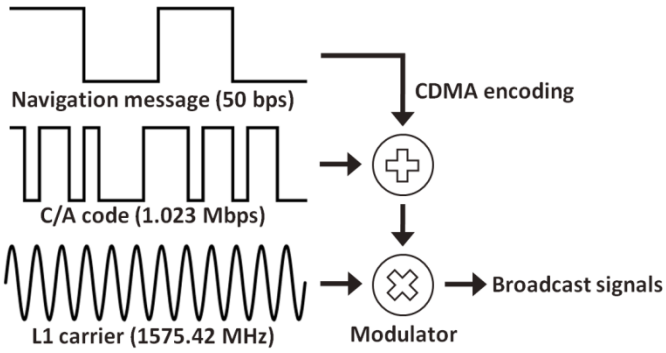

Figure 6.14. GPS signal modulation scheme

(from http://da.wikipedia.org/wiki/Global_Positioning_System).

6.2.2.2 GPS receiver types

Two different types of GPS receivers are available in terms of frequency usage: one is the single-frequency (L1) C/A code based GPS receiver, which is usually used for navigation purposes, and the other one is the dual-frequency (L1 & L2) carrier-phase based GPS receiver. The accuracy of receivers is generally a function of the ability of the receivers' electronics to accurately

compare the signal sent from the satellite and an internally generated copy of the same signal within the receiver. Using the time delay between the GPS signal and the receiver's signal, the distance from the satellite can be calculated. Considering the wavelengths of the C/A code (3×10^8 m/s / 1.023×10^6 Hz = 293.3 m) and the L1 carrier (3×10^8 m/s / 1575.42×10^6 Hz = 0.190 m), even a 1% alignment error, for instance, can cause 2.933 m of error for single-frequency GPS and 1.9 mm of error for dual-frequency GPS. Assuming the same alignment error, the accuracy of the dual-frequency GPS receiver that uses both the L1 and L2 carriers with frequencies 1575.42 MHz and 1227.6 MHz will be about 1500 times better than the single-frequency GPS receiver using C/A code with a frequency of 1.023 MHz. Of course, effects other than alignment error can introduce additional errors. The overall accuracy of GPS receivers is on the order of several meters for single-frequency GPS receivers and on th order of centimeters for dual-frequency GPS receivers.

Dual-frequency GPS systems have been widely used for displacement monitoring purposes because of their high accuracy. The Real Time Kinematic (RTK) technique, which provides real-time correction using a Differential GPS (DGPS) method, enables even millimeter level accuracy. However, due to high cost (typically tens of thousands of dollars per a unit), only a small number of units can be deployed on a structure.

C/A code based GPS receivers are cheap, small, and consume little power, which offers the potential for deploying a dense array of such sensors. However, their meter-level accuracy is still insufficient for SHM applications. As a result, neither the use nor the feasibility of using low-cost C/A code based GPS receivers for SHM applications has been reported to date.

Figure 6.15. Leica GMX902 dual-frequency GPS receiver (left) and AX1202 antenna (right) 0.2mm RMS accuracy, 2.4W power consumption, and up to 20Hz sampling rate (Leica, 2005).

6.2.2.3 MT3329 GPS chipset (C/A code based single-frequency GPS module)

Recently, GlobalTop has released a new high-sensitivity and low-power GPS module (Gms-u1LP, see Figure 6.16). It uses the MediaTek MT3329 GPS chipset (L1 frequency, C/A code, 66 channels), consumes only 24mA at 3.3V, contains an integrated ceramic antenna, features –162dBm of sensitivity, has 3.0m RMS of position accuracy, and is relatively small in size (16×16×6 mm). Also, it supports sampling rates up to 10Hz and costs only about $20 per unit. Although some core algorithms cannot be accessed, it comes with customizable software, which allows sampling rate change, power saving mode, binary protocol, data logging function, AGPS, and so on (http://www.gtop-tech.com). These characteristics offer the potential for implementation in a WSSN.

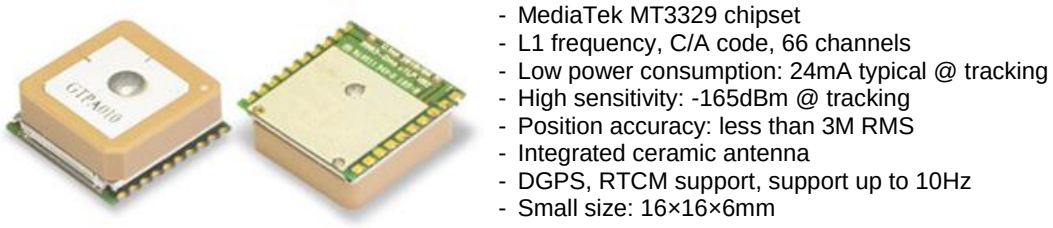

Figure 6.16. Gms-u1LP single-frequency GPS module with integrated antenna (GlobalTop, 2010).

6.2.3 Preliminary GPS testing

6.2.3.1 Experiment set-up

To assess the feasibility of low-cost GPS receivers for SHM applications, the achievable accuracy and limitations of the GPS need to be identified in both static and dynamic conditions. For this preliminary investigation, four GlobalTop Gms-u1LP GPS modules with the integrated ceramic antennas were used. The four GPS receivers were placed together on a small wooden plate, and FTDI cables were used to convert UART (TTL) serial data from the GPS receivers to USB signals, which were then transmitted to a laptop computer. The GPS data, in NMEA 0183 format, is recorded through the HyperTerminal program included in Microsoft Windows XP. Static and dynamic tests were performed on the roof of the Newmark Civil Engineering Laboratory (NCEL) building located in the University of Illinois at Urbana-Champaign campus. Even though there were several small steel chimneys, about 30 centimeters in diameter and 2 meters in height, the roof provided a quite open field environment, free from other buildings that may obstruct the view of low elevation satellites.

6.2.3.2 Static tests

Static calibration tests were carried out to assess the variation in the static measurements over time and to assess the possibility of using the DGPS concept with low-cost single frequency GPS receivers. Additionally, these tests were executed to quantify the background noise characteristics in actual GPS measurements on a structure. These four GPS receivers were placed at a fixed location on the roof of the NCEL building, and four consecutive days of data, from March 1st through 4th, 2011, were measured at a 1 Hz sampling rate. The first three days were sunny with no clouds, and the last day was rainy with weak thunderstorm conditions in the Champaign-Urbana area.

Because the full 24 hours day measurements are too long to be shown clearly, only12 hours of data, from midnight to noon, are plotted in Figure 6.17; the left column compares measurements from a single GPS receiver across 4 days and the right column compares readings from four GPS receivers on a single day.

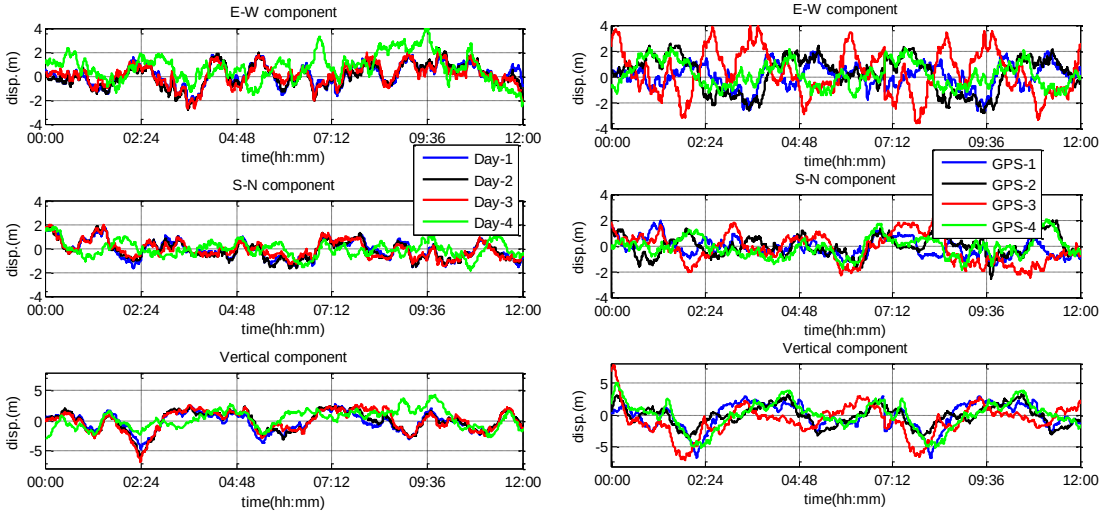

Figure 6.17. Static measurement comparisons: GPS-1 data for 4 days (left), GPS 1~4 data for 3rd day (right).

As shown in the left column of Figure 6.17, very strong correlation was found between the static data for the first three days for GPS-1, while the data for the fourth day deviated significantly from the previous three. Considering the orbital period of GPS satellites is 12 hours and the multipath-distortion would be repeated every orbital period, the correlated static noises can be predicted and subtracted from the actual structural measurements in the future. However, the elimination of this periodic noise seems to be valid only for days with clear skies; the static data measured in the rainy day (Day 4) was quite different from the other three days' data.

To utilize DGPS technique, which can be realized with a correction signal from a reference

GPS station placed at a fixed location, the reference and mobile GPS modules need to be assumed to have same amount of static noise. However, even on a sunny day, the static noises among the four different GPS modules did not show strong correlation (see Figure 6.17, right column). Thus, the DGPS concept with low-cost GPS sensors may not be useful in practice.

Figure 6.18 shows the correlation between the data from the first two days with clear skies in E/W, N/S, and vertical directions. The root mean square (RMS) value changes of the static measurements for all days are plotted in Figure 6.19. The RMS errors of the GPS modules, except GPS-3, for the first three sunny days' data were about 1m and slightly increased for the rainy day measurement in the horizontal directions. In comparison with other GPS modules, GPS-3 showed larger RMS errors in the E/W and vertical directions. However, these errors are still less than the position accuracy of 3m RMS specified in the datasheet of the GlobalTop Gms-u1LP module.

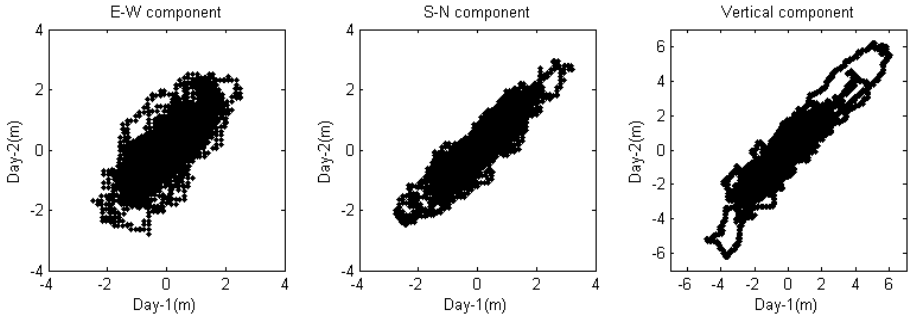

Figure 6.18. Correlation between days: East/West component (left), South/North (middle), and vertical component (right).

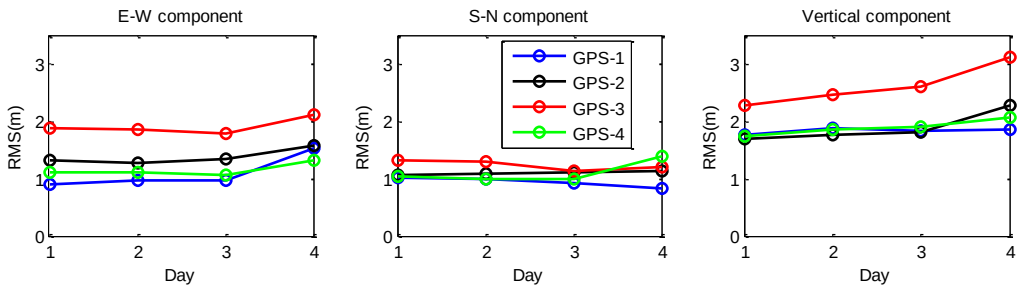

Figure 6.19. RMS value changes of static measurement over all days: E/W component (left), S/N (middle), and vertical component (right).

6.2.3.3 Dynamic tests

To check the applicability of low-cost GPS sensors to dynamic displacement measurements, calibration tests were performed. A horizontal rotor blade was constructed for the preliminary dynamic tests (see Figure 6.20). A wooden plank, 2.0m long and 0.3m wide, was fixed on top of a DC gear motor having 1/8 HP and a maximum rotational speed of 33 RPM. When assembled, the device equivalently has two 1.0m long blades extending in opposite directions from the central motor. The four GlobalTop Gms-u1LP GPS sensors were placed together at given locations on the blades, and a laptop was used to power and receive data from the GPS sensors. The laptop was powered using a rechargeable car battery, and both the battery and laptop were placed on the center of the wooden plank. Varied rotational speeds were tested to quantify the range of frequencies and amplitudes that could be successfully tracked using the low-cost single-frequency GPS sensors. A 5 Hz sampling rate was used for the dynamic tests.

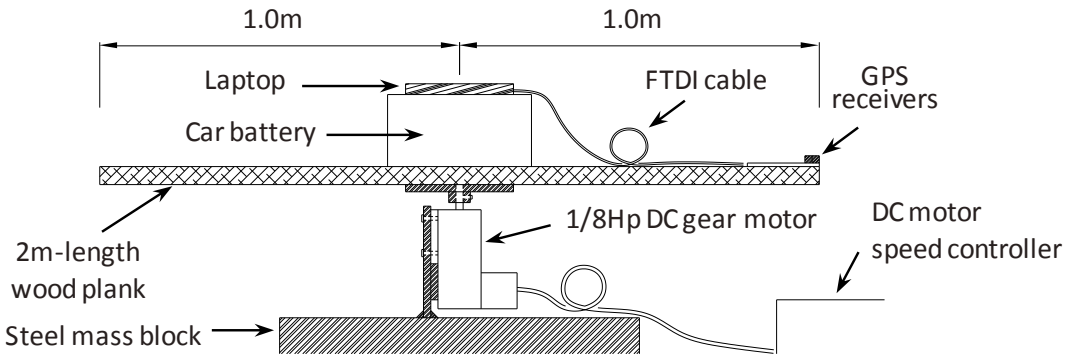

Figure 6.20. Rotor blade for GPS dynamic testing.

Figure 6.21 shows the time histories of 30 minutes of measurements in a circular motion at a 1.0m radial distance with a 2.3 second rotational period for all four GPS modules. The simultaneous E/W and N/S components shown in the left diagram of Figure 6.21 seems not to provide any appearance of circular motion; they even seem to be contaminated with drifting noises of over ±5m. However, clear sinusoidal waves were observed in the each directional component of the 1-minute detail plotted on the right in Figure 6.21. They measured the dynamic movement well; nevertheless some low-frequency drift errors are present.

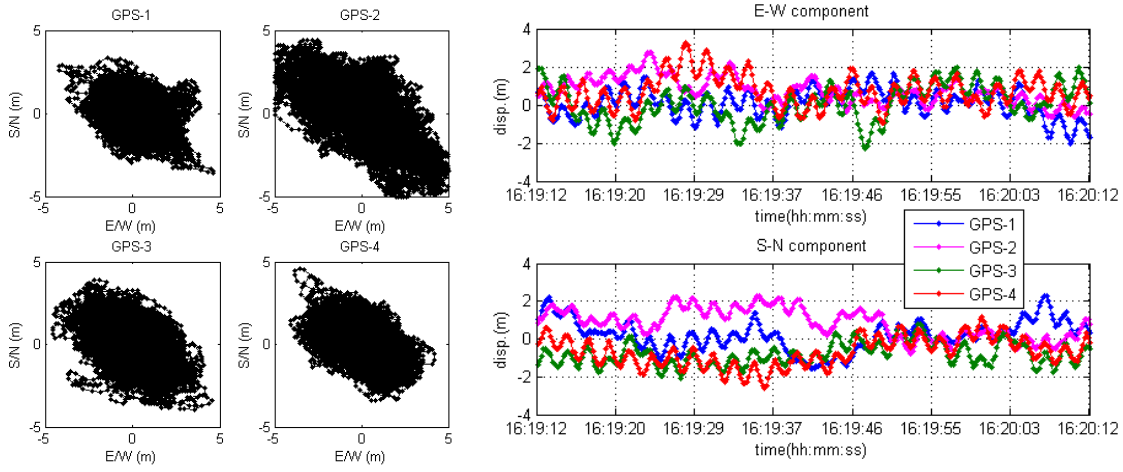

Figure 6.21. Dynamic measurements (1.0m radius and 2.3sec period): 30 minutes data in both directions (left) and each directional component of 1-minute data (right).

The power spectral densities (PSDs) clearly showed the frequency contents of the time histories in Figure 6.22. The frequency of 0.43Hz corresponding the rotor's rotational speed was shown in both E/W and N/S directions. However, unexpected additional peaks were observed around 0.86Hz and 1.29Hz. These additional frequencies may be attributed to the quantization error of the GPS measurements, which can cause periodical round-off error in circular movements; the resolution of the latitude and longitude measurements expressed in NMEA format (dddmm.mmmm) corresponds to about 0.142m.

The PSDs also show the noise characteristics of the GPS measurements, which look similar to a $1/f$-shaped noise spectrum; above the 1-Hz region, the noise is more white in nature and the level significantly increases towards the DC area. These $1/f$-type noise may cause the low-frequency drift error seen in the time histories of the right side of Figure 6.21. In general, displacement measurements have been known to be more accurate in the low-frequency region than other measurements, such as velocity or acceleration. However, this view may not be valid for displacement measurements using the single-frequency low-cost GPS receivers; the more dominant noises exist in the lower frequency region.

Another observation was made in the time and frequency domain. As shown in the right of Figure 6.21, the drift components of the signal, which are noise, seems to be quite random and uncorrelated. The PSD diagrams support this observation; the PSD of the average of the four GPS measurements showed lower noise levels (thick black lines in Figure 6.22), averaging the four time histories resulted in a 6dB decrease in the noise level over the entire frequency range. The cross power spectral density (CPSD) of the two signals also provides an indication of the uncorrelation of the signal drift. The cross PSD of GPS-2 and GPS-4, for example, showed lower noise levels than the auto PSD of each GPS measurement (see Figure 6.23).

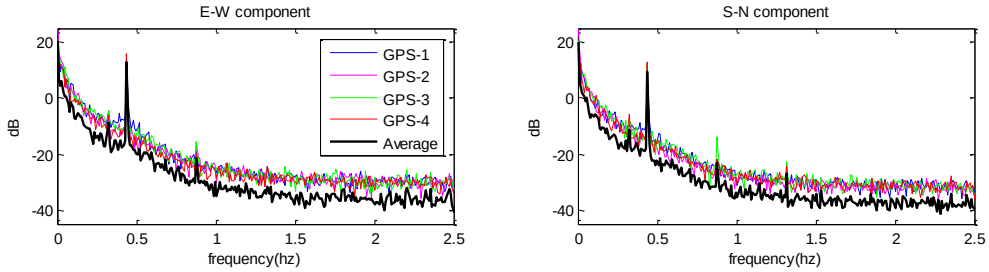

Figure 6.22. PSDs of the GPS measurements in E-W direction (left) and S-N direction (right): 1.0 m radius and 2.3 sec period.

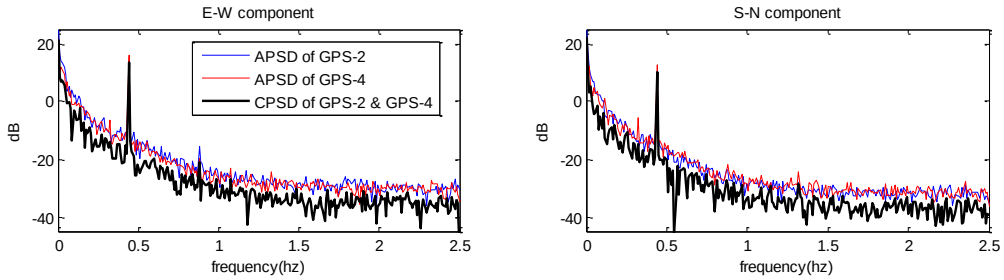

Figure 6.23. PSDs and CPSD of the GPS-2 & GPS-4 measurements in E-W direction (left) and S-N direction (right): 1.0 m radius and 2.3 sec period.

6.2.3.4 GPS signal simulation

Based on the previous observation made from Figure 6.22 & 6.23, a 1/*f*-type artificial noise is used to better understand the characteristics of the low-cost GPS modules and simulate their performance. Many researchers have previously tried to identify these noise characteristics and simulate them, considering numerous GPS noise sources (Genrich and Bock 2006, Amiri-Simkooei et al. 2007; Borsa 2007). In this study, however, only the statistical characteristics of the noise are of interest; consideration of specific effects of individual noise sources is not sought.

Passing white noise through an appropriate filter can produce the 1/*f*-type shaped noise. In

this study, the $1/f^{\alpha}$ power law noise model is used (Kasdin 1995). In a discrete representation, the resulting spectrum has the form of

$$S_d(f) = Q_d \Delta t^{1-\alpha} / (2\pi f)^{\alpha} \tag{6.6}$$

where Q_d is the variance of the input white noise. The transfer function of the $1/f^{\alpha}$ AR filter has the form of

$$H(z) = \frac{1}{a_0 + a_1 z^{-1} + a_2 z^{-2} + a_3 z^{-3} \cdots} \tag{6.7}$$

where $z = e^{j2\pi f \Delta t}$ and the filter coefficients for this are

$$\begin{aligned} a_0 &= 1 \\ a_k &= \left(k - 1 - \frac{\alpha}{2} \right) \cdot \frac{a_{k-1}}{k}, \quad k = 1, 2, 3... \end{aligned} \tag{6.8}$$

A sinusoidal wave of 0.43Hz was generated and then combined with the $1/f^{\alpha}$ shaped white noise to simulate the GPS measurement. A round-off error of 0.142m, corresponding to the previously mentioned quantization error, is introduced to see if additional frequency peaks appear in the PSD diagram. Figure 6.24 shows the time histories and PSDs of the simulated GPS measurements. In total, one-hundred GPS measurements are simulated; one of the typical time histories and the simulation procedure are shown on the left of Figure 6.24, and their PSDs on the right.

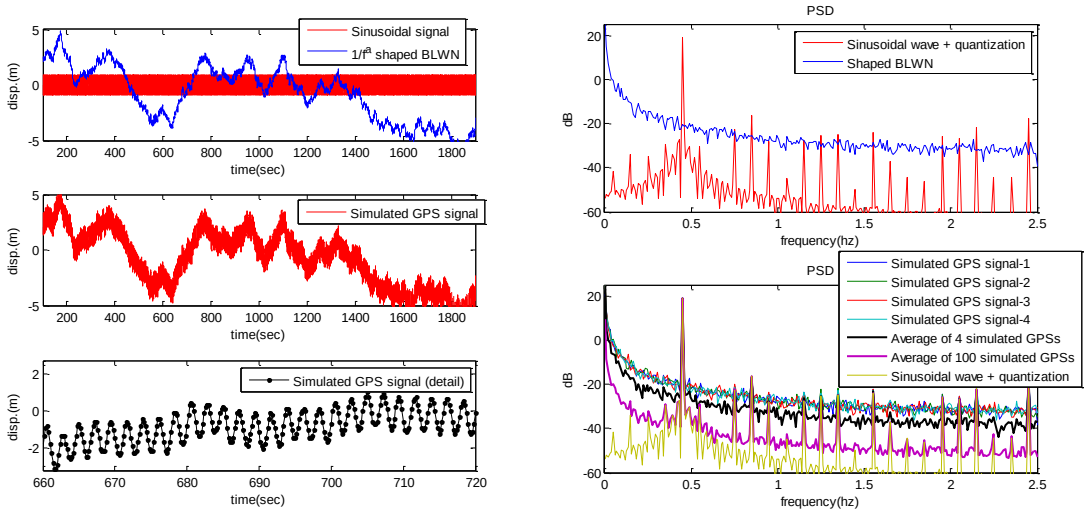

Figure 6.24. Time histories (left) and PSDs (right) of simulated GPS measurements.

As shown in Figure 6.24, the spectrum of the simulated noise has the mentioned 1/*f*-type form (right). The time history shows a drift noise, mainly due to more energy in the low-frequency area (left), as seen in the actual measurements in Figure 6.22 & 6.23. The round-off error introduced in the sinusoidal motions gives rise to extra peaks in the PSD, as expected (see the right of Figure 6.24); though not shown here, without the round-off error, there were no additional frequency peaks. Also, the noise reduction effects were observed when the simulated GPS signals were averaged (see the right bottom of Figure 6.24). Because the simulated GPS noises are based on uncorrelated white noise, the uncorrelated noises should be averaged out during the averaging process. Through the averaging process of four simulated GPS signals, around a 6dB noise reduction effect was observed, which is similar to the phenomenon seen in actual data (see Figure 6.22). The averaging process of one-hundred signals created additional noise reduction, in which the PSD of the averaged signal approaches the PSD of the sinusoidal signal (purple line in the right of Figure 6.24), indicating the potential of utilizing a dense array of low-cost GPS sensors.

6.2.3.5 Displacement amplitude change over time

In the dynamic tests, the radius of the circular movements was 1.0m. However, long-term records spanning 30 minutes showed lower amplitudes than the expected value. To better identify the characteristics of the measured GPS signals without noise, the time history data shown in Figure 6.21 were band-pass filtered. As shown in Figure 6.25, the band-pass filtered signals showed an amplitude which was about half of the actual value; moreover, the amplitudes changed both over time and over different GPS units. The RMS values of the ratio between the GPS measurements and the expected value were 0.43 for the E/W direction and 0.39 for the N/S direction for the average of four GPS modules; they were less than 1 and even had a different value in each of the directions.

The amplitude variation phenomenon also has been reported in a dual-frequency GPS testing (Casciati & Fuggini 2009). The measured displacement amplitudes using dual-frequency RTK GPS receivers (Leica GMX902) fluctuated over time; the RMS values of the ratio between the GPS measurement and the expected value differ (RMS=0.85~1.2) between different frequencies and different amplitudes, although the errors were the order of sub-centimeters. For the low-cost GPS sensors, the amplitude variation phenomenon seems more severe. More testing results with different amplitude and frequency combinations are discussed in the following section.

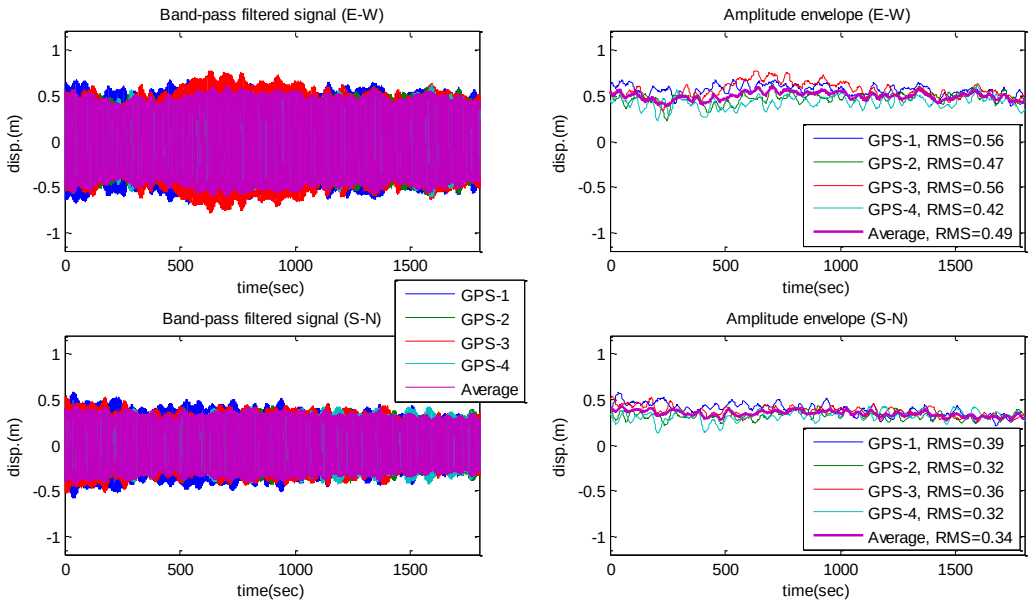

Figure 6.25. Bandpass filtered time histories (left) and amplitude envelope (right).

For the directional difference of the RMS values of measurement amplitude, one of the main reasons may be attributed to the uneven GPS satellite distribution across the sky in mid-latitude areas (Meng et al. 2004). Due to the 55° inclination of satellite orbits, no observation is possible in the northern sky quadrant. Figure 4.48 shows the satellite sky view on the roof of the NCEL building at Illinois, and also shows the large hole having no satellite traces in the northern sky area. Such a satellite sky distribution would result in worse accuracy in the North/South direction than in the East/West direction, as shown in the Figure 6.26. For this reason, in the following dynamic test, only the E-W component of the measurement will be considered.

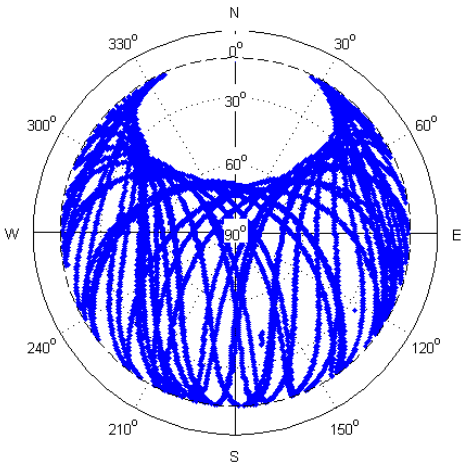

Figure 6.26. Satellite sky view on the NCEL building at Illinois on May 15th, 2011.

6.2.4 Parametric dynamic GPS testing

To evaluate the performance of the low-cost GPS receivers at different frequencies and displacement amplitudes, parametric dynamic tests were carried out for various combinations of frequencies and amplitudes by changing the rotational speed of the rotor blade and moving the GPS locations along the wooden rotor blade. In this test, six different amplitudes, 0.25m, 0.5m, 0.75m, 1m, 1.5m and 2m, and five different rotational frequencies, 0.098Hz, 0.195Hz, 0.215Hz, 0.461Hz, and 0.68Hz were used, while the other sensing parameters remained unchanged from the previous dynamic tests. The wooden rotor blade was extended to have a 2-m length from the center of rotation.

Because the generated data is extensive, only one of typical sets of measurements is plotted in Figure 6.27~6.29 (the 0.215Hz rotational frequency test). Figure 6.27 shows the time histories of measured displacements for the six different amplitudes from the four Gms-u1LP GPS sensors. Figure 6.28 shows the PSDs of the measurements, and Figure 6.29 shows the band-pass filtered time histories. Although some GPS sensors sometimes broke away from the behavior of the others, the average of the four GPSs showed consistent performance over time and for the

various testing cases.

As the rotational radius of the GPS sensors changed from 0.25m to 2m, obvious differences in the measured displacement amplitudes were observed (see Figure 6.27). This observation is even clearer in Figure 6.29, which shows the band-pass filtered signal; the larger the radius of rotation was used, the larger the displacement amplitudes were measured.

The PSDs for different amplitudes clearly show the corresponding rotational frequency peak at 0.215Hz, even for the 0.25m amplitude case (see Figure 6.28). The frequency peak magnitudes for different amplitude cases are different. In the frequency domain, the low-cost GPS sensors showed satisfactory performance. However, as the amplitude becomes smaller, it becomes more contaminated and affected by the low-frequency drift noise. Also, the additional peaks in the PSDs, which should not be there, appeared as expected; the periodical round-off error in the cyclic rotational movement may be the reason, as simulated in Figure 6.24.

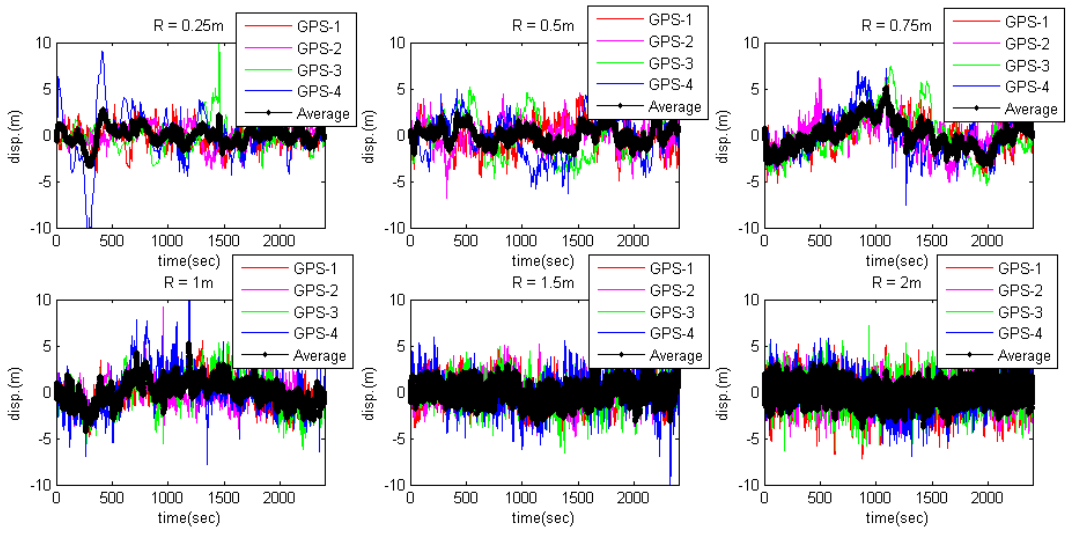

Figure 6.27. GPS displacement time histories for six different amplitudes at 0.215Hz.

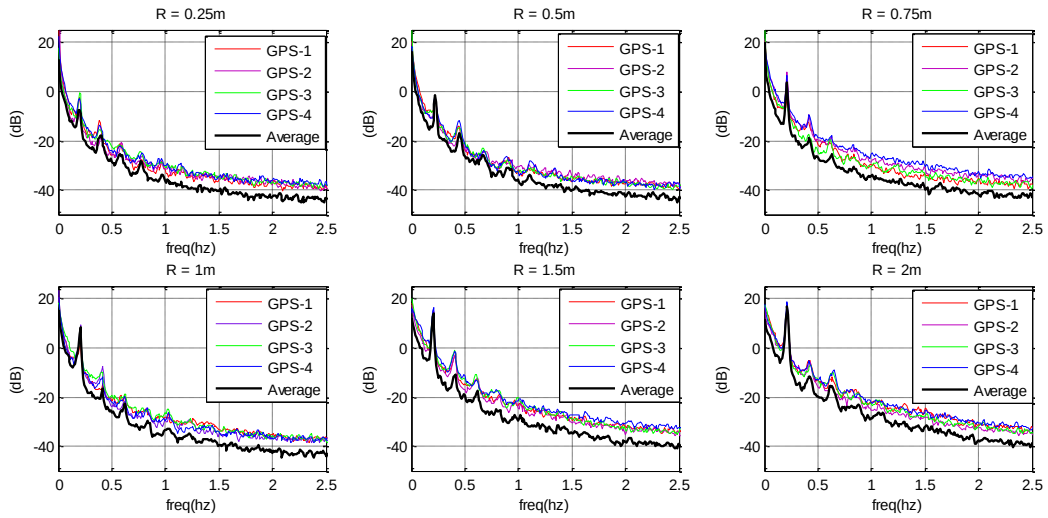

Figure 6.28. GPS displacement PSDs for six different amplitudes at 0.215Hz.

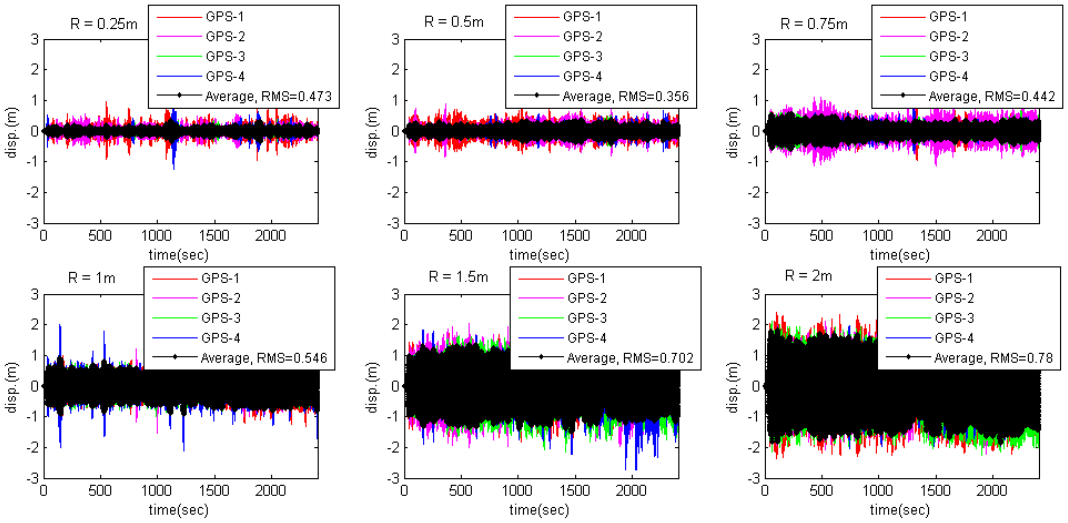

Figure 6.29. Band-pass filtered GPS time histories for six different amplitudes at 0.215Hz.

Figure 6.30 shows the RMS values of the ratio between the measured amplitudes and the expected amplitudes at different rotational frequencies and different displacement amplitudes. Even though further validation is required to draw a conclusion, a trend can be confirmed by

similar behaviors for tests with different cases. As shown in Figure 6.31, it is observed that as the rotation amplitude increases, the closer the RMS value is to 1 (left), and as the rotational frequency decreases, the closer the RMS value is to 1 (right).

For the lowest rotational speed of 0.098Hz, the measurements were contaminated with significant low-frequency noise. Though the RMS values for the 0.098Hz case, except R=0.25m case, were generally close to 1 (green line in the left of Figure 6.30); however, it was because the noise floor in low-frequency range is too high (1/*f* shape). Even for the 1-m amplitude case data was overwhelmed by the noise (see Figure 6.31, middle). The other higher frequency cases, on the other hand, showed consistently reasonable results (Figure 6.30, left); the larger amplitude cases yielded more accurate RMS values.

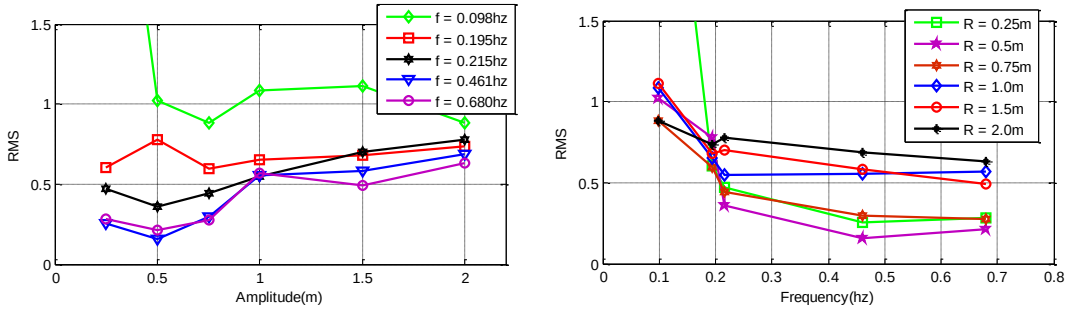

Figure 6.30. RMS value changes of measured displacement amplitude in different amplitudes (left) and different frequencies (right).

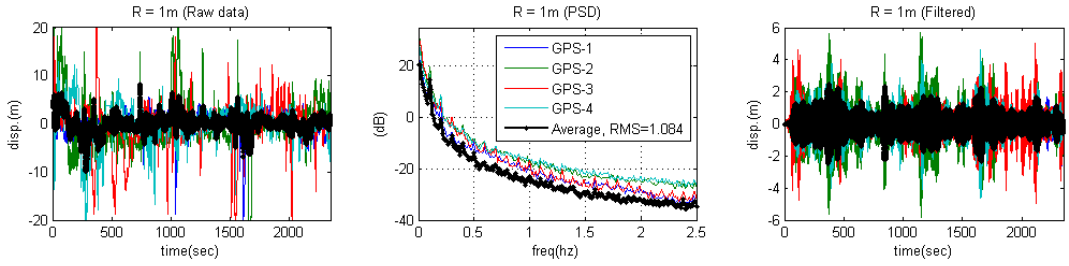

Figure 6.31. GPS measurement with 1m amplitude and at 0.098Hz frequency: time histories (left), PSD (middle), and band-pass filtered time histories (right).

As for the effect of rotational frequencies on the performance of the GPS receivers, (Figure 6.30, right), the data showed that better accuracies were present at lower frequencies; the GPS modules better caught the rotational movements at lower speeds. According to the manufacturer of the Gms-u1LP GPS receivers, GlobalTop, this kind of single-frequency GPS contains a function that filters erratic movements in order to obtain better tracking, which is usually used to optimize the receivers for car or pedestrian navigation purposes. Because the GPS sensors on the rotational blade recognize a change in direction each time the position is sampled, as the rotational speed increases, the directional angle change also increases; this could be recognized as the erratic change by the GPS receivers, so long as the angle change is larger than a certain threshold. Of course, this sort of filtering technique will undoubtedly lead to degradation in positioning accuracy in such rotational movements.

6.2.5 Discussion

The feasibility of low-cost single frequency GPS receivers for SHM applications has been investigated in this paper. To understand the potential of using the low-cost GPS receivers, diverse static and dynamic experimental tests have been performed. Also, simulated GPS data has been used and compared with real measurements to figure out the GPS noise characteristics.

In the static tests, periodic static noise in individual GPS modules over several days were observed, which could be predicted and subtracted from measurements. However, long-term tests using multiple GPS sensors showed that the repeatability of the static data is affected by weather conditions and non-uniform hardware qualities of sensors.

Through the dynamic tests using a horizontal rotor system, low-frequency drift was observed in the GPS measurements, which had a $1/f$ spectrum. Similar to how the electric fish averages

signals from many low-resolution skin sensors to extract necessary information, averaging multiple GPS measurements reduced the noise level, consequently making more apparent frequency peaks in PSD; the noise had low correlation, so averaging process could reduce the noise levels, and the cross PSD of two different GPS measurements and the simulated GPS data confirmed that GPS noises have low correlation.

The ability of the GPS receivers to capture dynamic displacement responses was quite satisfactory. Even at 0.25m amplitude, oscillations were captured and appeared clearly in frequency domain. However, amplitude fluctuations and lower amplitude were observed over time. The dynamic tests with various combinations of amplitudes and frequencies showed that the precision depended on the amplitude and frequency of the signal. Furthermore, the displacement measurements at very low frequencies were very noisy due to $1/f$-noise. Also, poor distribution of the GPS satellites in northern sky diminished positioning accuracy in the North/South measurement direction.

6.3 **Summary**

This chapter described multi-scale SHM strategies to better utilize the obtained outcomes from SHM systems. Multi-scale use of different sensitivity sensors in WSSN shows great promise for enhancing the performance of the stochastic modal identification without sacrificing the cost effectiveness of WSSN; even with a small number of high-sensitivity sensors (SHM-H board), the use as the reference sensors significantly improves the performance of the NExT/ERA-based decentralized WSSN.

The opportunities and challenges to the use of low-cost GPS sensors for SHM applications also have been explored in this chapter. The accuracy and resolution of the single-frequency C/A

code-based GPS sensors are not sufficient for monitoring of structural displacements; the use of multiple low-resolution GPS sensors allows better-accuracy displacement measurements through an averaging and cross-correlation process. However, the hardware and software capabilities of the low-cost GPSs are not yet advanced enough for broader SHM applications.

CHAPTER 7 FULL-SCALE VALIDATION

Through a tri-lateral collaborative research efforts between University of Illinois at Urbana-Champaign (USA), KAIST (South Korea), and the University of Tokyo (Japan), an autonomous long-term SHM system using the Imote2 WSS platform and SHM-A boards has been successfully implemented on a cable-stayed bridge in South Korea (Jang et al. 2010; Cho et al. 2010). This chapter presents the subsequent efforts to extend the autonomous capabilities of the WSSN-based SHM system with significant improvements in hardware and software. The network size has been greatly increased, constituting the world's largest WSSN for civil infrastructure monitoring, and entire sensor network is self-powered with energy harvesting systems. Fault tolerant features for the robust WSSN are carefully implemented, and the new hardware and software developed by this research are applied to this WSSN and validated through short- and long-term operation of the WSSN.

7.1 **Bridge description**

The Jindo Bridges are twin cable-stayed bridges, which connect Jindo Island and the southwestern tip of Korean Peninsula near the town of Haenam. The subject of this study is the 2nd Jindo Bridge that is newer one constructed in 2006 (left of Figure 7.1). The bridge is a three-span steel-box girder cable-stayed bridge composed of a 344 m of main span and 70 m of side spans. The streamlined steel-box girder is supported by the sixty stay cables connected the two A-shaped steel pylons on concrete piers.

Figure 7.1. The Jindo Bridges.

7.2 **Finite element (FE) model of the 2nd Jindo Bridge**

A finite element (FE) model of the 2nd Jindo Bridge has been constructed for understanding the structural behavior of the bridge prior to sensor deployment. A commercial structural analysis software, MIDAS/CIVIL (MidasIT 2009), was used for the FE modeling. All the design documents and detailed drawings of the bridge were carefully reviewed to reflect their details as accuratly as possible in modeling (see example drawings in Figure 7.2).

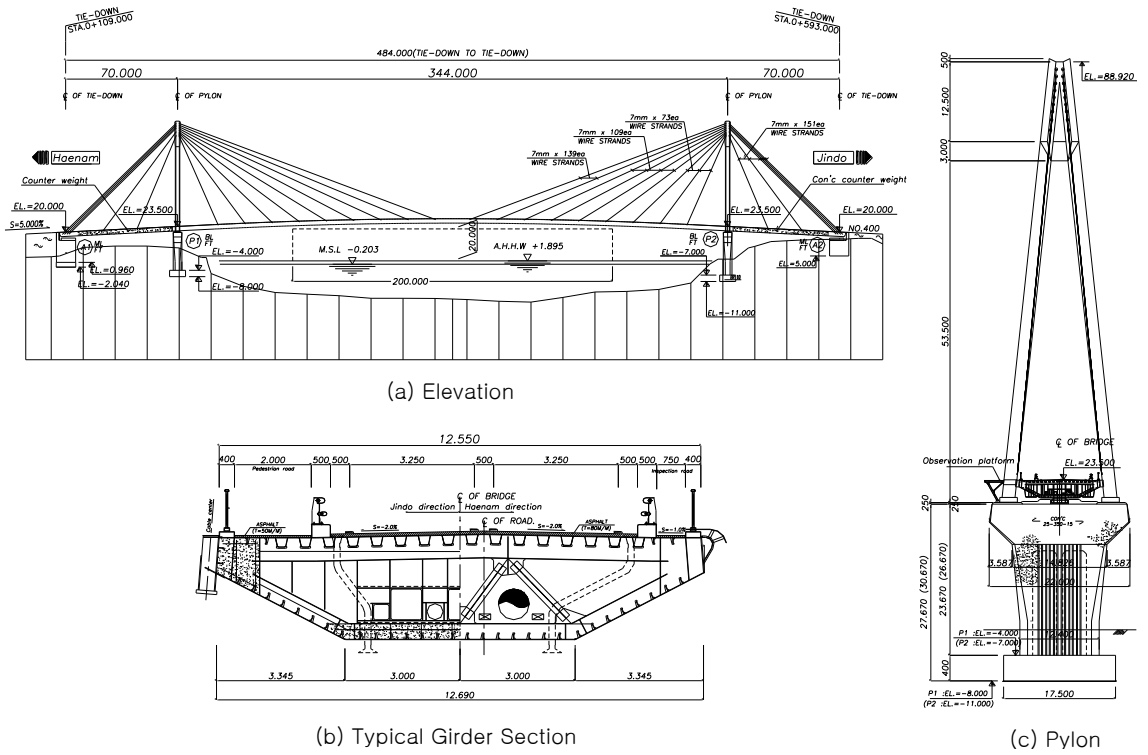

Figure 7.2. Elevation, typical section, and pylon of the 2nd Jindo Bridge.

7.2.1 Construction of FE model using MIDAS/CIVIL

Considering the thickness changes of the flanges and webs, cable anchorage points on the girder, diaphragm locations, boundary conditions and nodal load placements, the girder is modeled by total 128 frame elements with 6 different sectional properties. And the pylons are modeled by 110 frame elements with 7 sectional properties. Additional masses are appended to the girder to represent the pavement, guard rails, water supply pipes, curb, and diaphragms. The spread footings of the pylons are on the stiff rock and thus modeled as fixed boundary conditions. The cables are modeled by truss elements with Ernst equivalent elastic moduli to consider the nonlinear effect caused by self-weight of cables with resulting tension forces and sag (Ernst 1965).

The Auto CAD model is imported into MIDAS/CIVIL to construct the basic FE model for the bridge. All the sectional properties calculated using MIDAS/SPC (Sectional Property Calculation) and load information obtained from design documents are applied to the FE framework. Subsequently, the boundary conditions are applied to the FE model. The tapered sections of pylon and the variation of the sectional center along the girder are considered automatically in MIDAS. Figure 7.3 shows the final FE model of the 2nd Jindo Bridge.

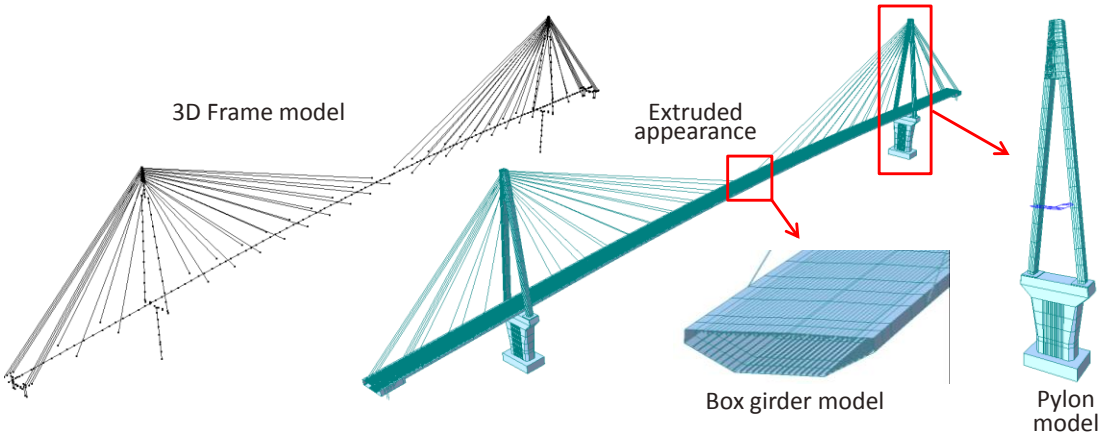

Figure 7.3. FE model of Jindo Bridge using MIDAS/CIVIL.

7.2.2 Validation of the FE model

A preliminary validation of the FE model is achieved by comparing the computed modal properties with those extracted from acceleration responses measured in 2007 using the existing wired monitoring system. Figure 7.4 shows the first six mode shapes evaluated from the FE model, including longitudinal, lateral, vertical, and torsional modes. The first 10 natural frequencies of the vertical modes are obtained as 0.442, 0.647, 1.001, 1.247, 1.349, 1.460, 1.586, 2.115, 2.139, and 2.561Hz. Figure 7.5 shows the power spectral density (PSD) of a vertical acceleration record, which contains vertical and torsional mode information, measured at a quarter span of the deck in 2007. The first 3 peak frequencies (*i.e.*, 0.440, 0.659, and 1.050Hz)

are in very good agreements with the FE analysis results, while the higher modal frequencies are little larger than the FE results. However the differences in these higher modes are within 16%, which shows the general validity of the FE model.

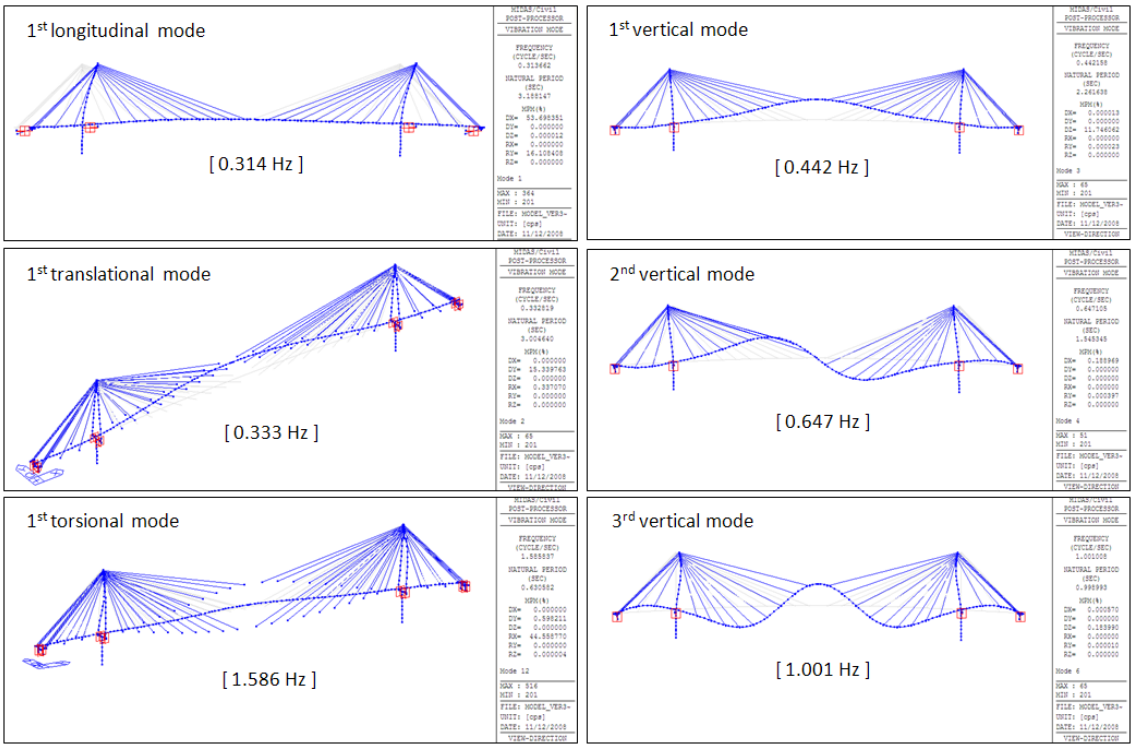

Figure 7.4. Natural frequencies and mode shapes of Jindo Bridge (from FE analysis).

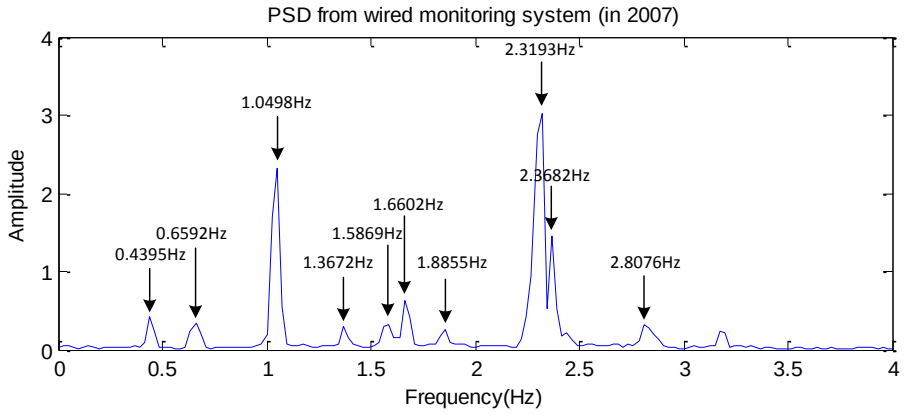

Figure 7.5. PSD of an acceleration record collected in 2007 using the existing wired monitoring system.

7.3 **Multi-scale Framework for WSSN-based SHM**

For the long-term operation of full-scale SHM system using WSSNs, diverse considerations should be taken into account, such as energy harvesting, weather resistance, power efficient operation, reliable communication, network monitoring, environmental effect monitoring, high-quality sensing, scalability to large network, continuous and autonomous monitoring, and fault tolerant features. The ISHMP has tried to resolve those issues with a number of hardware and software developments and implemented all the up-to-date technologies and experiences on a cable-stayed bridge during past years, which established the comprehensive multi-scale framework for WSSN-based full-scale SHM to the end. Figure 7.6 shows the multi-scale SHM framework for the 2nd Jindo Bridge using WSSN and main components of the framework.

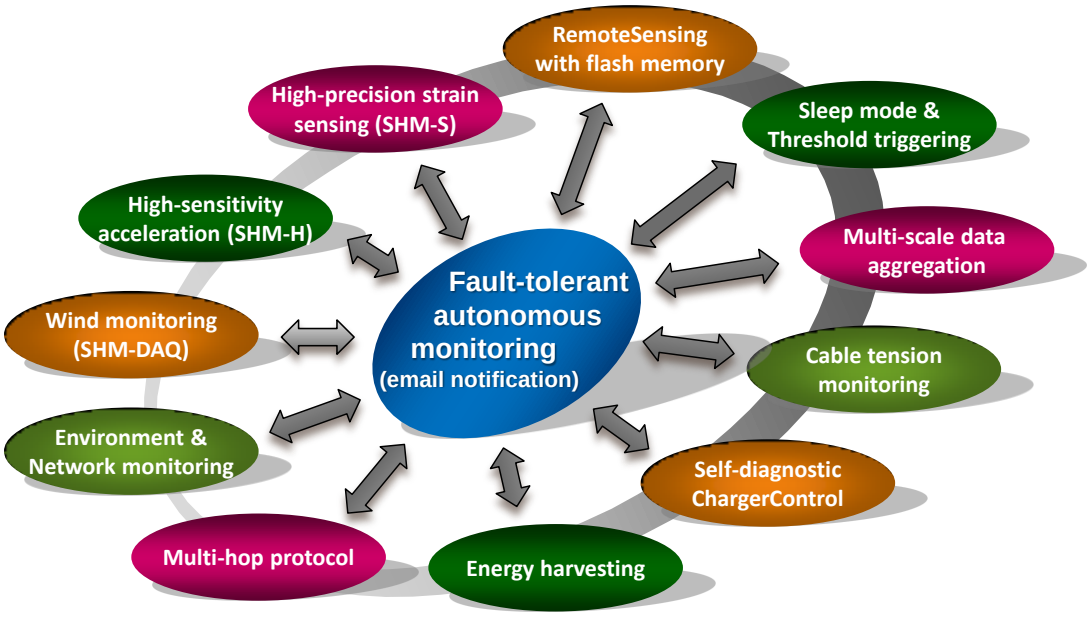

Figure 7.6. Multi-scale SHM framework using WSSNs.

7.4 **Full-scale Deployment on the 2nd Jindo Bridge**

7.4.1 Sensor topology and network division

The most recent deployment in 2010 and updates in 2011 includes total 669 channels of acceleration, temperature, humidity, light, and wind with 113 sensor nodes in four sub-networks. Two base stations were used, one for the Haenam and one for the Jindo side networks, with each of them including two gateway nodes (for deck and cable networks). All sensor nodes are equipped with solar power energy harvesting systems. Several services from the ISHMP Services Toolsuite were employed, including: *AutoMonitor* for autonomous network operation, self-diagnostic *ChargerControl* for long-term operation of WSSN, *ThresholdSentry* for triggering based network activation, and *SnoozeAlarm* for power management using sleep mode, network *AutoUtilCommand* for network status and environmental monitoring, and *RemoteSensing* for synchronized wireless data acquisition. In addition, *CableTensionEstimation* was used for acceleration-based decentralized cable tension force estimation, and *DecentralizedDataAggregation* was used for decentralized data acquisition, which reduces wireless communication and consequent power consumption. Finally, a multi-hop communication protocol was used for one of the sub-networks, and diverse fault tolerant and power efficient features were implemented for stable and long-term WSSN-based SHM system. Figure 7.7 shows the sensor topology of the 2nd Jindo Bridge SHM system and the description of each network are summarized in Table 7.1.

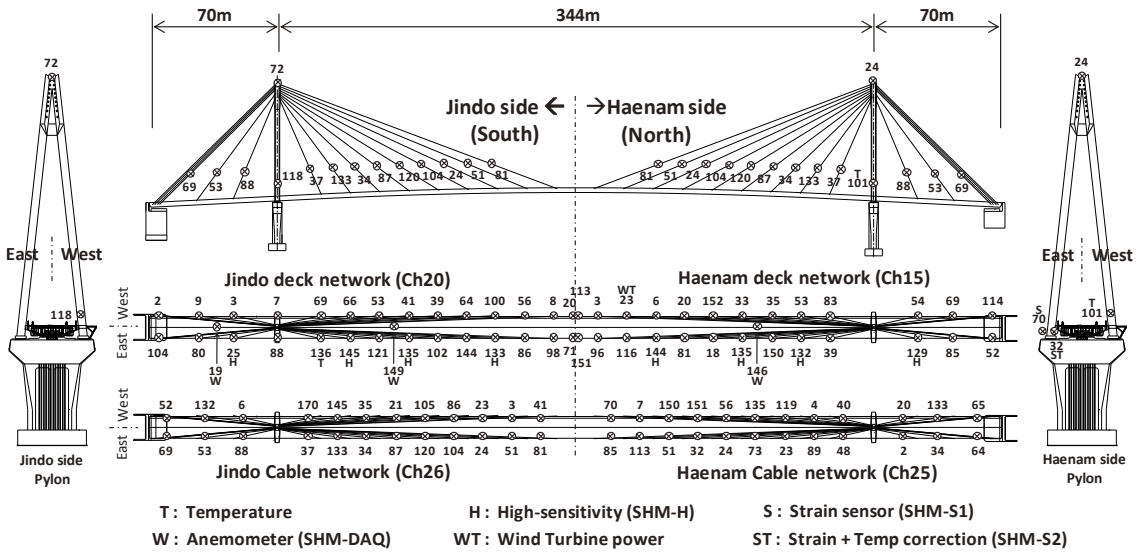

Figure 7.7. Sensor topology with node IDs (2011 deployment on the 2nd Jindo Bridge).

Table 7.1. Functionalities of four sub-networks.

		Haenam side		Jindo side	
		Deck	Cable	Deck	Cable
Communication channel		Ch 25	Ch 15	Ch 26	Ch 20
Network size		30 nodes	26 nodes	31 nodes	26 nodes
SHM-H board (cluster head)		5 nodes	-	5 nodes	-
SHM-DAQ board (wind)		1 nodes	-	2 nodes	-
SHM-S board (strain)		2 nodes	-	-	-
Sentry node		3 nodes	2 nodes	3 nodes	2 nodes
Temperature node (exposed)		1 nodes	-	1 nodes	1 nodes
Functionalities	Common	*RemoteSensing*, *AutoUtilsCommand*, *ChargerControl*, *ThresholdSentry* and *SnoozeAlarm*			
	Optional	*DDA*	*CTE*	*DDA*	*CTE*
Communication protocol		Single-hop	Single-hop	Single-hop	Multi-hop

7.4.2 Energy harvesting

A noticeable enhancement for the second and thrid year deployments, compared with the first year deployment (Jang et at. 2010; Cho et al. 2010), was that all the sensor nodes are self-powered with energy harvesting devices. Even though the battery life could be extended by efficient power management strategies and data condensation using in-network processing, the use of ordinary batteries implies the inconvenience of regular battery replacement. In the first year deployment, 8 nodes of 70 nodes were equipped with solar panels and rechargeable batteries for testing purpose. The size and type of the energy harvesting devices used in the first year deployment have been shown to be adequate for the WSSN. Thus, the power harvesting is expanded to entire network in this deployment. Power harvesting device in this deployment include SCM-3.3W from SolarCenter (9V-370mA) shown in Figure 7.8 (left) for solar panels and the Ainsys lithium-polymer rechargeable battery (3.7V-10,000mAh). In addition, a prototype wind turbine (HR-W35V, Hankukrelay), shown in Figure 7.8 (right), is used to power a sensor node underneath the deck (Park et al. 2012).

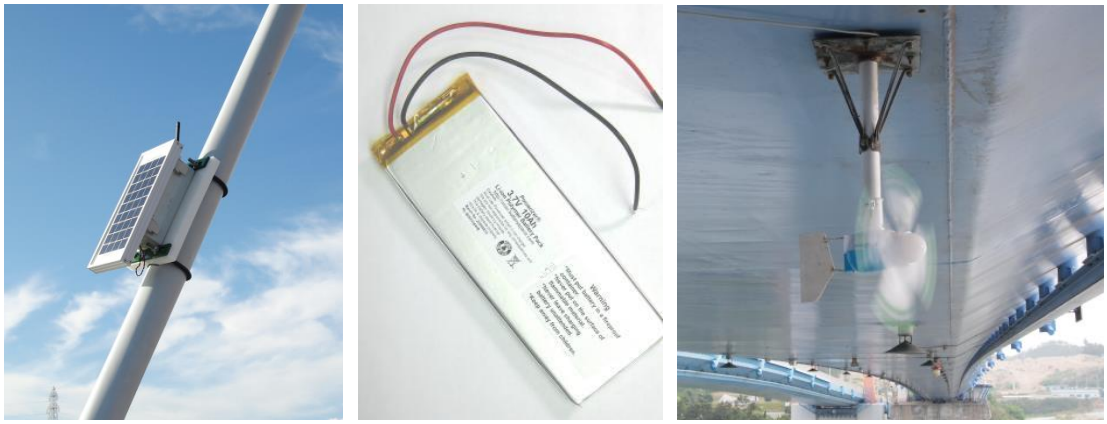

Figure 7.8. Rechargeable battery (middle) and energy harvesters; solar panel (left) and wind turbine (right).

7.4.3 Advanced self-diagnostic charging control

The new *ChargerControl* software developed in this research has been implemented in the WSSN. Because the bridge is frequently exposed to bad charging conditions, such as rainy season in summer and long-duration of cold winter in Korea, such self-diagnostic charging control approach is essential to make the WSSN survive in such harsh conditions. The *ChargerControl* has been installed on all leaf nodes, as the entire network is self-powered by energy harvesting system.

7.4.4 Environmental hardening and sensor installation

Sensor nodes should be protected from environmental effects that can cause the electrical or mechanical malfunctioning. PVC enclosures are used for all the leaf nodes, which has silicon packing for water-proofing, a hinge-latch type cover for easy opening and closing and sufficient space that can accommodate a battery, sensor module, cables and accessories (Figure 7.9). A sensor module (combined set of battery board, Imote2 and sensorboard) is bolted to an acrylic base plate boned on the bottom of the enclosure. The enclosures are mounted on the bottom plate of the deck using magnets shown in Figure 7.9 (right), and a specially designed PVC plate and U-shaped screws are used for cable nodes installation (Figure 7.8, left).

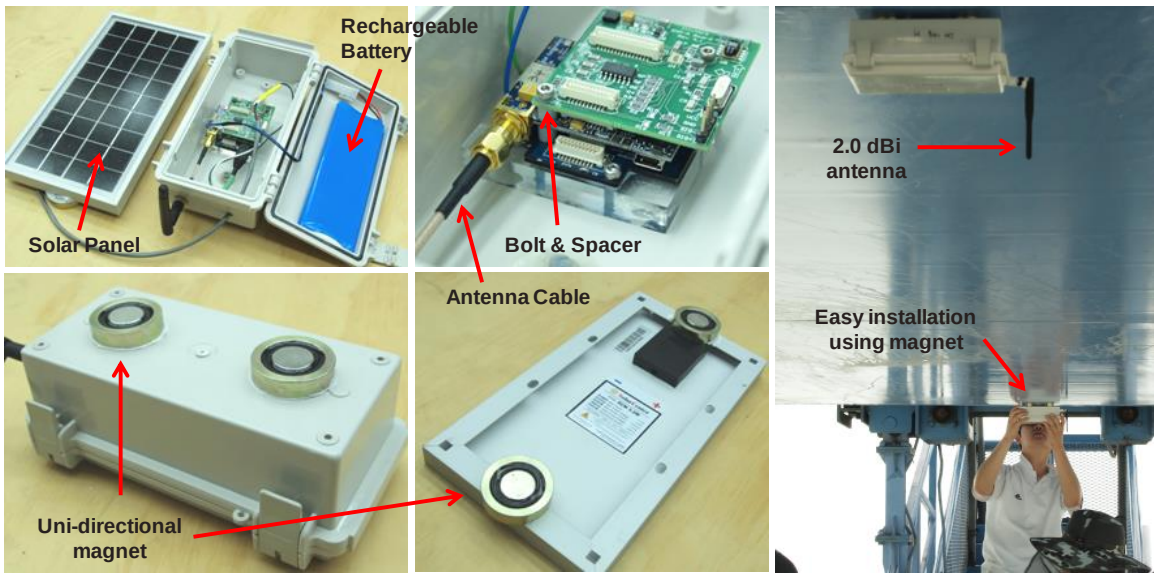

Figure 7.9. Enclosure assembly (left), sensor module mounting (middle) and installation using magnet (right).

7.4.5 High-sensitivity acceleration sensing using SHM-H sensor board

To measure low-level ambient vibration of massive pylons, the new high-sensitivity accelerometer boards (SHM-H) developed in this research (see the Section 4.1.1) has been deployed. And some of SHM-H boards have been used as the cluster heads of the *DDA* to reduce measurement noises of entire network in cost-effective manner by multi-scale use of different sensitivity sensors.

7.4.6 Environmental monitoring

Environmental monitoring of this deployment includes temperature and wind speed. To track temperature change, the temperature sensors (SHT11, Sensirion) on SHM-A board are utilized. As the SHM-A board is placed inside the enclosure, the temperature sensors of several nodes are

pulled out and placed below the cover of the enclosure to be able to measure outside temperature through a hole shown in Figure 7.10.

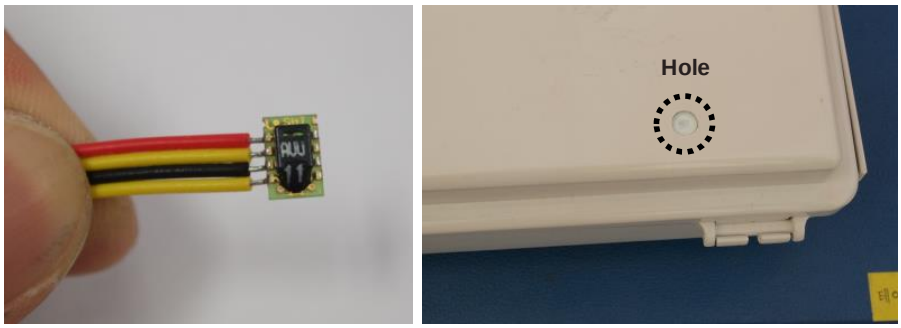

Figure 7.10. Temperature sensor (left) and exposed outside enclosure (right).

7.4.7 Wind monitoring using SHM-DAQ data acquisition board

The test bed structure, the 2nd Jindo Bridge, for this project is located in coastal windy area, in particular, on the way of typhoon path, which is supposed to experience several typhoons every year. Considering that the wind loading is one of the most critical loadings on a cable-stayed bridge, the wind loading monitoring is an indispensable option for the SHM system for a cable-stayed bridge. The 3D ultra-sonic anemometers (Model 81000, RM Young) are used to get high-precision wind information of wind speed, wind directions (horizontal/vertical) for this project, which can measure wind speed of 0 ~ 40m/s range at 0.01m/s resolution and wind direction of 0~360 degrees (-60~60 degrees for elevation). In total three anemometers are installed with 5m-length stainless poles (Figure 7.11) on the bridge, two in the center span and the other in the side span (see Figure 7.7). To collect wind information from the anemometer into the WSSN, the data acquisition board (SHM-DAQ board) developed in this research (see the Section 4.1.2) is used. The three-channel signals (wind speed, horizontal & vertical wind directions) of 0 ~ 5V from the ultra-sonic anemometer are linked to the first three channels of the ADC through the terminal

blocks on the top of the board, which allows synchronized sensing of wind (with SHM-DAQ boards) and accelerations (with SHM-A and SHM-H boards) in the WSSN using the *RemoteSensing*.

Figure 7.11. RM Young 8100 ultrasonic 3D anemometer (left) and installation on girder (right).

7.4.8 High-precision strain sensing using SHM-S strain sensor board

The newly developed wireless strain sensing system (SHM-S board) was installed on the lower part of the Haenam-side steel pylon (node ID 70 and 32 in the Haenam pylon of Figure 7.12). Traditional foil-type 350-ohm strain gages were used and connected to the SHM-S boards. Because the bridge is located in a coastal area with a corrosive environment, removing the exterior paint of the bridge for strain gage installation was not allowed. So the strain gages were installed inside the pylon to measure pylon strain in the vertical direction (Figure 7.12, left) and wired to the strain sensor nodes located outside the pylon (Figure 7.12, right). Among the two strain nodes, only one sensor node (node ID 32) used the half-bridge option with a dummy strain

gage for temperature compensation. The SHM-S board was stacked on the SHM-A board for multi-metric sensing of both acceleration and strain in synchronized manner (i.e., tri-axial acceleration in the first three channels and strain in the fourth channel). The Wheatstone bridge of the strain sensor board is balanced after installation; subsequently, the gain of the amplification was increased to 2007 times.

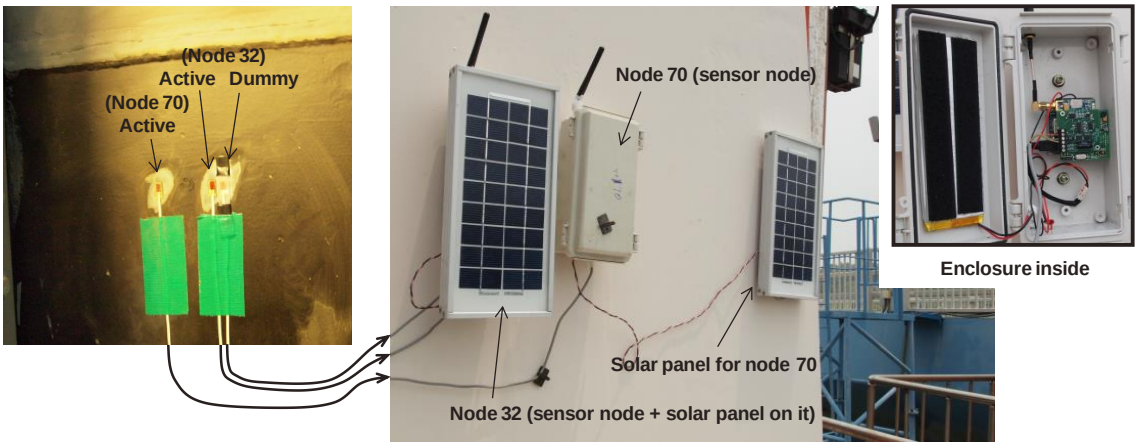

Figure 7.12. Strain gages inside pylon (left) and sensor nodes outside pylon (right).

In addition to strain measurements on the pylon, strain sensing on the girder of the Jindo Bridge also has been carried out. In contrast to strain sensing on the pylon, the inside of the girder was not accessible for strain gage installation. To measure strain without peeling the paint, therefore, the friction-type magnet strain checker (FGMH-1) combined with the SHM-S board was used. Girder strains were measured at two different locations: one was on the bottom surface of the steel box girder at midspan of the bridge, and the other measurement was on the bottom surface of the girder around pylon bearing position as shown in Figure 7.13. 25Hz sampling rate and gain of 1001 times were used for this measurement.

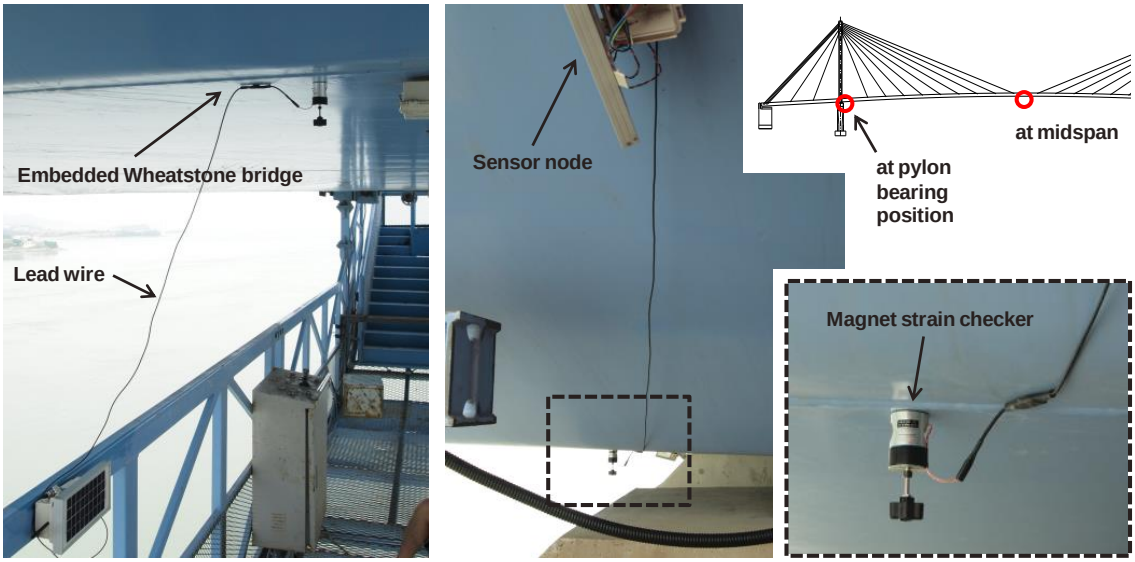

Figure 7.13. Strain sensing on the girder using magnet strain checker with SHM-S board: at midspan (left), at pylon bearing position (middle) and close-up (right).

7.4.9 Base station

The base station provides access to the entire WSSN; hence, the base station is a critical component in the WSSN. For the long-term monitoring, the base stations are carefully designed to endure the harsh environment in the Jindo Bridge. A temperature and humidity durable industrial-grade PC (AEC-6905, AAEON) is selected as the base station. The UPS backup (ES550, APC) is supplemented to protect the PC from unexpected electric surges and outages. In this deployment, two base stations are installed on each pylon pier of Jindo and Haenam sides. The base stations are environmentally protected with water-proof PVC enclosures (Figure 7.14, left) and have two gateway nodes that control deck and cable subnetworks. A wired internet line is installed to the base station, and the PC is remotely controlled with TeamViewer that is a screen-sharing and file-transfer application. For the single-hop networks, a 8 dBi antenna (PM-0M07 8dB Volcano, Daeheung) with a noise compensator (SLIM54M-500mW, Daeheung) is

used for each gateway node (Figure 7.14, right), while 2 dBi smaller antenna (PM-DI02A, Daeheung) is used for the gateway node of the multi-hop network (Jindo side cable network) to make optimal condition for multi-hop communication.

Figure 7.14. Basestation with PVC enclosure (left) and 8 dBi antenna for single-hop gateway node (right).

7.5 **Evaluation of the WSSN**

The hybrid WSSN described in the previous section provides a wide variety of valuable information in assessing the state of the Jindo Bridge. This section focuses on describing wind monitoring, performance of power harvesting, and centralized/decentralized data processing for modal analysis and cable tension monitoring.

7.5.1 Wind monitoring

The Jindo Bridge has experienced a Typhoon having the 960 hPa of central pressure and 40m/s of max wind speed, named Kompasu, after the deployment (Aug.31th ~ Sep.2nd, 2010). The typhoon passed the bridge quite closely shown in Figure 7.15. Based on the Korea Meteorological Administration (KMA) records, the wind speed was 14~20 m/s (green line, Figure 7.16) and the wind was blowing from the southeast, which is the orange dots in Figure

7.16 (left) and reproduced with an arrow in Figure 7.16 (right), in the Jindo area around 9pm on September1st, 2010. The measurements from the 3D ultra-sonic anemometer installed on the bridge, which were collected by the SHM-DAQ board, showed the 15~25 m/s of wind speed (Figure 7.17, top left) and 170~200 degree of wind direction (Figure 7.17, top right); the anemometer was installed in perpendicular direction to the bridge axis and the wind direction is calculated in clockwise from the anemometer axis (Figure 7.16, right). Considering that the KMA record is from a mountain (Cheomchal-san) in Jindo Island, not from the Jindo Bridge, the wind data measurements are acceptable.

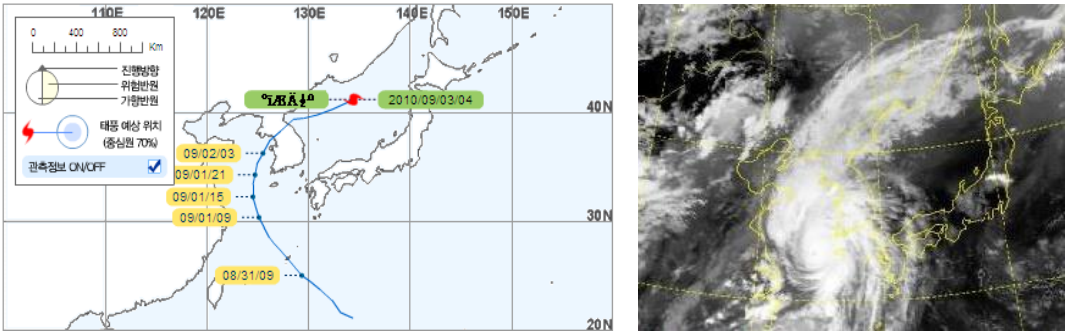

Figure 7.15. Typhoon Kompasu route (left) and satellite picture at 5:30pm in September 1st, 2010 (right).

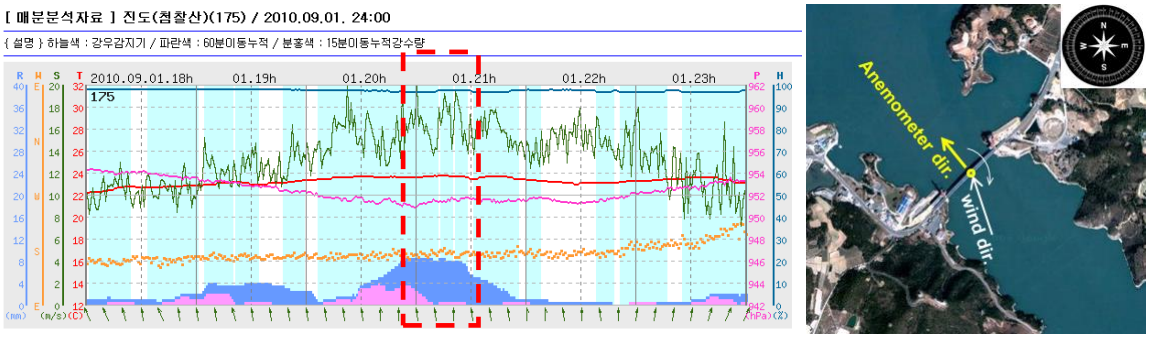

Figure 7.16. KMA record (left), anemometer and wind direction in September 1st, 2010 (right).

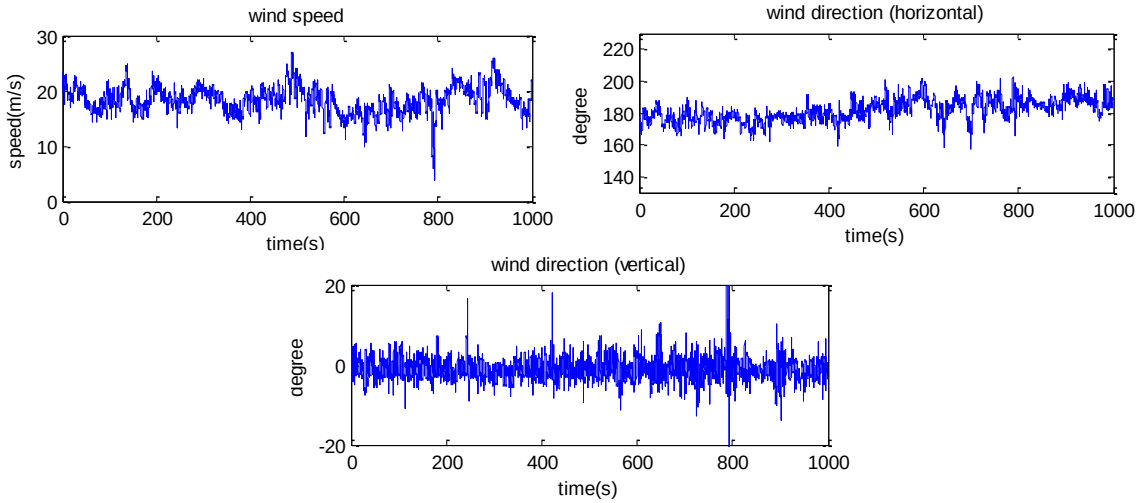

Figure 7.17. Wind measurements from Haenam side anemometer (9pm, September 1st, 2010).

7.5.2 Long term performance of WSSN

Network power conditions and temperature have been monitored using *AutoUtilCommand*. Figure 7.18 shows an example of the monitored results for six months (October 2011 ~ March 2012), since the new self-diagnostic *ChargerControl* has been implemented. During that period, battery voltage changes, charging conditions, the number of responsive nodes, and temperature changes have been monitored every 2 hours.

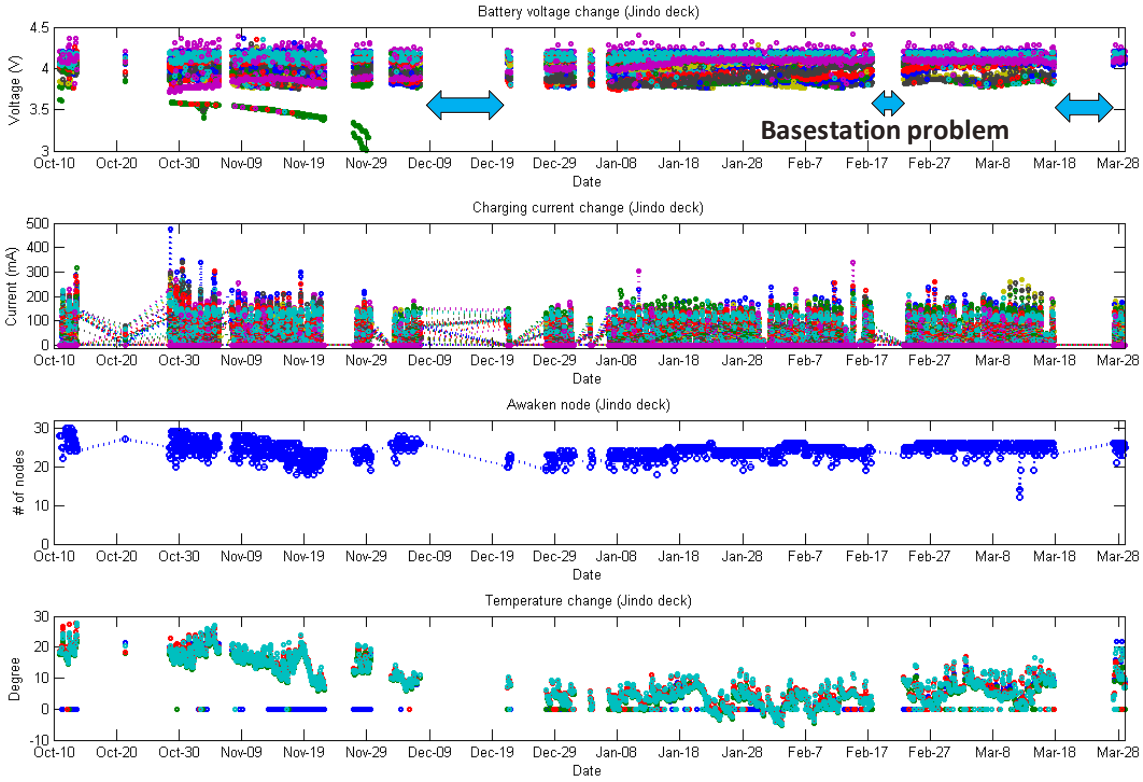

Figure 7.18. Long-term performance of the WSSN for Jindo-side deck network (October 2011 ~ March 2012).

As shown in the plot in the third-row of Figure 7.18, the number of responsive node has been around 18~29 nodes, which corresponds to 58~94% of total number of nodes in the network. The fluctuations may be attributed to the battery status changes, however unstable radio communication environment may be the fundamental reason, because the fluctuations have been too much even in short period of 1~2 days.

The plot in the first row shows the battery voltage changes, one can recognized that the battery voltages are mostly larger than 3.75V. Because the threshold for the *LongTermSleep* (within *ChargerControl*) has been set to 3.75V, if the battery voltage of a sensor node get lower that that value, it goes to the long-term sleep mode until it is charged sufficiently. However, some of sensor nodes showed the lower battery voltage than the threshold in the beginning of

that period (see the very beginning of the plot in the first row), it might be due to that wrong-version of software were installed on those nodes. This unexpected behavior has not been seen since all the nodes were reprogrammed with right-version of software in the beginning of December, 2011.

The plot in the second row shows charging current changes, which are discussed in following section, and the average charging current changes between 100~200mA. The last plot in the Figure 7.18 shows the temperature changes during that period. The temperature was more than 20℃ in October, 2011, and decreases lower than 0℃ in the beginning of February, 2012, and shows large variation of 5~20℃ in March, 2012. It should be noted that the network survived over the cold winter season in Korea.

Over the six month period, sometimes, there have been problems in the basestation PC, including the internet or gateway node disconnections, which caused some the loss of some data, as shown in the Figure 7.18.

The multi-hop network implemented in the Jindo-side cable group showed somewhat different behavior during same period (see Figure 7.19). As compared with the corresponding single-hop network, the number of responsive nodes was significantly lower. Most of sensor nodes worked fine in October, 2011. But the number of responsive nodes dropped beginning in November, 2011. Very large variations in the number of responsive nodes, 3~15 nodes, were observed, particularly fromJanuary ~ Februrary, 2012, as shown in the plot in the second row of Figure 7.19. A similar pattern was observed in the plot of the battery voltage changes (the plot in the first row); the battery voltages gradually decreased from the fully charged condition of 4.2V to the *LongTermSleep* threshold of 3.75V, then the nodes were disappeared from the network, and many of them came back to work after a couple of days with full charging condition. These

battery variation phenomenon observed in the multi-hop network may indicate that the power consumption of multi-hop communication protocol is much larger than in the single-hop network. Considering the multi-hop network needs to wake up the entire network whenever any communication is required and that the data transmission process using multi-hop communication intrinsically consume more power, the phenomenon was not absolutely strange; but it showed more power consumption than imagined.

However, in the *LongTermSleep* perspective, the WSSN showed good performance; if the battery voltage is lower than the threshold (3.75V), the node went to the long-term sleep mode, and revitalized after it is charged enough. Otherwise most of multi-hop sensor nodes would have permanently disappeared from the network in short time.

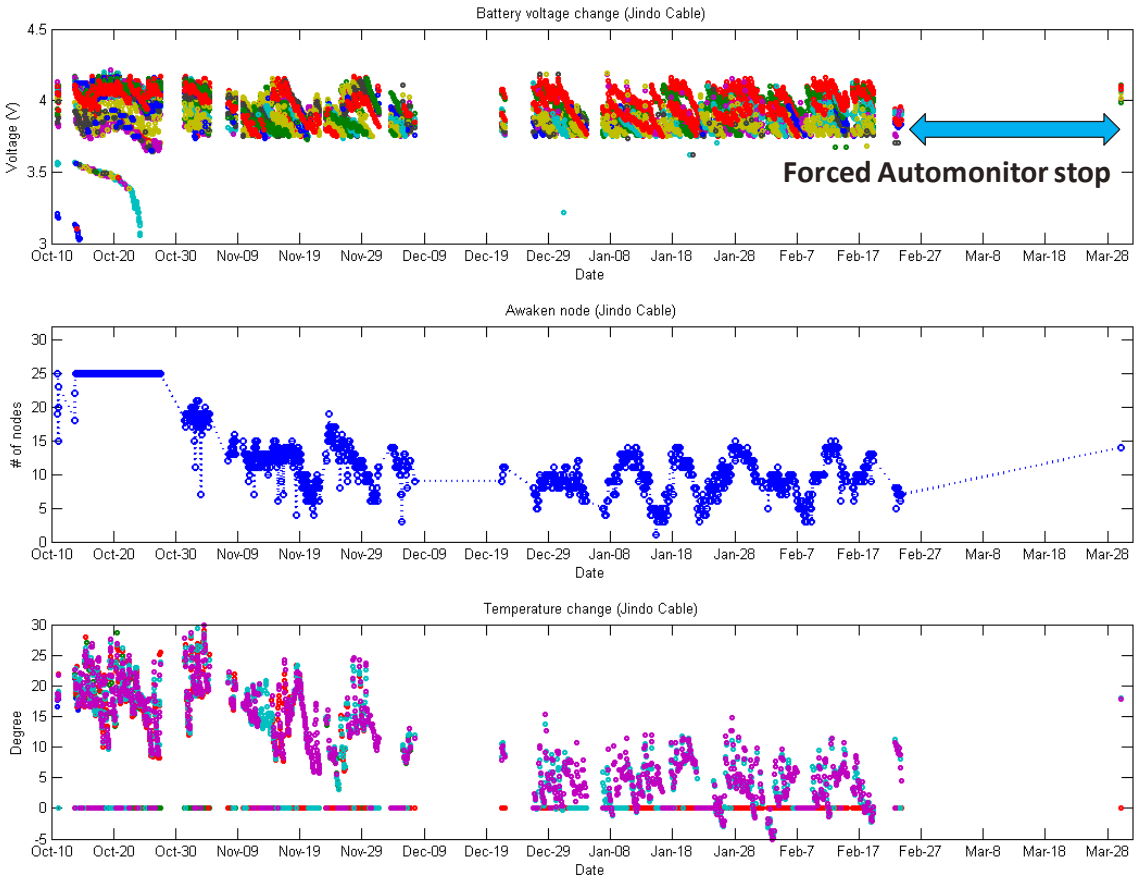

Figure 7.19. Long-term performance of the WSSN for Jindo-side cable network with multi-hop communication protocol (October 2011 ~ March 2012).

7.5.3 Energy harvesting

To check the charging performance in detail, the typical charging status obtained for two days in September, 2010, is presented in Figure 7.20; here, the charging current and charging voltage changes were measured every 1 hour for better resolution of the plots.

The first day was sunny and the second day (Sep. 11~12th, 2010) was rainy according to the Korea Meteorological Administration records. In this deployment, the default checking cycle is 1 hour for the charging currents and battery voltages of all sensor nodes. As shows in the Figure 7.20 (bottom), the charging starts around 6~7AM, then keep the average charging current of

140mA during daytime and stop charging in the night in the September 1st. The battery voltages (Figure 7.20, top) were little pulled up (from 4.08V to 4.17V in average) for fast charging by PMIC charger controller, and went back to the actual battery voltages after charging mode off. The actual voltage increase of the 10,000mAh Li-ion battery with one day charging was about only 0.02~0.04V around 4.1V level at that time; this is because the battery was in almost fully charged status. As the charging level goes up, the charging speed becomes slower for safe charging. The second day was rainy, and the average charging current was around 70mA. However, some of them (node 150, 116 and 85) showed higher charging current of about 130mA, because the sensor nodes are sentry nodes and two solar panels were used for the sentry nodes which are supposed to consume more power due to periodic sensing with *ThresholdSentry*.

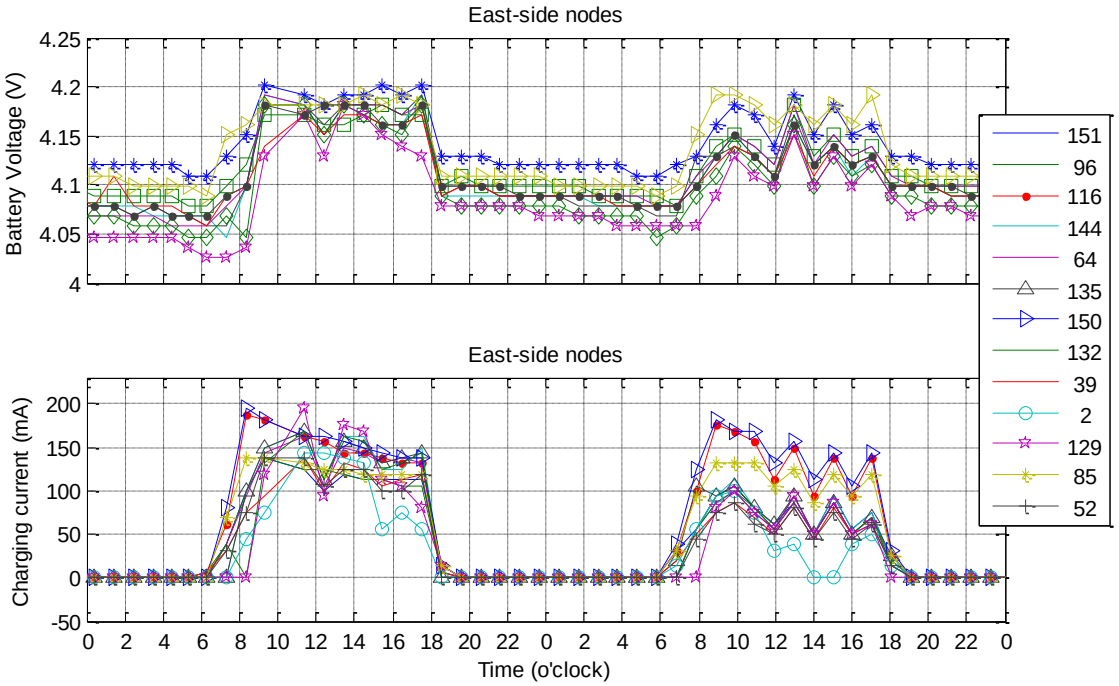

Figure 7.20. Example of charging status monitoring using *AutoUtilsCommand* (Sep. 11~12th, 2010).

7.5.4 Acceleration response measurements and modal analysis

Each sensor node equipped with SHM-A or SHM-H sensor board provides 3-axes accelerations at given sampling rate of 25Hz (user selectable among 25, 50, 100 and 280Hz). Figure 7.21 shows the example acceleration time histories measured at the center span of Haenam-side deck (*z*-axis) during the typhoon Kompasu. The acceleration levels were about 20mg in average at that time and quite evenly distributed over the period. Figure 7.22 shows the power spectral densities (PSD) for the *z*-axis acceleration of Haenam-side deck.

The centrally collected acceleration responses are used NExT/ERA method to identify natural modes as shown in Table 7.2 and Figure 7.23. The modal properties from two deck networks are combined to provide the global information. To construct the global mode shapes, a least-square method is applied to link the modes together at the four overlapped sensor nodes at the center of the deck (node 20, 73, 113 and 151, see Figure 7.7). The estimated modal properties are consistent with those from the previously performed modal survey using the wired sensor system.

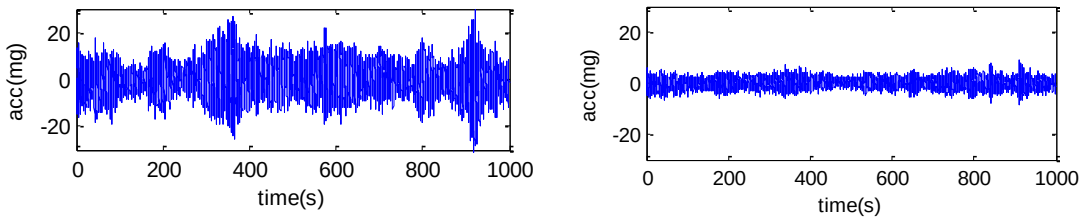

Figure 7.21. Example time histories; vertical acceleration of Haenam-side deck at midspan (left) and middle of side span (right).

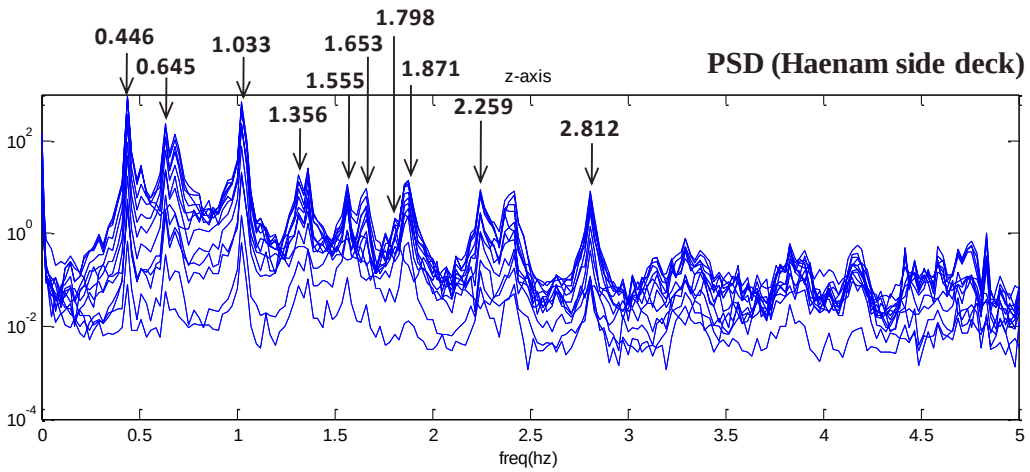

Figure 7.22. Power spectral densities for vertical accelerations of Haenam-side deck.

Table 7.2. Identified natural frequencies and comparisons.

Mode	NExT/ERA (Haenam)	NExT/ERA (Jindo)	from Wired SHM	FE analysis
Deck **V**ertical -1	0.4462	0.4462	0.4395	0.4422
DV 2	0.6454	0.6471	0.6592	0.6471
DV 3	1.0331	1.0326	1.0498	1.0010
DV 4	1.3559	1.3421	1.3672	1.2472
DV 5	1.5549	1.5490	1.5869	1.3490
DV 6	1.6528	1.6346	1.6602	1.4596
Deck **T**orsion -1	1.7977	1.8022	-	1.7888
DV 7	1.8710	1.8704	1.8555	1.5858
DV 8	2.2594	2.2609	2.3193	2.1154
DV 9	2.8121	2.8133	2.8076	2.5612

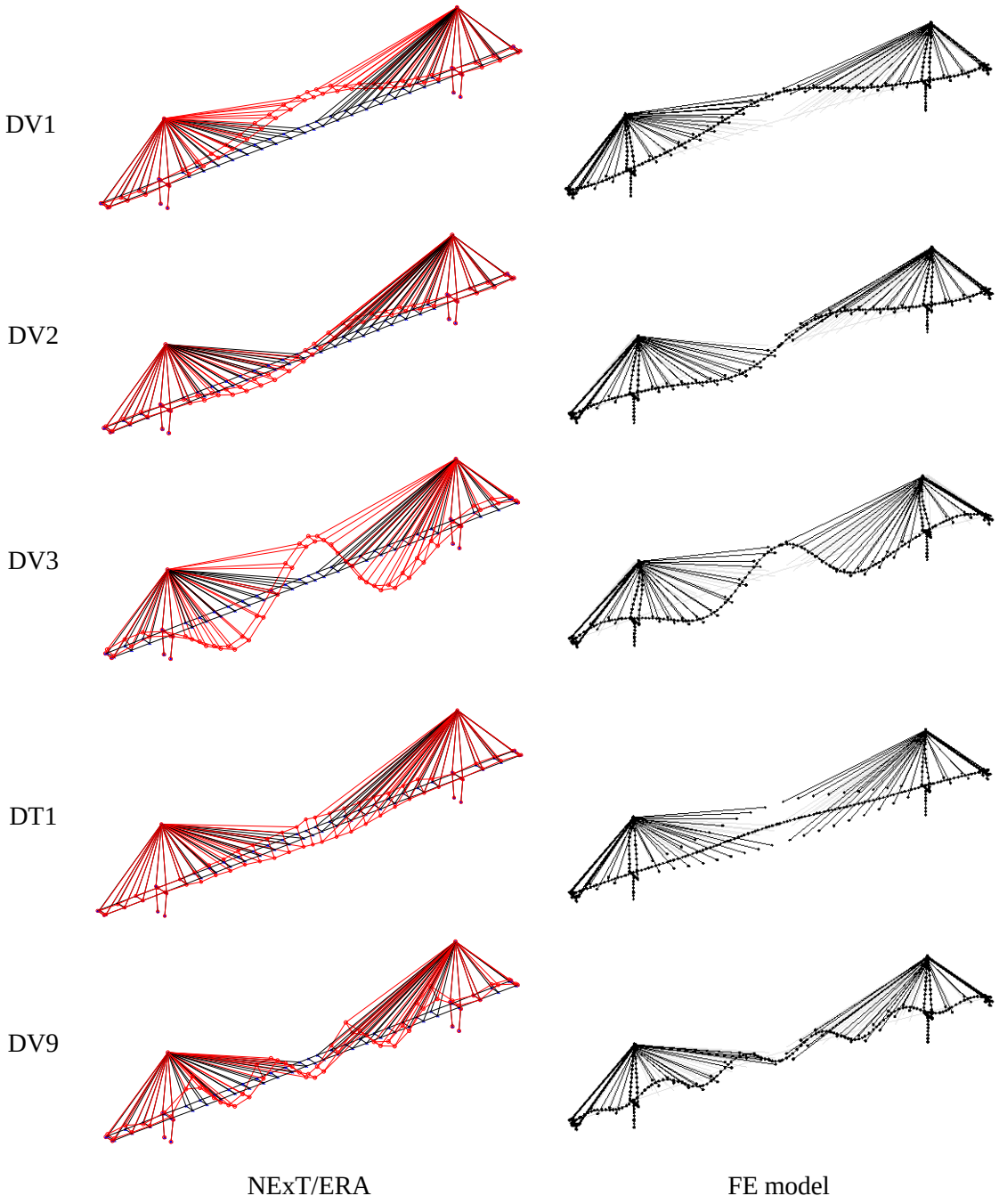

Figure 7.23. Mode shapes identified from data (left) and from FE analysis (right).

7.5.5 Strain response measurements using SHM-S board and analysis

7.5.5.1 Strain measurements on the pylon

The results for the acceleration and strain measurements on the pylon, 400 seconds of data at 25Hz sampling rate, are shown in Figure 7.24. The acceleration levels for the three-axes acceleration measurements are about 2mg and strain level was 3~5 μs (compression), corresponding to quite low level of vibration. As shown in the PSDs of Figure 7.24, only the *z*-axis (i.e. longitudinal direction of the bridge) acceleration PSD shows meaningful mode around 2.4Hz (the 1st pylon bending mode, Cho et al. 2010). Additionally, the strain measurements provide more information in the low frequency range, showing four distinct peaks below 2Hz, corresponding to the 1st ~ 4th girder bending modes. The proposed wireless strain sensing system functioned well for ambient vibration monitoring for this cable-stayed bridge; the strain measurement was even more informative than acceleration measurements in the low frequency region.

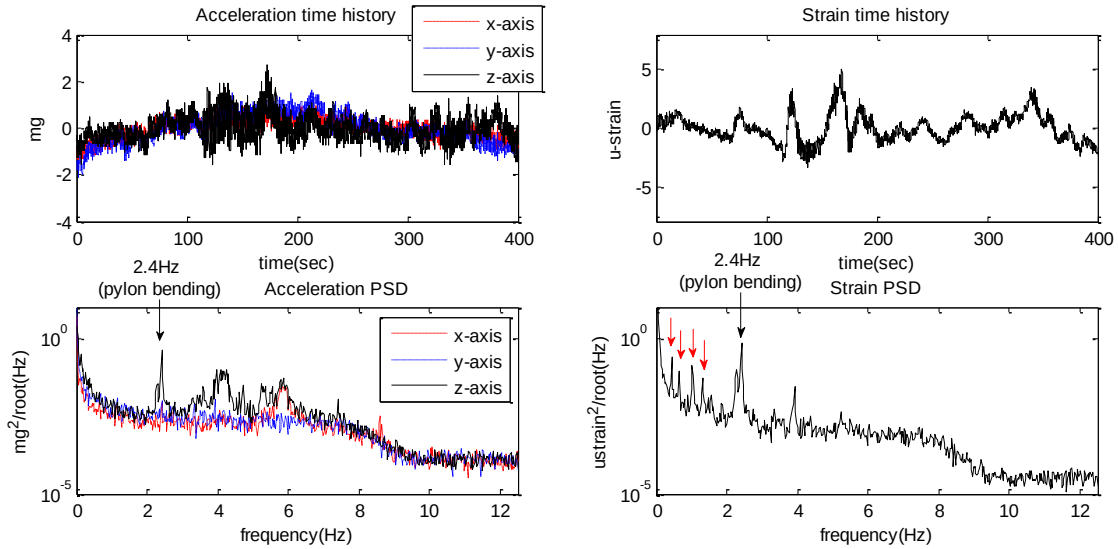

Figure 7.24. Example of synchronized acceleration (left) and strain measurements (right) on pylon.

To check the performance of the temperature compensation method using the half-bridge configuration with a dummy strain gage, mean values of several strain measurements on different day and at different times are compared in Figure 7.25. Once the Wheatstone bridge of the SHM-S board was balanced on September 21th, the strains were measured over three weeks without changing the bridge balance. A sensing event was activated only when the structural responses exceed a certain level specified by *AutoMonitor* and *ThresholdSentry*. As a result, the times of the measurements were random. Figure 4.78 shows the mean strains, which should be zero and can be viewed as representing strain drift due to temperature; a clear difference is observed between the compensated and uncompensated configurations. While the strain measurement at node 70 using the quarter-bridge option shows significant drifts over three weeks, node 32 data with temperature compensation is quite well balanced.

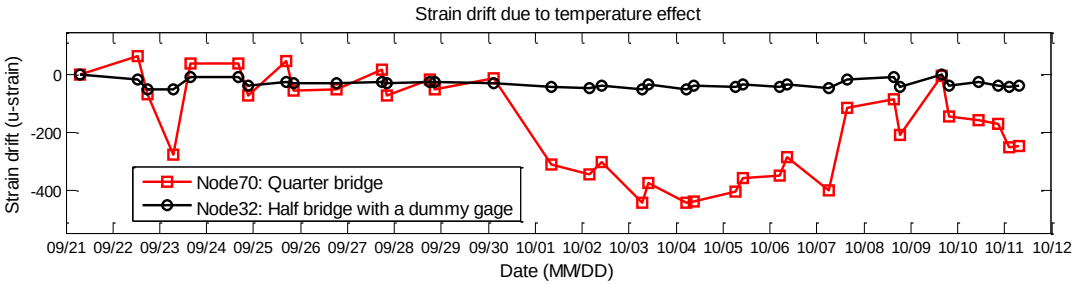

Figure 7.25. Strain drifts due to temperature change over three weeks.

The temperature compensation approach shows good performance, although some temperature effects are still present over the measurement period. These residual drifts may be attributed to the real effects of temperature change on structural strain responses or the different temperature sensitivities of resistors of 10~100 ppm comprising the Wheatstone bridge arms;

further investigation will be required. However, if only dynamic strain measurements are of interest, the static strain drift due to temperature effect would not be an issue.

7.5.5.2 Strain measurements on the girder

Figure 7.26 shows the typical strain measurements on the girder subjected to traffic loading; several cars were passing the bridge at that time of the measurements, and the apparent peaks shown in the Figure 7.26 may be attributed to the car traffic. The strain measurements at pylon bearing location (top of Figure 7.26) and at midspan (bottom of Figure 7.26) show clear differences. While the strain peaks in the pylon location measurement are downward, which means compression, however, the peaks in the midspan measurement are upward in tension direction. This phenomena is because the bottom surface of the steel box girder at the pylon bearing location is subjected to compressive force due to the negative bending moment when cars passing, and the bottom of the girder at midspan is in tension with positive bending.

The amplitudes of the peaks are quite different for the different sensing locations. The strain peak amplitudes are just 2~8 μs at the pylon bearing location, whereas they are 10~50 μs at midspan. Though the peak amplitudes vary depending on the car weight and speed, similar trends (i.e., higher amplitude strains at the midspan) were observed with other measurements; thus, the sensitivity of strain to traffic loading appears to be higher at midspan than at the pylon.

An abrupt signal drop was found after a high tension peak in the midspan strain measurement around 315 seconds (bottom of Figure 7.26). This change may be attributed to the lateral slip of the magnet checker due to the heavy loading that caused a quite significant tension strain peak about 50 μs. Because the attractive force of the magnet is unidirectional perpendicular to the girder surface, the resistance to the lateral movement is relatively weak.

Applying little silicon or modeling clay around the strain checker would help to prevent the possible slippage.

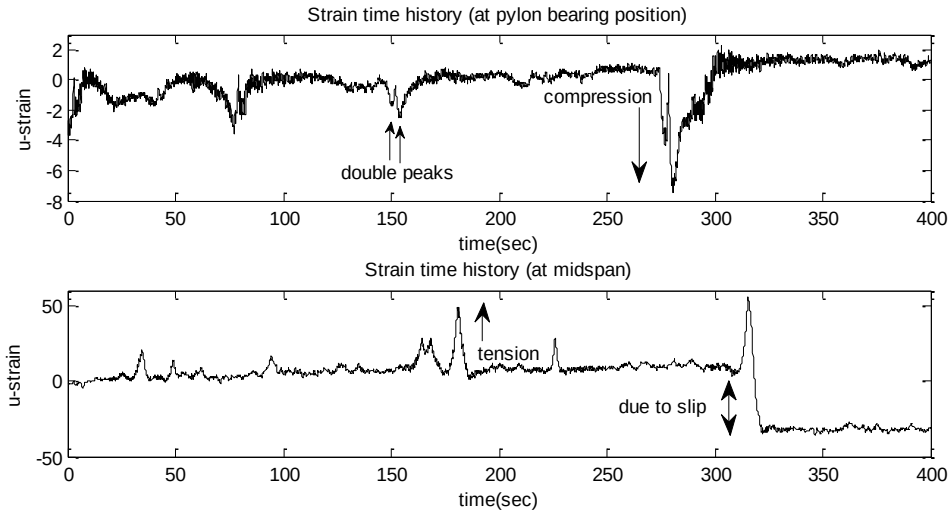

Figure 7.26. Example strain measurements on the girder subjected to traffic loading: at pylon bearing location (top) and at midspan (bottom).

Taking a close look at the strain peaks in the pylon location measurement, each set of compression peak is composed of two different-height peaks, which is not shown in the midspan strain measurement. For the peak around 75 seconds, a somewhat larger peak appeared first, followed by a smaller peak (top of Figure 7.26). In contrast, the peaks around 150 seconds and 280 seconds show a smaller peak first, followed by a larger peak. This phenomenon is attributed to the double-concave shaped stress influence line for the bottom flange of multi-span continuous girder at intermediate the support (see the left of Figure 7.27). Each of the double peaks occur when a car passing the lowest point of each of the concaves of the influence line. Additionally, if either-side span has different length, the double peaks may have different amplitudes.

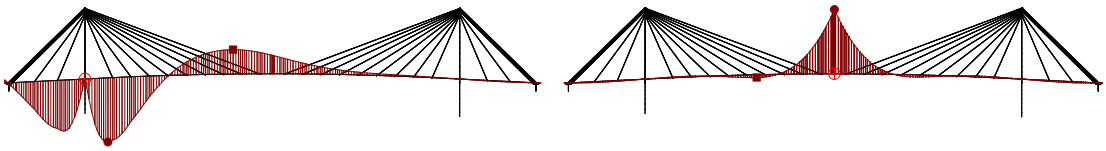

Figure 7.27. Stress influence lines for girder bottom flange of the 2nd Jindo Bridge: at pylon bearing location (left) and at midspan (right).

7.5.5.3 Numerical simulation for traffic-induced girder strain of Jindo Bridge

For understanding better the characteristic of observed girder strain of the bridge, a numerical simulation of the Jindo Bridge under moving truck loading has been conducted. The same FE model used in the Section 7.2 was utilized for this. To simulate moving loads, one of typical 5-tonf capacity trucks that can be easily found in Korea was used. It has two axles, and the distance between front and rear axle is 5.8m. The weight of the empty truck is about 6.9 tonf and fully loaded truck weights about 12 tonf. In this simulation, a fully loaded truck of 12 tonf was used and the truck was moved from the Jindo side to the Haenam side of the model (north bound) at 60 km/hour speed. Newmark method, one of direct integration methods, was used for time history analysis, and 0.01 second of time step was used. And 2% modal damping was assumed for entire structure, and the stress/strain responses were sampled at 25Hz as same as previous field measurements.

Figure 7.28. Truck used in simulation (Hyundai Motors Co., Ltd.).

Strain responses from the FE model under the fully loaded 12-tonf moving truck loading are shown in Figure 7.29. Once the stress responses were obtained considering the combined effects of both bending moment and axial force of girder on the stress of bottom flange, and then divided by Elastic modulus to get strain responses. Compared with real measurement shown in Figure 7.26, the simulated strain time histories may include more dynamic components (noise). This may be due to the free vibration effects generated during the passage time interval between nodal points when the truck loading passes the finite number of nodal points, of which effects would be minimized with more closely spaced nodal points by using more number of elements in the girder model; such dynamic noise would not happen in real measurements because the real girder and truck movement are continuous.

As shown in Figure 7.29, the maximum level of the simulated girder strain was about 9.5 μ-strains in compression at pylon bearing location and 45 μ-strains in tension at midspan under the 12-tonf moving truck loading. For the same weight truck, the midspan response showed higher strain amplitude; which means the girder strain response has higher sensitivity to traffic loading at midspan than at pylon location.

The double peaks phenomenon happened, as expected, in the simulated girder strain response as well at pylon bearing location (see the left of Figure 7.29). Little smaller peak of 7.5 μ-strains was appeared first, and then higher peak of 9.5 μ-strains followed after about 3.1 seconds. This is attributed to the uniquely shaped stress influence line of the 2nd Jindo Bridge shown in the left of Figure 7.30; the influence line has double concave around the pylon. For the north bounding truck moving, the first strain peak happened when the truck passed the lowest point of the first concave in the side span of the bridge, and the following higher peak happened at the lowest

point of the second concave. Considering that the distance between the lowest points of the two concaves was about 51m (see the left of Figure 7.30) and the time difference between the strain peaks was 3.1 seconds (see the left of Figure 7.29), the estimated truck speed was about 59.2 km/hour, which was similar with the simulation speed of 60 km/hour. Also the strain peak in the midspan response can be utilized to estimate the truck speed; though it is not easy to find the clear base width of the strain time-history peak due to the dynamic noise, about 6.0 seconds of base width of the strain peak could be assumed (see the right of Figure 7.29) and the base width of the influence line of 100m (see the right of Figure 7.30) result in the speed estimation of 60 km/hour.

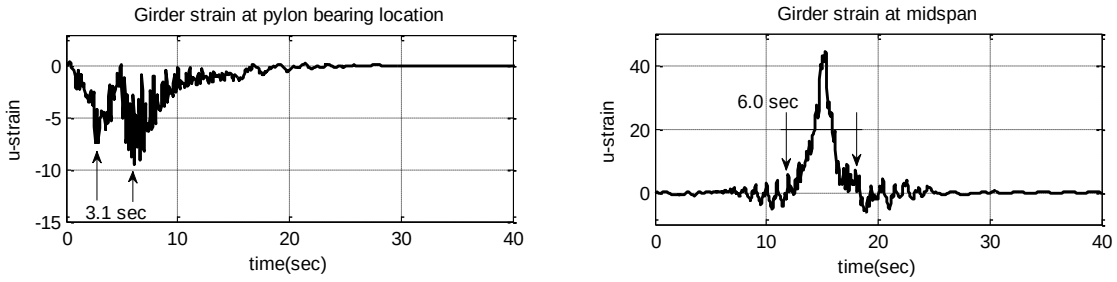

Figure 7.29. Simulated girder strain responses from the 2nd Jindo Bridge FE model under truck loading: at pylon bearing location (left) and at midspan (right).

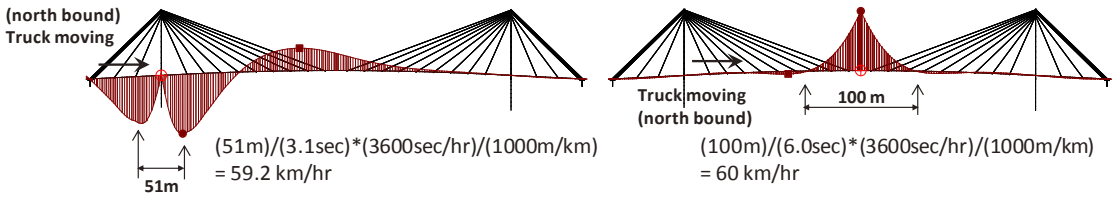

Figure 7.30. Vehicle's moving speed calculation examples using influence lines.

7.6 **Summary**

The world's largest WSSN for monitoring civil infrastructure, 669 sensing channels with 113 sensor nodes, has been successfully deployed for long-term operation on a cable-stayed bridge in South Korea. The performance of the power management software and the autonomous network/environment monitoring software have been experimentally validated through the full-scale deployment, demonstrating the potential for practical implementation. And the multi-metric sensor boards (SHM-H, SHM-DAQ, and SHM-S boards) developed by this research have shown great performance, providing broader applications of the WSSN for SHM.

CHAPTER 8 CONCLUSIONS AND FUTURE STUDIES

8.1 **Conclusions**

The research outlined in this dissertation provides an enabling foundation for wireless smart sensor (WSS) technology to be widely embraced in structural health monitoring (SHM) practice and pointed to promising new directions for SHM. The multi-scale SHM framework using WSS incorporates hardware for high-sensitivity multi-metric sensing, software for long-term and robust operation of a self-powered wireless smart sensor network (WSSN), multi-scale and hybrid SHM strategies for optimized use of the information obtained from the SHM systems, and full-scale implementation to validate the potential of its practical applications.

To further extend the WSS technology beyond conventional SHM practice, hybrid SHM strategy combining numerical modeling and multi-metric physical monitoring has been presented in this research. Such a model-based approach has allowed comprehensive prediction of structural responses at arbitrary locations, and particularly, the use of multi-metric measurements significantly improved the accuracy of the predicted information; of which model-based prediction and multi-metric update of the prediction are enabled by the Kalman filter. Two numerical examples, one for fatigue life assessment of a steel truss structure, the other for displacement monitoring of a tall column structure, validated the efficacy of the hybrid method.

A variety of high-sensitivity multi-metric sensor boards have been developed by this research, since existing Imote2-based WSS technology has not supported necessary capabilities for multi-metric measurements; which is essential for successful hybrid SHM method and broader SHM applications. A high-sensitivity accelerometer (SHM-H) board has been developed for low-level ambient acceleration measurements, which incorporates 16-bits ADC, low-noise analog

accelerometer, and carefully designed analog signal processing circuit. The multi-purpose data acquisition (SHM-DAQ) board developed in this research accommodates external analog and digital sensor information into WSSN. And the high-precision strain sensor (SHM-S) board has been designed for Imote2 to measure ambient strain responses of structures. Autonomously balanceable Wheatstone bridge has been developed for the board to allow up to 2500 times signal amplification, and onboard temperature compensation and onboard shunt calibration can be conducted in automated way using the software developed for this strain sensor board. Subsequent development of 24-bits data acquisition (SHM-DAQ24) board by this research addresses many issues in wireless sensing due to limited resolution. Compare with 16-bits ADC-based sensing, the additional 8-bits of resolution results in signal amplification effect of 256 times without sacrificing the sensing range. Low-cost and low-power 24-bits ADCs have been available in recent years by the delta-sigma modulation technology, which consequently enabled its WSS application.

In addition, this research addresses the software required for robust and long-term operation of WSSN, which is one of the critical issues in practical application of WSSN for SHM. Two main application services have been developed and integrated in Imote2-based WSSN by this research. The *AutoUtilCommand* allows autonomous monitoring of network and environment condition, which provides essential information required for managing the WSSN and taking account the effects on the outcomes obtained from the WSSN. And the *ChargerControl* provides the self-diagnostic network power management by regular diagnosis of power/charging condition in each sensor node and decision making on its involvement in network activities on the leaf node's own, which consequently allows long-term operation of self-powered WSSN.

Building on the developments of hardware and software for high-sensitivity multi-metric WSSN and its robust and long-term operation, this research proposes two new innovative SHM strategies for optimized utilization of limited capabilities of given SHM systems. First, multi-scale use of different-sensitivity sensors in WSSN has been explored to improve the performance of modal identification in decentralized WSSN without sacrificing the cost effectiveness. Even with a small number of high-sensitivity sensors (SHM-H boards), the use as the reference sensors in NExT/ERA-based modal identification significantly improved the performance in decentralized WSSN of which majority are general-purpose accelerometer boards (SHM-A). Second, this research validates that combined use of multiple sensors, despite of low-resolution sensors, can enhance the quality of obtained outputs from the sensor network. For this, the feasibility of low-cost GPS sensors for structural displacement monitoring applications has been investigated. The use of multiple low-resolution (C/A code-based) single-frequency GPS sensors has shown better accuracy in dynamic displacement measurements, while the hardware capability of the low-cost GPS are not yet advanced enough for actual SHM applications.

Finally, the components for multi-scale SHM using WSSN developed in this research have been validated through a full-scale implementation. A total of 113 WSS nodes with 669 sensing channels has been successfully deployed and operated for long-term monitoring of a cable-stayed bridge, the Jindo Bridge, in South Korea, constituting the world's largest WSSN for SHM applications. SHM-H boards have been used as the reference sensors in decentralized network, SHM-DAQ boards for accommodating wind information from ultra-sonic anemometers into WSSN, and SHM-S boards for measuring strain responses of steel pylons and girder; all the multi-metric boards showed great performances. The *AutoUtilCommand* application service has been successfully operated, providing valuable information about the network and environment

conditions. The *ChargerControl* also has well managed the network power by providing stable solar charging to the network and controlling the network activity involvements of sensor nodes based on the power conditions, consequently allowing long-term operation of the WSSN.

The multi-scale SHM framework using WSSN developed in this research allows practical implementation of WSS technology for broad SHM applications. A variety of hardware developed by this research enables high-quality sensing of various-metrics and types of signals, allowing extensive applications to broad monitoring domain. Moreover, robust operation of self-powered WSSN makes the technology be more feasible for its practical applications. In particular, multi-scale use of (1) different-sensitivity sensors (low-resolution & high-sensitivity sensors) in WSSNs, (2) different domain monitoring systems (numerical model & physical system) with the aid of the Kalman filter method, and (3) densely arrayed low-resolution sensors through averaging/correlation process provides promising cost-effective tools that can overcome the limitations of conventional SHM practice, in conjunction with WSS technology. Developments and findings from this research will serve as an enabling foundation to revolutionize the way that civil infrastructure is monitored.

8.2 **Future Studies**

8.2.1 Hardware enhancement

Though the sensor boards presented in this research provides high-quality multi-metric sensing capabilities using WSS, resolving some of the issues identified in this research will allow for even broader application of WSS technology.

Multi-channel 24-bits data acquisition board

Due to limited capability of 32-bit PXA271 XScale processor of Imote2, all the four channel data could not be obtained from the TI's ADS1274; the ADS1274 sends out the 96 bits of all four channel at once in a single SPI transaction, which cannot be treated with Imote2, consequently allowing only the 1st channel data measurement from the ADC. Unless another higher-performance WSS platform is developed, other ADCs that send out the data channel by channel in a transaction may be considered.

Wireless wind pressure sensor

Wind pressure measurement provides essential information about the source of wind-induced vibration. Laboratory-scale wind pressure measurement on scale-models through wind-tunnel tests is common practice. However, full-scale wind pressure measurement is a challenging task; a dense array of pressure sensors is intrinsically required to obtain reasonably accurate wind pressure profiles for a structure; however, the currently available wired approach for wind pressure measurement cannot sufficiently realize such a dense sensor network. Moreover, many of available air pressure transducers rarely support low-level pressure measurement. The development of high-sensitivity wireless wind pressure measurement system will provide a groundbreaking way for full-scale monitoring of wind pressure for civil infrastructure.

Scour monitoring using WSSN

The principle of the bio-inspired sensing strategy described in the section 6.2, electric fish's skin sensing method and its application to displacement monitoring using low-cost GPS, can be applied for scour monitoring using low-cost sonar sensors. Scour monitoring is one of the most critical tasks to secure the safety of bridges over river. However, monitoring the underwater conditions is a challenging task, particularly using WSS.

A sonar sensor measures the distance between the sensor and river bed using the reflected sonar wave from the floor. Considering the noisy underwater condition due to floating particles, dust, and etc., however, the distance sensing accuracy of sonar sensors may not be secured in actual applications particularly with low-cost sonar sensors. As similar way of above GPS sensing, the idea of using densely-arrayed sonar sensors would be helpful to improve the accuracy. Assuming the noise signals are not correlated, averaging and cross correlation process between the data obtained from densely-arrayed sonar sensors can significantly reduce the measurement noise, allowing better accuracy in estimating the distance from the sensor to the river bed.

8.2.2 Further applications of Hybrid SHM

The hybrid monitoring approach presented in this research is not restricted to just structural response monitoring. As long as there exist appropriate models and measured data, the information from both domains can be combined to better estimate the system's behavior.

Moving load identification using model-based Kalman filter

The augmented system described in Eqn. (3.7) ~ (3.12) of the Chapter 3 implies that input excitations can also be estimated with this hybrid method. As the state vector to define the input excitation is merged into the existing state vector for structural responses (i.e., displacement and velocity), the Kalman filter can estimate the input excitation as the part of the augmented state vector. As long as the input excitation has the stochastic and zero-mean nature, the method presented in Chapter 3 can be used, as is, for identifying the input excitation such as ambient wind loadings.

However, the Kalman filter method presented in Chapter 3 may not effectively handle the vertical traffic loadings applied to bridge structures. In nature, because such vertical traffic loadings are not zero-mean process, the zero-mean input assumption considered in the conventional Kalman filter approach is not valid any more. To handle such nonzero mean excitation effectively, further study is required.

Full-scale validation

The efficacy of the hybrid SHM method has been numerically validated in the Chapter 3. However, further validation of the method is required through full-scale tests to make it feasible for real-world applications. An ongoing SHM project on the Xihoumen bridge, the world's 2nd longest cable-suspension bridge in China, will be utilized for the full-scale validation of hybrid method. As an internal collaborative research project between University of Illinois and Harbin Institute of Technology (China), wind-induced vibration monitoring using WSSN is main objective of interest. In addition to acceleration and wind measurements at few locations, limited number of strain response measurements will provide comprehensive information about the bridge behavior (i.e., structural responses at arbitrary locations) and input loading (i.e., wind load and traffic load) in conjunction with the model-based Kalman filter.

Other possible applications

As long as numerical models are available and multi-metric measurements can be obtained, the applications of the hybrid SHM method are limitless; which can include below, but not limited to,

- Hybrid scour monitoring, which combines the wireless scour monitoring system mentioned in section 8.2.1 and a numerical model for scour phenomenon simulation.

- Citi- and state-wide air quality monitoring: combination of numerical model to simulate air quality/wind environment over a city/state and multi-metric measurement of air quality (i.e., CO, NO_2, O_3, SO_2, etc…) and wind information.
- Hybrid land slide monitoring, which combines the numerical model to simulate land slide phenomenon and multi-metric measurements of underground water level, pore pressure, velocity of surface wave, and etc.

REFERENCES

[1] Abdalla, M.O. Zimmerman, D.C. Grigoriadis, K. M. (1999), "Structural Damage Detection using Strain Data via Linear Matrix Inequaly Based Methods", *American Control Conference*, San Diego, Califórnia, pp. 1114-1118.

[2] Abdel-Ghaffar, A.M., & Scanlan, R.H. (1985), "Ambient vibration studies of golden gate bridge: I. suspended structure", *Journal of Engineering Mechanics*, 111(4), 463-482.

[3] Amiri-Simkooei, A.R., Tiberus, C.C.J.M, and Teunissen, P.J.G. (2007), "Assessment of noise in GPS coordinate time seriesL methodology and results", *Journal of Geophysical Research*, Vol. 112, Doi 10.1029/2006JB004913.

[4] Arms, S. P., Townsend, C. P., Churchhill, D. L., Hamel, M. J., Galbreath, J. H., and Mundell, S. W. (2004), "Frequency agile wireless sensor networks." *Proc., SPIE - Smart Electronics, MEMS, BioMEMS, and Nanotechnology*, 5389, 468-475.

[5] Arms, S.W., Townsend, C.P., Churchill, J.H., Galbreath, B., Corneau, R.P., and Ketcham, N.P. (2009), " Energy harvesting, wireless, structural health monitoring and reporting system", *Materials Forum*, 33, 220-234.

[6] Ashkenazi, V., Dodson, A., Moore, T., and Roberts, G. (1997), ''Monitoring the movements of bridges by GPS.'' *Proc., ION GPS 1997, 10th Int. Technical Meeting of the Satellite Division of the U.S. Institute of Navigation*, Kansas City, Mo., 1165–1172.

[7] ASTM E-1049 (1985), Standard Practices for Cycle Counting in Fatigue Analysis.

[8] Austin, K.J., Calder, M., and McAree, P.R. (2005), "Machine monitoring with wireless sensor networks", *Proc. of CRC Mining Technology Conference*, Fremantle, WA.

[9] Battista, N.D., Westgate, R., Koo, K.Y., Brownjohn, J. (2011), "Wireless monitoring of the longitudinal displacement of the Tamar Suspension Bridge deck under changing environmental conditions," *Proc. of SPIE*, San Diego.

[10] Benedetti, M., V. Fontanari, and D. Zonta. (2011), "Structural Health Monitoring of Wind Towers: Remote Damage Detection Using Strain Sensors", *Smart Materials and Structures*, 20(5), 055009 (13pp).

[11] Bennett, P.J., Soga, K., Wassell, I.J., Fidler, P., Abe, K., Kobayashi, Y., and Vanicek, M. (2010), "Wireless sensor networks for underground railway applications: case studies in Prague and London", *Smart Structures and Systems*, 6 (5–6), 619–639.

[12] Bennett, R., Hayes-Gill, B., Crowe, J. A., Armitage, R., Rodgers, D., and Hendroff, A. (1999), "Wireless Monitoring of Highways, in Smart Systems for Bridges, Structures, and Highways", *Proc. of the SPIE*, Vol. 3671, 173–182.

[13] Bischoff, R., Meyer, J., Enochsson, O., Feltrin, G. and Elfgren, L. (2009), "Event-based strain monitoring on a railway bridge with a wireless sensor network," *Proc. of 4th International Conference on Structural Health Monitoring of Intelligent Infrastructure*, Zurich, Switzerland.

[14] Borsa, A.A. and Minster, J.B. (2007), "Modeling long-period noise in kinematic GPS applications," *Journal of Geodesy*, Vol. 81, 157-170.

[15] Brownjohn, J. M. W. (2007), "Structural health monitoring of civil infrastructure. Philosophical Transactions of the Royal Society A", *Mathematical, Physical and Engineering Sciences*, 365, 589-622.

[16] Caffrey, J., Govindan, R., Johnson, E., Krishnamachari, B., Masri, S., Sukhatme, G., Chintalapudi, K., Dantu, K., Rangwala, S., Sridharan, A., Xu, N., and Zuniga, M. (2004), "Networked sensing for structural health monitoring," *Proc. of 4th Internal Workshop on Structural Control*, New York, NY; 57-66.

[17] Caglayan, B.O., Ozakgul, K., and Tezer, O. (2009), "Fatigue life evaluation of a through-girder steel railway bridge", *Engineering Failure Analysis*, 16, 756-774.

[18] Caicedo, J. M., Clayton, E., Dyke, S. J., Abe, M., & Tokyo, J. (2002), "Structural health monitoring for large structures using ambient vibrations", *Proc. of the ICANCEER Conference*, Hong Kong, August, 15-20.

[19] Casciati, F. and Fuggini, C. (2009), "Engineering vibration monitoring by GPS: long duration records", *Earthquake Engineering and Engineering Vibration*, Vol. 8(3), 459-467.

[20] Celebi, M., & EERI, M. (2006), "Real-time seismic monitoring of the new cape girardeau bridge and preliminary analyses of recorded data: An overview", *Earthquake Spectra*, 22, 609.

[21] Chan, T.H.T., Li, Z.X., and Ko, J.M. (2001), "Fatigue analysis and life prediction of bridges with structural monitoring data – part II: application", *International Journal of Fatigue*, 23, 55-64.

[22] Chang, S. J. and Kim, N. S. (2011), "Estimation of displacement response from FBG strain sensors using empirical mode decomposition technique", *Experimental Mechanics*, in press [http://dx.doi.org/10.1007/s11340-011-9522-z].

[23] Chatterjee, P., O'Brien, E., Li, Y. and Gonzalez, A. (2006), "Wavelet Domain Analysis for Identification of Vehicle Axles from Bridge Measurements", *Computers and Structures*, 84, 1792-1801.

[24] Cho, N.S. and Kim, N.S. (2008), "Prediction of the static deflection profiles on suspension bridge by using FBG strain sensors", *Journal of Korean Society of Civil Engineering*, 22(6-A), 699–707.

[25] Cho, S., Jo, H., Jang, S., Park, J., Jung, H.J., Yun, C.B., Spencer Jr., B.F. and Seo, J.-W. (2010), "Structural health monitoring of a cable-stayed bridge using smart sensor technology: Data analyses," *Smart Structures and Systems*, 6(5-6), 461-480.

[26] Choi, H., Choi, S., and Cha, H. (2008), "Structural Health Monitoring System based on strain gauge enabled wireless sensor nodes", *5th international conference on networked sensing systems*, 2(4), 211-214.

[27] Crossbow Technology, Inc, "MICA2 Wireless Measurement System", San Jose, CA (2007).

[28] Crossbow Technology, Inc., "ITS400, Imote2 Basic Sensor Board", San Jose, CA, (2007).

[29] Daliri, A., Galehdar, A., John, S., Rowe, W.S.T., and Ghorbani K. (2010), "Strain measurement in composite materials using microstrip patch antennas", *Proc. of ASME Conference on Smart Materials*, Adaptive Structures and Intelligent Systems (SMASIS), 3703.

[30] Doebling, S. W., Farrar, C. R., Prime, M. B. and Shevitz, D. W. (1996), "Damage identification and health monitoring of structural and mechanical systems from changes in their vibration characteristics: a literature review", *Los Alamos National Laboratory Report*, LA-13070-MS.

[31] Downing, S. and Galliart, D. and Bereyni, T. (1976), "A Neubers rule fatigue analysis procedure for use with a mobile computer", *Proc. of SAE Automotive Engineering Congress*, Paper 760317.

[32] Downing, S. D., and Socie, D. F. (1982), "Simple rainflow counting algorithms," *International Journal of Fatigue*, 4(1), 31-40.

[33] Escamilla, P.J. and Mort, N. (2002), "Multisensor data fusion architecture based on adaptive Kalman filters and fuzzy logic performance assessment", *Proc. of 5th International Conference on Information Fusion*, Annapolis, USA.

[34] Farrar, C. R. (2001), "Historical overview of structural health monitoring", Lecture Notes on Structural Health Monitoring using Statistical Pattern Recognition.

[35] Farrar, C. R., Allen, D. W., Ball, S., Masquelier, M. P., and Park, G. (2005), "Coupling Sensing Hardware with Data Interrogation Software for Structural Health Monitoring", *Proc. of the 6th International Symposium on Dynamic Problems of Mechanics (DINAME)*, Ouro Preto, Brazil, February 29–March 4.

[36] Farrar, C.R., Allen, D.W., Park, G., Ball, S., and Masquelier, M.P. (2006), "Coupling sensing hardware with data interrogation software for structural health monitoring", *Shock and Vibration*, 13(4), 519-530.

[37] Fisher, J.W. and Roy, S. (2011), "Fatigue of steel bridge infrastructure", *Structure and Infrastructure Engineering*, 7(7-8), 457-475.

[38] Fisher, J.W. (1984), "Fatigue and Fracture in Steel Bridges: Case Studies", Wiley. New York.

[39] Flood, I. (2000), "Developments in Weigh-in-Motion Using Neural Nets", *Computing in Civil and Building Engineering*, Vol. 2, 1133-1140.

[40] Fujino, Y., Murata, M., Okano, S., and Takeguchi, M. (2000), "Monitoring system of the Akashi Kaikyo Bridge and displacement measurement using GPS," *Proc. of SPIE, nondestructive evaluation of highways, utilities, and pipelines IV*, 229–236.

[41] Galbreath J.H., Townsend C.R., Mindell S.W., Hamel M.J., Esser B., Hutson D., Arms S.W. (2003), "Civil structure strain monitoring with power-efficient, high speed wireless sensor networks", *4th international workshop on structural health monitoring*, Stanford, CA.

[42] Gao, Y. and Spencer Jr., B.F. (2007), "Experimental Verification of a Distributed Computing Strategy for Structural Health Monitoring", *Smart Structures and Systems*, 3(4), 455-474.

[43] Gao, Y. and Spencer Jr., B.F. (2008), "Structural health monitoring strategies for smart sensor networks", *NSEL Report Series. No. 011*, University of Illinois at Urbana-Champaign, (http://hdl.handle.net/2142/8802).

[44] Gao, Y., Spencer Jr., B.F., Ruiz-Sandoval, M. (2006), "Distributed computing strategy for structural health monitoring", *Journal of Structural Control and Health Monitoring*, 13(1), 488-507.

[45] Garmin International Inc. (2008), "GPS 20x data sheet", Olathe, KS, USA.

[46] Gavin, H.P., Morales, R., and Reilly, K. (1998), "Drift-freeintegrators", *Review of Scientific Instruments*, 69 (5), 2171–2175.

[47] Genrich, J.F., Bock, Y. (2006), "Instantaneous geodetic positioning with 10-50Hz GPS measurements: noise characteristics and implications for monitoring networks," *Journal of Geophysical Research*, Vol. 111 (B03403), Doi 10.1029/2005Jb003617.

[48] GlobalTop Technology Inc (2010), "Gms-u1LP GPS module data sheet", Tainan, Taiwan, http://www.gtop-tech.com.

[49] Gnawali, O., Greenstein, B., Jang, K.-Y., Joki, A., Paek, J., Vieira, M., Estrin, D., Govindan, R., and Kohler. E. (2006), "The TENET architecture for tiered sensor networks", *ACM Conference on Embedded Networked Sensor Systems* (SenSys).

[50] Guan, H. and Karrbhari, V.M. (2008), "Improved damage detection method based on element modal strain damage index using sparse measurement", *Journal of Sound and Vibration*, vol. 309, 465-494.

[51] Guo, J., Xu, L., Dai, L., McDonald, M., Wu, J. and Li, Y. (2005), "Application of real-time kinematic global positioning system in bridge safety monitoring", *Journal of Bridge Engineering ASCE*, 10(2), p.163-168.

[52] Hao, S. (2010), "I-35W Bridge Collapse", *Journal of Bridge Engineering-ASCE*, 15(5), 608-614.

[53] Harvey, A.C. (1991), "Forecasting, structural time series models, and the Kalman filter", Cambridge University Press.

[54] Hautamaki C., Zurn S., Mantell S.C., and Polla D.L. (1999), "Experimental Evaluation of MEMS Strain Sensors Embedded in Composites", *Journal of Microelectromechanical Systems*, Vol. 8, No. 3, 272-279.

[55] Heather, M., O'Connell, R.J., Dexter, P.E., and Bergson, P.M. (2001), "Fatigue Evaluation of the Deck Truss of Bridge 9340", Report to Minnesota DOT.

[56] Hong, Y.H., Kim, H.K., Lee, H.S. (2010), "Reconstruction of dynamic displacement and velocity from measured accelerations using the variational statement of an inverse problem", *Journal of Sound and Vibration*, 329(23), 4980–5003.

[57] Inaudi, D., Casanova, N, and Vurpillot, S. (1999), "Bridge Deformation Monitoring with Fiber Optic Sensors", *Proc. of the IABSE Symposium Structures for the Future-The Search for Quality*, Rio de Janeiro, Brazil.

[58] Intel Corporation Research (2005), "Intel Mote2 Overview, Version 3.0", Santa Clara, CA.

[59] James, G. H., Carne, T.G., and Lauffer, J.P. (1993), "Dynamic testing and system identification of a multispan highway bridge," SAND92-1666, UC-261, Sandia National Laboratories, Sandia, N.M.

[60] Jang, S., Sim, S. and Spencer Jr., B.F. (2007), “Structural damage detection using static strain data”, *Proc. of World Forum on Smart Materials and Smart Structures Technology*, China.

[61] Jang, S.A., Dahal, S., Contreas, G.K., Fitch, J., Karamavros, J., and Bansal, R. (2012), “Hybrid structural health monitoring using wireless multi-scale sensors”, *Proc. of SPIE*, San Diego.

[62] Jang, S.A., Jo, H., Cho, S., Mechitov, K.A., Rice, J.A., Sim, S.H., Jung, H.J., Yun, C.B., Spencer Jr., B.F., and Agha, G. (2010), “Structural health monitoring of a cable-stayed bridge using smart sensor technology: deployment and evaluation”, *Smart Structures and Systems*, 6(5-6), 439-459.

[63] Jensen, S. (2003), “Summary Outlook to 2005 for the European Construction Market”, Website: <http://www.cifs.dk/scripts/artikel.asp?id=775&lng=2>

[64] Jetto, L., Longhi, S., and Vitali, D. (1999), “Localization of a wheeled mobile robot by sensor data fusion based on a fuzzy logig adapted Kalman filter”, *Control Engineering Practice*, 7, 763-771.

[65] Juang, J.N. and Pappa, R.S. (1985), “An eigensystem realization algorithm for modal parameter identification and model reduction”, *Journal of Guidance, Control, and Dynamics*, 8(5), 620-627.

[66] Kalman, R.E. (1960), "A new approach to linear filtering and prediction problems", *Journal of Basic Engineering*, 82(1), 35–45.

[67] Kasdin, N.J. (2005), “Discrete simulation of colored noises and stochastic process and 1/f α power law noise generation,” *Proc. of the IEEE*, Vol. 83(5), 802-827.

[68] Kijewski-Correa, T., Su, S., Abittan, E. and Antsaklis, P.J. (2006), "On the use of heterogeneous, wireless sensor networks for damage assessment in bridges under unknown excitations", *Proc. 4th World Conference on Structural Control and Monitoring*.

[69] Kim S., Pakzad S., Culler D., Demmel J., Fenves G., Glaser S. and Turon, M. (2007), “Health monitoring of civil infrastructures using wireless sensor networks”, *Proc. 6th International Conference on Information Processing in Sensor Networks*, 254-263.

[70] Kim, J., Lynch, J.P., Lee, J., and Lee, C. (2011), "Truck-based mobile wireless sensor networks for the experimental observation of vehicle-bridge interaction", *Smart Material and Structures*, 20, 1-14.

[71] Kim, S., Fonseca, R., Kumar Dutta, P., Tavakoli, A., Culler, D.E., Levis, P., Shenker, S. and Stoica, I. (2006), "Flush: A Reliable Bulk Transport Protocol for Multihop Wireless Network", EECS Department, University of California, Berkeley, Technical Report No. UCB/EECS-2006-169.

[72] Kim, S., Pakzad, S.N., Culler, D., Demmel, J.,Fenves, G.L., Glaser, S. and Turon, M. (2007), "Health Monitoring of Civil Infrastructures Using Wireless Sensor Networks", *Proc. of the 6th International Conference on Information Processing in Sensor Networks (IPSN 2007)*, Cambridge, MA,.

[73] Kuhn, B., Lukic, M., Nussbaumer, A., Gunther, H.-P., Helmerich, R., Herion, S., Kolstein, M.H., Walbridge, S., Androic, B., Dijkstra, O., and Bucak, O. (2008), "Assessment of Existing Steel Structures: Recommendations for Estimation of Remaining Fatigue Life", Joint Report Prepared under the JRC-ECCS cooperation agreement for the evolution of Eurocode 3 (programme of CEN / TC 250).

[74] Kurata, M., Kim, J., Zhang, Y., Lynch, J.P., Linden, G.W., Jacob, V., Thometz, E., Hipley, P. and Sheng, L.H. (2010), "Long-term assessment of an autonomous wireless structural health monitoring system at the New Carquinez Suspension Birdge", *Proc. of SPIE*, San Diego.

[75] Law, S.S., Li, X.Y., Zhu, X.Q. and Chan, S.L. (2005), "Structural damage detection from wavelet packet sensitivity," *Engineering Structures*, 27(9), 1339-1348.

[76] Lee, H.S., Hong, Y.H., and Park, H.W. (2010), "Design of an FIR filter for the displacement reconstruction using measured acceleration in low-frequency dominant structures", *International Journal for Numerical Methods in Engineering*, 82, 403–434.

[77] Lee, K. and Yun, C. (2008), "Extended Kalman filter for identification of nonlinear earthquake responses of bridges", *Proc. of the 17th World Congress: The International Federation of Automatic Control*, Seoul, Korea.

[78] Lesniak, A., Danek, T., and Wojdyla, M. (2009), "Application of Kalman Filter to Noise Reduction in Multichannel Data", *Schedae Informaticae*, 17-18, 63-73.

[79] Li, X. Rizos, C. Ge, L. Ambikairajah, E. Tamura, Y. Yoshida, A. (2006), "The Complementary Characteristics of GPS and Accelerometer in Monitoring Structural Deformation", *Inside GNSS*, 48-55

[80] Liu, Y., He, Y., Li, M., Wang, J., Liu, K., Mo, L., Dong, W., Yang, Z., Xi, M., Zhao, J. (2011), "Does wireless sensor network scale? a measurement study on greenorbs", *Proc. of IEEE INFOCOM* , pp. 873–881.

[81] Lund, R. and Alampalli, S. (2004), "Estimating Fatigue Life of Patroon Island Bridge Using Strain Measurements", Special Report 142, Transportation Research and Development Bureau, New York DOT.

[82] Lynch, J.P., & Loh, K.J. (2006), "A summary review of wireless sensors and sensor networks for structural health monitoring", *The Shock and Vibration Digest*, 38(2), 91-28.

[83] Lynch, J.P., Law, K.H., Kiremidjian, A.S., Kenny, T.W., Carryer, E., and Partridge, A. (2001), "The Design of a Wireless Sensing Unit for Structural Health Monitoring", *Proc. of the 3rd International Workshop on Structural Health Monitoring*, Stanford, CA, September 12–14.

[84] Lynch, J.P., Wang, Y., Law, K.H., Yi, J.-H., Lee, C.G., and Yun, C.B. (2005), "Validation of a large-scale wireless structural monitoring system on the Geumdang bridge", *Proc. of the Int. Conference on Safety and Structural Reliability*, Rome, Italy.

[85] Lynch, J.P., Sundararajan, A., Law, K.H., Kiremidjian, A.S., and Carryer, E. (2004), "Embedding damage detection algorithms in a wireless sensing unit for operational power efficiency", *Smart Materials and Structures*, 13(4), 800-810.

[86] Lynch, J.P., Wang, Y., Loh, K., Yi, J.H. and Yun, C.B. (2006), "Performance monitoring of the Geumdang Bridge using a dense network of high-resolution wireless sensors", *Smart Mater. Struct.*, 15(6), 1561-1575.

[87] Maroti, M., Kusy, B., Simon, G., and Ledeczi, A. (2004). "The flooding time synchronization protocol", *Proc. of 2nd International Conference on Embedded Networked Sensor Systems*, Baltimore, MD, 39-49.

[88] Matsuishi, M. and Endo, T. (1968), "Fatigue of Metals Subject to Varying Stress", Japan Society of Mechanical Engineers.

[89] Matsuzaki R. and Todoroki A. (2005), "Wireless strain monitoring of tires using electrical capacitance changes with an oscillating circuit", *Sensors and Actuators*, A119, 323-331.

[90] MAXIM Inc. (2003), "MAX4194, Micropower precision instrumentation amplifier", Sunnyvale, CA.

[91] MAXIM Inc. (2006), "MAX5479, Dual-nonvolatile digital potentiometer", Sunnyvale, CA.

[92] Mechitov, K., Kim, W., Agha, G., and Nagayama, T. (2004), "High-frequency distributed sensing for structure monitoring", *Proc. of 1st Int. Workshop on Networked Sensing Systems*, Tokyo, Japan, 101–105.

[93] MEMSIC (2006), "Imote2, Advanced wireless sensor network node platform", Andover, MA.

[94] MEMSIC (2007), "MICA2, Wireless measurement system", Andover, MA.

[95] Meng, X., Dodson, A.H., and Roberts, G.W. (2007), "Detecting bridge dynamics with GPS and tri-axial accelerometers", *Eng Struct*, 29, 3178–3184

[96] Meng, Q., Sun, Y., and Cao, Z. (2000), "Adaptive extended Kalman filter-based mobile robot localization using sonar", *Robotica*, 18, 459-473.

[97] Meng, X., Roberts, G.W., Dodson, A.H., Cosser, E., Barnes, J. and Rizos, C. (2004), "Impact of GPS satellite and pseudolite geometry on structural deformation monitoring: analytical and empirical studies", *Journal of Geodesy*, Vol. 77, 809-822.

[98] Meo, M., Zumpano, G., Meng, X.L. (2006), "Measurements of dynamic properties of a medium span suspension bridge by using the wavelet transforms", *Mech Syst Signal Pr*, 20, 1112–1133.

[99] MicroStrain Inc. (2011), "SG-Link–mXRS, Wireless strain node", Williston, VT.

[100] MidasIT (2009), http://www.midasit.com

[101] Miller, T., Spencer Jr., B.F., Li, J., Jo, H. (2010), "Solar energy harvesting and software enhancements for autonomous wireless smart sensor networks", *NSEL Report, Series 022*, University of Illinois at Urbana-Champaign.

[102] Miner, M.A. (1945), "Cumulative damage in fatigue", *Applied Mechanics Transactions (ASME)*, 12(3), 159-164.

[103] Mitchell, K., Rao, V.S., and Pottinger, H.J. (2002), "Lessons Learned About Wireless Technologies for Data Acquisition", *Proc. of the SPIE*, San Diego, CA.

[104] Mohammadi, J., Guralnick, S.A., Polepeddi, R. (1998), "Bridge fatigue life estimation from field data", *Practice Periodical on Structural Design and Construction*, 3(3), 128-133.

[105] Mori, T., Lee, H.-H., and Kyung, K.-S. (2007), "Fatigue life estimation parameter for short and medium span steel highway girder bridges", *Engineering Structures*, 29, 2762-2774.

[106] Moses F. (1979), "Weigh-In-Motion system using instrumented bridges", *ASCE Transportation Engineering Journal*, 105, 233-249.

[107] Meyer, J., Bischoff, R., Feltrin, G., and Motavalli, M. (2010), "Wireless sensor networks for long-term structural health monitoring", *Smart Structures Syst.*, 6(3), 263–275.

[108] Kim, N.-S. and Cho, N.-S. (2004), "Estimating deflection of a simple beam model using fiber optic Bragg-grating sensors", *Experimental Mechanics*, 44 (4), 433–439.

[109] Nagayama, T. and Spencer Jr., B.F. (2007), "Structural health monitoring using smart sensors", *NSEL Report, Series 001*, University of Illinois at Urbana-Champaign, http://hdl.handle.net/2142/3521.

Nagayama, T., Abe, M., Fujino, Y. and Ikeba, K. (2005), "Structural identification of a non-proportionally damped system and its application to a full-scale suspension bridge", *Journal of Structural Engineering*, 131(10), 1536-1545.

[110] Nagayama, T., Moinzadeh, P., Mechitov, K., Ushita, M., Makihata, N., Leiri, M., Agha, G., Spencer Jr., B.F., Fujino, Y., and Seo, J.-W. (2010), "Reliable multi-hop communication for structural health monitoring", *Smart Structures and Systems*, Vol. 6(5-6), 481-504.

[111] Nagayama, T., Ruiz-Sandoval, M., Spencer Jr., B.F., Mechitov, K.M., and Agha, G. (2004), "Wireless Strain Sensor Development for Civil Infrastructure", *Proc. of First International Workshop on Networked Sensing Systems*, Tokyo, Japan, 97-100.

[112] Nagayama, T., Ushita, M., Fujino, Y., Ieiri, M., and Makihata, N. (2010). "The combined use of low-cost smart sensors and high accuracy sensors to apprehend structural dynamic behavior", *Proc. of SPIE Smart Structures/NDE*, San Diego, CA, 764716, (doi: 10.1117/12.848323).

[113] Nakamura S. (2000), "GPS measurement of wind-induced suspension bridge girder displacements", *Journal of Structural Engineering ASCE*, 12, 1413–1419

[114] National Instruments (2007a), "NI SCXI-1520, 8-Ch Universal strain gauge input module", Austin, TX.

[115] National Instruments (2007b), "NI SCXI-1314, Front-mounting Wheatstone bridge terminal block", Austin, TX.

[116] National Instruments (2011), "NI WSN-3214, 4ch strain gage node", Austin, TX.

[117] Ni, Y. Q., Ye, X. W., and Ko, J. M. (2010), "Monitoring-based fatigue reliability assessment of steel bridges: analytical model and application", *Journal of Structural Engineering*, 136(12), 1563-1573.

[118] Nickitopoulou A, Protopsalti K, Stiros S. (2006), "Monitoring dynamic and quasi-static deformations of large flexible engineering structures with GPS: accuracy, limitations and promises", *Engineering Structures*, 28(10), 1471–1482.

[119] Nikaido, M. and Tamaru, N. (2003), "Noise reduction for gray image using Kalman filter", *Proc. of SICE Conference*, Fukui, Japan.

[120] O'Brien E.J, Znidaric A, Dempsey A.T. (1999), "Comparison of two independently developed Bridge Weigh-In-Motion systems. Heavy Vehicle Systems", *Int. J. of Vehicle Design*, 6(1/4), pp. 147-162.

[121] O'connor S., Kim J., Lynch J.P., Law K.H., Salvino L. (2010), "Fatigue life monitoring of metallic structures by decentralized rainflow counting embedded in a wireless sensor

network", *Proc. of ASME Conference on Smart Materials, Adaptive Structures and Intelligent Systems (SMASIS)*, 3745.

[122] Ojio, T. and K. Yamada. (2002), "Bridge Weigh-In-Motion Systems Using Stringers of Plate Girder Bridges," *Proc. of the Third International Conference on Weigh-In-Motion*, 209-218.

[123] Okamura, H. and Sakai, S. and Susuki, I. (1979), "Cumulative fatigue damage under random loads", *Fatigue Engeering of Materials and Structures*, 1(4), pp. 409-419

[124] Pakzad, S.N. and Fenves, G.L. (2004), "Structural Health Monitoring Applications Using MEMS Sensor Networks", *Proc. of the 4th International Workshop on Structural Control*, Columbia University, New York, 47-56.

[125] Pakzad, S.N., Fenves, G.L., Kim, S. and Culler, D.E. (2008), "Design and implementation of scalable wireless sensor network for structural monitoring", *J. Infrastruct. Eng.*, 14(1), 89-101.

[126] Palmgren, A. (1924), "Die Lebensdauer von Kugallagern," *VDI-Zeitschrift*, 68(14): 339-341.

[127] Papadimitriou, C., Fritzen, C.P., Kraemer, P., and Ntotsios, E. (2011), "Fatigue predictions in entire body of metallic structures from a limited number of vibration sensors using Kalman filtering", *Structural Control and Health Monitoring*, 18(5), 554-573.

[128] Park, J.W., Jung, H.J., Jo, H., and Spencer Jr., B.F. (2012), "Feasibility Study of Micro Wind Turbines for Powering Wireless Sensors in a Cable-stayed Bridge", *Energies*, 5, 3450-3464.

[129] Park, K.T. and Kim, S.H. (2005), "The determination of bridge displacement using measured acceleration", *Engineering Structures*, 27, 371-378.

[130] Quickfilter Technologies, Inc. (2007), "QF4A512, 4-Ch programmable signal conditioner", Allen, TX.

[131] Rahimi, M., Hardik, S., Sukhatme, G. S., Heideman, J., & Deborah, E. (2003), "Studying the feasibility of energy harvesting in a mobile sensor networks", *Proc. of IEEE Int. Conference on Robotics and Automation*, Taipai, Taiwan.

[132] Rahmatalla, S. and Eun, H.C.A. (2010), "Damage detection approach based on the distribution of constraint forces predicted from measured flexural strain", *Smart Mater. Struct*., 19, 1-9.

[133] Reid, R.L. (2010), "Damaged Eyebar Section Replaced on San Francisco- Oakland Bay Bridge", *Civil Engineering* , 18-23.

[134] Rice, J.A. and Spencer Jr., B.F. (2008), "Structural health monitoring sensor development for the Imote2 platform," Proc. of SPIE, San Diego.

[135] Rice, J.A. and Spencer Jr., B.F. (2009), "Flexible smart sensor framework for autonomous full-scale structural health monitoring", *NSEL Report Series 018*, University of Illinois at Urbana-Champaign.

[136] Rice, J.A., Mechitov, K., Sim, S.H., Nagayama, T., Jang, S., Kim, R., Spencer Jr., B.F., Agha, G. and Fujino, Y. (2010), "Flexible smart sensor framework for autonomous structural health monitoring", *Smart Structures and Systems*, Vol. 6(5-6), 423-438.

[137] Roberts G W, Meng X L, Dodson A H. (2004), "Integrating a Global Positioning System and accelerometers to monitor the deflection of bridges", *Journal of Survey Engineering ASCE*, 130, 65–72.

[138] Roumeliotis, S.I. and Bekey, G.A. (2000), "Bayesian estimation and Kalman filtering: A unified framework for mobile robot localization", *Proc. of the 2000 IEEE International Conference on Robotics and Automation*, San Fransisco, CA, pp. 2985-2992.

[139] Ruiz-Sandoval, M.E., Spencer Jr., B.F., and Kurata, N. (2003), "Development of a high sensitivity accelerometer for the mica platform", *Proc. of the 4th Int. Workshop on Structural Health Monitoring*.

[140] Sadegh, M. and Nazar, M. (2009), "A comparative study of different Kalman Filtering methods in multi sensor data fusion", *Proc. of the International Multi Conference of Engineering and Computer Scientists*, Hong Kong.

[141] Salgado, A. and Esteva, L. (1996), "System identification and response prediction of nonlinear structural systems", *Proc. of the 11th World Conference on Earthquake Engineering*, 1416.

[142] Sasiadek, J.Z. and Hartana, P. (2000), "Odometry and sonar data fusion for mobile robot navigation", *Proc. of the 6th IFAC Symposium on Robot Control-SYROCO2000*, Vienna, Austria.

[143] Sato, T. and Kaji, K. (2001), "Adaptive Monte Carlo filter and structural identification", *Proc. of the 1st International Conference on Monte Carlo Simulation*, pp. 441-447.

[144] Shin, S.B. and Yun, B.K. (2008), "Identification of dynamic displacement from measured strains", *Journal of Korea Inst Struct Maint Ins*, 447–451

[145] Silicon Designs, Inc., "Model 1221 Low Noise Analog Accelerometer", Issaquah, WA (2007).

[146] Sim, S.H. and Spencer Jr., B.F. (2009), "Decentralized strategies for monitoring structures using wireless smart sensor networks", *NSEL Report Series 019*, University of Illinois at Urbana-Champaign.

[147] Sim, S.H., Carbonell-Marquez, J.F., Spencer Jr., B.F., and Jo, H. (2011), "Decentralized random decrement technique for efficient data aggregation and system identification in wireless smart sensor networks", *Probabilistic Engineering Mechanics*, 26, 81-91.

[148] Sim, S.H., Spencer Jr., B.F., and Nagayama, T. (2011), "Multimetric sensing for structural damage detection", *Journal of Engineering Mechanics ASCE*, 137(1), pp. 22-30, doi:10.1061/(ASCE)EM.1943-7889.0000199.

[149] Sim, S.H., Spencer Jr., B.F., Zhang, M., and Xie, H. (2010), "Automated decentralized modal analysis using smart sensors", *Journal of Structural Control and Health Monitoring*, 17(8), 872-894, (doi: 10.1002/stc.348).

[150] Siriwardane, S.A.S.C., Ohga, M., Dissanayake, P.B.R. and Kaita, T. (2010), "Structural Appraisal based Different Approach to Estimate the Remaining Fatigue Life of Railway Bridges", *Structural Health Monitoring*, 9, 323-339.

[151] Small, E.P., Philbin, T., Fraher, M., and Romack, G.P. (1999), "The current status of bridge management system implementation in the United States", *Proc. of 8th International Bridge Management Conference*, Denver, Colorado.

[152] Smyth, A. and Wu, M.L. (2007), "Multi-rate Kalman filtering for the data fusion of displacement and acceleration response measurements in dynamic system monitoring", *Mechanical Systems and Signal Processing*, 21(2),706–723.

[153] Snyder, R. and F. Moses. (1985), "Application of In-Motion Weighing Using Instrumented Bridges", *Transportation Research Record*, 1048, 83-88.

[154] Sobczyk, K. and Spencer Jr., B.F. (1992), "Random fatigue: from data to theory", Academic Press.

[155] Sohn, H., Farrar, C. R., Hemez, F. M., Shunk, D. D., Stinemates, D. W. and Nadler B. R. (2003), "A review of structural health monitoring literature: 1996-2001", *Los Alamos National Laboratory Report*, LA-13976-MS.

[156] Solh, M. (2006), "An Adaptive Kalman Filter Approach for Infrasound Signal Noise Reduction", Master Thesis, Florida Institute of Technology.

[157] Spencer Jr., B.F., Ruiz-Sandoval, M. and Kurata N. (2004), "Smart Sensing Technology: Opportunities and Challenges", *Journal of Structural Control and Health Monitoring*, 11(4), 349-368.

[158] STMicroelectronics (2005), "LIS2L02AL MEMS Inertial Sensor", Geneva, Switzerland.

[159] STMicroelectronics (2008), "LIS344ALH 3-axes MEMS Inertial Sensor", Geneva, Switzerland.

[160] Straser, E. G and Kiremidjian, A. S. (1998), "A modular, wireless damage monitoring system for structures," Report No. 128, John A. Blume Earthquake Engineering Center, Department of Civil and Environmental Engineering, Stanford University, Stanford, CA,

[161] Su, D., Fujino, Y., Nagayama, T., Hernandez, J., and Seki, M. (2009), "Vibration of reinforced concrete viaducts under high-speed train passage: measurement and prediction including train-viaduct interaction", *Structure and Infrastructure Engineering: Maintenance, Management, Live-Cycle Design and Performance*, 1744-8980.

[162] Swartz, R.A., Jung, D., Lynch, J.P., Wang, Y., Shi, D. and Flynn, M.P. (2005), "Design of a wireless sensor for scalable distributed in-network computation in a structural health monitoring system", *Proc. of the 5th International Workshop on Structural Health Monitoring*, Stanford, CA, June.

[163] Tanner, N.A., Wait, J.R., Farrar, C.R., and Sohn, H. (2003), "Structural health monitoring using modular wireless sensors", *Journal of Intelligent Material Systems and Structures*, 14(1), 43-56.

[164] Tata U., Huang H., Carter R.L., Chiao J.C. (2009), "Exploiting a patch antenna for strain measurements", *Measurement Science and Technology*, 20, 015201 (7pp).

[165] Tokyo Sokki Kenkyujo Co., Ltd. (2005), "FGMH-1, Strain checker", Tokyo, Japan.

[166] Tokyo Sokushin Co., Ltd. (2010), http://www.to-soku.co.jp/, Tokyo, Japan.

[167] Turner, R., Deisenroth, M.P., and Rasmussen, C.E., (2009), "System Identification in Gaussian Process Dynamical Systems", *Proc. of the Nonparametric Bayes Workshop at NIPS 2009*, Whistler, Canada.

[168] U.S. Department of Transportation (2010), "2010 Status of the National Highways, Bridges, and Transit: Conditions and Performance", Report to Congress.

[169] Vurpillot, S., Inaudi, D., and Scano, A. (1996), "Mathematical model for the determination of the vertical displacement from internal horizontal measurements of a bridge", *Proc. of SPIE*, San Diego,USA

[170] Wang, Y., Lynch, J. P., and Law, K. H. (2005), "Wireless Structural Sensors Using Reliable Communication Protocols for Data Acquisition and Interrogation", *Proc. of the 23rd International Modal Analysis Conference (IMAC XXIII)*, Orlando, FL, January 31–February 3.

[171] Watson, C., Watson, T., and Coleman, R. (2007), "Structural monitoring of cable-stayed bridge: Analysis of GPS versus Modeled Deflections", *Journal of Survey Engineering ASCE*, 133, 23–28.

[172] Weng, J.-H., Loh, C.-H., Lynch, J.P., Lu, K.-C., Lin, P.-Y., and Wang, Y. (2008), "Output-only modal identification of a cable-stayed bridge using wireless monitoring systems", *Eng. Struct.*, 30(7), 1820-1830.

[173] Whelan, M. J., Gangone, M. V., Janoyan, K. D., Hoult, N. A., Middleton, C. R. & Soga, K. (2010), "Wireless operational modal analysis of a multi-span prestressed concrete bridge for structural identification", *Smart Material and Structures*, 6(5-6), 579–93.

[174] Whelan, M.J. and Janoyan, K.D. (2009), "Design of a robust, high-rate wireless sensor network for static and dynamic structural monitoring", *Journal of Intelligent Material Systems and Structures*, Vol. 20(7), 849-864.

[175] Wong, K.Y. (2004), "Instrumentation and health monitoring of cable-supported bridges", *Structural Control and Health Monitoring*, 11(2), 91-124.

[176] Wong, K.Y. (2007), "Design of a structural health monitoring system for long-span bridges", *Structure and Infrastructure Engineering*, 3,169–185.

[177] Yang, J.N., Lin, S., Huang, H., and Zhou, L. (2006), "An adaptive extended Kalman filter for structural damage identification", *Structural Control and Health Monitoring*, 13(4), 849-867.

[178] Ye, X., Zhu, T., Yan, Q., and Wang, W. (2011), "Experimental verification of decentralized approach for model identification based on wireless smart sensor network", *Advanced Materials Research*, 3(11), 291-294, (doi:10.4028 /www.scientific.net/AMR.291-294.3).

[179] Yi, T,H,, Li, H.N., and Gu, M. (2010), "Full scale measurement of dynamic response of a suspension bridge subjected to environmental loads using GPS technology", *Sci China Tech*, 53, 469–479

[180] Yin, J., Syrmos, V.L., and Yun, D.Y. (2000), "System identification using the extended Kalman filter with applications to medical imaging", *Proc. of the 2000 IEEE American Control Conference*, Chicago, USA, pp. 2957-2961.

[181] Yun, C-B., Lee, J-J., Kim, S-K., and Kim, J-W. (2003), "Recent R&D Activities on Structural Health Monitoring for Civil Instrastructures in Korea", *KSCE Journal of Civil Engineering*, 7(6), 637-645.

[182] Zhou, Y.E. (2006), "Assessment of bridge remaining fatigue life through field strain measurement", *Journal of Bridge Engineering-ASCE*, 11(6), 737-744.

[183] Zimmerman, A.T., Shiraishi, M., Swartz, R.A., and Lynch, J.P. (2008), "Automated modal parameter estimation by parallel processing within wireless monitoring systems", *Journal of Infrastructure Systems*, 14(1), 102-113.

[184] ZMD AG (2004), "ZMD31050, Advanced differential sensor signal conditioner", Dresden, Germany.

[185] Znidaric, A., Lavric, I., and Kalin, J. (2008), "Measurements of bridge dynamics with a bridge weigh-in-motion system", *Proc. of 5th International Conference on Weigh-in-Motion (ICWIM5)*, ISTE/Hermes, London.

[186] Zonta, D., Wu, H., Pozzi, M., Zanon, P., Ceriotti, M., Mottola, L., Picco, G.P., Murphy, A.L., Guna, S., and Corra, M. (2010), "Wireless sensor networks for permanent health monitoring of historic buildings", *Smart Structures and Systems*, 6(5-6), 595-618.